STUDY AND CHARACTERIZATION OF MAGNETIC AND MULTIFERROIC MATERIALS BY FIRST-PRINCIPLES CALCULATIONS

ANDRÉS CAMILO GARCÍA CASTRO

Faculté des Sciences
Université de Liège
&
Centro de Investigación y de Estudios Avanzados IPN

Abril 2016

STUDY AND CHARACTERIZATION OF MAGNETIC AND MULTIFERROIC MATERIALS BY FIRST-PRINCIPLES CALCULATIONS

ANDRÉS CAMILO GARCÍA CASTRO

Supervisors:
Prof. Aldo Humberto Romero Castro, CINVESTAV-Querétaro
Dr. Eric Bousquet, Université de Liège (Secretary)
Jury Members:
Prof. Nicola Spaldin, ETH-Zürich
Prof. Philippe Ghosez, Université de Liège (President)
Prof. Sergio Jiménez Sandoval, CINVESTAV-Querétaro
Prof. Rebeca Castanedo Pérez, CINVESTAV-Querétaro
Prof. Arturo Mendoza Galván, CINVESTAV-Querétaro

—-

Ph.D-Candidate
Physics Department
Université de Liège
&
Centro de Investigación y de Estudios Avanzados IPN

Abril 2016

Dedicated to my father and my grandfather memory that always encouraged me to follow my dreams and be consistent with it.

Dedicada a mi padre y a la memoria de mi abuelo que siempre me motivaron a seguir mis sueños y actuar consistentemente con ellos.

ABSTRACT

In the last fifteen years, multifunctional materials, and more specifically, multifunctional oxides have been widely studied due to its wide range of properties. Properties that go from superconductivity to ferroelectricity passing through magnetism and multiferroism have been reported. Nonetheless, the fluoride family was left aside and little information is known about its possible ferroelectricity or multiferroism. In this Ph.D thesis, we explored the electronic, vibrational, structural and magnetic properties of fluoride perovskite-based compounds. To such purposes, We performed *ab-initio* calculations based in the density-functional theory (DFT) as implemented in VASP and CRYSTAL codes.

Our first step was to perform vibrational analyses in a large set of fluoroperovskites $\mathsf{ABF_3}$. Based on the results, we proposed a model that establishes an A-site geometrically driven ferroelectric vibrational instability in fluorides. Our studies reveal a different behavior as a function of isotropic pressure for $NaBF_3$ with respect to oxides (*e.g.* $BaTiO_3$) with B = Ca, V, Mn, and Zn. For these compounds we found an increase of the ferroelectric instability as a function of hydrostatic pressure. This probably due to the "transformation" of eigendisplacements responsible for the mode that creates the corresponding instability. In particular, an increase of ionic A-site radii present a strong influence in FE-polar instability.

We also have shown, based on our first-principles calculations and symmetry theory analysis that all post-perovskites $\mathsf{ABX_3}$ with an active magnetic B-site cation can exhibit a noncollinear magnetic configuration, which happens to be allowed by symmetry. With these findings, the magnetic properties found experimentally were clarified for this particular high-pressure phase perovskite found at the Earth's mantle. Additionally, We have predicted that $NaMnF_3$ suffers a structural phase transition under pressure to a post-perovskite phase, where noncollinear ferromagnetism and large magnetic moment components are obtained within this high-pressure phase..

Going beyond, We have shown that it is possible to achieve multiferroic-induced state in $NaMnF_3$ under epitaxial strain at compressive or tensile strain. We found a nonlinear behavior of the ferroelectric instability as well as a non-linear piezoelectric response as a function of epitaxial strain. The later completely different as the one found in oxide perovskites. Similarly, an out-of-plane polarization was observed, a property that has not been observed in oxides. We observed a Na + Mn sites cooperative ferroelectric ordering for compressive strain against a pure A-site geometrically driven ferroelectricity at tensile values of the ac-strain.

Magnetic ordering reveals a non-collinear ground state with the $G_zA_xF_y$ representation. Even more interesting, and non-linear magnetoelectric coupling was found under the strained $Pna2_1$ ground state becoming the first known multiferroic/magnetoelectric perovskite fluoride.

Later, in order to go further, We studied the electronic and structural properties of novel heterostructures based on oxyfluorides $(KTaO_3)_n/(KBF_3)_l$ B = Zn and Ni interfaces. We found that the orbital levels splitting at the interfaces is strongly modified by the O–B–F coordination. The polar catastrophe phenomena also takes place in the oxyfluoride interfaces similarly to oxide heterostructure, however, we found that less number of layers are needed in order to achieve the insulator-to-metal transition when comparing to $SrTiO_3/LaAlO_3$ superlattices. We observed that the magnetism in the $KTaO_3/KNiF_3$ exhibits a moment magnitude modulations. Nevertheless, the magnetic structure keeps the G-type antiferromagnetism such as in the bulk former compound. Surprisingly, we observed a large k^3-Rashba type splitting in at the oxyfluoride interfaces, at least four times larger than the one reported in $SrTiO_3/LaAlO_3$ interface and twice of the $KTaO_3$-based transistor.

In conclusion, we observed that fluorides-perovskites are good prototypes for multifunctional properties as oxides. Therefore, based on the results reported in this thesis, we expect that experimentalist and theoreticians can be motivated in characterization of fluorides, which can lead to a new set of unexplored materials with potential novel applications in electronics.

RÉSUMÉ

Durant les quinze dernières années, les matériaux multifonctionnels et plus particulièrement les matériaux multifonctionnels à base d'oxyde ont été extrêmement étudiés du fait de leurs propriétés très diverses. Ces propriétés vont de la supraconductivité à la ferroélectricité en passant par le magnétisme ou le multiferroïsme. Dans cet engouement pour les oxydes, la famille des fluorites a cependant été délaissée de telle manière que peu d'informations sont connues quant à leur propension à être ferroélectrique ou multiférroïque. Dans cette thèse de doctorat, nous nous sommes proposés d'explorer les propriétés électroniques, vibrationnelles, structurales et magnétiques des matériaux perovskites à base de fluor. Cette étude repose principalement sur des calculs *ab-initio* basés sur la théorie de la fonctionnelle de la densité. Les codes de calcul utilisés sont principalement VASP et CRYSTAL.

Dans un premier temps nous avons analysé les propriétés vibrationnelles d'une large gamme de fluoro-perovskites ABF_3. Cette première étude nous a permis de montrer que ces cristaux présentent une instabilité ferroélectrique dans leur phase cubique qui est d'origine géométrique et qui est dominée par le cation A. Cette origine géométrique rend la dépendance de l'instabilité ferroélectrique à une pression hydrostatique très différente de celle observée dans les oxydes. Dans les fluorites la pression a tendance à augmenter l'instabilité ferroélectrique tandis que dans les oxydes elle a tendance à la supprimer.

En nous basant sur une analyse des symétries et sur des calculs *ab-initio*, nous avons aussi montré que les phases perovskites *Pnma*, observées à basse pression, et les phases post-pérovskites, observées à haute pression, contenant un cation B magnétique ont toutes une structure magnétique non-colinéaire. Cette étude a permis de clarifier les propriétés magnétiques observées expérimentalement et de prédire une transition *Pnma*/post-perovskite dans le $NaMnF_3$ sous haute pression avec un ferromagnétisme léger bien plus important que dans tous les autres systèmes reportés jusqu'à présent.

Au delà d'une simple caractérisation de matériaux, nous avons aussi prédit la possibilité d'induire une phase multiferroïque dans le $NaMnF_3$ en jouant avec des contraintes d'épitaxie. Contrairement à ce qui est observé dans les oxydes, la polarisation est induite dans la direction perpendiculaire à la contrainte bi-axiale et le couplage entre la polarisation et la contrainte est dominé par une réponse piézoélectrique non-linéaire. Cette dominante non-linéaire permet d'obtenir une réponse originale de la polarisation où cette dernière est augmentée pour des contraintes d'épitaxie aussi bien positives que négatives. Nous expliquons cette

réponse inhabituelle à une modification du vecteur de déplacement ferroélectrique des atomes où sous tension la polarisation est dominée par un déplacement géométrique du cation A et sous compression par le déplacement des cations A et Mn. L'analyse du magnétisme montre un ordre antiferromagnétique dominant de type G associé à des ordres non-colinéaires de type A et F ($G_z A_x F_y$). L'association de l'ordre ferroélectrique et du ferromagnétisme léger (F_y) fait que $NaMnF_3$ sous contrainte d'épitaxie est un nouveau multiferroïque. L'étude de la réponse magnétoélectrique sous champ magnétique montre qu'elle s'effectue également à l'ordre non-linéaire.

Enfin, dans un dernier temps nous avons aussi étudié la structure électronique et les propriétés structurales d'heterostructures oxyfluorites $(KTaO_3)_n/(KBF_3)_l$ où B = Zn et Ni. Dans ces interfaces entre un oxyde et une fluorite nous avons observé que la levée de dégénérescence des orbitales atomiques est fortement modifiée par la liaison O–B–F. Un phénomène de catastrophe polaire est aussi observé où l"epaisseur critique pour l'apparition d'un gaz bidimensionnel est plus petite que celle reportée dans les super-réseaux $SrTiO_3/LaAlO_3$. Dans le cas B = Ni, le magnétisme dans la couche de $KNiF_3$ reste globalement du type G mais présente une modulation en amplitude des moments magnétiques près de l'interface. De manière surprenante, nous avons aussi observé une levée de dégénérescence de type k^3-Rashba à l'interface de ces heterostructures oxyfluorites et d'amplitude au moins quatre fois supérieure à celle rapportée dans l'interface $SrTiO_3/LaAlO_3$ et deux fois supérieur à celle des transistors à base de $KTaO_3$.

En résumé, notre étude a permis de conclure que les cristaux perovskites à base de fluorites sont de bons candidats à considérer dans la recherche de propriétés multifonctionnelles. Nous espérons que nos résultats motiveront des expérimentateurs et d'autres théoriciens dans l'étude et la caractérisation des fluorites dans la recherche de nouveaux matériaux aux propriétés inédites et à haut potentiel pour des applications technologiques et industrielles.

RESÚMEN

En los últimos quince años, los materiales multifuncionales, y más específicamente, los óxidos multifuncionales han sido ampliamente estudiados debido a su basta gama de propiedades. Se han reportado propiedades que van desde la superconductividad y ferroelectricidad pasando por el magnetismo y multiferroismo. Sin embargo, la familia de fluoruros perovskita a sido dejada de lado y poca información se conoce sobre su posible ferroelectricidad y/o multiferroismo. En mi tesis doctoral, he explorado las propiedades electrónicas, vibracionales, estructurales y magnéticas de los compuestos base fluoruro perovskita. Para tal fin, he realizado *ab*-initio cálculos basados en la teoría del funcional de la densidad (DFT) tal como esta implementada en los códigos VASP y CRYSTAL.

Los análisis vibracionales se llevaron a cabo en fluoroperovskitas tipo ABF_3. En base a los resultados, hemos propuesto un modelo que muestra la presencia de una inestabilidad ferroeléctrica geométricamente dominada por el sitio A en estos fluoruros. Mis estudios revelan un comportamiento diferente para los compuestos $NaBF_3$ con B = Ca, V, Mn y Zn como función de la presión isotrópica, esto en comparación con los óxidos (*por ejemplo* $BaTiO_3$). Para estos compuestos se encontró un aumento de la inestabilidad ferroeléctrico como función de la tensión hidrostática. Lo anterior posiblemente debido a la "transformación" observada de eigendisplacements responsables de este modo. Así mismo,El incremento del radio iónicos del sitio A presentan una fuerte influencia en la inestabilidad FE-polar.

También se ha demostrado, que todos las post-perovskitas ABX_3 con una sitio B magnéticamente activo exhiben la posibilidad de presentar un comportamiento magnético no colineal permitido por la simetría. Lo anterior con base en los cálculos de primeros principios y el análisis de teoría de grupos. Con estos resultados fueron aclaradas las propiedades magnéticas encontrados experimentalmente en esta fase perovksita de alta presión encontrada principalmente en el manto de la Tierra. Además, fue posible predecir la existencia de esta transición a fase post-perovskita en el compuesto $NaMnF_3$. Con esto, este fluoruro se convertirse en un nuevo miembro de esta familia en el cual, las propiedades magnéticas, y sobre todo, su ferromagnetismo no colineal muestra un alta componente de momento magnético.

Yendo más allá, se ha demostrado que es posible alcanzar el estado multiferroico en $NaMnF_3$ inducido bajo tensión epitaxial para esfuerzos de compresión o expansión. Se encontró un comportamiento no lineal de la inestabilidad ferroeléctrico seguida por una respuesta piezoeléctrica no lineal como una función de la tensión epitaxial. Este último completamente diferente a los hallazgos en óxidos tipo

perovskita. Además, se observó una polarización fuera de plano en la tendencia opuesta a lo encontrado en óxidos. Se encontró ademas un ordenamiento ferroeléctrico cooperativo entre los sitios de Na y Mn para el esfuerzo de compresión. Lo anterior en contraste con una ferroelectricidad geométricamente dominada por el sitio A a valores de tensión en el plano ortorrómbico xz. El ordenamiento magnético revela un estado fundamental no colineal bajo la representación $G_z A_x F_y$. Aún más interesante, se observó un acople magnetoeléctrico no lineal en este material bajo la simetría $Pna2_1$ de estado fundamental, convirtiéndose con esto en el primer multiferroico/magnetoeléctrico conocido en estructura perovskita base fluoruro.

Con el fin de ir más lejos aún, se estudiaron las propiedades electrónicas y estructurales de nuevas heteroestructuras basadas en interfaces de oxifluoruros tipo $(KTaO_3)_n/(KBF_3)_l$ con B = Zn y Ni. Se encontró que la simetría de los niveles orbitales en las interfaces está fuertemente modificado por la coordinación del enlace O–B–F. El fenómeno conocido como "polar-catastrophe" también tiene lugar en las interfaces de oxifluoruro, sin embargo, se encontró que se necesita menos cantidad de capas con el fin de lograr la transición de aislante a metal cuando se compara con superredes como $SrTiO_3/LaAlO_3$. Hemos observado que el magnetismo en el sistema $KTaO_3/KNiF_3$ exhibe modulaciones el la magnitud de momento magnético. Sin embargo, la estructura magnética mantiene el ordenamiento G-antiferromagnetico tal y como en el compuesto en bulto. Sorprendentemente, se encontró en las interfaces tipo oxifluoruro un gran desdoblamiento de espín tipo k^3-Rashba, el cual es al menos cuatro veces mayor que el reportada en la interfaz $SrTiO_3/LaAlO_3$ y el doble del encontrando en el transistor basado en $KTaO_3$.

En conclusión, se observó que los fluoruros-perovskita son buenos materiales prototipos para propiedades multifuncionales tal y como los óxidos. Por ende, esperamos que nuestros resultados puedan motivar a experimentales y teóricos en la búsqueda de las propiedades de estos sistemas, que son, a nuestro entender, inexplorados y representan una gran promesa para el descubrimiento de propiedades interesantes.

PUBLICATIONS

Some ideas and figures have appeared previously in the following publications:

[1] **A. C. Garcia-Castro**, A. H. Romero, E. Bousquet, *Strain-engineered multiferroicity in Pnma $NaMnF_3$ fluoroperovskite*, Physical Review Letters, 116, 117202 (2016).

[2] **A. C. Garcia-Castro**, Nicola A. Spaldin, A. H. Romero, E. Bousquet, *Geometric ferroelectricity in fluoroperovskites*, Physical Review B. 89, 104107 (2014) *editor's suggestion.*

[3] **A. C. Garcia-Castro**, A. H. Romero E. Bousquet, *First-principles study of vibrational and noncollinear magnetic properties of the perovskite to postperovskite pressure transition of $NaMnF_3$*, Physical Review B. 90, 064113 (2014).

[4] **A. C. Garcia-Castro**, A. H. Romero, E. Bousquet, *Non-collinear Magnetism in Post-perovskites from First-principles: comparing $CaRhO_3$ and $NaNiF_3$*, Physica Status Solidi B. 252, 689 (2015) *Front cover.*

[5] **A. C. Garcia-Castro**, M. Vergniory, E. Bousquet, A. H. Romero, *Spin-texture induced by oxygen vacancies is strontium perovskites surfaces: A theoretical comparison between $SrTiO_3$ and $SrHfO_3$ (001)*, Physical Review B. 93, 045405 (2016).

[6] P. Borisov, Trent A. Johnson, **A. C. Garcia-Castro**, K. Amit, D. Schrecongost, C. Cen, A. H. Romero, D. Lederman, *Multiferroic $BaCoF_4$ in thin film form: ferroelectricity, magnetic ordering, and strain*, ACS Applied Materials and Interfaces, 8, 2694 (2016).

[7] Weitao Dai, Sanjay Adhikari, **A. C. Garcia-Castro**, Aldo H. Romero, Hyungwoo Lee, Jung-Woo Lee, Sangwoo Ryu, Chang-Beom Eom, Cheng Cen, *Tailoring $LaAlO_3/SrTiO_3$ interface metallicity by oxygen surface adsorbates*, Nano Letters, 16, 2739 (2016).

[8] Sanjay Adhikari, **A. C. Garcia-Castro**, Aldo H. Romero, Sangwoo Park, Chang-Beom Eom, Cheng Cen, *The importance of water adsorption in shaping $LaAlO_3/SrTiO_3$ interface properties*, Advanced Functional Materials. (2016 - Under consideration).

[9] Sobhit Singh, **A. C. Garcia-Castro**, Irais Valencia-Jaime, Francisco Munoz, and Aldo H. Romero, *Prediction of a controllable Weyl semi-metallic phase in inversion-asymmetryc BiSb*, Advanced Materials, (2016 - To be submitted).

[10] P. Borisov, Trent A. Johnson, W. Ibarra-Hernandez, **A. C. Garcia-Castro**, E. Bousquet, K. Amit, D. Schrecongost, C. Cen, A. H. Romero, D. Lederman, *Muliferroic behavior of $NaMnF_3$ thin films growth by molecular beam epitaxy*, Journal of Applied Physics. (2016 - To be submitted).

"Because success is stumbling from failure to failure with no loss of enthusiasm"
—Wiston S. Churchill.

ACKNOWLEDGEMENTS

Sometimes, you face the difficult decision to leave your country and your home in the search for better opportunities and to explore new horizons. This path that I traced in my life 7 years ago now is rewarded with this amazing achievement not just for my professional life, but also for my personal formation as well. Thus, the culmination of the last 4 year of this journey, full of nice and not that good experiences, is condensed in the present manuscript. Therefore, I'm taking this chance, and a few words, to acknowledge all this people that were and have been there for me and support me along this journey, because, I have always believed that when you achieve something worthy in your life, this is the sum of all the efforts of the people around you.

First, I would like to thank to prof. Aldo H. Romero for his great supervision and friendship that always extended to me kindly, and for bring me the opportunity to join his research group. I also want to thank him for encouraging and support my scientific travels used to interact with the scientific community.

I would also equally thank to Dr. Eric Bousquet for all his help, guidance and friendly patience to explain me a lot of scientific aspects, but more important than that, for being there to help me even in small things such as finding an apartment to rent.

I am very grateful to my fiancée, Sara Orozco, who was always there for me listening my scientific explanations and ideas, even knowing that she is not a scientist. Who has been there for me and had understood when I have to travel for a long time and leave her alone.

Especial thanks to prof. Beatriz Cruz in Colombia that introduced me in the research world and in the meanwhile bring me her unconditional support which make me take the change lo look beyond the colombian horizons

I would like to thanks to all my colleagues at the department of physics at the Université de Liège: Henu, Julien, Nicholas, Antoine, Dr. Eric, prof. Philippe, prof. Matthieu, Dra. Zeila, Begum, Denis, Safari, Naihua, Marco, Hanen, Sebastian, Alain, Brahim, and Fabio.

To the Euraxess fellowship and its stuff for their friendly help and support that allowed me to be in Liège for more than a year and enjoy the delicious chocolates,

nice beers and tasty food.

I thank to prof. Nicola A. Spaldin and her research group at the ETH-Zürich for the chance to work with them and have the opportunity to be in the beautiful Zürich for several months.

To CONACyT for the invaluable opportunity that bring me to México as a starting point of my professional career that opened the world for me.

To my friend and colleague Irais Valencia for her support and patience to hear my ideas even when they did not take me to a successful results.

It is worth to mention that all the computational work presented here was possible thanks to support —for more than 3 millions of computational hours— from the Extreme Science and Engineering Discovery Environment, XSEDE at United States with the supercomputers Stampede and Ranger (project TG-DMR140031). Thanks also to the computational time provided by the Belgian CECI projects and specially the Zenobe stuff.

At last, but not least, I would like to thanks to my parents, Alberto and Martha, for teaching me the value of the honesty, hard work, and respect. Thanks to my sister Cindy Johana, that is constantly in touch with me giving me the courage to go forward. I thank to my friends Luis Alberto, Sebastian, and Catalina that were always worried about my thesis progress and were continuously asking: "how is the thesis going?". Finally and specially, thanks to Wilfredo and his wife Rosa Elisa, that opened their home for me and were a friendly face every time that I traveled from México to Belgium.

CONTENTS

ACRONYMS

AFD Antiferrodistortive

AFM Antiferromagnetism

A-AFM A-type Antiferromagnetism

BZ Brillouin Zone

C-AFM C-type Antiferromagnetism

DFPT Density-Functional Perturbation Theory

DFT Density-Functional Theory

FE Ferroelectric

FM Ferromagnetism

G-AFM G-type Antiferromagnetism

GGA Generalized Gradient Approximation

HSEo6 Heyd-Scuseria-Ernzerhof

IMT Insulator-to-Metal Transition

LDA Local Density Approximation

LDOS Local-Density Of States

LSDA Local Spin Density Approximation

ME Magnetoelectric

MF Multiferroic

PAW Projected Augmented-Wave

PBE Perdew Burke Erznzerhof

PBEsol Perdew Burke Erznzerhof Revised for Solids

Pv Perovskite

pPv Post-perovskite

SOC Spin-Orbit Coupling

VASP Vienna Ab-initio Simulation Package

INTRODUCTION

Since its discovery in $BaTiO_3$, ferroelectricity in perovskite oxides has attracted tremendous interest, ranging from fundamental studies to technological applications [11]. Indeed, the transition-metal/oxygen bond, with its large polarizability, is particularly favourable for promoting the transition-metal off-centering that can result in a ferroelectric ground state [12, 13]. Ferroelectrics also exist, of course, in many material chemistries that do not contain oxygen, with a particularly extensive range of fluorine-based examples, including both polymers [14] and ceramics in many crystal classes (for a review see Ref. [15]). Perhaps not surprisingly given the low polarizability of bonds with fluorine, the mechanism for ferroelectricity in fluorine-based ferroelectrics are distinct from that in oxides, ranging from molecular reorientation in polymers [16], to geometric reconstructions in ceramics [17]. These alternative mechanisms are of particular interest because, again unlike the oxides, they are not contra-indicated by transition metal d-electrons, and so allow simultaneous ferroelectricity and magnetic ordering (multiferroism) as we are going to discuss in this thesis..

Fluoride materials tend to exhibit multiferroism —defined by the coexistence of ferroic order parameters— and magnetoelectricity —known as the induced magnetic (electric) polarization by means of an applied external electric (magnetic) field— as mentioned in the work by Scott and Blinc [18]. However, there is no mention of such behavior in ternary perovskite fluorides and even when a few of them have been identified as possible ferroelectrics —with a $R\bar{3}c$ polar symmetry group—. Therefore, there is no mention in the literature related to this topic of a single multiferroic fluoroperovskite as possible multiferroic nor magnetoelectric, while the perovskite family is an extremely important class of materials for multifunctional applications due to their simple cubic block structure easily manageable for growing in thin films, superlattices, etc [19, 20, 21, 22, 23].

In the field of multiferroics and magnetoelectrics, there are still some open questions and challenges to be addressed that concerns the achievement of a room temperature multiferroic or a magnetic-field switchable polarization. The breakthrough results we present in this thesis stand for the realization of a strain engineering multiferroism/magnetoelectric in a class of materials that nobody has anticipated. Moreover, in the community of ferroelectrics no one would have looked at ionic compounds with very low polarizability. Besides, due to the low polarizability and large electronegativity of the fluorine atom, novel and unexpected nonlinear strain/polarization properties can be found, which to our knowledge, has never been reported before in any ferroelectric perovskite-based systems. Thus, the unexplored behavior in perovskite fluorides is very appealing at the funda-

mental level —that it has never been considered— and at the experimental level —that it has never been observed— and it opens totally new and unexpected perspectives in the hot field of ferroelectrics and magnetoelectrics, which is in a constant search for new materials that can be addressed experimentally and drive novel responses and applications.

From the industrial point of view, fluorides have proven to be of high interest for numerous long term applications, such as fluorides-based glasses with a large thermal expansion, low refractive and non-linear index [24, 25], strong magnets with an optically transparency in the visible light [26, 27], electrochemical devices, solid-state batteries, gas sensors, and electrochromic systems [28] or catalyst surfaces based on metal fluorides such as AlF_3 [29]. Thus, adding multiferroic properties in fluoroperovskites would open an exciting opportunity to their use in novel and extended applications.

Therefore, in this thesis we propose to analyze and understand the microscopic origin of the fluoroperovskites through first-principles simulations and to highlight new and unexpected multiferroic properties to offer some understanding on the properties of fluoride perovskites. We analyze their vibrational behavior, ferroelectricity, magnetic canting and non-collinear magnetism, pressure and strain effects, mixed interfaces and electronic structure. These results are organized as follows:

An introduction to DFT is presented in Chapter 1 where it is presented a basic theoretical background focused around the many-body problem, density-functional theory as well as its fundaments and principal implementation considerations.

The vibrational and structural properties of ABF_3 will be addressed in the Chapter 2. This analysis will give us the fundamental background to the understanding of the hidden properties that lie beneath the fluoroperovskites.

Taking advantage of the explored properties of fluorides, we analyze the hydrostatic pressure effects on the structural and magnetic properties of $NaMnF_3$ where we predict a transition toward a post-perovskite phase at relatively low pressure —in Chapter 3—. We also present in this chapter the symmetry analysis of the possible non-collinear magnetic orders we can found in the post-perovskite space group and compare it with our calculations and other *pPv* systems such as $CaRhO_3$ and $NaNiF_3$ —at Chapter 4—.

Moving forward, in Chapter 5 we present the study of the epitaxial strain-engineered multiferroic/magnetoelectric state in $NaMnF_3$ where a deep discussion on the non-collinear magnetism, ferroelectricity, magnetoelectric-coupling

and non-linear piezoelectric effect is carried out.

Finally, the electronic structure at oxide/fluoride perovskite (oxyfluoride) interfaces are analyzed in Chapter 6. Surprisingly, the results suggest a larger Rashba effect at these interfaces, in comparison to oxide/oxide interfaces, calling for a deeper understanding of this mixed type of heterostructures.

At the end of this document several appendixes are presented. The magnetic properties —exchange constants, group theoretical details, etc— of fluoride perovskites and post-perovskites is explained in Appendixes A and B. We also present in Appendices C, D, and E additional side studies we performed during our thesis such as strained $BaCoF_4$ thin films, the role of water adsorptions in STO/LAO interfaces and the spin texture at the $SrBO_3$ (B = Ti and Hf) surfaces in the presence of an oxygen vacancy respectively.

Part I

DENSITY FUNCTIONAL THEORY AND ELECTRONIC STRUCTURE

Density-Functional Theory is nowadays, one of the most successful theoretical developments for electronic structure calculations in solid-state physics. Within this theory, the approximations used have shown to provide an excellent balance between computational accuracy and cost ideal for the study of the physics behind many materials. In next section is described the theoretical foundations for the research and the developed work presented in this thesis. Then, a short but condensed review of the theory, implementation, and computational methods is described in order to give to the reader enough background to address the thesis content.

1 THEORETICAL BACKGROUND

In condensed matter physics, several theoretical methods have been developed and consequently used to explain various phenomena and properties in materials. Within these methods, first-principles approaches and specifically, density-functional theory (DFT) have gained a lot of attention and recognition. DFT has been applied successfully to a wide range of materials providing a deeper understanding of their properties and microscopic origins. All the research shown in the development of this PhD thesis was performed within the framework of DFT. Then, in this chapter, the reader can find a brief, but focused description of the theoretical and mathematical background needed in the development of the results condensed in this thesis. This theoretical background address a density-functional theory description starting from the well-known problem in the description of many-body systems. Later, the discussion of the Hohenberg-Kohn theorems and the Kohn-Shan *ansatz* that makes possible the practical solution and application of the theory is carried out. After, a small description of the functionals, pseudopotentials and more practical solid-state theory will be addressed. The later in order to fill the gap between the theory and the implementation leading with this, to a powerful use of its advantages. All of this with the aim to investigate and predict the origin of many novel and exciting materials and properties.

1.1 Many-Body Problem

Taking the quantum mechanics as the basis to describe the ions and interacting electrons, we know that a system is represented by the wavefunctions and their interactions expressed by the Schrödinger's equation in the time-independent[1] approach as [30]:

$$\hat{H}\,|\Psi\rangle = E\,|\Psi\rangle\,, \tag{1.1}$$

where the Hamiltonian operator ($\hat{H}$) acting over the wavefunction ket ($|\Psi\rangle$) has as a result, the energy eigenvalues (E) times the wavefunction. The $\hat{H}$ operator for the ions composed by the nuclei and electrons is described by the kinetic and potential energy interactions taking the expression:

$$\hat{H}(\mathbf{R},\mathbf{r}) = \hat{T}_N(\mathbf{R}) + \hat{T}_e(\mathbf{r}) + \hat{V}_{NN}(\mathbf{R}) + \hat{V}_{ee}(\mathbf{r}) + \hat{V}_{eN}(\mathbf{r},\mathbf{R}), \tag{1.2}$$

1 The time-dependent Schrödinger's equation present the form: $\hat{H}(t)\,|\Psi\rangle = i\hbar(\frac{\partial}{\partial t})|\Psi\rangle$

here, the operators for the kinetic energy of the nuclei ($\hat{T}_N$) and the electrons ($\hat{T}_e$) are as follows:

$$\hat{T}_N(\mathbf{R}) = -\frac{\hbar^2}{2}\sum_I \frac{1}{M_I}\nabla_I^2, \tag{1.3}$$

$$\hat{T}_e(\mathbf{r}) = -\frac{\hbar^2}{2m_e}\sum_i \nabla_i^2, \tag{1.4}$$

by notation, the coordinates related to the ions and electrons are given in upper and lower cases subscripts respectively (*i.e.* I, J, etc. and i, j, etc.). M_I and m_e are the masses for the ions and the electrons respectively.

The electrostatic potentials for the ion-ion, electron-electron, and electron-ion interactions are given by:

$$\hat{V}_{NN}(\mathbf{R},\mathbf{R}) = \frac{e^2}{2}\sum_{I\neq J}\frac{Z_I Z_J}{\|\mathbf{R}_I-\mathbf{R}_J\|}, \tag{1.5}$$

$$\hat{V}_{ee}(\mathbf{r},\mathbf{r}) = \frac{e^2}{2}\sum_{i\neq j}\frac{1}{\|\mathbf{r}_i-\mathbf{r}_j\|}, \tag{1.6}$$

$$\hat{V}_{eN}(\mathbf{r},\mathbf{R}) = -e^2\sum_{i,I}\frac{Z_I}{\|\mathbf{r}_i-\mathbf{R}_I\|}, \tag{1.7}$$

In order to reduce the number of terms in the Hamiltonian presented in Eq. 1.2 it can be assumed that the relation between the ions and electrons masses is $M_I >> m_e$. This can be understood in terms of the motion velocity of the electrons with respect to the ionic motion, which turns out to be almost instantaneously (adiabatically) with respect to the nucleus. Therefore, the kinetic energy of the ions can be neglected and the wavefunction can be treated only based in the electronic degrees of freedom. The later statement is called *Born–Oppenheimer approximation* and have the effect on the Hamiltonian as shown in the Eq. 1.8:

$$\hat{H}_e(\mathbf{R},\mathbf{r}) = \hat{T}_e(\mathbf{r}) + \hat{V}_{NN}(\mathbf{R}) + \hat{V}_{ee}(\mathbf{r}) + \hat{V}_{eN}(\mathbf{r},\mathbf{R}). \tag{1.8}$$

The ion-ion potential, $\hat{V}_{NN}$ is recognized such as the Madelung energy, which can be easily computed in periodic systems. The exact calculation of this term can be reviewed in the appendix F by Kaxiras [31]. The $\hat{V}_{eN}$ potential is now independent of the ion $\mathbf{R}_I$ coordinates and can be represented only as a function of the electron positions ($\mathbf{r}_i$). After these considerations, the electronic Hamiltonian, $\hat{H}_e$, assuming a fixed nuclei, is described by the sum shown in Eq 1.9:

$$\hat{H}_e = \hat{T}_e + \hat{V}_{ee} + \hat{V}_{ext} = \hat{T}_e + \hat{V}_{ee} + \sum_i v(\mathbf{r}_i). \tag{1.9}$$

Thus, the electronic energy can be computed such as:

$$E_e = \langle \Psi_e | \hat{H} | \Psi_e \rangle = \langle \Psi_e | \hat{T}_e + \hat{V}_{ee} + \hat{V}_{ext} | \Psi_e \rangle , \tag{1.10}$$

where $\Psi_e = \Psi_e(\mathbf{r}_1, \mathbf{r}_2, \dots, \mathbf{r}_N)$ for the N electrons. As we know from quantum mechanics, this wavefunction must be normalized (*i.e* $\langle \Psi | \Psi \rangle = 1$) and antisymmetric under the exchange of two particles (*i.e.* $\Psi_e(\mathbf{r}_1, \mathbf{r}_2, \dots, \mathbf{r}_N) = -\Psi_e(\mathbf{r}_2, \mathbf{r}_1, \dots, \mathbf{r}_N)$).

At this point, even when several approximations have been taken into account, the problem of solving the Eq. 1.10 and finding the $|\Psi_e\rangle$ wavefunctions in a crystal is by far, a very complicated task due to the large number of electrons (of the order of 10^{23}) and degrees of freedom in a crystal. Some methods were developed to find the solution to this problem, being the density functional theory (DFT) one of the most successful.

1.2 Density-Functional Theory

In DFT, we will find one of the most successful methods for electronic structure calculations in solid-state physics. The later because the approximations used have shown to provide an excellent balance between computational accuracy and cost. Then, much larger systems can be studied than with others *ab* initio methods. Additionally, DFT is a completely rigorous and formally methodology to model a many-body interacting system (as shown previously). This is achieved by "switching" the point of view to a much simpler and easier route to solve the non-interacting problem. For those reasons, the DFT methodology has been, is and it will be one of the most applied methodologies to understand and unveil the physics behind materials in a large variety of fields.

Lets start by saying that we can define the number of electrons in a system by integrating the electronic density ($n = n(\mathbf{r})$) over a volumetric space as follows:

$$N = \int n(\mathbf{r}) d\mathbf{r}. \tag{1.11}$$

Now, lets take the electronic density as a function of Ψ such as:

$$n(\mathbf{r}) = N \int \dots \int |\Psi(\mathbf{r}_1, \mathbf{r}_2, \dots, \mathbf{r}_N)|^2 d\mathbf{r}_1, d\mathbf{r}_2, \dots, d\mathbf{r}_N, \tag{1.12}$$

here, if we think into invert the dependence of terms in the expression in Eq. 1.12, we will see that the wavefunction will become $\Psi = \Psi[n(\mathbf{r})]$, which is indeed

a functional of the density[2]. Even if the later reasoning looks quite simple, it is indeed the foundation of the density-functional theory as shown next.

1.2.1 *The Hohenberg-Kohn Theorems*

As previously discussed, the wavefunctions can be expressed in terms of the electronic density. This argument is very powerful because it means that now we can think in solving the Schrödinger's equation just by defining a functional of the electronic density with only three spatial variables instead of the $3N$-variables in the wavefunctions. This statement was condensed and proved by the Hohenberg-Kohn theorems [32]:

Theorem 1: *The ground-state energy from Schrödinger's equation is a unique functional of the electron density* [32].

Theorem 2: *The electron density that minimizes the energy of the overall functional is the true electron density corresponding to the full solution of the Schrödinger's equation* [32].

The proofs for these theorems are beyond the aim of this chapter and it can be find in several electronic structure textbooks such as Martin [30]. The previous theorems establish that there is a one-to-one relationship between the ground state energy and the electronic density $n(\mathbf{r})$ determined by a unique external potential. Besides, if the "true" functional is known, then, we can perform a minimization of the energy in order to find the related electron density.

Thus, just after considering these theorems, we can redefine the energy (presented in Eq. 1.10) as:

$$E[n(\mathbf{r})] = \langle \Psi_e | \hat{T}_e + \hat{V}_{ee} | \Psi_e \rangle + \langle \Psi_e | \hat{V}_{ext} | \Psi_e \rangle \tag{1.13}$$

$$= F[n(\mathbf{r})] + \int v(\mathbf{r}) n(\mathbf{r}) d\mathbf{r}, \tag{1.14}$$

being $n(\mathbf{r})$ the electronic density for the ground state and $F[n(\mathbf{r})]$ a functional of the density that regroups the kinetic and potential energies added to the external potential energy. Nevertheless, in all the development shown by Hohenberg and Kohn, the $F[n(\mathbf{r})]$ is unknown and to find a solution to the Schrödinger's equation it is still a problem at this stage of the framework. Then, it was only after the seminal work by Kohn and Sham [33] that some light was shed onto this problem.

2 As a simple example of a functional lets take first the function $f(x) = x^2 + 1$, then a functional $F[f(x)]$ of the function $f(x)$ can be written as: $F[f] = \int_{-1}^{1} f(x) dx$. After evaluating the later expression we have that $F[f] = \frac{3}{8}$.

1.2.2 *Kohn-Sham Equation*

The main idea of Kohn and Sham was to map the many-electron system into a single-particle description [33]. For that purpose, the $F[n(\mathbf{r})]$ functional was redefined as:

$$F[n(\mathbf{r})] = T_{ks}[n(\mathbf{r})] + V_H[n(\mathbf{r})] + E_{xc}[n(\mathbf{r})], \tag{1.15}$$

here, T_{ks} is the kinetic energy of a system with density n but, excluding the electron-electron interactions. V_H is known as the Hartree potential derived from the classic Coulomb potential for the electrons. Finally, E_{xc} defines the exchange-correlation energy missing in T_{ks} and V_H. It is important to note at this point that T_{ks} is not the real kinetic energy, nonetheless, its magnitude is comparable and can be computed without any approximation. Then, all the terms in the Eq. 1.15 can be evaluated exactly, except for the exchange-correlation energy, which as we will see, it is the main concern in the theory. As a next step, by considering the Eqs. 1.1, 1.4, 1.14, and 1.15 we have the Schrödinger's equation with the form:

$$\left[-\frac{\hbar^2}{2m_e}\nabla^2 + \int \frac{n(\mathbf{r}')}{|\mathbf{r}-\mathbf{r}'|}d\mathbf{r}' + v_{xc}(\mathbf{r}) + v(\mathbf{r})\right]|\psi_i\rangle = \epsilon_i\,|\psi_i\rangle\,, \tag{1.16}$$

where the exchange-correlation potential is defined as a functional derivative of the exchange energy E_{xc}:

$$v_{xc} = \frac{\delta E_{xc}[n(\mathbf{r})]}{\delta n(\mathbf{r})}. \tag{1.17}$$

As we can see in the Eq. 1.16, if we regroup the terms with a potential character, we have the non-interacting one-electron Schrödinger's equation expressed in the Eq. 1.18:

$$\left[-\frac{\hbar^2}{2m_e}\nabla^2 + v_{eff}\right]|\psi_i\rangle = \epsilon_i\,|\psi_i\rangle\,. \tag{1.18}$$

The Eq. 1.18 will be renamed from now on as the Kohn-Sham equation. Based in the new Konh-Sham orbitals, $|\psi_i\rangle$, the electronic density can be computed as:

$$n_{KS}(\mathbf{r}) = \sum_i |\psi_i(\mathbf{r})|^2. \tag{1.19}$$

Then, the advantage of solving the Kohn-Sham equations is evidently based in the knowledge of the solution of the single-particle Schrödinger's equation with

a local effective potential, assuming that the core-valence and valence-valence electrostatic interactions can be directly evaluated. Nevertheless, E_{xc} is different because cannot be calculated explicitly and some approximations must be used in order to obtain it.

Another small trouble will become visible if you carefully check the equations, thus you will realize that in order to solve the Kohn–Sham equations (Eq. 1.18), you need to define the Hartree potential (Eq. 1.16), and to define the Hartree potential, you need to have the knowledge of the electron density. However, to find the electron density, you must get the single-electron wave functions (Eq. 1.19), and to know these wavefunctions we must solve the Kohn–Sham equations, going back again to the Eq. 1.18. To break this loop and obtain a real solution, the proposed process is treated as an iterative method as outlined in the following algorithm:

1. Define an initial, trial electron density, $n(\mathbf{r})$.
2. Compute the effective potential (Eq. 1.16) using the electron density.
3. Solve the Kohn–Sham equations defined (Eq. 1.18) by using the trial electron density and the effective potential to find the single-particle wavefunctions, $\psi_i(\mathbf{r})$.
4. Calculate the electron density $n_{KS}(\mathbf{r})$ using the Eq. 1.19 defined by the Kohn–Sham single–particle wavefunctions as obtained from the previous step.
5. Compare the calculated electron density, $n_{KS}(\mathbf{r})$, with the electron density used to solve the Kohn–Sham equations, $n(\mathbf{r})$. If the two densities are the same, then it means that this is the electron density for the ground state, and it can be used to compute the total energy. If the two densities are different, then the trial electron density must be updated to the $n_{KS}(\mathbf{r})$. Once this is done, the process begins again going back to the step 2.

1.3 Exchange–Correlation Energy and Functionals

As commented previously, the density functional theory is exact with the exception of the exchange–correlation energy, which needs to be computed by means of numerous approximations. Here we present some of the most used ones, which show great accuracy in explaining and predicting material's properties.

1.3.1 *LDA and GGA*

The most basic form, but at the same time, the most used methodology to approximate the exchange–correlation energy is by means of the local-density ap-

proximation (LDA). Within this approximation, the exchange-correlation energy is defined as:

$$E_{xc}^{LDA}[n(\mathbf{r})] = \int n(\mathbf{r})\epsilon_{xc}^{hom}[n(\mathbf{r})]d\mathbf{r}, \tag{1.20}$$

where ϵ_{xc}^{hom} is the exchange–correlation energy per particle in a homogeneous electron gas[3]. Here, it is assumed that the energy per particle at the point $\mathbf{r}$ is only a function of this point, besides, the exchange energy of a homogeneous electron is known having the form as follows:

$$\epsilon_{x}^{hom}[n] = -\frac{3}{4\pi}(3\pi^2 n)^{\frac{1}{3}}. \tag{1.21}$$

The missing correlation part can be computed using the quantum Monte Carlo approach as shown in Ref. [34]. Surprisingly, even when this approximation looks quite rudimentary, nowadays, it is one of the most used and gives a good agreement with experimental results (*e.g.* ferroelectric properties in materials [35]). Nonetheless, one of its disadvantages is the over estimation of the cohesive energy that it can be appreciated in smaller lattice cell parameters in comparison to experimental data. The wrong computation of the electronic band gap with an underestimation of its value is also a known disadvantage of the approximation.

The updated representation of the exchange–correlation energy to overcome some misdescribed issues is based onto the generalized gradient approximation (GGA). In this approximation, the variation of the electron density is taken into account in the ϵ_{xc} term as:

$$E_{xc}^{GGA}[n(\mathbf{r})] = \int n(\mathbf{r})\epsilon_{xc}[n(\mathbf{r}), |\nabla n(\mathbf{r})|]d\mathbf{r}. \tag{1.22}$$

There are hundreds of exchange–correlation functionals used in condensed mater and chemistry. Nonetheless, the most used ones are the Ceperley-Alder (CA) [34], Perdew Burke Ernkzerhof (PBE) [36], AM05 [37, 38], PBE revised for solids (PBEsol) [39], and the Perdew-Wang 91 (PW91) [40].

Even when several of the mentioned functionals give a large amount of precision in the computed properties of materials; some physical and chemical phenomena related to strongly correlated electrons [41] shows a lack in the description when are obtained using the same functionals. Then, more advanced approaches (with respect to LDA and GGA) have been developed in order to overcome this problem. Approaches such as DFT+U and hybrid functionals have been successfully applied to explain the electronic properties in systems such as $A^{2+}TiO_3/R^{3+}TiO_3$ superlattices [42] and other interfaces [41]. These methodologies are described in the next sub-sections.

3 Spin-polarized systems can be taken into account just by having the energy such as: $E[n(\mathbf{r})] \Rightarrow E[(n_\uparrow(\mathbf{r}), n_\downarrow(\mathbf{r}))]$

1.3.2 *DFT+(U,J)*

In strongly correlated systems such as transition metal oxides, rare-earth based-materials, and interfaces, DFT calculations show a wrong description of the electronic properties due to the lack in the definition of the exchange–correlation energy. This is due to the non-systematic development of the XC functionals and the lost of information of the highly localized –and then highly interacting– electronic systems. A correction of the on-site Coulomb interaction (U) and the on-site exchange (J) has been implemented by means of the DFT+U approach. For that purpose, there are two main strategies developed to solve the DFT+U Hamiltonian: a first one in which the U and J parameters enter as independent corrections in the calculations [43]; and a second one in which only a single effective $U_{\text{eff}} = U - J$ parameter accounts for the Coulomb interaction, neglecting thereby any higher multi-polar terms [44]. In the DFT+U approach, an additional orbital-dependent interaction is included. Then, the total energy of the system can be expressed in the most general form as [45]:

$$E^{DFT+U}[n(\mathbf{r})] = E^{DFT}[n(\mathbf{r})] + E^{Hub}[\rho^{l\sigma}_{mm'}] - E^{dc}[\rho^{l\sigma}], \tag{1.23}$$

here, the correction term E^{Hub} is known as Hubbard Hamiltonian for correlated states. E^{dc} is the correction term for the double-counting of the states. This problem arises because the Kohn-Sham energies already include the interactions effects within the Hartree and exchange correlations terms. Then, adding the Hubbard Hamiltonian leads to a double-counting of some interactions that needs to be corrected. Note that in the E^{Hub} and E^{dc} the atomic site index, the state, and the spin are taken into account with the l, m, and σ lower and upper indices respectively. Finally, the $\rho^{l\sigma}_{mm'}$ are the occupation numbers of the localized orbitals. In order to solve the Eq. 1.23, the E^{Hub} and E^{dc} terms can be computed as follows:

$$E^{Hub}[\rho^{l\sigma}_{mm'}] - E^{dc}[\rho^{l\sigma}] = \sum_{l}\left[\frac{U^{l}}{2}\sum_{j}\left(\rho^{l\sigma}_{m}\rho^{l\sigma'}_{m'}\right) - \frac{U^{l}}{2}\rho^{l}(\rho^{l}-1)\right], \tag{1.24}$$

with $j = m, \sigma \neq m', \sigma'$ and occupation numbers computed from the projection of the Kohn–Sham orbitals onto the states of a localized basis set as: $\rho^{l\sigma}_{mm'} = \sum_{k,\nu} f^{\sigma}_{k,\nu} \langle \psi^{\sigma}_{k,\nu} | \phi^{l}_{m'} \rangle \langle \phi^{l}_{m} | \psi^{\sigma}_{k,\nu} \rangle$, where the $f_{k,\nu}$ coefficients are the occupations of the KS states.

One of the problems within this approach is that there is no exact determination of the U and J values, and then, they must be adjusted based on experiment data such as magnetic moment, magnetic anisotropy, and electronic band gap. An alternative method to overcome this issue was proposed by Cococcioni and de Gironcoli [46]. In this method, a linear response approach is used in order to calculate the interaction parameters entering to the LDA+U functional. This

calculation is performed internally and self-consistently to avoid the ill-defined parameters into the Hubbard Hamiltonian. Even when this method has been tested and show great accuracy in describing the electronic properties of highly-correlated systems, it is not commonly implemented in most of the available DFT codes.

For a better understanding of the theory involved in the development of the E^{Hub} and E^{dc} the reader can have a look into the review by Himmetoglu *et al.* [45] and the original papers of Liechtenstein *et al.* [43] and Dudarev *et al.* [44].

1.3.3 *Hybrid Functionals*

The hybrid functionals own their name to the mixture character of the exchange–correlation energy. This energy is defined in terms of an amount of an orbital-dependent Hartree-Fock (HF) energy plus and explicit DFT part. As far as we know, those are among the most accurate methods up to day —in addition to Dynamical Mean-Field Theory, DMFT [47] and GW [48] methods for example—. The exchange-correlation functionals can be expressed in their most general form as:

$$E_{xc} = \alpha E_x^{HF} + (1-\alpha) E_{xc}^{DFT}, \tag{1.25}$$

where, the E_x^{DFT} denotes any GGA or LDA functional. Thus, a non- and fully-interacting electronic system will be equivalent to $\alpha = 0$ and $\alpha = 1$ respectively. Several "mixing" functionals have been developed and here we will comment about some of them. The B3LYP [49] is among the most used ones and it is expressed as follows:

$$E_{xc}^{B3LYP} = E_{xc}^{LDA} + a_0(E_x^{HF} - E_x^{DFT}) + a_x E_x^{B88} + a_c E_c^{PW91}, \tag{1.26}$$

here the a_0, a_x, and a_c coefficients are fixed to 0.20, 0.72 and 0.81 values respectively adjusted to fit atomic and molecular data. E_x^{B88} is the exchange energy term taken from the Becke's 1998 gradient correlation within LSDA functional [50]. Finally, the correlation term E_c^{PW91} is taken from the Perdew-Wang 91 functional [40].

Another example is the functional developed by J. Perdew, M. Ernzerhof, and K. Burke (PBE0) [51]:

$$E_{xc} = E_{xc}^{LDA} + \frac{1}{4}(E_x^{HF} - E_{xc}^{DFT}), \tag{1.27}$$

in this functional, $1/4$ of mixing is employed based in several test in which the E_{xc}^{DFT} is set to the PBE functional.

The B1WC [52] hybrid functional was developed especially to be used in perovskite oxides. In this functional the GGA approach is taken within the Wu-Cohen [53] representation and it is employing an 16% of mixing as shown in the Eq. 1.28:

$$E_{xc}^{B1} = E_{xc}^{GGA} + 0.16(E_x^{HF} - E_{xc}^{GGA}). \tag{1.28}$$

The hybrid Heyd-Scuseria-Ernzerhof exchange–correlation functional, HSE06 [54, 55] is differentiated from the previous ones basically by employing a screened Coulomb potential. Starting from the exchange part of the PBE0 representation (Eq. 1.27) and splitting the terms into long- and short-range components (denoted as SR and LR respectively) we obtain:

$$E_x^{PBE0} = a[E_x^{HF,SR}(\omega) + E_x^{HF,LR}(\omega)[+(1-a)[E_x^{PBE,SR}(\omega) + E_x^{PBE,LR}(\omega)], \tag{1.29}$$

where ω is an adjustable parameter governing the interplay between the SR and LR interactions. For this parameter, several numerical tests show that if we take $\omega = 0.15$, the interaction up to the second neighbors are well reproduced. Besides, it has been established that the HF and PBE long-range interactions are rather small and can be neglected. Then, we obtain a screened Coulomb potential hybrid functional as follows:

$$E_{xc}^{\omega PBEh} = aE_x^{HF,SR}(\omega) + (1-a)E_x^{PBE,SR}(\omega) + E_x^{PBE,LR}(\omega) + E_c^{PBE}. \tag{1.30}$$

In the Eq. 1.30 the ωPBEh term converges to PBE0 and PBE for $\omega \to 0$ and $\omega \to \infty$ respectively. For more detailed information about the derivation of the SR and LR terms, please refer to the reference of Heyd *et al.* [54].

It is important to note that some of these hybrid functionals will be used in the analysis of oxide/fluoride interfaces in the chapter 6.

1.4 Density Functional Perturbation Theory

At this stage of the theory, a quite wide description of the electronic and structural landscape of materials is possible within DFT. But to improve the properties characterization, analysis, and consequently to move forward with the theory, the density functional perturbation theory (DFPT) [56] was successfully developed and implemented. With this advance, the study on phonons, dielectric response functions, nonlinear optical susceptibilities, electro-optic coefficients, and electron-phonon interactions became more accessible. To achieve that, the dependence of the energy and its derivatives with respect to several parameters of interest need to be computed (see Eq. 1.31). Then, the main idea is to expand the energy into a power serie around the ground state based in the perturbation parameter λ. The later can be equivalent to the atomic displacements τ, electric field $\mathcal{E}$, and/or

strain η depending the case. Thus, taking the expansion up to the first-order we can access to the forces ($F \equiv \partial E/\partial\tau$), polarization ($P$) and strain constants ($\sigma$) as shown in the Table 1.1. When the expansion is carried out up to second-order, information related to phonons (*i.e* Interatomic force constants, C), Born effective charges ($Z^* \equiv \partial^2 E/\partial\tau\partial\mathcal{E} \equiv \partial P/\partial\tau$) and the internal strain coupling parameters (γ) can be obtained (see the Table 1.1). Other quantities like the clamped-ion elastic constant (c^0), the clamped-ion piezoelectric tensor (e^0), and the optical dielectric tensor (ϵ^∞) can be also computed as presented in the Table 1.1. The third order derivatives give information about nonlinear response such as Raman tensors, optical susceptibilities and electro-optic properties.

$$E(\lambda) = E(0) + \sum_i \frac{\partial E}{\partial\lambda_i}\bigg|_0 \lambda_i + \frac{1}{2}\sum_{i,j} \frac{\partial^2 E}{\partial\lambda_i\partial\lambda_j}\bigg|_0 \lambda_i\lambda_j + \\ + \frac{1}{6}\sum_{i,j,k} \frac{\partial^3 E}{\partial\lambda_i\partial\lambda_j\partial\lambda_k}\bigg|_0 \lambda_i\lambda_j\lambda_k + \dots \tag{1.31}$$

The calculations of the derivatives shown in Eq. 1.31 are based on a variational principle involving a minimization procedure giving also access to non-linear responses based in the "2n+1" theorem [57]. In this theorem is established that the energy of the 2n+1 state can be obtained with the knowledge of the states from 0 through n.

Table 1.1: Available physical quantities through the first- and second-order energy derivatives with $\lambda = \tau$, η, and $\mathcal{E}$, (see the Eq. 1.31). Table adapted from Ref. [35].

	1^{st}-order	2^{nd}-order		
		$\partial/\partial\tau$	$\partial/\partial\eta$	$\partial/\partial\mathcal{E}$
$\partial/\partial\tau$	F	C	γ	Z^*
$\partial/\partial\eta$	σ	γ	c^0	e^0
$\partial/\partial\mathcal{E}$	P	Z^*	e^0	ϵ^∞

An alternative method to obtain the energy derivatives used in the dynamical analysis is based in the so-called, frozen-phonon technique [58]. In this approach, higher-order derivatives are determined by a finite amplitude perturbation of the structure. Then, the energy of both, distorted and undistorted structures are computed and related to the displacements from one to another having with this an estimation of the energy derivative. This process can be performed for several distortions and then, the dynamical matrix can be obtained accessing with this to phonon-dispersion curves (widely used in this thesis), dielectric tensors and elastic constants.

1.5 From the theory to the implementation

Even when all the theory has been developed and the KS equations have set a tangible solution to numerically solve the many-body problem, the implementation still requires a lot of computational efforts in order to make it affordable. Then, another simplification has been made by taking advantage of the periodicity of the crystals as shown in the next subsections.

1.5.1 *Plane-waves expansions*

In a periodic crystal with periodic boundary conditions, an electronic wavefunction can be written in terms of the plane-waves basis set and using the Bloch theorem as follows:

$$\psi_{n,\mathbf{k}}(\mathbf{r}) = \frac{1}{\sqrt{\Omega}} u_n(\mathbf{k},\mathbf{r}) e^{i\mathbf{k}\mathbf{r}} \tag{1.32}$$

where $\mathbf{k}$ is a lattice wave-vector into the reciprocal space, Ω represents the cell volume and n stands for the band number. u_n is the periodic function that holds all the information related to the crystal periodicity. Later, for a more practical view of the Bloch wavefunctions, those are decomposed into a Fourier expansion of the form:

$$\psi_{n,\mathbf{k}}(\mathbf{r}) = \frac{1}{\sqrt{\Omega}} \sum_{\mathbf{G}} C_{n,\mathbf{k}}(\mathbf{G}) e^{i(\mathbf{k}+\mathbf{G})\mathbf{r}} \tag{1.33}$$

Here, $C_{n,\mathbf{k}}$ are the Fourier coefficients and $\mathbf{G}$ is a vector in the crystal reciprocal space. Therefore, for any reciprocal lattice vector we have that $\psi_{n,\mathbf{k}}(\mathbf{r}) = \psi_{n,\mathbf{k}+\mathbf{G}}(\mathbf{r})$. Nonetheless, from the computational point of view this expansion must be limited up to a finite number of plane-waves. For this purposes, a cut-off energy E_{cut} condition is established as:

$$\frac{\hbar^2}{2m}|\mathbf{k}+\mathbf{G}|^2 \leqslant E_{cut} \tag{1.34}$$

The E_{cut} value is independent for each crystal, symmetry and atomic species and then, a correct selection of an energy value should be set in each particular case which is commonly known as the energy cutoff convergence.

One of the disadvantages of this methodology is that a large number of plane-waves is required to describe the electronic wavefunctions close to the nucleus. This due to the faster change of the valence electrons wavefunctions in the region close to the atomic nucleus. Thus, a very large E_{cut} —and thus, a large number of plane-waves— is necessary to describe these wavefunctions correctly in comparison to the energy needed for the electrons close the valence states. In order to overcome this issue, another approximation has been developed known as the pseudopotential approach as it will be described later.

1.5.2 *Periodic Boundary Conditions*

The Eq. 1.32 take advantage of the Born-von Karman periodic boundary conditions, which allow us to represent an infinite periodic crystal into a representative building block of construction known as unit cell. At the same time, thanks to the periodic boundary conditions, the wavefunctions can be presented in the form of the Bloch functions as commented previously. In order to calculate the wavefuntions from the Eq. 1.32 —and consequently, the electronic density as shown previously—, an integration over the reciprocal space involving all the bands and the Bloch functions over an infinite k-points number is required. In practice, this is impossible and needs to be truncated into a finite number of k-points in a similar way as done with the $\mathtt{E_{cut}}$. Therefore, the convergence of the calculations require enough k-points in order to reach a sufficient precision within a reasonable computation time. The later process is usually known as the k-points sampling and determine the accuracy level in the calculations (*i.e.* bigger is the number of k-points, higher is the calculation's precision but larger is the computational time).

Several methods to sample the reciprocal space and then, to select the k-points mesh have been developed. This is the case for example, of the Monkhorst-Pack [59] mesh in which essentially the k-points are distributed homogeneously in the Brillouin zone. In this technique, rows and/or columns of k-points are running parallel with respect to the reciprocal lattice vectors in the specific Brillouin zone.

The previous considerations within the periodic boundary conditions are very convenient when bulk materials and/or superlattices are represented. Nevertheless, the modeling of molecules, isolated surfaces, thin films and/or material's defects require the definition of special computational unit cells. For more details in these special systems, please check the reference of Sholl and Steckel [60].

1.5.3 *Pseudopotentials*

The pseudopotential approach [61] is based on the idea of replacing the strong Coulomb potential of the nucleus by an effective ionic potential (*i.e.* shielding potential) acting on the valence electrons only. This approximation can be done because most of the electronic properties of materials are mainly determined by the valence electrons while the core electrons can be considered as frozen. The later statement has a few exceptions in which, deeper electronic levels in comparison to the valence states have an influence on the properties (*e.g.* ferroelectric materials under pressure [62, 63]). Thus, the pseudo wavefunction have no radial nodes in the core region and the pseudopotential is smoother than the all-electron potential near to the nucleus but identical beyond the cut-off radius, $\mathtt{r_c}$. The key feature of a pseudopotential lies in its transferable and accurate character, then, even if the pseudopotential was constructed in one environment (the atom itself), it should faithfully reproduces the properties of a material when it is placed in different environments such as molecules, solids and ions.

Finally, we can remark that the pseudopotential approximation allows us to decrease the number of plane-waves needed in the Bloch expansion (shown in the previous subsection). Besides, the number of electrons considered explicitly in the Kohn-Sham equations is reduced to only the interacting valence electronic configuration, achieving with this, a considerable saving of the calculation time.

1.5.4 *Projector Augmented-Waves (PAW) method*

The PAW method was proposed by Blöchl [64] in 1994. This method deal with the main shortcoming of the pseudopotential approach, in which, most of the information regarding to the wavefuntion is lost in the region close to the nuclei. Here is important to recall that in the bonding region the wavefunction is smooth, but close to the nuclei it displays rapid oscillations that are very demanding on the numerical representation (*i.e.* large number of plane-waves in the pseudopotential approach). Then, to address this problem the PAW method proposed the following mathematical formalism:

Lets define a linear transformation $\hat{\mathcal{T}}$, which transform the true all-electron KS single particle wavefunction (*i.e.* $|\psi_n\rangle$) to an auxiliary smooth one ($|\tilde{\phi}_n\rangle$), then: $|\psi_n\rangle = \hat{\mathcal{T}}\,|\tilde{\psi}_n\rangle$. However, it is known that the true wavefunctions are already smooth at a certain minimum distance from the core. Thus, $\hat{\mathcal{T}}$ should only modify the wavefunction close to the nuclei. Based on the later statement, we define the operator for that region only as:

$$\hat{\mathcal{T}} = 1 + \sum_a \hat{\mathcal{T}}^a, \tag{1.35}$$

where the a index is an atom, and $\hat{\mathcal{T}}^a$ is the atom-centered transformation that has no effect outside a certain atom-specific augmentation region defined by $|r - R_a| < r_c^a$. Here, the cut-off radii r_c^a should be chosen to avoid the overlap of the augmentation spheres. Now, for convenience, we choose a complete basis inside the sphere known as *partial waves*, $|\phi_i^a\rangle$. In the same way as for the wavefunctions, the $\hat{\mathcal{T}}$ acts on the smooth partial waves as:

$$|\phi_n^a\rangle = (1 + \hat{\mathcal{T}^a})\,|\tilde{\phi}_i^a\rangle \Leftrightarrow \hat{\mathcal{T}^a}\,|\tilde{\phi}_i^a\rangle = |\phi_i^a\rangle - |\tilde{\phi}_i^a\rangle\,. \tag{1.36}$$

Here is important to remark that the $\hat{\mathcal{T}}$ operator is only acting inside the sphere, then, $|\phi_n^a\rangle = |\tilde{\phi}_n^a\rangle$ when $r > r_c^a$. Under the assumption that the smooth partial waves form a complete set inside the augmentation sphere, we can expand the smooth all-electron wavefunctions as:

$$|\tilde{\psi}_n\rangle = \sum_i P_{ni}^a\,|\tilde{\phi}_i^a\rangle\,, \tag{1.37}$$

where P^a_{ni} are the expansion coefficients. If we multiply by $\hat{\mathcal{T}}$ in both sides of the Eq. 1.37 we find that the same is also true for the non-smooth wavefunctions (*i.e.* $|\psi\rangle_n = \sum_i P^a_{ni} |\phi^a_n\rangle$). Therefore, the P^a_{ni} expansion coefficients are the same for both, smooth and non-smooth wavefunctions. In order to find such coefficients, we choose a smooth *projector functions*, $\left|\tilde{p}^a_i\right\rangle$ that satisfies the orthogonality condition and must be complete inside the augmentation spheres, then:

$$\langle \tilde{p}^a_i | \tilde{\phi}^a_j \rangle = \delta_{ij}. \tag{1.38}$$

$$\sum_i |\tilde{\phi}^a_i\rangle \langle \tilde{p}^a_i| = 1. \tag{1.39}$$

Then, multiplying the Eq. 1.37 by $\left\langle \tilde{p}^a_i \right|$ and using the Eq. 1.38 condition we have that:

$$\langle \tilde{p}^a_i | \tilde{\psi}_n \rangle = \sum_j P^a_{nj} \langle \tilde{p}^a_i | \tilde{\phi}_j \rangle = \sum_j P^a_{nj} \delta_{ij} = P^a_{ni}, \tag{1.40}$$

now, we have the expansion coefficients as a function of the projectors and the smooth wavefunctions. Finally, we have to write down the operator $\hat{\mathcal{T}}$ as a function of the projectors and the partial waves using the Eq. 1.39 and the Eq. 1.36 as follows:

$$\begin{aligned} \hat{\mathcal{T}}^a &= \hat{\mathcal{T}}^a \cdot 1 = \hat{\mathcal{T}}^a \sum_i |\tilde{\phi}^a_j\rangle \langle \tilde{p}^a_i| = \sum_i (\hat{\mathcal{T}}^a |\tilde{\phi}^a_j\rangle) \langle \tilde{p}^a_i| \\ &= \sum_i (|\phi^a_i\rangle - |\tilde{\phi}^a_i\rangle) \langle \tilde{p}^a_i|, \end{aligned} \tag{1.41}$$

Then, the full operator (based in the Eq. 1.36) can be expressed as:

$$\hat{\mathcal{T}} = 1 + \sum_{i,a} (|\phi^a_i\rangle - |\tilde{\phi}^a_i\rangle) \langle \tilde{p}^a_i|, \tag{1.42}$$

In conclusion, the KS wavefunctions can be obtained in terms of the projectors and the partial waves (knowing that $|\psi_n\rangle = \hat{\mathcal{T}} \left|\tilde{\psi}_n\right\rangle$) as follows:

$$|\psi_n\rangle = \left|\tilde{\psi}_n\right\rangle + \sum_{i,a} |\phi^a_i\rangle P^a_{ni} - \sum_{i,a} \left|\tilde{\phi}^a_i\right\rangle P^a_{ni}. \tag{1.43}$$

The relation 1.43 can be schematically represented as in the Fig. 1.1. In the figure it can be noted that the full wavefunction is expressed as the sum of the pseudo plane waves (first term in Eq. 1.1) plus the all-electron "on-site" interaction (close to the nuclei and inside de augmentation spheres, second term in Eq. 1.1) minus the "on-site" part from the pseudo wavefunctions (third term in Eq. 1.1).

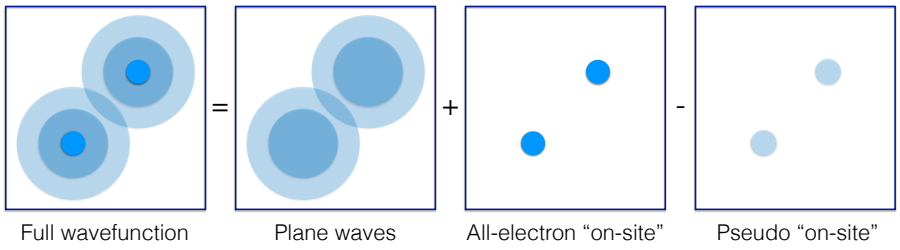

Figure 1.1: Schematic representation of the main PAW method that exemplifies the Eq 1.43.

In this way, we are keeping the information about the wavefunction around the core region without expending large computational time. The later because the number of plane waves is considerably reduced in comparison to the regular pseudopotential approach discussed in the previous section. With this, the accuracy is significantly increased and the computational efforts are reduced.

For a deeper understanding of the pseudopotentials generation, its basis, and the PAW method the reader can refer to the chapter 11 in the electronic structure book of Martin [30].

1.5.5 *Zeeman applied magnetic field*

In order to study the electronic properties as a function of the magnetic applied field, we used the implementation of Bousquet *et al.* [65]. In this implementation, the magnetic energy is added to the Hohenberg-Kohn energy functional. Then, the Legendre transformation of this functional becomes:

$$\Lambda[n_{\sigma\sigma'}(\mathbf{r}), \mathbf{H}] = E_{HK}[n_{\sigma\sigma'}(\mathbf{r})] - \mu_0 \mathbf{H} \cdot \mathbf{m}_{tot}, \tag{1.44}$$

where $n_{\sigma\sigma'}(\mathbf{r})$ is the spin-density matrix, which takes into account a non-collinear framework in the 2×2 matrix allowing to take into account the magnetization spin-density variations (*i.e.* its magnitude and direction). The E_{HK} term is the zero-field energy functional as shown in the previous sections. $\mathbf{H}$ is the applied magnetic field, μ_0 is the magnetic permeability of free space, and $\mathbf{m}_{tot}$ is the total spin magnetic moment of the system obtained from the spatial integration of the $\mathbf{m}(\mathbf{r})$. In the same way as shown previously, the Eq. 1.44 can be solved by the Kohn-Sham approach into the single-particle spinor orbitals schema. Then, in addition to the usual terms, an external magnetic field acting on the spinor orbitals is obtained and the related potential shift have the form:

$$\Delta V_{\sigma\sigma'} = -\frac{g}{2}\mu_B \mu_0 \begin{pmatrix} H_z & H_x + iH_y \\ H_x - iH_y & -H_z \end{pmatrix}, \tag{1.45}$$

here, the g term is the Landé factor, H_j (with j= x, y, and z) are the magnetic field vector components and μ_B is the Bohr magneton. This implementation allow us the computation of several properties of interest such as the magnetoelectric coupling as shown in the Chapter 5 for the $NaMnF_3$ compound. This, opening the possibility to unveil the properties in multifunctional compounds with a related magnetic behavior.

1.5.6 *Used codes: VASP and CRYSTAL*

VASP— The Vienna *ab*-initio simulation package (VASP) is the main code used in the development of this thesis [66, 67]. Projector Augmented-Waves (PAW) [64] pseudo-potentials were used to represent the valence and core electrons. The exchange correlation was represented within the GGA - PBEsol parametrization [39]. The magnetic character of these systems was include and *d*-electron localization corrected by means of the GGA+U within the Liechtenstein formalism [43], for which, the U value was found by fitting the gap and the magnetic moment as a function of this parameter. The periodic solutions of these crystalline structures were represented by using Bloch states with fully converged k-points and energy cut-off values. The spin-orbit coupling was include into non-collinear calculations [68]. Born effective charges and phonon calculations were performed within the density functional perturbation theory (DFPT) [69]. The dynamical matrix was then unfolded using the Phonopy code [70]. The ferroelectric spontaneous polarization computed through the Berry phase approach [71].

CRYSTAL14— For big cells and large number of atoms, hybrid calculations have been performed using the linear combination of atomic orbitals (LCAO) as implemented in the CRYSTAL code [72]. This code is based in a Gaussian-type basis sets including polarization orbitals with the advantage of decrease considerably the computation time comparing to plane-wave basis set as in VASP.

In conclusion, a basic landscape of all the theory involved in the development of this thesis has been described, Nonetheless, for more and deeper information the reader can check also the references of Martin [30], Kaxiras [31], Dobson *et al.* [73], and Sholl and Steckel [74, 75].

Part II

STRUCTURAL PROPERTIES OF PEROVSKITES ABF_3

Interestingly, none of the known perovskite fluorides have been reported to be ferroelectric and no explanation has been addressed in the literature about the absence of ferroelectricity in this crystal class. In this section we use first-principles density functional calculations to investigate computationally the tendency towards ferroelectricity in perovskite fluorides. Our goals are two-fold: First, by comparing to the behavior of ferroelectric perovskite-structure oxides, we further understanding of the driving forces for, and competition between, polar and non-polar structural distortions in both systems. Second, we aim to identify conditions, for example of strain or chemistry, under which ferroelectricity, and perhaps multiferroism, could be stabilized in the fluoride perovskites.

2

VIBRATIONAL BEHAVIOR IN FLUOROPEROVSKITES ABF_3

Ferroelectricity in perovskite oxides has attracted a huge interests going from fundamental studies to technological and industrial applications. Nowadays, this interest is even stronger because of the great challenge of finding materials that exhibits both ferroelectricity and magnetism —AFM or FM orderings—, although the highly electronic correlated systems, ABO_3 perovskites are considered as the most attractive and promising candidates [76]. Interestingly, Scott and Blink have recently pointed out that multiferroism and magnetoelectricity can also be widely found in the leaved aside fluoride-based materials [18]. Examples of these systems recently studied are the multiferroics based on barium-fluorides $BaBF_4$ (B = Mn, Fe, Co, Ni) [17] that present a quasi-2D layer-by-layer structural octahedral arrangement. This arrangement leads to octahedral rotations with an unstable phonon mode yielding to a net spontaneous polarization that generates its ferroelectricity. This fluoride family also presents an antiferromagnetic behavior due to transition magnetic metal ions located at fluorine-octahedra center. These ions possess partially filled d-levels that give rise to magnetic order with magnetic moments that tend to align in the bc-plane making an angle of 120° with respect to the b-axis [77]. Other examples are $KMnFeF_6$ and $Ba_2Ni_7F_{18}$ with a magnetoelectric behavior predicted by phenomenological Landau analysis [78]. $KCrF_4$ with *Pnma* structure and quasi-1D antiferromagnetic ordering with infinite Cr-F_6 octahedra columns along b-axis [79]. This material possess a spontaneous polarization components of P_y (or P_z) as a function of applied magnetic field along z (or y) crystalline direction. The family $Ba_6B_nF_{12+2n}$ (BMF) [79] also make part of this kind of materials with a magnetic frustration due to corner-sharing octahedra phenomena and spontaneous polarization induced in all three directions by the application of a magnetic field. Then, as shown previously, ferroelectricity has been analyzed only in a few number of fluoride compounds with a lack in the understanding of the microscopic origin of the polarization within. Thus, as one of the aims of our work is to explore this question by scrutiny analyze the origin of the polar ferroelectric instabilities in magnetic perovskite fluorides. Interestingly, we found that the ferroelectric instability in ABF_3 has a totally different origin and behavior than in oxides even if their structural and vibrational properties are very similar. Ferroelectricity in ABO_3 has been first described by the softening and the condensation of a soft[1] polar mode when cooling down the temperature going from the cubic $Pm\bar{3}m$ high temperature structure to po-

1 A soft mode is a phonon mode with a frequency that falls to zero, as a function of temperature, at the phase transition.

lar ferroelectric ground state [80]. This was first attributed by a subtle balance between the short-range (SR) forces and the long-range (LR) Coulomb interactions in which the later destabilizes the crystal toward a ferroelectric state [81]. Later on, first-principles calculations evidenced that the microscopic key ingredient for ferroelectricity is a dynamical charge transfer between the oxygen anions and the B-cation due to hybridization between O-2p and empty B-site d-orbitals [82]. This effect is highlighted by the presence of anomalously large Born effective charges (Z^*) on these atoms [83] and by an unstable polar phonon mode at the center of the Brillouin zone of the cubic high temperature phase [84]. Thus, to our knowledge, almost all experimental and theoretical researches in the field of magnetoelectrics and multiferroics have been dedicated to oxide systems, with special focus to perovskite structures and only a few works and reports —in comparison to oxides— have been focused in analogous systems such as fluorides. Then, the understanding of physical phenomena is particular to each material and cannot be generalized. Here, as an alternative, emerge some structures based on fluoride systems with a similar crystal structure than the already discussed oxides, such as KBF_3 [85], and $NaBF_3$ [86, 87]. In these systems, the physical phenomena such as superexchange interaction, stabilization of octahedral-tilting, and possible multiferroic or magnetoelectric behavior is still unclear. According to our previous discussion, we carried out a research on ABF_3 fluoroperovskites in order to explore the possibility to include this material as a new multiferroic in this selected group.

In terms of the tolerance factor (t), perovskite fluorides follows pretty well the trend of the phase as a function of the t factor. For example, for values below $t = 0.78$ the ABF_3 adopts the $R\bar{3}c$ structure, the $Pnma$ symmetry can be found for t between 0.78 to 0.88. The $Pm\bar{3}m$ in 0.88 to 1.00 range and $P6_3/mcm$ from 1.00 to 1.08 respectively. There are a few exceptions due to the Jahn-Teller distortion in $KCuF_3$, $KCrF_3$ with a $I4/mcm$ structure [88]. Besides, taking into account the large change on the ionic radii of the A-site going from Li to Cs, it is expected to observe a large change in the expected structure and then, the vibrational landscape that suppress the ferroelectricity. A systematic study of the structural instabilities in the high symmetry cubic halide perovskites was carried out in the 80's using interionic potentials [89]. Phonon frequencies were calculated at the Γ, X, M and R high symmetry points of the cubic Brillouin zone for ABX_3, with A = Li, Na, K, Rb or Cs, B = Be, Mg or Ca, and X a halide (F, Cl, Br or I). While none of these perovskites has a ferroelectric ground state —although some, mostly Li members of the series have the *non-perovskite* ferroelectric $LiNbO_3$ structure as their ground state—, 24 of the 60 cases were found to show a ferroelectric (FE) instability. The instability was usually absent in compounds with a larger A cations, which anyway usually form in a non-perovskite hexagonal structure, and so it was concluded that the Na compounds should be the most promising candidates for ferroelectricity. It was found, however, that in all cases a competing antiferrodistortive (AFD) zone boundary instability corresponding to rotations

and tilts of the X octahedra around the B cation, dominated over the weaker polar instability, resulting in a centrosymmetric AFD ground state [90]. Such competition between AFD and FE instabilities has been widely discussed in the perovskite oxides literature [91, 90, 92, 93] and recently shown, in the case of *Pnma* perovskites to result from a mutual coupling to an X_5^+ mode involving antipolar displacements of the A-cations and X-sites along the [101] axis. Indeed artificially removing the X_5^+ mode in the calculations for perovskite oxides was shown to induce a ferroelectric ground state [92]. Thus, in the next sections we are going to go further in this vibrational analysis in order to obtain a deeper understanding of the structural properties in fluoroperovskites to be later used in the "tuning" and study of their properties.

2.1 Computational Details

Our density functional calculations of the electronic and structural properties were performed using the VASP code [66, 67]. PAW [64] pseudo-potentials were used to represent the valence and core electrons. The electronic configurations — for valence and semicore electrons— taken into account in the pseudo-potentials are presented in Table 2.1. The exchange correlation was represented within the GGA - PBEsol parametrization [39]. Due to the large d-electron localization, we corrected the high correlation by means of the DFT+U method [43] (GGA+U, U = 4 eV), with a U value converged for all magnetic compounds. Due to the magnetic character of these systems, we have included the spin in the calculation and make the proper use of the exchange correlation (LSDA+U). The periodic solution of these crystalline structures was represented by using Bloch states with a Monkhorst-Pack k-point mesh of (8×8×8) and 700 eV energy cut-off, which has been tested already to give forces convergence to less than 0.0001 eV/Å and an error in total energy around ± 0.4 meV in all of the tested compound. Additionally, vibrational modes were fully converged with respect to energy and k-point to obtain values in error less than 1 cm^{-1}. Full Phonon-dispersion curves were computed by calculating the dynamical matrix from the 2×2×2 supercell and mapped to the unit cell. The Dynamical matrices and Born effective charges were obtained through the DFPT formalism [69] as implemented in VASP and post-processed in the Phonopy code [94]. Additionally, the phonon dispersion curves were also interpolated from the interatomic force constants (IFCs) using the `anaddb` module provided with the Abinit software [95].

2.2 Ionic A- and B-site Radii Size Effects

Vibrational properties and stability were analyzed by DFT in fluoroperovskites ABF_3. The analysis were carried out first in the family $NaBF_3$ for B = Mn, V, Ni. Additionally to that, some non-magnetic cases were also taken into account (*i.e.* B = Ca, Zn) in order to study the ferroelectric behavior among some elements in

Table 2.1: Electronic configuration of pseudopotentials. Valences and semicore electrons taken into account for calculations.

A-site	B-site	X-site
Li ($1s^2 2s^1$)	Ca ($3s^2 3p^6 4s^2$)	O ($2s^2 2p^4$)
Na ($2p^6 3s^1$)	V ($3p^6 3d^3 4s^2$)	F ($2s^2 2p^5$)
K ($3p^6 4s^1$)	Mn ($3p^6 3d^5 4s^2$)	
Rb ($4p^6 5s^1$)	Ni ($3p^6 3d^8 4s^2$)	
Cs ($5s^2 4p^6 6s^1$)	Zn ($3d^{10} 4s^2$)	

period IV. This with the aim to understand the possible influence of ionic radii size and magnetic ordering in the structure and the vibrational behavior. The later will help us to understand the ground state at the fluoroperovskite familie by studying and knowing the nature of the displacive transitions posible in the perovskite fluorides. In this type of transition, the modes that drives the transformation are the same phonon modes driving the lattice dynamics. Therefore, it is of high importance to understand the vibrational landscape of the materials investigated on this thesis. For a better understanding of the nature of the displacive transitions and the theory beneath it, the reader can check the references from Dove [96] and Lines and Glass [11].

First at all, we start by defining the phonon frequencies and eigenvectors within the harmonic approximation as:

$$\sum_{k',\beta} \tilde{D}_{k\alpha,k'\beta}(\mathbf{q})\gamma_{m\mathbf{q}}(k'\beta) = \omega^2_{m\mathbf{q}}\gamma_{m\mathbf{q}}(k'\alpha) \tag{2.1}$$

where α and β are the cartesian coordinates of displacement, κ and κ' are the atoms of interest, $\omega_{m\mathbf{q}}$ is the phonon frequency of a m mode at a wave vector $\mathbf{q}$, $\gamma_{m\boldsymbol{q}}$ is the associated phonon eigenvector corresponding to the eigendisplacement defined as: $\eta_{m\mathbf{q}} = \sqrt{M}\gamma_{m\mathbf{q}}$ and finally, $\tilde{D}_{k\alpha,k'\beta}$ is the dynamical matrix, formed by the Fourier transform of the interatomic force constants matrix (IFC, $\tilde{C}_{k\alpha,k'\beta}$) as:

$$\sum_{k',\beta} \tilde{D}_{k\alpha,k'\beta}(\mathbf{q}) = \tilde{C}_{k\alpha,k'\beta}(\mathbf{q})/\sqrt{M_k M_{k'}} \tag{2.2}$$

In the real space the IFC matrix is defined in terms of the energy of the system as follows:

$$C_{\kappa\alpha,\kappa'\beta}(l,l') = \frac{\partial^2 E}{\partial\tau_{\alpha\kappa}(l)\partial\tau_{\beta\kappa'}(l')}, \tag{2.3}$$

where E is the total energy, l and l' are the cells of respective atoms and τ is the displacement. In Fig. 2.1 are presented the fully relaxed phonon-dispersion bands for $NaMnF_3$ computed in the high temperature symmetric cubic $Pm\bar{3}m$ perovskite [97]. Structural instabilities (*i.e.* imaginary modes represented as negative frequency values) can be seen from the phonon-dispersion curve through the entire Brillouin zone. A polar ferroelectric mode is observed at zone-center Γ-point that has been also found in all ferroelectric systems based on oxides such as $BaTiO_3$, $PbTiO_3$, and antiferroelectric $PbZrO_3$ [84].

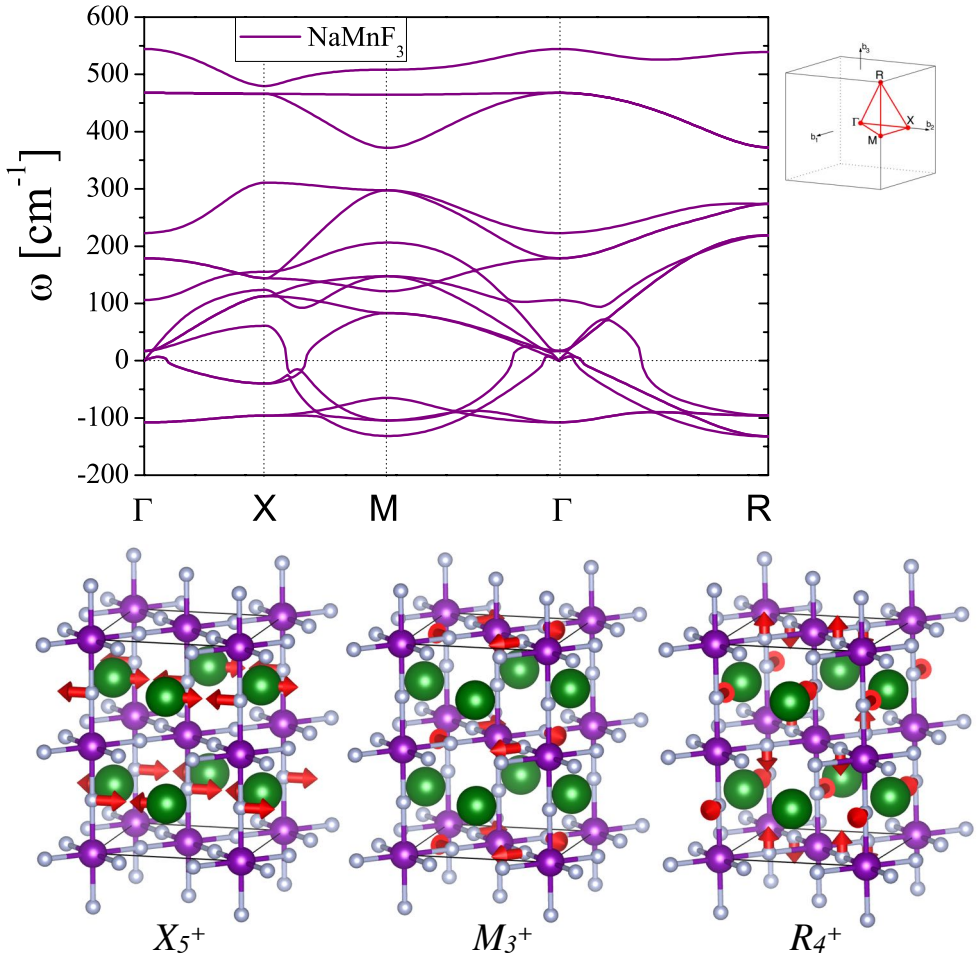

Figure 2.1: (Above) Phonon-dispersion curves for $NaMnF_3$ computed at the $Pm\bar{3}m$ phase. The Brillouin zone is presented in the inset. The imaginary modes are plotted as negative values . Atomic displacement for each unstable mode. (Below) Antipolar displacements, octahedral rotations and tilts (depicted by arrows) can be observed for the X_5^+, M_3^+, and R_4^+. modes.

Additionally, two instabilities with high intensity in frequency value were also observed at R-point showing a flat branch along the R–M path characteristic of the AFD modes reported in some oxides too. It is believed that this geometrical instability competes with FE mode and, in some cases can completely suppress

it in the ground state. Thus, all these instabilities combined leads most of the $NaBF_3$ compounds to an orthorhombic *Pnma* (62) ground state, in which, ferroelectricity is totally suppressed by symmetry. As an exception to the rule, the $NaCaF_3$ case has been reported in a rhombohedral *R3c* structure in ground state symmetry with possible ferroelectric ordering [86]. Nevertheless, up to now there is no experimental results corroborating the FE behavior in this material. The phonon-dispersion bands for B = Ca, V, Ni, and Zn are similar to B = Mn and because of that, are not presented here.

According to these vibrational results, we have found for all structures a clear dependence of FE-instability as a function of the ionic B-site radii for B^{2+} state, of course, taken into account the number of coordination (*i.e.* B-F_6 bonding) [98]. Then, as the ionic B-site radii decrease, the FE-mode decrease as well as a function of this parameter (see Table 2.2). Additionally, we observed the same behavior for one of two instabilities at R-point, meanwhile the second one remains almost constant. In the same table we also presented the computed values for $BaTiO_3$ for comparison with oxide systems.

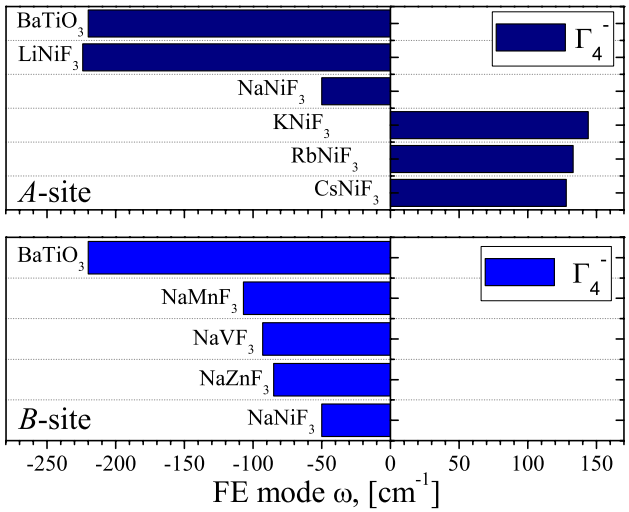

Figure 2.2: Polar Γ_4^- mode, into the Bethe's notation [99], as a function of the A- and B-site in ABF_3 perovskites, the imaginary modes are presented as negative values.

Now, we are going to talk about the A-site effect, for this proposes the B-site was fixed to Ni case, this in order to keep small lattice parameters. From Table 2.2 it can be appreciated that FE polar instability present a more critical dependence with respect to the ionic A-site radii size than B- one. The later findings are presented graphically in the Fig. 2.2. Therefore, an increase of this parameter can totally suppress the FE imaginary mode and AFD instabilities, which leads the structure to a totally different crystal ground state symmetries as listed in Table 2.2. This behavior can be explained in terms of eigendisplacements, η (see Table 2.3) for this mode, in which the dominant contribution in the FE-mode is precisely the A-site displacements. Increasing the A-site radii, the displacements

decreases as well and with that a strong reduction of the frequency it is appreciated, meanwhile, the imaginary mode is suppressed for A = K, Rb, and Cs (see Table 2.2).

Table 2.2: Summary of most unstable high symmetry point phonon eigenvalues, relaxed lattice constants for cubic $Pm\bar{3}m$ symmetry, ionic A and B sites radii and reported ground state symmetry for all compounds [88]. HS: High Spin, LS: Low Spin. All modes in (Γ_4^-, R_4^+, R_5^+, X_5^+ and M_3^+) in cm^{-1}.

Compound	a_o [Å]	B-radii[a] [pm]	Godschmidt, t	FE - Γ_4^-	R_4^+	R_5^+	X_5^+	M_3^+	Ground State [88]
$BaTiO_3$	3.9851	74.5	0.97	220i	Non	Non	189i	165i	$P4mm$ [100]
$NaCaF_3$	4.3762	114	0.71	127i	135i	120i	114i	132i	$R\bar{3}c$ [86]
$NaMnF_3$	4.1441	97 (HS)	0.77	107i	131i	94i	96i	132i	$Pnma$
$NaVF_3$	4.1117	93	0.78	93i	132i	92i	95i	131i	$Pnma$
$NaZnF_3$	4.0004	88	0.80	85i	130i	59i	70i	129i	$Pnma$
$NaNiF_3$	3.9245	83 (LS)	0.82	50i	127i	15	47i	126i	$Pnma$
		A-radii [pm]							
$CsNiF_3$	4.1553	181	1.05	128	186	258	226	193	$P6_3/mmc$, z=2
$RbNiF_3$	4.0628	166	1.00	133	149	258	212	153	$P6_3/mmc$, z=6
$KNiF_3$	4.0021	152	0.95	144	94	142	111	97	$Pm\bar{3}m$
$NaNiF_3$	3.9245	116	0.82	50i	127i	15i	47i	126i	$Pnma$
$LiNiF_3$	3.8766	90	0.73	224i	214i	166i	213i	190i	$R\bar{3}c$[b]

[a]Ions are 6-coordinate [98]

[b]Expected ground state

Table 2.3: Eigendisplacements (η) for all compounds at relaxed cubic structure. $X_{\perp}$ and $X_{\parallel}$ are the sites located perpendicular and parallel to the M-F bonding respectively

η, (ABF_3) [a.u.]				
Compound	*A*-site	*B*-site	$X_{\perp}$	$X_{\parallel}$
$BaTiO_3$	*0.001*	*0.098*	*-0.071*	*-0.155*
$NaMnF_3$	0.174	-0.005	-0.020	-0.088
$NaVF_3$	0.181	-0.018	-0.019	-0.077
$NaZnF_3$	0.177	-0.005	-0.025	-0.084
$NaNiF_3$	0.186	-0.002	-0.025	-0.068
$CsNiF_3$	0.057	-0.096	-0.075	-0.031
$RbNiF_3$	0.081	-0.073	-0.068	-0.034
$KNiF_3$	0.138	-0.053	-0.051	-0.034
$NaNiF_3$	0.186	-0.018	-0.025	-0.068
$LiNiF_3$	0.347	0.003	-0.010	-0.065

As previously discussed, the 3-fold degenerated eigendisplacements in FE-instabilities, condensed in Table 2.3, taken at the relaxed volume for each compound, reveal a strong influence of the A-site in the FE-mode. The ionic B-site radii size have a weaker influence in the FE-instability than the A-site. Additionally, the eigendisplacements of F ions along the atomic movement (perpendicular to B-F bonding direction) has an important contribution that decreases as ionic B-site radii does. From the analysis of values obtained for different A-sites, we can also noted an induced "transition", from negative to positive, in FE-polar mode eigendisplacements of the B-site (Table 2.3), going from positive displacements in Li to a negative ones at K, this means an opposite movement of Li against the B-sites in comparison with the other compounds. The later change can also contribute to the totally different structural stabilization symmetries for ground states in A-site = Li, Na, K as listed in Table 2.2.

Phonon-dispersion curves computed for A = K, Rb, and Cs do not exhibit any instabilities at any point of Brillouin zone, suggesting a cubic symmetry as a ground state for this compounds. Here, it is important to remark that the previous conclusion is only true for $KNiF_3$ compound which present a $Pm\bar{3}m$ symmetry. For A = Cs and Rb cases the experimentally reported ground state belongs to a hexagonal symmetry. As it is well known, there is no direct structural transition path from cubic to hexagonal symmetries through octahedral tilting. Then, a phase transition from cubic to hexagonal structure requires the break of bondings at octahedral corner-shearing site. This fact explains the vibrational behavior of these compounds at the assumed cubic structure as it has been taken into account in our studies. We can now analyze the dependence of distorted

structure perovskites as a function of the ionic radii ratio. We start from the respectively tolerance factor (*i.e.* t, Table 2.2) defined by Goldschmidt as follows:

$$t = \frac{r_A + r_X}{\sqrt{2}(r_B + r_X)}, \tag{2.4}$$

where r_A, r_B, and r_X are the ionic radii for the A-, B- and X-sites respectively. It can be noted that the Eq. 2.4 shows a close relationship between the tolerance factor and ionic sites radii, which at the same time, it can be related to the ground state and the FE/AFD instabilities ratio. Then, for smaller t values (*i.e.* $LiNiF_3$ and $NaCaF_3$) we observed that the FE frequency is higher in comparison to AFD one. Here, this partial conclusion suggest that the FE freezing is sufficient enough to lead these systems from the cubic high temperature structure to a rhombohedral $R\mathfrak{Z}c$ ground state as previously reported for $NaCaF_3$ but, to out knowledge, found for a first time in $LiNiF_3$. This opens the possibility for a novel G-type AFM multiferroic fluoride-based perovskite. For other compounds, an orthorhombic *Pnma* structure is expected at tolerance factors that lies between 0.77 to 0.88. From 0.88 to 1.00 a cubic $Pm\bar{3}m$ ground state is expected. At higher values, above $t = 1.00$ are anticipated different hexagonal symmetries. A few exceptions such as $KCuF_3$ and $KCrF_3$ have been reported due to Jahn-Teller distortions [88]. All these results are in full agreement with the our computed vibrational properties listed in Table 2.2.

In Fig. 2.3 are presented the results for the ferroelectric instability as a function of the tolerance factor. Here, the $LiBF_3$ and $NaBF_3$ series are shown, in which, it can be observed that the values of the frequency for the Li family are well above 200 icm^{-1}. These values are close to the ones observed in oxides perovskites. For the Na family we found frequency values between 50 to 150 icm^{-1} showing and stronger dependence on the B-site radii.

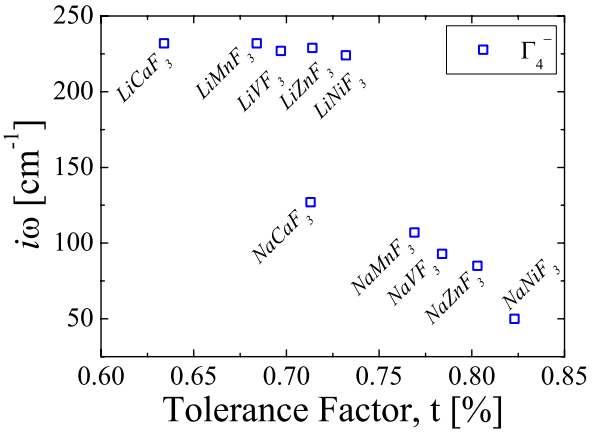

Figure 2.3: Ferroelectric instability in $LiBF_3$ and $NaBF_3$ (B = Ca, Mn, V, Zn, and Ni) as a function of the tolerance factor, t.

Another useful parameter used to characterize the ferroelectricity in oxides, is the calculation and analysis of the Born effective charges (Z^*) tensor. In oxides, the Z^* components exhibit anomalous values far from the nominal charges. The later due to the covalent character of the B–O bonding and the dynamical charge transfer widely studied and reported [101]. The Z^* tensor is defined as:

$$Z^*_{\kappa,\alpha\beta} = \Omega \frac{\partial P_\beta}{\partial \tau_{\alpha,\kappa}} |_{\mathcal{E}=0}, \tag{2.5}$$

where α and β are the cartesian coordinates, P is the polarization and $\mathcal{E}$ is the macroscopic electric field. Our computed Z^* values for all fluorides in question and $BaTiO_3$ compounds are presented in Table 2.4. For both, A- and B-sites we found that Z^*s are close to nominal charge (*i.e.* A^{1+}, B^{2+}). However, for F-ions the Z^* are 0.7 e^- away from its valence, which could be possibly due to a weak covalent interaction in the F-(B-site)-F bonding. It is clear that these values are lower than in the oxides case, but are strong enough to contribute to the superexchange magnetic interaction. The later interaction responsible for the antiferromagnetic ordering observed experimentally in most of perovskite fluorides —with a magnetically active B-site— at their ground state structure [88]. In the same table, the Z^* components for barium titanate are also presented. Anomalous Z^* for Ti and O sites parallel to the bonding are observed as expected due to the strong covalent contribution that allows the stabilization of the FE ground state in this oxide. These Z^* close to nominal charges stand for another substantial difference of the fluorides in comparison to oxides perovskites that can be exploited.

In order to achieve a better understanding of the vibrational properties in fluorides, we analyzed the interatomic force constants (IFC) calculated from Eq. 2.3. The analysis of IFCs reveals information about interatomic interactions that are predominant in the vibrational instabilities and lead to a stable structure. We present our calculated on-site force constants (on-site IFC) in Table 2.5. The on-site IFC are positive for all the elements in the ABX_3 compounds, showing that they are all stable under an isolated atomic displacement. Then, the phonon instabilities observed in phonon dispersions and discussed above, only can be removed or compensated by a cooperative movement of all atoms in order to gain energy and lower the total enthalpy of the system. One exception inside the analyzed compounds is the negative on-site IFC for Li atoms in $LiNiF_3$ perovskite suggesting a necessary collective movement of Li ions in lattice to reach a stable state. This fact can explain the $R\bar{3}c$ crystalline group expected as ground state for $LiNiF_3$ in which a huge displacement and distortion of cubic structure is required to achieve the structural transition. From the Table 2.5 can be also noted that B = V and Ni presents the highest values of on-site IFC values for A, B, and F sites, this fact suggest a low movement of self-site ions from its position in comparison with the other compounds. The remarkable low value in the on-site IFC for Na in $NaCaF_3$ suggest a possible A-site distortion needed to stabilize the structure and then, suppress the unstable phonon branch exhibited at zone-center. Additionally,

Table 2.4: Born Effective Charges (Z^*, e^- units) in for all compounds computed at relaxed cubic structure computed according to the Eq. 2.5. The $X_\perp$ and $X_\parallel$ are the components perpendicular and parallel to the B–X bonding.

Z^* (ABX_3) [e^-]				
Compound	A-site	B-site	$X_\perp$	$X_\parallel$
$BaTiO_3$	*2.750*	*7.368*	*-2.145*	*-5.857*
$NaCaF_3$	1.171	2.204	-0.862	-1.715
$NaMnF_3$	1.166	2.211	-0.829	-1.723
$NaVF_3$	1.179	1.988	-0.712	-1.749
$NaZnF_3$	1.153	2.218	-0.842	-1.686
$NaNiF_3$	1.154	2.048	-0.737	-1.729
$CsNiF_3$	1.460	2.327	-1.028	-1.729
$RbNiF_3$	1.279	2.222	-0.874	-1.752
$KNiF_3$	1.210	2.147	-0.803	-1.750
$NaNiF_3$	1.154	2.048	-0.737	-1.729
$LiNiF_3$	1.210	2.030	-0.757	-1.728

it is observed a clear increase of on-site IFC for A-site in $NaBF_3$ compounds as a function of B-site radii, making more difficult the movement of this ion within the structure due to the reduced volume. This conclusion is also consistent with the trend of the FE instabilities at the zone center as a function of ionic radii presented in Table 2.2. For comparison, we also presented the values for two well known ferroelectric oxides, $BaTiO_3$ and $PbTiO_3$. For the first one, a high value of on-site IFC in Ba reveal a stable position of this site making difficult its movement. This is in full agreement with the ferroelectric mechanism in this compound which strongly depend on the Ti–O–Ti chain displacement [102]. Instead of that, in $PbTiO_3$ the on-site IFC for Pb is low and it is related to the strong role of Pb site in the ferroelectricity in lead titanate, in which Pb–O movements presents a strong participation in the phenomena added to Ti–O–Ti chain displacements [84]. On-site IFC for fluorine sites presents a remarkable difference between $F_{x=y}$ sites (*i.e.* that lies in A-F plane) and F_z (*i.e.* that lies along B–F bonding) values. This difference suggests a stable position for F_z interaction, however, the low value for $F_{x=y}$ indicate a possible movement of this sites inside of A–F planes which could reinforce the BF_6 tilting expected for the compounds. The later in comparison with oxides also presented in Table 2.5, in which no oxygen octahedral tilting is expected.

Table 2.5: On-site interatomic constants (on-site IFC, in eV/Å^2 units) for the ABX_3 flouroperovskites. The on-site IFC for the $BaTiO_3$ and $PbTiO_3$ are also presented for comparison. The $F_{x=y}$ sites lies in A-F plane meanwhile the F_z lies along B–F bonding.

On-site IFC for ABX_3 [eV/Å^2]				
Compound	A-site	B-site	X	X
	$x=y=z$	$x=y=z$	$x=y$	z
$BaTiO_3$	*8.27*	*13.09*	*+6.74*	*+11.70*
$PbTiO_3$ [84]	*2.40*	*13.51*	*+4.38*	*+14.72*
$NaCaF_3$	**0.02**	12.79	0.43	12.78
$NaMnF_3$	0.17	13.14	0.76	13.35
$NaVF_3$	0.23	19.00	0.88	17.29
$NaZnF_3$	0.43	12.63	1.22	13.81
$NaNiF_3$	0.60	17.07	1.63	16.13
$CsNiF_3$	5.34	8.76	3.93	6.11
$RbNiF_3$	4.16	11.76	3.46	9.52
$KNiF_3$	2.88	13.94	2.85	12.18
$NaNiF_3$	0.60	17.07	1.63	16.13
$LiNiF_3$	**-0.34**	18.25	1.14	17.52

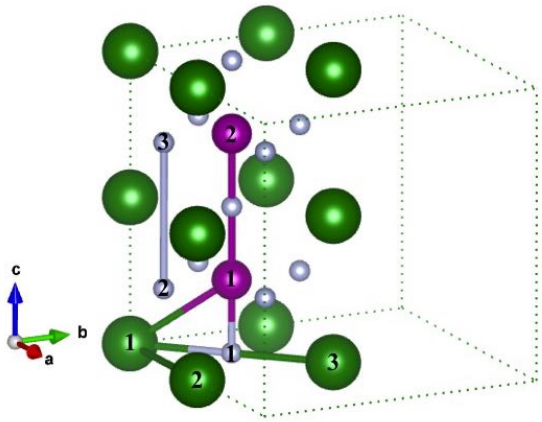

Figure 2.4: Selected IFC interactions in the 2×2×2 supercell. A- B- and F-sites are depicted in green, violet and grey respectively. Additionally, the atoms are labeled to correlate the IFCs shown in the Table 2.6.

Table 2.6: Selected IFC according to interactions illustrated in the Fig.2.4 for the A-, B-, and F-sites respectively.

IFC for ABF_3 compounds one quarter of unit cell [eV/Å^2]													
Compound	A_1-A_3		A_1-A_2		A_1-B_1		B_1-B_2		A_1-F_1			B_1-F_1	
	xx=yy	zz	∥	⊥	xy	xx	∥	⊥	xx=yy	xy	zz	∥	⊥
$NaCaF_3$	-0.19	+0.09	-0.46	+0.20	-0.32	-0.10	**-2.73**	+0.29	+0.21	+0.37	-0.30	**-4.31**	-0.62
$NaMnF_3$	-0.20	+0.09	-0.51	+0.21	-0.33	-0.09	**-2.77**	-0.24	+0.18	+0.34	-0.33	**-4.62**	-0.55
$NaVF_3$	-0.21	+0.11	-0.52	+0.22	-0.30	-0.10	**-1.96**	+0.08	+0.16	+0.31	-0.30	**-6.78**	-0.97
$NaZnF_3$	-0.20	+0.09	-0.56	+0.21	-0.35	-0.10	**-3.21**	+0.18	+0.15	+0.32	-0.36	**-4.39**	-0.46
$NaNiF_3$	-0.21	+0.10	-0.59	+0.23	-0.34	-0.10	**-2.62**	+0.07	+0.13	+0.29	-0.31	**-5.69**	-0.91
$CsNiF_3$	-0.17	+0.07	-0.87	+0.23	-0.35	-0.15	**-2.47**	+0.07	-0.41	-0.40	-0.24	**-1.34**	-0.88
$RbNiF_3$	-0.17	+0.08	-0.74	+0.22	-0.35	-0.13	**-2.59**	+0.06	-0.29	-0.21	-0.26	**-2.73**	-0.92
$KNiF_3$	-0.18	-0.09	-0.68	+0.22	-0.34	-0.12	**-2.62**	+0.06	-0.14	-0.02	-0.29	**-3.88**	-0.93
$NaNiF_3$	-0.21	+0.10	-0.59	+0.23	-0.34	-0.10	**-2.62**	+0.07	+0.13	+0.29	-0.31	**-5.69**	-0.91
$LiNiF_3$	-0.25	+0.11	-0.57	+0.25	-0.34	-0.09	**-2.64**	+0.06	+0.24	+0.42	-0.33	**-6.35**	-0.89

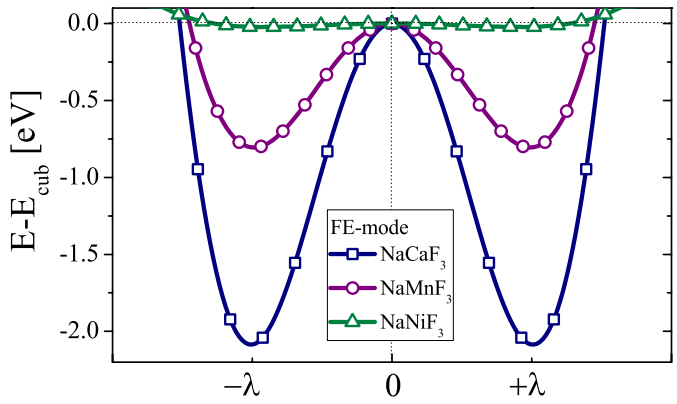

Figure 2.5: Double-well energy obtained at the FE-mode freezing in $NaBF_3$ compounds. The gain in energy is in agreement with previous results that shows that the bigger is the B-site, bigger is the FE instability and with this, the possibility to be ferroelectric. ± λ denotes the full amplitude of the freezing.

Additionally to on-site IFC, some selected IFC for interactions were computed within a quarter of a 2×2×2 supercell as labeled in Fig.2.4 and presented in Table 2.5. The analysis were taken into account for components parallel and perpendicular to the direction of line that connects the related atoms. This analysis was performed with the aim to study some selected interactions and analyze the relationship between the ions that present the highest contribution in the total energy. First, it is noted the significantly high repulsion force between $(B_1–F_1)\|$ sites, which induce the movement of all B-sites with the fluorine ions instead of against them, like in barium and lead titanates. The IFCs values as a function of A-site radii shows that B–F repulsion interaction decrease when A-radii increase as well, and then, a freezing of octahedra tilting and stabilization of cubic structure is achieved in the $KNiF_3$ case. Besides, the $B_1–B_2$ ‖ IFCs values and the high on-site IFC obtained for the center-sites suggest that B-ions cannot move easily in comparison with the center-site displacement observed in some oxides (*e.g.* barium titanate). Nevertheless, these B-sites are still presenting a small contribution in the FE-mode that cannot be neglected as discussed above based on eigendisplacements values. The contributions from another interactions such as A–A and A–F listed in the Table 2.6 are smaller than those discussed previously and do not present a considerable contribution.

Moving forward, we analyze the energy landscape of the ferroelectric mode. In Fig.2.5 are presented the double-well energy curves obtained through the freezing of ferroelectric instabilities along z-axis. From this figure it is observed a clear dependence of energy minimum as a function B-site, in which the higher value of FE frequency corresponds to a lowest energy value. These results are in full agreement with our previous analysis and are summarized in the next section. In $NaCaF_3$ case, the double-well analysis suggests a prominent predisposition of

these materials to freeze the FE ground state over the AFD one due to the high energy gain.

2.3 Ferroelectricity Model Proposed for ABF_3 Fluorides

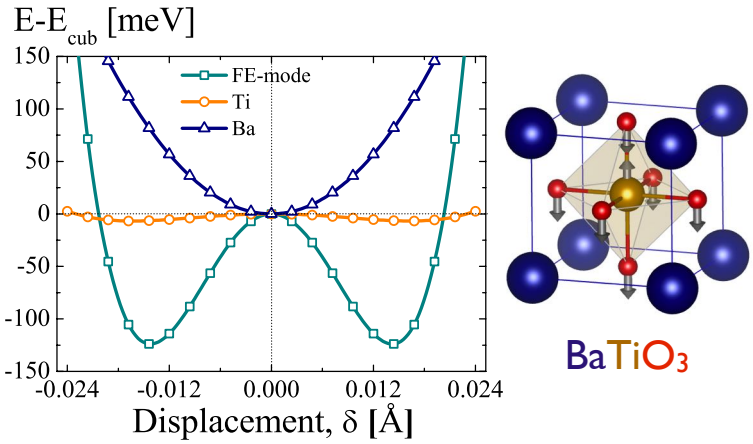

(a)

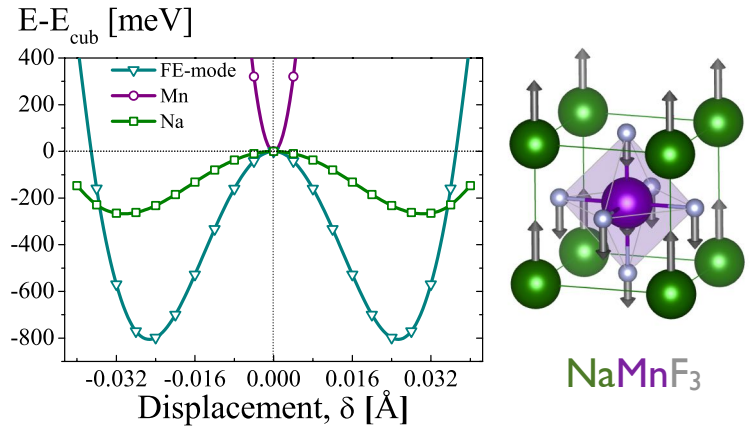

(b)

Figure 2.6: Double-Well energy curves and schematic representation of atomic displacements in different models of ferroelectricity for oxides a) $BaTiO_3$ and b) $NaMnF_3$.

As all the previous discussion and analysis suggest, the mechanism responsible for the ferroelectric mode is based on the A-site movement, which is strongly dependent of vacuum space or free space for A-site displacements related then, to a steric effect. Thus, a decrease of B-site radii, reduce the lattice volume and then, reduce the free space for A-site movement. Also, this fact explains the strongly correlated dependence of FE-mode as a function of A-site radii, thus, a complete

suppression of the FE mode is observed for ionic radii beyond Potassium. Additionally, it is noted that F-ions present a strong participation in the FE-instability, and also exhibit the same trend as a function of ionic B-site radii. Besides that, the ferroelectric polar mode is less dependent on the covalent interaction present along the B–F bonding, making this phenomena more stable than in oxides. In order to corroborate this idea, double-well energy curves were computed for the $NaBF_3$ compounds (As discussed before and shown in Fig.2.5).

To compute this curves, the polar FE phonon-branches were frozen in order to obtain the energy barrier for this mode. Additionally, we computed the curves for the independent freezing of each A and B-sites eigendisplacements in fluorides and $BaTiO_3$ oxide. In Fig.2.6a it can be appreciated the energy curves for which in the oxide case, the lowering in energy is induced by the B-site movement as widely studied and expected. Any contribution of the A-site (*i.e.* Ba) was observed according to the curves. In contrast, for the fluoride case —here choosing the $NaMnF_3$ as example— the largest contribution comes from the A-site displacements (see Fig.2.6b), and no contribution of B-site was observed. The later is in agreement with all the previous results that explains the A-site geometrically driven FE mode. In the same figures are also schematically shown —with arrows— the atomic displacements for FE-modes in each case. As discussed above, we found different contributions from the A- and B- sites in the fluoride and oxide cases respectively. This substantial difference is making this phenomena completely characteristic of the fluoroperovskites in comparison to oxides. In conclusion, all the results demonstrates an A-site geometrically-driven FE-instability mechanism in fluorides rather than a B-site charge-transfer one as in most of the oxides.

2.4 Ferroelectric Instability Enhancement in $NaBF_3$ Fluorides

Interestingly, in some oxide-based compounds —such as $BaTiO_3$ and $PbTiO_3$— has been found a particular behavior of ferroelectricity and then, of the FE-instability as a function of isotropic external strain or pressure [100, 103]. In these compounds the FE ordering can be totally suppressed by pressure. The study of the later physical phenomena widely discussed in oxides, but less known in fluorides, has been considered in the framework of this research. First, we have studied the isotropic pressure effects in the vibrational properties of fluorides perovskites. Fig.2.7 shows the squared frequency for the FE-mode instability as a function of isotropic pressure, here shown as expansion and compression cell percentage with respect to the relaxed volume. From the expansion zone (*i.e.* negative pressure) it can be observed that the squared frequency for all compounds converge almost to the same value, -10×10^3 cm^{-2}. This could be a consequence of structural distortions induced by mixed phenomena between ionic charge effects and ionic B-site radii that needs further studies. For compression values (*i.e.* posi-

tive pressure) it is observed a non-linear increase of the FE instability in opposite direction to the values obtained for $BaTiO_3$ [100] in which, a FE suppression by pressure has been demonstrated. Our results also show a "transition" of eigendisplacements responsible of this mode (Fig.2.9). We found an exception to the main trend in the $NaNiF_3$ case. This fluoroperovskite shows a total suppression of FE-instability at positive pressure equivalent to -2%. The suppression of the FE is in the same way as observed for $BaTiO_3$ (see Fig.2.7). The different trend for nickel-based compound will be discussed in more detail later. From Fig.2.7 it is also observed that the increase of the instability as a function of pressure also present a clear dependence of the ionic B-site radii size, which is higher for Ca and lower for Zn. It is important to remark that close to the relaxed cubic lattice parameter value (*i.e.* P ≈ 0), the slope in the ω^2 vs. P line is small in comparison with the one observed $BaTiO_3$. This facts indicates a strong stability of the ferroelectric instability as a function of pressure in the ABF_3 compounds. The analysis of the electronic structure as a function of pressure do not show an influence of unoccupied or occupied d-levels in the B-site and/or an electronic hybridization between F ($2s^2$) and Na ($2p^6$) as demonstrated in some oxide perovskite systems at high pressure [63].

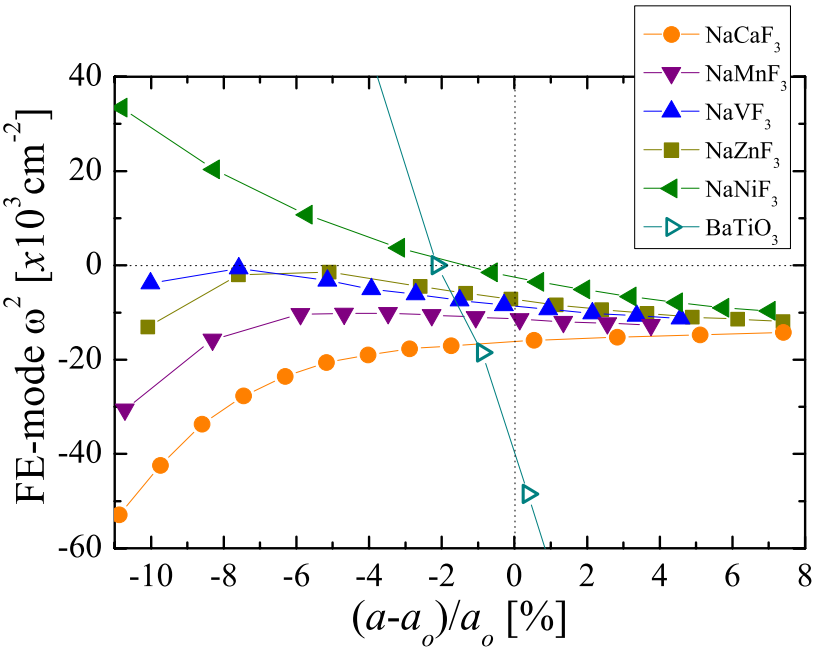

Figure 2.7: Unstable FE mode at the cubic $Pm\bar{3}m$ structure in ABX_3 compounds.

In order to go deeper in the understanding of the FE-instability behavior for all compounds, except $NaNiF_3$ discussed later, we carried out an analysis of the eigendisplacements and eigenvectors for the polar ferroelectric modes. In Fig.2.8 we presented the eigendisplacements as a function of lattice parameter variation (*i.e.* hydrostatic pressure). Most of the fluoroperovskites exhibit the same qualitative behavior, then, only the $NaCaF_3$ case is presented. We found a predominant

influence of the A-site for pressure regions located close to the relaxed lattice and expansion strain. In the region of constrain values, below -4% with respect to the relaxed volume in cubic $Pm\bar{3}m$ structure, the influence of the A-site decreases and the mode is dominated by B-site displacement. We found that the eigendisplacements behave similarly in all of the $NaBF_3$ materials, with the exception of B = Ni. To reinforce this change in A- and B-sites displacements, the F-sites also present a η_z transformation. For η_z parallel to B–F bonding, a "transition" of eigendisplacements from negative, at expansion strain values, to positive values are observed beyond strain pressures of -5%. The eigendisplacements for F-site perpendicular to B–F bonding remains negative but goes from η_z = -8 to η_z = -13 a.u. indicating an increase on their movement amplitude. The eigendisplacements are schematically represented in the Fig.2.8 for two regions of strain. The transformation on the nature of the eigendisplacements is possibly the cause for the frequency variation as a function of pressure observed in $BaTiO_3$ (Fig.2.9). In this oxide, the same change in η is observed for the ferroelectric mode at the FE-mode suppression when the hydrostatic pressure is applied.

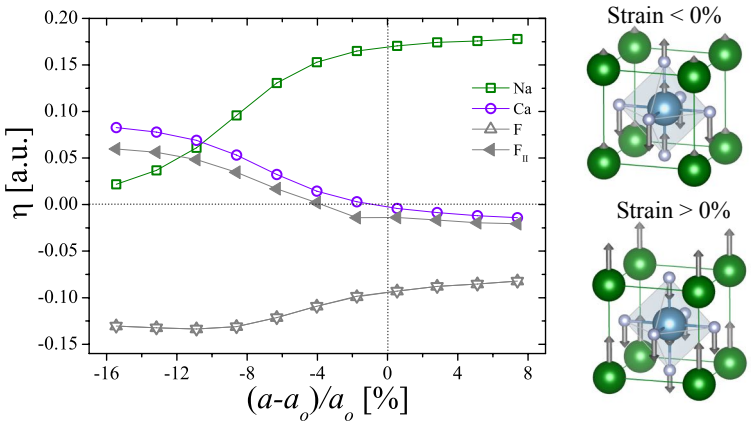

Figure 2.8: Eigendisplacements for $NaCaF_3$ compound showing the η transition also found in B-site: V, Mn, and Zn (left). Schematic representation of eigendisplacement in the fluorides compounds for strain values above and below of the relaxed structure (right).

In Table 2.7 we presented the on-site IFC values for all $NaBF_3$ compounds computed at a fixed volume that is equivalent to an expansion pressure in all of them. The later analysis in order to understand the B-site radii effect on the IFC. It can be noted that the A-site IFC constants are negative and close to zero, this indicating a possible uniform displacement of these sites required to lower the total energy. The on-site IFC values for F-sites increase as the B-site radii decrease, going from Ca to Ni. Therefore, the cubic lattice volume reduction leads to a lower F free space. The F_z values decrease with B-site radii, which implies a reduction of the attractive interaction force allowing a larger F_z-site displacement. The close value observed for on-site IFC site of A-ions could be the reason of the

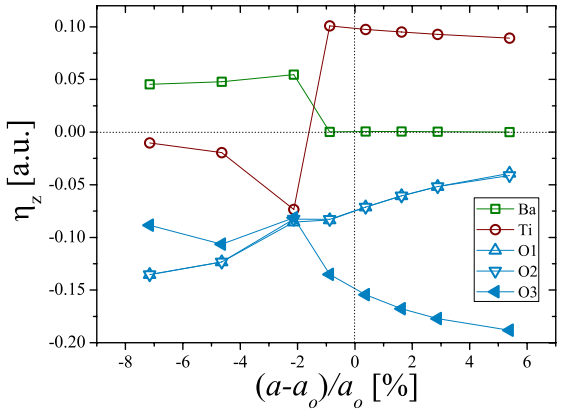

Figure 2.9: Eigendisplacements for $BaTiO_3$ showing the change of the mode as cause of suppression of ferroelectric instability as a function of isotropic pressure.

observed concurrence of the FE-mode frequency at expansion strain, taken into a count that this site dominates the ferroelectric mode in ABF_3 structures.

Table 2.7: On-site IFC for all $NaMF_3$ compounds at same lattice parameter equivalent to expansion.

On-site IFC [eV/Å^2], a = 4.30 Å				
Compound	A-site	B-site	F	F
	x=y=z	x=y=z	x=y	z
$NaCaF_3$	-0.05	+12.18	+0.49	+11.97
$NaMnF_3$	-0.04	+8.98	+1.06	+8.06
$NaVF_3$	-0.04	+12.10	+1.25	+9.63
$NaZnF_3$	-0.05	+5.39	+1.42	+3.93
$NaNiF_3$	-0.04	+7.91	+1.70	+5.60

On-site IFCs as a function of pressure are presented in Fig. 2.10 for each site. It can be seen that for a certain value in each case, between -3% to -8%, each of the $F_{x=y}$ constants exhibit a "transition" from positive to negative valued, which implies a change of interaction from attraction to repulsion respectively for these atoms. This transformation in the nature of interaction possibly induces some instabilities responsible for the increment of the FE-mode frequency as a function of pressure observed in the Fig.2.7. It can be also noted that on-site IFC values for $NaNiF_3$ remain positive, this could explain the different behavior of this compound in comparison with the rest of the members of this family discussed above. Additionally, A-, B- and F_z constants are quite larger for B = Ni in comparison with the Ca, Mn, V, and Zn.

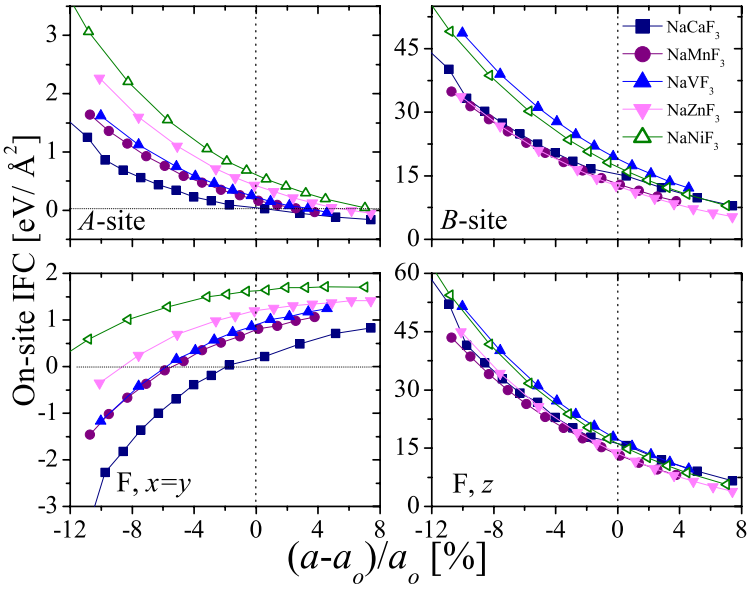

Figure 2.10: On-site IFC for A-, B- and F-sites (x=y, and z) as a function of strain for each of sites in $NaBF_3$ with B = Ca, Mn, V, Zn, and Ni.

2.4.1 *Modes Contribution in $Pm\bar{3}m$ to Pnma Transition in $NaBF_3$ Fluorides*

The analysis and study of vibrational properties allow us to understand the nature of the ferroelectric behavior in perovskite compounds. Based on that, a deeper analysis was carried out in order to understand the coexistence of ferroelectric, antipolar, rotational and tilting distortions in the $NaBF_3$ family of fluorides. First of all, it can be noted that in fluorides the contribution of the antipolar X_5^+ mode is higher than in oxides (compare Fig.2.11 with the values reported in Ref. [92]). This mode is related to antipolar distortions dominated by the A-site eigendisplacements. The R_5^+ mode contribution can be appreciated as well which is almost missing in oxides [92]. R_5^+ mode is also related to the A-site motion. M_2^+ mode present a smaller effect and, in the range of scale it cannot be observed. The R_4^+ mode and M_3^+ are also present as in oxides. This fact clearly modifies the balance picture between the contribution of modes to distortion when going from $Pm\bar{3}m$ to *Pnma*.

Here, the picture of the competition of modes is more interesting because the polar ferroelectric instability —present at Γ-point—, the antipolar mode —at X-point— and the antiferroelectric mode —at R-point— depend as well to the A-site displacements. Despite the picture in oxides, where the ferroelectric instability is leaded by B-site displacement meanwhile the A-site dominated antipolar X_5^+ mode suppresses the ferroelectric one in the *Pnma* symmetry as demonstrated by Benedek and Fennie [92].

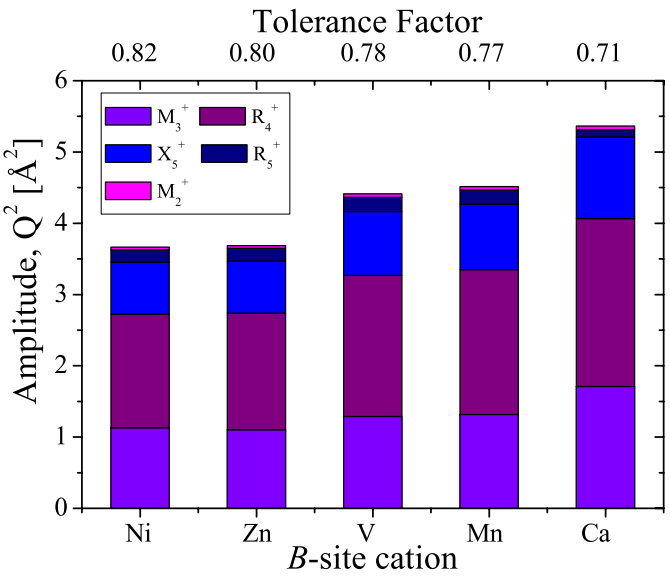

Figure 2.11: Contribution of modes in the phase transition from $Pm\bar{3}m$ to $Pnma$ in the $NaBF_3$ fluoroperovskites.

2.4.2 *Special cases: $LiNiF_3$ and $NaNiF_3$*

For $NaNiF_3$, we found a total suppression of FE instability as a function of external pressure as shown in Fig.2.7. In Fig.2.12 is presented the squared frequency for all the unstable modes as a function of external pressure. A total suppression of FE-instability at Γ is appreciated for strains above -2% with respect to the cubic relaxed lattice parameter. Additionally, the same behavior was observed for one of the instabilities located at R-point. The suppression of the instabilities is clearly different in contrast to the behavior observed for the others $NaBF_3$ compounds previously mentioned. We noticed that for this case, Ni posses the smallest ionic radii in comparison with all others compounds that belong to the fluoroperovskites family considered in this work.

Fig.2.13 depicts the eigendisplacements as a function of hydrostatic pressure for three of polar modes at the zone-center Γ-point including the FE-instability. For this mode, no transition or considerable change in eigendisplacements were observed. While for the others two modes, a quasi-constant dependence was observed. Then, no anomalous trend responsible for transition of FE-mode was appreciated.

We also analyzed the Born effective charges as a function of strain. A decrease of Z^* for Ni and F ions was observed at high expansion strain values going from 2.21 e^- (in expansion) to 1.65 e^- (in compression) and -1.84 e^- to 1.44 e^- for Ni and F respectively. A small fluctuation in values can be appreciated close to the eigendisplacements transition pressure.

Then, up to this point, some questions remain open around this compound: Why this compound is the only one to present this behavior? Is there a different

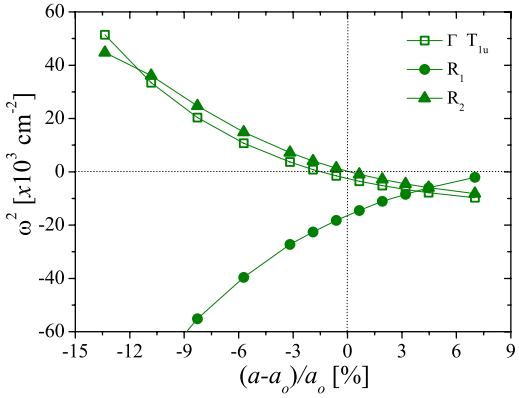

Figure 2.12: Behavior of FE and R-point instabilities as a function of hydrostatic pressure for $NaNiF_3$.

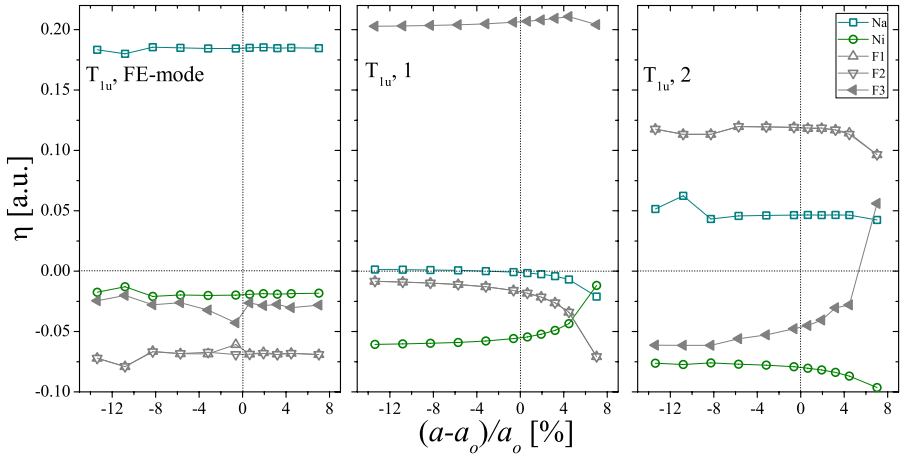

Figure 2.13: Eigendisplacements for all polar modes in $NaNiF_3$.

covalence bonding nature evidenced by the deviations in Z^*? Further studies are needed to find the origin of this out-of-trend behavior.

Finally, to conclude the ABF_3 analysis, we stress that the ionic A and B site radii size have a direct influence on FE-instability. From the theoretical analysis carried out and discussed above, the $LiNiF_3$ compound was chosen due to its higher FE-instability. This compound presents a relaxed cubic lattice parameter of 3.87 Å and its ferroelectric instability is higher than AFD-modes. This fact could lead to a stable ferroelectric ordering at the relaxed ground state structure, in which a *R3c* crystal symmetry type —like in $LiNbO_3$— is expected as suggested by Claeyssens *et al.* [104]. In Fig.2.14 are presented the analysis of instabilities as a function of strain at the Brillouin zone-center and boundary zone. For strain values around 3% of the relaxed volume, the FE-instability shows the highest frequency value but below -4% the AFD-instability becomes dominant in the vibrational landscape for this compound. The eigendisplacements for the

FE-mode as a function of strain (see Fig.2.14) show an A-site dominated mode at the relaxed structure. For hydrostatic pressure below the unconstrained volume, the influence of A-site decreases non-linearly and mode begin to be dominated by B-site movement. A sign change of the eigendisplacements was found at high strain around -7%. This behavior is similar such as the one observed previously in $NaBF_3$. It is important to remark that for all compounds a high stability of η as a function of external expansion and compression strain around relaxed volume has been found.

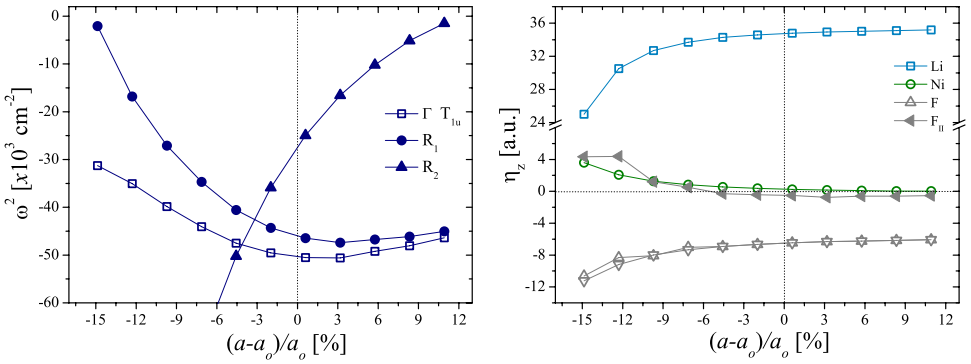

Figure 2.14: Squared frequency at the vibrational instabilities. We can observe the FE-mode at Γ and AFD-modes at R-point as a function of hydrostatic strain for $LiNiF_3$ (left). Eigendisplacements of FE-mode instability in $LiNiF_3$ are also shown (right).

As future work an analysis is necessary in order to understand the freezing of the FE-modes, and then, to corroborate the ground state of the system and its possible ferroelectricity.

2.5 Conclusions

Vibrational analysis were carried out in fluoroperovskites ABF_3. Different behavior for in $NaBF_3$ in comparison with oxides (*e.g.* $BaTiO_3$) was found for B = Ca, V, Mn, and Zn. For these compounds we found an increase of ferroelectric instability as a function of hydrostatic strain, this possible due to the "transition" of eigendisplacements responsible for polar mode. The increase of ionic A-site radii present a strong influence in FE-polar instability, generating totally different ground states symmetries for all compounds going from Li to K. The compound $NaNiF_3$ present a quite different trend in comparison with fluoride family, for this case, we observed a suppression of FE instability. However, it was not found change in mode eigendisplacements. The compound $LiNiF_3$ reveal a apparently predisposition to ferroelectric behavior with a strong FE-mode instability in comparison with the others instabilities observed along M–R branch in the phonon-dispersion curve. A model for an A-site geometrically driven ferroelectricity in fluorides is proposed according to results and analysis. Some questions

remain unclear such as: what is the mechanism for cancellation of FE mode at the ground state? How can be tuned the polar mode in a fluoride structure to engineer a ferroelectric fluoroperovskite? Some of these questions will be addressed in the next chapters.

Part III

STRAIN AND PRESSURE EFFECT IN FLUOROPEROVSKITES

Taking advantage of the vibrational analysis performed in fluoroperovskites, the pressure and biaxial strain was tested and the results are accordingly presented in the following chapters. The perovskite to post-perovskite (pPv) transition in fluoroperovskites will be discussed in the following two chapters including a detailed analysis on the non-collinear magnetic behavior of the pPv. Afterwards, the epitaxial strain effect on the multifunctional properties is discussed and the successful engineering of a multiferroic/magnetoelectric in a fluoroperovsite is described.

3

PREDICTION OF THE pPv TRANSITION IN $NaMnF_3$

Perovskite materials with stoichiometry ABX_3 are well known in material sciences due to their numerous properties and their high interest for technological applications. These properties are very diverse such as ferroelectricity [82], ferromagnetism [105], piezoelectricity [106], pyroelectricity [107] or superconductivity [108]. Going further, recent researches focused on the achievement of multifunctionalities in a single material that would open the door to new types of applications such as computer memories or spintronics [109, 110].

One of the main features of these compounds is that their properties can be conveniently tuned by external control parameters such as electric and/or magnetic fields, temperature, strain or pressure [111, 112]. Hydrostatic pressure appeared to be an interesting external parameter to be considered to enhance our understanding of the perovskite physics, since they exhibit profuse structural, electronic and magnetic phase transitions [113] under this parameter. A particularly appealing transition is the perovskite to post-perovskite (*pPv*) structural phase transition (see Fig. 3.2a) that has been observed in $MgSiO_3$ crystal in 2004 [114, 115]. The discovery of this *pPv* phase transition have important consequences in the physics of the earth mantle where $MgSiO_3$ is abundant, under very high pressure conditions [114, 115]. The *pPv* transition has then attracted great interest and it has been observed in other oxide and fluoride perovskites such as $MgGeO_3$[116], $CaSnO_3$[117], $NaMgF_3$[118] or $NaCoF_3$[119, 120] (see Table 3.1 for more details). Interestingly, the fluoroperovskite crystals have a lower pressure and temperature *pPv* phase transition than the oxides and thus making them attractive for the study of the *pPv* phase. Furthermore, it has been reported the possibility of keeping the *pPv* phase at atmospheric pressure after releasing the pressure in fluroroperovskites [121], while all the oxides return to their *Pnma* distorted perovskite ground state [119].

Besides the interest for the *pPv* transition in earth mantle studies, we have recently highlighted the existence of a ferroelectric instability in the cubic phase of ABF_3 perovskites that originates from a geometric effect rather than a dynamical charge transfer, as is it the case in oxides —for more details see Chapter 2 and Ref. [2]—. It was demonstrated that ferroelectric polarization in $NaMnF_3$ is induced by applying an epitaxial strain, an observation that leads to new possibilities of engineering multiferroic materials within the family of fluoroperovskites. This makes $NaMnF_3$ a good candidate for multifunctional properties based on its particular behavior as a function of external constraints. Additionally, in the family of 3d metal transition *pPv* fluorides, $NaMnF_3$ remains unexplored along the

pPv transition. The study of $NaMnF_3$ under pressure is then of high interest for scrutinizing the origins of its unique properties and its potential multifunctional character.

Table 3.1: Lattice parameters of the *pPv* phase (a, b, and c) and related temperature (T) and pressure (P) transition parameters from the *Pnma* phase to the *pPv* phase of fluoride and oxide perovskites. In the *pPv* phase, the A and B cations occupy the 4a and 4c Wyckoff positions and the O/F anions occupy the 4c and 8d positions. Most of the oxides have higher pressure and temperature transitions than the fluorides.

Crystal	a/b/c [Å]	P [GPa]	T [K]	Ref.
Oxides ABO_3				
$MgSiO_3$	2.456/8.042/6.093	121	300	[114]
$MgGeO_3$	2.613/8.473/6.443	78	300	[116]
$MnGeO_3$	2.703/8.921/6.668	57 - 65	1200 - 2400	[117]
$CaSnO_3$	2.854/9.343/7.090	56	300	[117]
$CaIrO_3$	3.145/9.862/7.298	1 - 3	1648 - 1798	[122, 123]
$CaRuO_3$	3.115/9.827/7.296	21 - 25	1173 - 1373	[124, 125, 126]
$CaPtO_3$	3.126/9.920/7.351	4	1073	[127, 128]
$CaRhO_3$	3.101/9.856/7.264	12 - 27	1273 - 1673	[129, 130]
$NaIrO_3$	3.040/10.358/7.177	4 - 5	1073	[131]
Fluorides ABF_3				
$NaMgF_3$	2.716/8.381/6.849	18 - 30	300 -	[118]
$NaZnF_3$	3.034/10.032/7.450	13 - 18	300 -	[132]
$NaFeF_3$	3.138/10.209/7.459	9	300 -	[133]
$NaCoF_3$	3.064/10.123/7.468	11 - 14	300 -	[119, 120]
$NaNiF_3$	3.026/10.058/7.401	16 - 18	1273 - 1473	[121, 120]
$NaMnF_3$	3.042/9.839/7.416	8	0	[3]

In this chapter we present the results on the structural, electronic and magnetic properties of $NaMnF_3$ as function of applied hydrostatic pressure. The results are presented as follows. We first determine the structural ground state structures over a wide range of pressure conditions and we predict a transition from the *Pnma* ground state to a *pPv* phase that has not been previously explored experimentally. We analyse the *pPv* phase transition through a vibrational characterization and a structural study. We then focus on the analysis of the magnetic behaviour with a special interest on the non-collinear magnetic ground states allowed in the *pPv*. We found a high-spin ground state associated with a large ferromagnetic canting that has not been reported in any of the previous *pPv*

transition observed in other compounds. The validity of the results are discussed with respect to the values of the Coulomb, U and exchange, J parameters within the DFT+U approach.

3.1 Computational Details

Total energy calculations were performed with the VASP code [66, 67] and within PAW method to describe the valence and core electrons.[64] The electronic configurations taken into account in the PAW pseudopotentials are presented in Table 2.1. We used the GGA exchange correlation functional within its PBEsol variant [39] and corrected it to increase the d-electron localization by means of the DFT+U approximation, with $U = 4.0$ eV and $J = 0.0$ eV within the Liechtenstein formalism [43]. Due to the magnetic character of $NaMnF_3$, the spin degree of freedom have been included in the calculations. Non-collinear magnetism calculations have been carried out by including the spin-orbit coupling as implemented in VASP by Hobbs *et al.*[68]. Different values of the U and J parameters were systematically varied to study the influence of these parameters on the results. The reciprocal space has been discretized by a Monkhorst-Pack k-point mesh of (6×4×6) and the plane wave expansion has been limited by an energy cut-off of 800 eV. These convergence parameters were necessary in order to have a resolution on the force of less than 1×10^{-4} eV/Å and a resolution on the energy of 0.01 meV. Analysis of the optimal structure as a function of pressure was carried out according to the third-order Birch-Murnaghan equation of state (BM-EOS) [134] by fitting the total energy dependence of the primitive cell volume per molecule. Vibrational properties were computed through the formalism of density functional perturbation theory (DFPT) [135, 136] as implemented in VASP and post-processed with the Phonopy code [94].

3.2 Structural and vibrational properties of the *Pnma* phase of $NaMnF_3$

At room temperature and atmospheric pressure, the sodium manganese fluoride compound $NaMnF_3$ crystallizes in the *Pnma* structure (space group number 62), which is composed by tilted Mn–F_6 octahedra along the three cubic directions and antipolar motions of the Na cations [137]. This is the result of the condensation of zone-boundary antiferrodistortive unstable modes observed in the cubic reference structure phonon-dispersion curves [2]. By performing the structural relaxation of the atomic positions and of the cell parameters of $NaMnF_3$ in the *Pnma* phase, we obtain the lattice parameters a = 5.750 Å, b = 8.007 Å and c = 5.547 Å. This corresponds to a difference of 0.2% with respect to the experimental measurements reported by Daniel *et al.* [137].

In Tables 3.2 and 3.3 we report the calculated silent, Raman and infra-red (IR) phonon modes as well as the mode Grüneisen parameters (γ_i) of the relaxed *Pnma* ground state. The irreducible representation of the *Pnma* perovskite phase is $\Gamma = 8A_u \oplus 10B_{1u} \oplus 8B_{2u} \oplus 10B_{3u} \oplus 7A_g \oplus 5B_{1g} \oplus 7B_{2g} \oplus 5B_{3g}$. Both the Raman ($A_g$, B_{1g}, B_{2g} and B_{3g} labels) and IR modes (B_{1u}, B_{2u} and B_{3u} labels) are in good agreement with the available experimental reports [137, 138]. We note that a very soft polar B_{2u} mode is present with a frequency of 18 cm^{-1}. This indicates that the *Pnma* phase is close to a ferroelectric phase transition and this mode is responsible for the epitaxial strain induced ferroelectricity of $NaMnF_3$ as we reported in the Refs. [2, 1] and explain in detail in Chapter 5. From the Grüneisen parameters reported in Table 3.3, we observe that two phonon modes are particularly sensitive to a change in volume: the soft B_{2u} mode at 18 cm^{-1} with $\gamma = 7.957$ and the A_g mode at 79 cm^{-1} with $\gamma = 4.844$, both can be easily detected from Raman experiments. Phonon modes, corresponding to a A_u symmetry (at 59 cm^{-1} and 114 cm^{-1}), have negative γ and correspond to the modes that become soft as the volume decreases, which indicates that probably these two phonon modes are close to a nearest neighbour force instability. Besides, these modes can contribute to a competition between positive and negative thermal expansion of the material, depending on how the phonon modes are populated [139].

In regards to the magnetic ordering, the total energy differences between the ferromagnetic (FM), C- and A-type antiferromagnetic (AFM) with respect to G-type AFM ordering in the *Pnma* structure are respectively 79.03, 54.08 and 24.18 meV/u.c. The lowest energy is thus given by the G-type AFM ordering, in agreement with the experimental measurements that establish a G-type AFM ordering for the *Pnma* phase of $NaMnF_3$ [140]. All of that confirms that our choice of parameters for the DFT calculations (GGA PBEsol and $U = 4.0$ eV) of $NaMnF_3$ gives good results when comparing to the experimental measurements.

3.3 Study of $NaMnF_3$ under hydrostatic pressure

In this section we study the pressure phase transitions of $NaMnF_3$. In order to identify the enthalpy ground state under hydrostatic pressure, we fitted the total energy versus the volume through the Birch-Murnaghan equation of state (BM-EOS) [134] for the following common structures found in perovskites: *Cmcm* (*pPv* phase), *I2/m*, *I4/mcm*, *P4/mbm*, *P2$_1$/c*, *P2$_1$/m*, *P6$_3$cm*, *P6$_3$/mmc*, $P\bar{1}$, $Pm\bar{3}m$, and *Pnma*. For all of them, the G-type AFM magnetic ordering was considered in our calculations. In Fig. 3.1a we report the total energy values per atom as a function of the volume change with respect to the equilibrium volume. As we would expect, the *Pnma* and *Cmcm-pPv* structures exhibit the lowest energy values at low volumes. In order to identify the lowest energy phase, we report the enthalpy (H), as obtained from the equation of state, versus the pressure in Fig. 3.1b.

Table 3.2: Calculated Raman, Infra-red (IR) and silent modes frequencies (cm^{-1}) of the *Pnma* phase of $NaMnF_3$ (at zero pressure). In brackets are presented the experimental values of the Raman [137] and the IR [138] modes.

Raman modes			
A_g	B_{1g}	B_{2g}	B_{3g}
79 (88)	86 (—)	132 (140)	87 (96)
135 (143)	154 (160)	145 (155)	191 (—)
175 (183)	220 (182)	191 (201)	252 (—)
202 (212)	303 (312)	216 (226)	294 (302)
242 (250)	414 (346)	260 (—)	462 (—)
259 (270)	—	281 (293)	—
309 (319)	—	449 (—)	—
Silent		IR modes	
A_u	B_{1u}	B_{2u}	B_{3u}
59 (—)	114 (103)	18 (—)	91 (103)
114 (—)	125 (132)	118(120)	148 (132)
124 (—)	180 (161)	180 (181)	152 (161)
133 (—)	196 (194)	205 (—)	183 (208)
198 (—)	223 (228)	280 (—)	222 (220)
278 (—)	255 (256)	367 (—)	237 (256)
363 (—)	272 (289)	387 (—)	307 (289)
396 (—)	312 (—)	—	347 (—)
—	402 (—)	—	389 (—)

Going from the lowest to the highest pressure, we found the following low enthalpy phases. Between -10 GPa and -8.9 GPa the hexagonal $P6_3/mmc$ phase is the most stable structure. Between -8.9 GPa and -6.5 GPa we found the $P2_1/c$ structure to be the most stable. Then between -6.5 GPa and 8.0 GPa the orthorhombic *Pnma* structure is the ground state and thus passing through the atmospheric pressure as expected from the experimental results. At higher pressures (above 8 GPa, up to 35 GPa) the orthorhombic *Cmcm pPv* structure is the lowest energy phase. Then, we found that $NaMnF_3$ presents a phase transition at relatively low pressure (8 GPa) from the *Pnma* perovskite phase to the *Cmcm pPv* phase.

In Fig. 3.2a we represent a schematic view of the *Pnma* and the *pPv* phases. It is clear that the structural transition between the *Pnma* and the *pPv* phase is reconstructive since a breaking of Mn–F–Mn bonds is needed to connect the two

Table 3.3: Calculated mode Grüneisen parameters (γ_i) for the $NaMnF_3$ *Pnma* phase at Γ and around atmospheric pressure.

A_g	B_{1g}	B_{2g}	B_{3g}	A_u	B_{1u}	B_{2u}	B_{3u}
4.844	1.425	1.226	3.017	-1.018	1.674	7.957	1.752
0.857	1.168	2.710	1.110	-0.668	1.323	0.559	1.546
2.196	2.416	2.872	1.351	0.172	0.574	-0.139	0.486
2.273	1.714	1.401	1.833	1.692	0.707	1.663	1.717
3.063	1.023	1.855	0.897	0.990	2.983	1.274	2.252
1.706	—	1.627	—	1.512	1.980	1.632	2.632
1.417	—	0.919	—	1.713	1.884	1.507	0.906
—	—	—	—	1.452	0.992	—	1.026
—	—	—	—	—	1.421	—	1.471

structures. This corresponds to a transition between corner-shared octahedra in the *Pnma* phase to edge-shared octahedra in the *pPv* phase. The *pPv* phase can be viewed as layers of edge-shared octahedra separated by layers of Na cations along the y-direction. In Fig. 3.2b we report the calculated X-ray diffraction patterns (XRD) for the *Pnma* and the post-perovskite *Cmcm* phases with a Cu-K_α = 1.5418 Å X-ray wavelength. The simulated XRD pattern of the room temperature *Pnma* is in good agreement with the experimental reports shown as a triangles in Fig. 3.2b [141, 137, 138]. No experimental data exists for the *pPv* phase of $NaMnF_3$ but the calculated XRD pattern fit the *pPv* symmetry found in other compounds such as $MgGeO_3$ [116].

An interesting parameter to be analysed in the *Pnma* to *pPv* phase transition is the dependence of the octahedral tilting angle of the *Pnma* structure as function of pressure. It has been reported that the transition from the *Pnma* to the *pPv* structure takes place when the octahedra tilting angle reaches 25° in $A^{2+}B^{4+}O_3$ [142] and $Na^{1+}B^{2+}F_3$ [119] compounds, where the octahedral angle has been calculated according to O'Keeffe *et al.* [143]. This criteria is structurally based on the relationship between AX_{12} and BX_6 polyhedral volumes, (V_A and V_B respectively), which establishes that the V_A/V_B ratio decreases with pressure due to the smaller compressibility of the polyhedral V_B with respect to V_A. Thus, a critical ratio is reached where the *Pnma* perovskite becomes structurally unstable and a transformation to a post-perovskite structure is observed. This critical volumes ratio is reached when the octahedral BX_6 tilting angle is equal to 25° [144]. Additionally, this condition is achieved in materials for which the tilt angle is at least 15° at ambient pressure in the *Pnma* phase [115, 142]. For this purpose, we computed the pressure dependence of the octahedra titling angle ϕ of the *Pnma* structure following to the relationship deduced by O'Keeffe *et al.* [143] such as $\phi = \cos^{-1}(\sqrt{2}c^2/ab)$ where a, b and c are the optimized cell parameters for

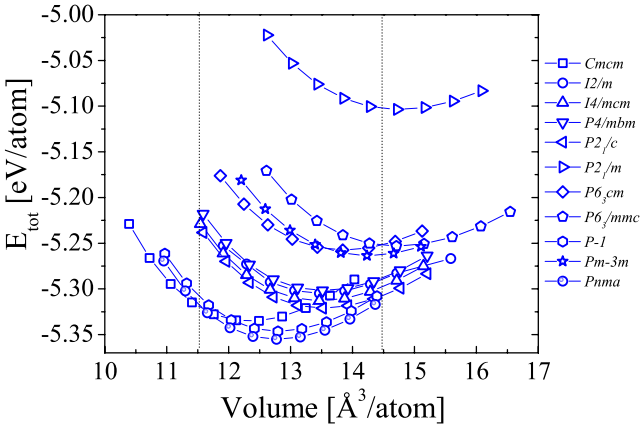

(a)

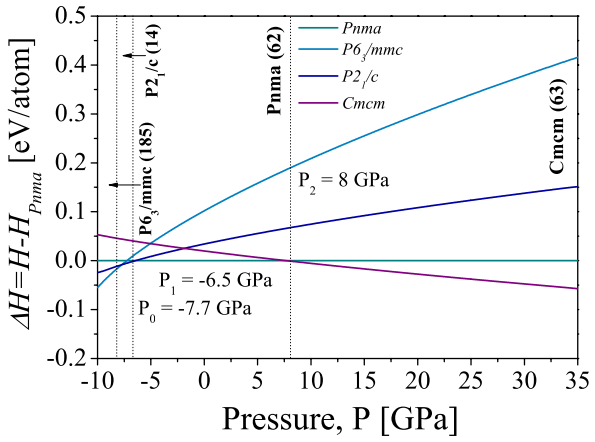

(b)

Figure 3.1: (a) Total energy of $NaMnF_3$ as a function of the volume per atom for all different crystal structures. *Cmcm* and *Pnma* structures show the lowest energy values for lower volumes. (b) ΔH/atom as a function of external pressure in $NaMnF_3$ structures. *Pnma* to *Cmcm* structural transition can be seen at the critical pressure of 8 GPa.

an specific pressure. We report our results as a function of pressure for $NaMnF_3$ and the experimental data for $NaBF_3$ compounds with B = Zn, Ni, Co, Mg, and Mn in Fig. 3.2c. The experimental results for B = Zn, Ni, Co and Mg are taken from Yusa *et al.* [119]. Experimental data for lattice parameters used in the calculation of ϕ were extracted from the report of Katrusiak *et al.* [97]. As it can be appreciated, all the experimental measurements follow the tilting criterion proposed by O'Keeffe, *i.e.* a *pPv* phase transition at ϕ =25°. The experimental results for $NaMnF_3$ (filled squares) are in good agreement with our calculations (open squares) up to 5.6 GPa (maximum pressure explored experimentally). Our calculations predict that the tilt angle reaches 25° at 8 GPa, where the transition

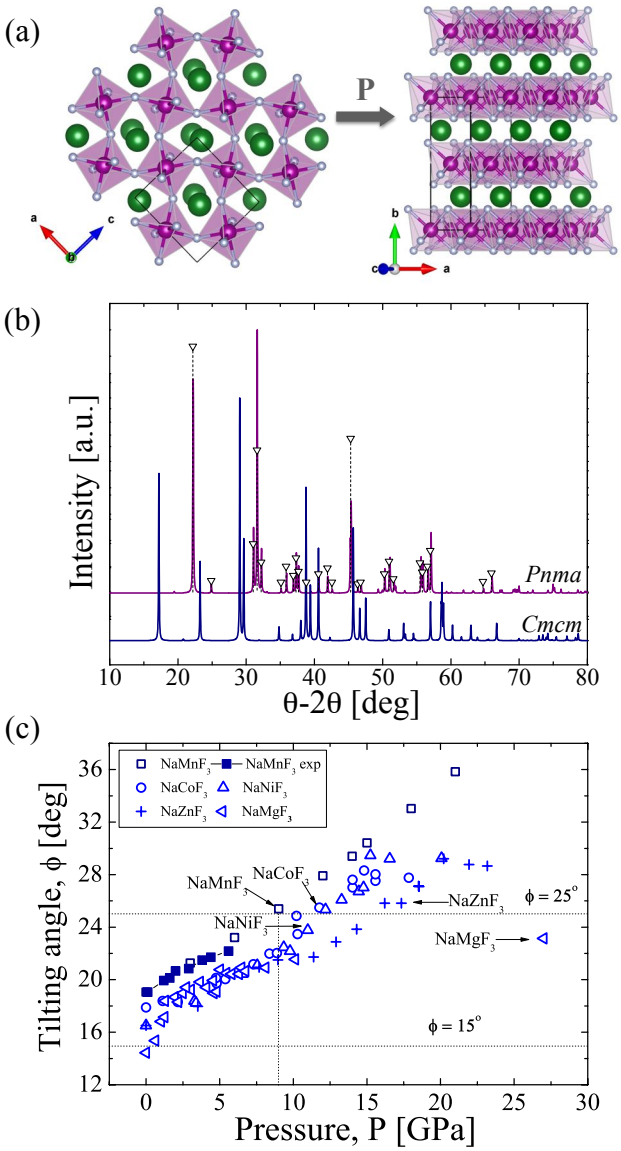

Figure 3.2: (a) Schematic view of the phase transition from *Pnma* to *Cmcm*. Na, Mn and F atoms are represented in green, violet and grey colors respectively. The breaking of bondings for the transition from corner-shared to edge-shared octahedra can be appreciated. (b) Simulated XRD patterns for *Pnma* and *Cmcm* structures. The room temperature *Pnma* phase is in good agreement with the experimental reports (open triangles) [141, 137, 138]. (c) Octahedra tilt angle as a function of pressure in $NaBF_3$. For B = Zn, Ni, Co and Mg experimental results are taken from Yusa *et al.* [119]. All of these compounds present the transition from the *Pnma* to the *Cmcm* structures at a tilting angle close to 25°. Experimental results for $NaMnF_3$ at low pressure were taken from Katrusiak *et al.* [97] Full agreement between experimental (filled squares) and our theoretical calculations (empty squares) can be appreciated.

should occur according to the O'Keeffe rule, which is indeed in agreement with our BM-EOS prediction of 8 GPa as the critical pressure.

Our theoretical findings for the transition between the *Pnma* and the *Cmcm* *pPv* phase do not follow the recent experimental report of Akaogi *et al.* [141]. In their pressure measurements at high temperature (T = 1273 K), Akaogi *et al.* do not observe a transition from the *Pnma* to the *pPv* structure up to 24 GPa but found, instead, a MnF_2 + $Na_3Mn_2F_7$ phase decomposition around 8 GPa. We note that Katrusiak *et al.* also report a transition from the *Pnma* to the cubic phase $Pm\bar{3}m$ at T_c = 970 K and ambient pressure [97] for this compound, which is not observed by Akaogi *et al.* at very high temperature (higher than T_c = 970K). We suggest that at the very high temperature where Akaogi *et al.* performed their measurements, it is indeed possible that a phase decomposition appears as they do not observe the *pPv* transition. We also remark that at such high temperature, the O'Keeffe rule is not fulfilled since the crystal is cubic or with titling angle smaller than the required critical value of 15° to observe the *Pnma* to *pPv* phase transition under pressure, therefore, our calculations are still valid at low temperatures. Following the suggested experimental analysis and in order to understand the decomposition phases, we performed calculations for $Na_3Mn_2F_7$ and MnF_2 compounds. The first stoichiometry is the one of the Ruddlesen-Popper (RP) phases [145] with $A_{n-1}A'_2B_nX_{3n+1}$ formula, which in our particular case corresponds to $n = 2$ and $A' = A$ = Na, B = Mn and X = F. To our knowledge, there is no previous report of the sodium-manganese based compound in the RP phase. Therefore, all reported phases for similar compounds (oxides [145] and fluorides [146]) were tested and the energy minimum per structure was analysed. Nevertheless, none of our simulated XRD patterns of the considered RP phases match the one reported by Akaogi *et al.* [141], while for the pristine MnF_2 compound, we obtain good agreement with the experiments [141]. We are thus confident that the crystal phase transition of $NaMnF_3$ from the perovskite to the *pPv* phase occurs at the predicted 8 GPa pressure. In any case, more experimental measurements would be required in order to clarify the pressure phase transition that takes place in $NaMnF_3$ at lower (room) temperature.

We now focus on the vibrational characterization of the *pPv* phase at 8 GPa. In Table 3.4 we report the computed phonon mode frequencies and the mode Grüneisen parameters (γ_i) in the *Cmcm* *pPv* structure with the lattice parameters relaxed at 8 GPa (also reported in Table 3.1). The irreducible representation at the Γ zone center point is: $2A_u \oplus 6B_{1u} \oplus 6B_{2u} \oplus 4B_{3u} \oplus 4A_g \oplus 3B_{1g} \oplus B_{2g} \oplus 4B_{3g}$. Two silent modes ($A_u$ label), sixteen IR active modes (B_{1u}, B_{2u} and B_{3u}) and twelve Raman active modes (B_{1g}, B_{2g} and B_{3g}) are thus expected. As we can see in Table 3.4, all the calculated modes at the Γ point of the BZ are positive, indicating a vibrational local stability of the *pPv* phase at 8GPa. The lowest frequency mode is a silent mode A_u at 62 cm^{-1} and the lowest polar mode is a B_{1u} mode with a frequency of 90 cm^{-1}. The obtained Grüneisen parameters are important in the vibrational identification of the transition related to Raman experiments under pressure. In general, they are smaller than the one obtained

Table 3.4: Computed Raman, Infra-red and silent modes of $NaMnF_3$ in post-perovskite *Cmcm* phase as well as the mode Grüneisen parameters (γ_i) at Γ around 12 GPa.

Raman, IR and silent modes [cm^{-1}]							
A_g	B_{1g}	B_{2g}	B_{3g}	A_u	B_{1u}	B_{2u}	B_{3u}
194	118	284	138	62	90	196	125
239	240	—	228	335	168	223	248
310	298	—	358	—	192	294	343
402	—	—	512	—	356	374	—
—	—	—	—	—	509	416	—
Mode Grüneisen parameters (γ_i)							
1.619	0.702	1.891	1.674	1.699	-0.137	-0.204	0.074
0.757	1.623	—	1.975	1.293	-0.204	0.449	2.011
1.265	2.107	—	1.301	—	2.558	1.427	1.384
1.050	—	—	1.171	—	1.265	0.972	—
—	—	—	—	—	1.543	1.156	—

in the *Pnma* ground state structure. This can be explained from an interatomic force stiffness larger in the *pPv* phase than in the *Pnma* phase. Even though there are some phonon modes with negative Grüneisen parameter (B_{1u} modes at 90 cm^{-1} and 168 cm^{-1} and the B_{2u} mode at 196 cm^{-1}), they are not large enough to have an effect on the thermal expansion such as the one observed in α-ZrW_2O_8 [139].

We also report in Fig. 3.3 the evolution of the Raman and IR modes as a function of pressure from 0 GPa to 15 GPa. After the transition, the system goes to a reduced crystallographic unit cell such as the number of modes is two times smaller in the *Cmcm pPv* phase than it is in the *Pnma* phase. We note that for both *Pnma* and *pPv* structure, all the phonon mode frequencies harden when increasing the pressure. This is also valid for the soft B_{2u} polar mode of the *Pnma* structure that hardens as the pressure increases and thus in agreement with the usual behaviour of perovskites in the presence of the AFD distortions, which are inimical to the ferroelectric distortions and are enhanced with pressure.

3.4 Magnetic properties of the *pPv* phase

Before performing the non-collinear magnetic calculations, it is useful to make a preliminary symmetry analysis in order to determine the magnetic orderings that are allowed in the *pPv* structure. The *Cmcm* space group belongs to the D_{2h} point

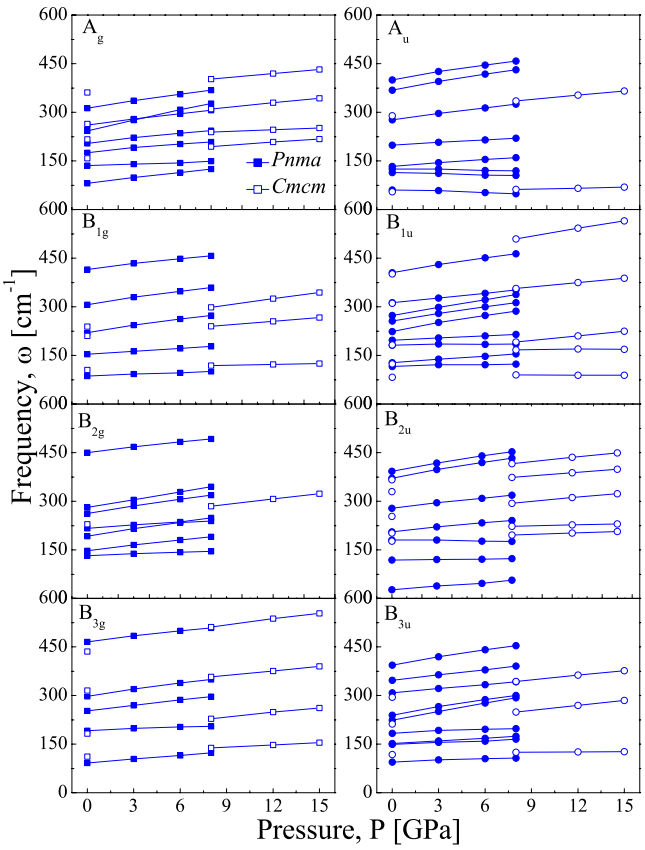

Figure 3.3: Vibrational behavior as a function of isotropic pressure for *Pnma* and *Cmcm* *pPv*. The open and filled symbols are the Raman and the Infra-red modes respectively.

group [147, 148] and the Mn atoms are placed at the 4c Wyckoff position with coordinates (0,0,0) for Mn_1, (0,0,$\frac{1}{2}$) for Mn_2, ($\frac{1}{2}$,$\frac{1}{2}$,0) for Mn_3 and ($\frac{1}{2}$,$\frac{1}{2}$,$\frac{1}{2}$) for Mn_4. From these 4 magnetic cations, we can define 4 collinear magnetic orderings depending on the sign of the magnetic moments of (Mn_1, Mn_2, Mn_3, Mn_4): F (+, +, +, +) for the FM ordering, A (+, +, −, −) for the A-type AFM ordering, C (+, −, +, −) for the C-type AFM ordering and G (+, −, −, +) for the G-type AFM ordering, where + and − correspond to spin up and down respectively. Of course, the ferrimagnetic ordering (+, +, +, −) could be considered but it is unlikely to appear in real conditions because of the symmetry of the system and the superexchange interaction [149, 150]. For the non-collinearity we have to consider the three Cartesian directions x, y and z for each magnetic moment which gives 4×3 possible states: F_x, F_y, F_z, A_x, A_y, A_z, C_x, C_y, C_z, G_x, G_y and G_z. Then, taking into account the fact that the spins are axial vectors, one has to apply the symmetry operations of the D_{2h} point group on each of the non-collinear magnetic orders defined above and see how they transform. The result of this approach applied on the *pPv* phase of $NaMnF_3$ is summarised in Table 3.5.

Table 3.5: Magnetic ordering allowed in the *Cmcm* structure according to the D_{2h} point group [147, 148]. The transformation of each magnetic ordering under each symmetry operation is labeled as +1 and -1, which indicates when the ordering is invariant under the related transformation (*i.e.* +1) or when it is reversed under the application of the symmetry operation (*i.e.* -1).

Magnetic Ordering[a]	I	2_z	2_y	2_x	-1	m_z	m_y	m_x	
F_x, A_x	1	-1	-1	1	1	-1	-1	1	B_{3g}
F_y, A_y, C_z, G_z	1	-1	1	-1	1	-1	1	-1	B_{2g}
F_z, A_z, C_y, G_y	1	1	-1	-1	1	1	-1	-1	B_{1g}
C_x, G_x,	1	1	1	1	1	1	1	1	A_g

a More detailed information can be found in the Appendix B.

As we can see from Table 3.5, the F_x and A_x orders have to the same character. This means that in an energy expansion with respect to these two order parameters the second order term $F_x \cdot A_x$ is invariant by symmetry. This implies that if one of the two order parameters condenses in the structure, the second one can develop as well but as a secondary or a slave order (*pseudo-proper* [1] [151]). This secondary order parameter usually appears as a spin canting in the real system and its intensity will depend on the amplitude of the $F_x \cdot A_x$ coupling. Going through the other magnetic orders, in Table 3.5 we also observe that F_y, A_y, C_z and G_z belong to the same B_{2g} character, F_z, A_z, C_y and G_y belong to the B_{1g} character and C_x and G_x belong to the A_g character. Interestingly, whichever is the main magnetic order we observe in the $NaMnF_3$ *pPv* phase, a canting of the spins is always possible. Additionally, we also remark that three of the four possible characters to which belong all the possible magnetic orders, three of them allow for ferromagnetism and so have the potential to exhibit weak FM.

As discussed above, $NaMnF_3$ compound in the *Pnma* phase has a G-type AFM ordering [97, 140, 137]. In Table 3.6 we report the computed Mn–F–Mn distances and angles of the *Pnma* phase at room pressure and of the *pPv* phase at 8 GPa. We note that in the *Pnma* structure, the Mn–Mn bonding in the three directions have similar Mn–F–Mn angles (about 140°) and distances (about 4 Å) while their are much more anisotropic in the *pPv* phase (angles of 92° and 134° and one non-existent angle due to the octahedral edge sharing of the structure with distances of 2.99 Å and 3.66 Å in the $x-z$ plane and 4.97 Å in the y direction). Having angles closer to 180° in the *Pnma* explains the G-type AFM ordering

1 A pseudo-proper transition appears when a secondary order parameter (Y) has the same symmetry as the main transition order parameter (X) such as they coupled linearly (first order coupling) in a free energy expansion: $F = aX^2 + bY^2 + cXY^2$. In the present case the ferromagnetic (secondary) order parameter transforms as the main antiferromagnetic order parameter, giving rise to the so-called weak-ferromagnetism.

Table 3.6: Comparison of the distances and the bond angles along the Mn–F–Mn bonds between the *Pnma* and the *Cmcm* structures of $NaMnF_3$.

Distance and Angle	*Pnma*		*Cmcm*	
d_{Mn-Mn} [Å]	[101]	3.9951	[100]	2.9903
	[10-1]	3.9951	[001]	3.6644
	[010]	4.0036	[010]	4.9731
$\gamma_{Mn-F-Mn}$ [deg]	[101]	142.58	[100]	92.46
	[10-1]	142.58	[001]	134.55
	[010]	140.14	[010]	—

since with such bond angle the superexchange interaction between the Mn-d^5 spins favours an AFM alignment [152, 153, 154]. In the *pPv* case, we can see that there is no direct bonding between the Mn atoms along the y direction such as we can expect a weak spin coordination between the spins along the y direction and one would expect a quasi-2D magnetic behaviour in the *pPv* structure. In the plane perpendicular to the y direction we have two types of bonding giving rise to an angle close to 180° along the z direction and to an angle close to 90° along the x direction. On the top of that, we also note that the 90° bonding along the x direction is given through two bonds since it is the direction where the octahedra share their edge. The superexchange interaction should thus drives strong FM ordering along the x axis and AFM ordering along the z axis and a weak interaction along the y axis. Interestingly, the magnetic ordering that fulfils these superexchange rules is the C-type AFM and it is indeed the lowest energy collinear magnetic ordering that we found in our calculations (see Fig. 3.4b). Therefore, we can only consider the set of non-collinear calculations containing the C-type AFM: (C_z, F_y, G_z, A_y), (C_y, F_z, A_z, G_y) and (C_x, G_z) as predicted by group theory. We can also expect the C_x case to be unlikely observed since it forces the spins to be antiferromagnetically aligned along the x direction while a strong FM interaction is expected from the double 90° bond angle connecting the Mn atoms in this direction.

Relaxing the spin structure within the non-collinear regime and within the C-type AFM ordering, we found that the lowest energy is obtained for the C_y orientation with a large F_z component along the z direction (no canting along the x axis is observed). This magnetic ground state is however dependent on the U and J values of the GGA+U exchange correlation functional. In Fig. 3.4a we report the energy difference between the C_yF_z ordering and the other lowest energy cases C_zF_y, C_zA_y, and G_yA_z versus the J value (fixing $J = 0$ eV). Here we remark that the C_yF_z, C_zF_y, C_zA_y, and G_yA_z states are very close in energy such as we can expect an easy magnetic phase transitions with small perturbations such as an applied magnetic field. Such a transition under a magnetic field has been observed experimentally in the *pPv* phase of $NaNiF_3$ where a field parallel

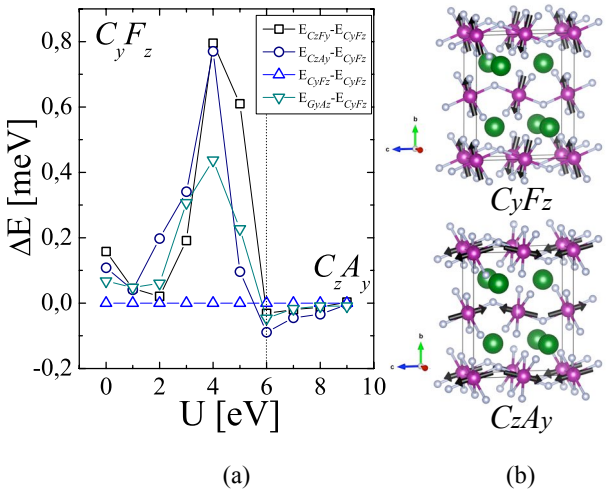

Figure 3.4: (a) Energy differences between the different magnetic orderings of the *pPv* phase of $NaMnF_3$ versus the U parameter. (b) Sketch of the C_yF_z and the C_zA_y magnetic orderings in the *pPv* phase of $NaMnF_3$. For $U < 6.0$ eV the system exhibits a AFM+FM magnetic state with a high ferromagnetic canting. For $U > 6.0$ eV, the system transit toward a canted AFM state with no weak FM.

to the y-axis induces a transition to a AFM+weak-FM ground state [121]. We can see from Fig. 3.4a that the C_yF_z corresponds to the lowest energy state from $U = 0.0$ eV to $U = 5.0$ eV while from $U = 6.0$ eV to $U = 9.0$ eV the C_zA_y is observed to be the most stable. This shows that a magnetic spin flop transition appears in the *pPv* phase of $NaMnF_3$ as function of the electronic Coulomb direct exchange U. In Fig. 3.5 we report the evolution of the spin canting with respect to U. The amplitude of the F_z canting goes from 0.01 to 1.6 μ_B/atom when varying U from 0.0 to 9.0 eV. We note that the F_z component strongly increase from $U =$ 0.0 to 6.0 eV and reach a saturation value beyond U=6.0 eV. Unfortunately, no experimental data of the non-collinearity of $NaMnF_3$ in its *pPv* phase has been reported in the literature such as it is not possible to validate which U value would be the best to reproduce the spin canting amplitude. In previous studies with d^5 half filled orbitals the range of U values that have been found to treat correctly the property of the systems is around $U = 4.0$ eV. It is important to note that the pressure calculations performed with $U = 4.0$ eV in the *Pnma* and *pPv* phase give the best agreement with experiments such as we will use U=4.0 eV in the rest of our analysis.

Beside the U parameter, for non-collinear magnetism within the DFT+U approach it is also necessary to check the dependence with respect to the J parameter [155]. In Fig. 3.5 we present the evolution of the spin canting versus the J parameter in the C_yF_z ground state of the *pPv* phase of $NaMnF_3$ with U= 4.0 eV. As we can see, the FM component F_z is strongly affected by J, going from 0.95 μ_B to 0.25 μ_B when J goes from 0.0 to 1.0 eV respectively. Here again, it

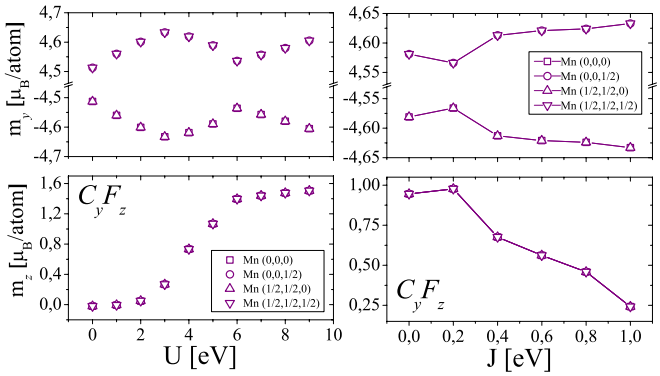

Figure 3.5: Magnetic canting dependence as a function of U and J parameters for $NaMnF_3$. Canting angle (φ) varies from 0.11° to 17.94° when U goes from 0.0 to 9.0 eV. The canting angle goes from 12.07° to 3.01° when J varies from 0.0 to 1.0 eV.

is difficult to predict what would be the best J value for $NaMnF_3$ without any experimental feedback. Previous studies about the DFT+U,J parameter report that low J values for d^5 orbital filling are usually the best values [155] such as the large values of the F_z canting we obtain at low J (close to 1 μ_B/atom) in the *pPv* phase of $NaMnF_3$ would be the optimal value.

In order to estimate the error bar of our calculations, we report in Table 3.8 a list of known magnetic *pPv* phase in oxide and fluoride perovskites with their related magnetic orderings, d-orbital filling and S quantum number. We note that in all oxide cases as well as in $NaNiF_3$, the ground state spin configuration always corresponds to the low spin state. According to our calculations, only $NaMnF_3$ has the high spin configuration as ground state. In order to verify if this is due to the DFT parameters used in our calculations or if this has a physical meaning, we performed calculations of the *pPv* phase of $NaNiF_3$ and $CaRhO_3$ with U=4.0 eV. We found a low spin ground state in both $NaNiF_3$ (S=1) and $CaRhO_3$ (S=$\frac{1}{2}$) and so in good agreement with the experimental results. Going further, we also estimated the non-collinear spin ground state of $NaNiF_3$ and $CaRhO_3$ in their *pPv* phase. As expected from the symmetry analysis, we observe canted magnetic ground state in the two systems. The ground state magnetic ordering of $NaNiF_3$ is found to be A_z with a G_y canting. Then, we did not find any weak ferromagnetic spin canting in $NaNiF_3$ in agreement with experimental data. We note that experimentally a transition towards an AFM state with a ferromagnetic canting is observed in the *pPv* phase of $NaNiF_3$ when applying a small magnetic field. The direction of the field induced canted FM spins in $NaNiF_3$ are the same than the one we report in the *pPv* phase of $NaMnF_3$ without magnetic field. This shows that the high-spin large FM canting we report in $NaMnF_3$ might be metastable in $NaNiF_3$ such as a small magnetic perturbation can switch to this state. More theoretical and experimental analysis would be welcome to understand this transition. In the case of $CaRhO_3$ we found C_y with a F_z canting as magnetic ground state.

Table 3.7: Magnetic orderings allowed in the *Cmcm* structure for ABX_3 systems with $U = 4.0$ eV and $J = 0$ eV. The large magnetic canting for fluorides compounds can be noted. The canting angle (φ) is measured with respect to the ab-plane on the *pPv* phase. For $NaNiF_3$, the two possible magnetic states C_zF_y and C_yF_z were computed.

Compound	F_i [μ_B/atom]	φ [deg]	Magnetic Ground-state
$CaRhO_3$	0.05	4.3	C_yF_z
$NaNiF_3$	0.12 (0.15)	86.1 (4.7)	C_zF_y (C_yF_z)
$NaMnF_3$	0.95	11.7	C_yF_z

We found that when considering the cases with ferromagnetic spin canting, the canting angle is much smaller in $CaRhO_3$ (4.3°) and in $NaNiF_3$ (4.7°) than it is in $NaMnF_3$ (11.7°, see Table 3.7). If we look at the amplitude of the canting per atom we observe a very large amplitude for $NaMnF_3$ (0.95 μ_B/atom) due to the high spin configuration while it is much smaller in the case of $NaNiF_3$ (0.12 μ_B/atom) and of $CaRhO_3$ (0.05 μ_B/atom). This large canting can be the result of a rather large Dzyaloshinsky-Moriya interaction [156, 157] or a large single-ion anisotropy [158]. A more detailed analysis in order to identify the exact origin of this large spin canting can be found in Chapter 4. These previous calculations allow us to be more confident about the unique high spin ground state of $NaMnF_3$ with a large ferromagnetic spin canting in its *pPv* phase.

We also report in Fig. 3.6 the local density of states (LDOS) of the *pPv* phase of $NaMnF_3$. The LDOS shows an overlap between the Mn-3d and F-2p states, suggesting a covalent contribution between the Mn and F atoms due to the $p-d$ hybridization, which is a fundamental requirement for the superexchange interaction. Moreover, we observe that the fluorine states are lower in energy then the Mn-d orbitals, which corresponds to the expected bonding-antibonding picture of covalency between magnetic cations and anions. Close to the Fermi level, no contribution of Na states to the DOS is observed such as mostly Na size effects are expected within the structure, a key-point parameter that is at the origin of the geometric ferroelectric instabilities observed in cubic fluoroperovskites [2]. The d_{xy}, d_{xz}, d_{yz}, d_{z^2} and $d_{x^2-y^2}$ orbital occupancy gives the 5 orbitals filled below the Fermi level for a spin channel and the 5 orbitals empty above of the Fermi level for the other spin channel, which confirms the high spin electronic configuration of Mn^{2+} in the *pPv* phase of $NaMnF_3$.

3.5 Conclusions

We have studied, by means of first-principles calculations, the high pressure phase diagram of $NaMnF_3$. We predicted a phase transition from the *Pnma* distorted perovskite to a *Cmcm* post-perovskite phase at a critical pressure of 8 GPa, which

Table 3.8: Magnetic ordering in fluorides and oxides post-perovskite systems, AFM: antiferromagnetic, DM: diamagnetic, FM: ferromagnetic, CWP: Curie-Weiss paramagnetic. All *pPv* compounds exhibit a low-spin magnetic configuration but $NaMnF_3$ that according to our calculations is found to be in the high-spin state.

Compound	Magnetic ordering			Ref.
pPv Oxides ABO_3				
$CaIrO_3$	quasi-1D AFM	$S=\frac{1}{2}$	Ir^{4+}: $5d^5$(LS)	[122]
$CaRuO_3$	quasi-1D AFM	S=1	Ru^{4+}: $4d^4$(LS)	[124, 126]
$CaPtO_3$	DM	S=0	Pt^{4+}: $5d^6$(LS)	[127, 128]
$CaRhO_3$	AFM+weak-FM	$S=\frac{1}{2}$	Rh^{4+}: $4d^5$(LS)	[130]
$NaIrO_3$	CWP	S=1	Ir^{5+}: $5d^4$(LS)	[131]
pPv Fluorides ABF_3				
$NaFeF_3$	AFM	S=1	Fe^{2+}: $3d^6$(LS)	[133]
$NaCoF_3$	AFM	—	Co^{2+}: $3d^7$(LS)	[119]
$NaNiF_3$	AFM[a]	S=1	Ni^{2+}: $3d^8$(LS)	[121, 4]
$NaMnF_3$	AFM+FM	$S=\frac{5}{2}$	Mn^{2+}: $3d^5$(HS)	[3]

a $NaNiF_3$ compound present a magnetic transition from AFM to AFM+FM ordering at applied external magnetic field [121].

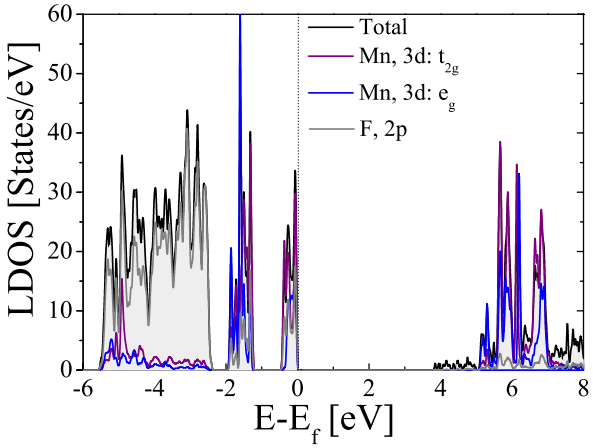

Figure 3.6: Projected local density of states (LDOS) of the *Cmcm* phase of $NaMnF_3$. A regular F-p bonding Mn-d antibonding is observed with small Mn:3d – F:2p overlaping DOS is responsible for the small superexchange interaction present in $NaMnF_3$.

is relatively low with respect to the similar phase transitions observed in other compounds. As expected from the tilting criteria[144, 143], this phase transition fits very well with the octahedra tilting angle requirements where the transition to the *pPv* is observed when the octahedra tilting angle reach the critical value of 25° with an initial ambient pressure tilting angle of 15°. Unfortunately high pressure experiments have been performed at very high temperature by Akaogi *et al.* et al.[141] where the tilting criteria requirement is not fulfilled and also by Katrusiak *et al.* [97] who unfortunately did not go beyond 5 GPa such as none of them observed the *pPv* transition. Because of the partially filled d orbitals of Mn^{2+} cation we also determined the magnetic ground state of $NaMnF_3$ in its *pPv* phase. Our calculations predicted a high spin ground state of the d^5 spins with a magnetic moment of $5\mu_B$ on each Mn. This high spin structure is particularly interesting and unique since all the other known magnetic compounds presenting the *pPv* phase shows a low spin ground state. We predicted an AFM magnetic ordering ground state of the C-type with the spins lying along the y-direction and with a surprisingly large ferromagnetic spin canting along the z-direction. This makes $NaMnF_3$ of particular interest for fundamental and geophysical studies since it has this unique property of high spin magnetic ground state with potentially large ferromagnetic spin canting and because it can be synthesized at relatively small pressure. The fact that the fluoride post-perovskites can be maintained when the pressure is released makes $NaMnF_3$ even more interesting to study.

It is important to remark that very recently, another transition at higher pressures was reported and named as a post-*pPv* [159]. In this phase, the structure transforms to a face-shared octahedra with a substantial compression along the crystallographic a-axis into a *ppPv-Pnma* phase —see Fig. 2 in Ref [159]—. Moreover, it has been found that some oxide compounds transforms directly from the room conditions *Pnma* to the post-*pPv* under isotropic pressures above 50 GPa. Interestingly, the magnetic ordering in the *ppPv* materials, with magnetically active A- and B-sites, shows magnetic "double" one-dimensional channels in addition to a triangular-like coordination of the B-site generating a geometrically frustrated magnetic system.

Therefore, we hope that our results on the *pPv* phase and the reported *ppPv* transition will motivate the experimentalist to carry out more studies of $NaMnF_3$ in order to confirm the *pPv* phase transition at low pressure and low temperature and to check its potential for high spin structure with a sizeable canted ferromagnetism.

4

NON-COLLINEAR MAGNETISM IN $CaRhO_3$ AND $NaNiF_3$ POST-PEROVSKITES

Perovskite (*Pv*) oxides are materials that have demonstrated to be a crucial family in the search for multifunctionality and controllable properties in simple stoichiometries where the keystone is to have several physical properties in a single crystal [160, 111]. The pressure have demonstrated to be a very important external parameter to understand the physics of these crystals because it is possible to modify and tune the structural parameters and the electronic and magnetic properties. For example, in perovskites, ferroelectricity can be suppressed or induced by pressure and strain [62]. Although, new and interesting phases can be synthetised such as the post-perovskite (*pPv*) phase [161]. In the case of the (*pPv*) phase, which can be found under high pressure in some ABX_3 compounds, several interesting properties have been reported such as 1D and 2D magnetism [122, 162, 163] related to the layered-like structure of the *pPv* phase or a Mott insulator state [164]. The interest in the magnetic ordering in *pPv*'s is mostly found through experimental studies such as the magnetic field induced antiferromagnetic (AFM) to ferromagnetic (FM) transition in $NaNiF_3$ [162] and the 1- and 2-dimensional magnetic ordering with a clear non-collinear magnetic contribution in some of these compounds [122, 165, 162]. The magnetic ordering in *pPv* compounds is induced by a magnetically active B-site cation where the $CaIrO_3$ crystal is one of the most studied system [122] because it presents a quasi-1D AFM ordering similar to $CaRuO_3$ [163]. Interestingly, it has also been observed that $CaRhO_3$ [165], $NaCoF_3$ [119] and $NaNiF_3$ [162] behave as a quasi-2D AFM system. Nonetheless, even though the magnetic properties have been measured in some of these *pPv*'s compounds, the source of the observed canted magnetic structure is still unclear and, to our knowledge, there are only few theoretical efforts to present a clear picture of its physical origin. Additionally, a wide range of properties remains unexplored in this phase such as the competition between the structural distortions and the non-collinear magnetism, suggesting promising and unexpected phenomena to be understood.

In this chapter, we present a study of the non-collinear magnetism in the prototype *pPv* phase by means of first-principles calculations. We have selected two different post-perovskite systems, one oxide $CaRhO_3$ and one fluoride $NaNiF_3$. The possible non-collinear ordering are explored through group theory symmetry analysis and simulated through density functional theory calculations. We then

scrutinised the origin of the non-collinear magnetism by computing the exchange magnetic couplings (J_{ij}), the anti-symmetric Dzyaloshinsky-Moriya ($\mathbf{D}_{ij}$) interaction and the single-ion anisotropy (SIA) parameters to determine the origin of the non-collinear magnetism.

4.1 Computational Details

First-principles calculations were performed within the VASP code [66, 67] and the PAW formalism to describe the valence and core electrons [64]. The electronic configuration of pseudopotentials as valences and semicore electrons taken into account for calculations are Na ($2p^6 3s^1$), Ni ($3p^6 3d^8 4s^2$), and F ($2s^2 2p^5$) for $NaNiF_3$ and Ca ($3s^2 3p^6 4s^2$), Rh ($4p^6 4d^8 5s^1$), and O ($2s^2 2p^4$) for $CaRhO_3$. The exchange correlation was represented within the GGA approximation, with the PBEsol pseudopotential [39] and corrected by means of the GGA+U formalism, with $U = 4.0$ eV and $J = 0$ within the Liechtenstein approach [43]. The magnetic character was taken into account in the calculations according to the spin polarized DFT approximation used for the exchange correlation functional [33, 36]. The periodic solution was represented through Bloch states with a Monkhorst-Pack k-point mesh of (6×4×6) and 600 eV of energy cut-off, which has been tested to achieve forces convergence less than 1×10^{-3} eV/Å and an accuracy of 1×10^{-6} eV in energies. Vibrational properties were computed through the formalism of density functional perturbation theory (DFPT) [135, 136] and the post-processing analysis was carried out with the Phonopy code [94]. For the non-collinear magnetic calculations, the spin-orbit coupling has been included as implemented in VASP [68].

4.2 Structural Characterization of $CaRhO_3$ and $NaNiF_3$

At atmospheric pressure and room conditions, $CaRhO_3$ and $NaNiF_3$ exhibit an orthorhombic *Pnma* structure (Space group No. 62). However, under high hydrostatic pressure, the $CaRhO_3$ and $NaNiF_3$ compounds crystalizes in the *pPv* phase (*Cmcm* space group No. 63) for pressures above 6 GPa and 16 GPa respectively [165, 162]. Based on the advantage of these two materials to conserve the *pPv* structure at ambient conditions once the pressure is released, we carried out calculations at atmospheric pressure in order to compare and validate our calculations with the available experimental findings. After the structural relaxation within the C-type AFM collinear magnetic ordering, we obtained lattice parameters $a = 3.085$ Å, $b = 9.824$ Å, $c = 7.206$ Å and $a = 3.001$ Å , $b = 9.946$ Å, $c = 7.342$ Å for $CaRhO_3$ and $NaNiF_3$ respectively. These results are in agreement with the experimental measurements with an error of about 0.8% [165, 162]. The corresponding XRD patterns (see Fig. 4.1) have the characteristic peaks observed in the *pPv* phase of $CaRhO_3$ [129, 165] and $NaNiF_3$ [166, 162], which demonstrates a good agreement between our calculations and the experi-

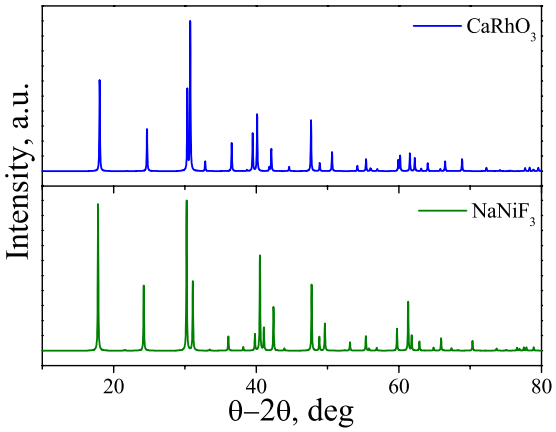

Figure 4.1: Simulated XRD patterns with Kα:Cu for $CaRhO_3$ (above) and $NaNiF_3$ (below) in the *Cmcm* phase at atmospheric pressure are observed.

ments. In Table 4.1 we present the calculated Raman, Infra-Red (IR) and silent mode frequencies of the *pPv* phase of $CaRhO_3$ and $NaNiF_3$ at ambient pressure. Even if the *pPv* is not the ground state structure at room pressure (The *Pnma* phase is the ground state), we do not observe any phonon instabilities confirming that this phase is a metastable phase (The *Pnma* phase has a lower energy than the *pPv* phase) and as observed experimentally when releasing the pressure [165, 162]. The stability of the *pPv* phase at room conditions is of great interest due to the possibility to explore the properties of the *pPv* structure and its use for technological applications.

4.3 Non-collinear Ordering

Having a correct description of the structure, we now focus on the magnetic ground state of the *pPv* phase. The magnetic behavior in perovskites and post-perovskites is strongly dependent on the coordination of the B-site magnetic cation in addition to the orbital symmetry and its electron filling [158]. In *pPv* oxides, the magnetism comes from the 4d and 5d electrons (*i.e.* Rh [165], Ru [163] and Ir [122]) while in fluorides it is due to the 3d elements (for example Co [119, 166] and Ni [166, 162]). This can induce different properties and behaviour when comparing the magnetism present in oxides and the one in fluorides *pPv* phases due to the change in the chemical environment provided by the fluorine compared to the oxygen. The octahedral tilting and rotation are known to affect the non-collinear arrangement of the magnetic moments as demonstrated by Weingart *et al.* in the $AFeO_3$ systems [167]. Thus, due to the strong modification of the octahedra coordinations in the *pPv* phase with respect to the *Pnma* phase (the octahedra share their edge in the *pPv* phase while they are corner-shared in the *Pnma* phase) we can expect a strong modification of the magnetic interactions in

Table 4.1: Vibrational characterization modes of $CaRhO_3$ and $NaNiF_3$ *Cmcm* phase at atmospheric pressure with the representation: $\Gamma = 2A_u \oplus 6B_{1u} \oplus 6B_{2u} \oplus 4B_{3u} \oplus 4A_g \oplus 3B_{1g} \oplus B_{2g} \oplus 4B_{3g}$.

Raman , IR and silent (A_u) modes [cm^{-1}]							
$CaRhO_3$							
A_g	B_{1g}	B_{2g}	B_{3g}	A_u	B_{1u}	B_{2u}	B_{3u}
219	112	151	260	108	157	248	188
324	196	—	301	481	195	269	391
464	409	—	524	—	347	405	499
562	—	—	697	—	502	547	—
—	—	—	—	—	622	569	—
$NaNiF_3$							
172	128	283	165	92	114	202	155
219	228	—	211	346	150	223	247
303	289	—	358	—	246	284	350
396	—	—	485	—	360	368	—
—	—	—	—	—	463	395	—

the *pPv* phase when comparing with the regular distorted perovskite structures as the *Pnma* phase.

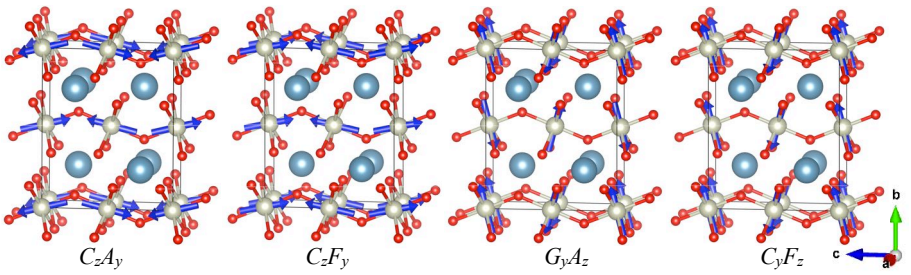

Figure 4.2: The non-collinear magnetic orderings in the *pPv Cmcm* symmetry labeled as C_zF_y, C_zA_y, C_yF_z and G_yA_z are presented in the figure. Two of them with pure AFM (C_zA_y and G_yA_z) behavior and two AFM+weak-FM (C_zF_y and C_yF_z) can be observed (Fig. elaborated with the VESTA software [168]).

Before performing the non-collinear magnetic calculations, it is important to first check the magnetic states that are allowed by symmetry. In Table 4.2 we present the main possible magnetic orderings and couplings in the ABF_3 *pPv* phase (*Cmcm* space group), where the magnetic B-cation are located at the Wyckoff positions 4c (see details in Ref. [3] and Appendix B). Including additional criteria such as the superexchange interaction related to the bondings, we

can neglect unlikely states and thus reducing the possible magnetic states to C_zF_y, C_zA_y, C_yF_z and G_yA_z, as summarized in Table 4.2 and depicted in Fig. 4.2.

Table 4.2: Magnetic orderings allowed in the *Cmcm pPv* structure according to the D_{2h} point group [3]. Here F is ferromagnetic ordering and A- C- and G- are the different AFM magnetic orderings where the subindex indicate the direction along the particular Cartesian axis.

Magnetic Ordering	Character
F_x, A_x	B_{3g}
F_y, A_y, C_z, G_z	B_{2g}
F_z, A_z, C_y, G_y	B_{1g}
C_x, G_x,	A_g

According to our total energy calculations, the ground state corresponds to the C_zF_y and G_yA_z magnetic states for $CaRhO_3$ and $NaNiF_3$ respectively (see Table 4.3). It can be noted that these magnetic ground states as well as their canting amplitude are in good agreement with available experimental data. In Table 4.3, we also report the experimental values of the magnetic state of $NaNiF_3$ under an applied magnetic field and we compare it with a calculation made with a higher energy configuration. The later corresponding to the magnetic ground state observed experimentally where we get a good agreement. We remark that the atomic magnetic moment in the $NaNiF_3$ case is almost three times larger that in the oxide $CaRhO_3$. This is due to the occupation of the B-site magnetic cation that drives a $S = 1$ state in $NaNiF_3$ and $S = \frac{1}{2}$ in $CaRhO_3$.

Table 4.3: Non-collinear ordering and moments in $CaRhO_3$ and $NaNiF_3$. Experimental and our theoretical calculations are in good agreement. The magnetic moments are in μ_B/atom for each magnetic B-site cation. The induced magnetic ground state by applied magnetic field (H_{ext}) in $NaNiF_3$ is also presented.

Compound	Ordering	C, G	F, A	F_i exp.
$CaRhO_3$	C_zF_y	0.65	0.04	0.03 [165]
$NaNiF_3$	G_yA_z	1.76	0.11	— [162]
$NaNiF_3$ ($H_{ext} > 5$ kOe)	C_zF_y	1.76	0.09	≈ 0.1 [162]

4.4 Exploring the Magnetic Interactions

In the *Pnma Pv* systems, in which the canting is allowed, the source of the non-collinear ordering lies in the DM vectors (see a detailed analysis in Ref. [167] for

the $AFeO_3$ systems). Here, we propose to analyse the origin of the non-collinear magnetism in the *pPv* phase of $NaNiF_3$ and $CaRhO_3$ by decomposing the magnetic interactions into its isotropic exchange (J), DM and SIA components. To that end, it is convenient to start by defining the magnetic Heisenberg Hamiltonian ($\mathcal{H}$) as follows:

$$\mathcal{H} = -2[J_{ij}\vec{S_i}\cdot\vec{S_j} + \vec{D_{ij}}\cdot(\vec{S_i}\times\vec{S_j}) + \vec{S_i}\cdot\vec{A_i}\cdot\vec{S_i}] \tag{4.1}$$

Here J_{ij} are the magnetic exchange constants between the $\vec{S_i}$ and $\vec{S_j}$ magnetic moments of the i and J interacting atoms. $\mathbf{D}_{ij}$ are the components of the antisymmetric exchange coupling known as the DM interaction [156, 157] and A_i are the SIA components. The J_{ij}, $\mathbf{D}_{ij}$ and A_i interactions were computed according to the methodology proposed by Xiang *et al.* [169] from the total energy of particular magnetic configurations summarized in Eqs. 4.2, 4.3, and 4.4 respectively. For this purpose, $3\times1\times1$, $1\times2\times1$ and $1\times1\times2$ supercells were used in order to completely isolate the interactions in each direction. Based on the symmetry of the *pPv* phase, the magnetic interlayer exchange interactions are defined such as: J_{12} (along x-axis) $\equiv J_a$ and J_{13} (along c-axis) $\equiv J_c$ as depicted in Fig. 4.3. The interaction between octahedral layers, J_{14} (in the xy-plane) $\equiv J_{ab}$ is also included. Using the same notation than for the exchange constants, the antisymmetric DM vectors are defined as: $\mathbf{D}_{12} \equiv \mathbf{D}^a$ and $\mathbf{D}_{13} \equiv \mathbf{D}^c$ (see Fig. 4.3). Due to the fact that there is no direct bonding of the B-sites between the layers, it is expected to have a quasi-null contribution from the DM interaction for that direction.

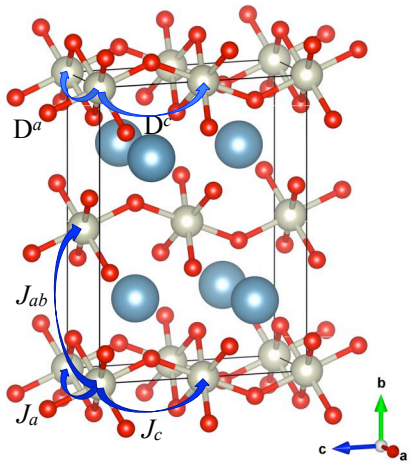

Figure 4.3: Schematic representation of the atomic sites and magnetic interactions in ABX_3 (A, B and X -sites in blue, yellow and red respectively). Exchange constants labeled as J_a, J_c and J_{ab} and DM interactions represented as D^a and D^c equivalent to D_{12} and D_{13} respectively are shown. (Fig. elaborated with the VESTA software [168]).

$$J_{ij} = \frac{E_{\uparrow\uparrow} + E_{\downarrow\downarrow} - E_{\uparrow\downarrow} - E_{\downarrow\uparrow}}{4S^2}, \tag{4.2}$$

$$D^{k}_{i'j'} = \frac{E^{ij}_{\uparrow\rightarrow} + E^{ij}_{\downarrow\leftarrow} - E^{ij}_{\uparrow\leftarrow} - E^{ij}_{\downarrow\rightarrow}}{4S^2}, \tag{4.3}$$

$$A_i = \frac{E^{j}_{\uparrow} + E^{j}_{\downarrow} - E^{k}_{\uparrow} - E^{k}_{\downarrow}}{2S^2}, \tag{4.4}$$

The values for the J_{ij} constants (see Table 4.4) demonstrate a ferromagnetic interaction along the x-axis with $J_a > 0$. Additionally, we can observe a strong AFM coupling along the z-axis and a weak interlayer interaction, in agreement with the non-collinear magnetism results reported in Table 4.3. In the $CaRhO_3$ compound, J_{ab} >0, which corresponds to a FM interlayer interaction as expected from the C_zF_y magnetic ground state. In $NaNiF_3$ $J_{ab} < 0$ which confirms the G_yA_z ordering and in agreement with the group theory analysis. It is important to remark that the magnetic constants in $CaRhO_3$ are at least one order of magnitude larger that in $NaNiF_3$. This can be explained by the lower covalence in the B–F–B bonding, when compared to the B–O–B and related also to the expected JT-distortion with Rh^{4+} cation as well as the fact that 4d and 5d electrons are known to have higher exchange constants than the 3d electrons [170].

As demonstrated by Kim and Min [171] in d^3, d^5 and d^8, B-sites, the DM vector in perovskites can be related to the inter ionic vectors as $\mathbf{D}_{ij} \propto (\hat{x}_i \times \hat{x}_j)$ [171], where $\hat{x}_i$ and $\hat{x}_j$ are unitary vectors along the B–X–B bonds. Thus, according to the previous relation and the symmetry of the *pPv* compounds, the $\mathbf{D}^a$ must be zero and the $\mathbf{D}^c$ has to be along the x-axis, then: $D^a_x = D^a_y = D^a_z =$ 0 and $D^c_y = D^c_z = 0$. However, if a Jahn-Teller distortion is present (*i.e.* such as in Mn^{3+} (d^4), Cu^{2+} (d^9) or Rh^{4+} with t^5_{2g} occupation), there is a change in the orbital symmetry, breaking the mirror symmetry and creating a deviation from the Kim and Min rule (as it happens in $LaMnO_3$ [171]). In Table 4.5 we report the components of the DM vectors for the two considered compounds. Analyzing the DM components, we conclude that $NaNiF_3$, with Ni^{2+}, perfectly fulfill the Kim and Min rule with a non-zero $D^c_x = 0.604$ meV. However, in the $CaRhO_3$ case, a deviation is observed where $D^a_x = -1.483$ meV. This is probably due to the t^5_{2g} state that induces a JT-distortion, which in turn changes the orbital symmetry and then, change the DM vectors.

According to the relation between the exchange constants and the magnitude of the DM vector, the magnetic canting angle φ can be defined as [158]:

$$\varphi = \frac{1}{2} tan^{-1}\left(\frac{|\vec{D}_{ij}|}{J_{ij}}\right) \tag{4.5}$$

if there is no SIA in the direction of the canting [158, 167]. We can estimate the canting angle from this simple formulae and compare the results with the

relaxed values obtained through the DFT calculations. For $NaNiF_3$ the canting angle coming from the relaxed DFT calculations are 3.57° and 2.93° for G_yA_z and C_zF_y respectively, and we obtain $\varphi = 2.97°$ according to the calculated $\mathbf{D}_{ij}$ and J_{ij} parameters and the use of Eq.4.5. In $CaRhO_3$ the canting angle coming from the fully relaxed calculations is 3.52° while it is 1.42° from Eq.4.5. The large discrepancy between the relaxed and estimated canting angle in $CaRhO_3$ can be related to the competition between JT-distortions, orbital symmetry [171] and electronic Coulomb localization [155] through the SIA. The contribution of SIA to the canting angle has been first reported by Moriya in NiF_2 where the DM interaction is forbidden by symmetry [157, 158].

Table 4.4: Computed magnetic exchange constants for *pPv* $CaRhO_3$ and $NaNiF_3$. Units in meV.

	J_a	J_c	J_{ab}
$CaRhO_3$	11.91	-35.81	0.60
$NaNiF_3$	1.06	-5.80	-0.07

Table 4.5: Dzyaloshinsky-Moriya ($\mathbf{D}_{ij}$) vectors computed for *pPv* $CaRhO_3$ and $NaNiF_3$. Here, $\mathbf{D}_{12} \equiv \mathbf{D}^a$ and $\mathbf{D}_{13} \equiv \mathbf{D}^c$ as shown in Fig. 4.3. Units in meV.

	$\mathbf{D}^a$			$\mathbf{D}^c$		
	D^a_x	D^a_y	D^a_z	D^c_x	D^c_y	D^c_z
$CaRhO_3$	-1.483	0.000	0.000	-1.770	0.000	0.000
$NaNiF_3$	0.000	0.000	0.000	0.604	0.000	0.000

To elucidate this problem, we report in Table 4.6 our calculated amplitude of the SIA components obtained using the Eq. 4.4. The SIA amplitude of $NaNiF_3$ is one order of magnitude smaller than its DM vector components which suggest a DM driven magnetic canting in the fluoride compound. However, in $CaRhO_3$, the A_x and A_y parameters are two times larger than the D^c_x component of $\mathbf{D}^c$, which suggests a strong interaction between the DM and SIA interactions. This can explain why the simple tangent formula Eq. 4.5 that takes into account only J and DM interactions gives a bad estimation of the canting angle in the $CaRhO_3$ case while it works pretty well in the case of $NaNiF_3$. According to the larger canting observed in the fully relaxed calculations with respect to one obtained with Eq. 4.5, we can conclude that the SIA is cooperative with the DM vector in developing a canting of the magnetic moments.

Table 4.6: Computed SIA parameters for *pPv* $CaRhO_3$ and $NaNiF_3$. Units in meV.

	A_x	A_y	A_z
$CaRhO_3$	-2.398	2.748	0.365
$NaNiF_3$	0.031	0.038	-0.067

4.5 Summary and Conclusions

By means of first-principles calculations we have studied the non-collinear magnetism in the high pressure post-perovskite phases of $CaRhO_3$ and $NaNiF_3$. We have found that according to group theory the magnetic canting is allowed by symmetry in all of the *pPv* ABX_3 with a magnetically active B-site cation. The exchange constants, the single-ion anisotropy parameters and the Dzyaloshinsky-Moriya vectors components were computed and we found a ferromagnetic exchange interaction along the x-axis and an AFM interaction along the z-direction. The exchange coupling J_{ab} between layers along the y-axis is much smaller than the interlayer J_a and J_c constants by at least two orders of magnitude, which confirms the quasi-2D magnetic behaviour observed in the magnetic *pPv* crystals. Interestingly, we found that the DM interaction is responsible for the spin canting in $NaNiF_3$ while the single-ion anisotropy is found to play an important role in the canting of $CaRhO_3$ and cannot be neglected if one wants to understand the non-collinear magnetism in this system. The origin of this difference can be due to the presence of a Jahn-Teller active cation in $CaRhO_3$ that strongly affects the magnetism of the Rh cation. With this work, we hope to motivate the experimentalist to further analyze the magnetic properties of the quasi-2D magnetic post-perovskites materials.

5

INDUCED MULTIFERROIC AND MAGNETOELECTRIC BEHAVIOR IN $NaMnF_3$

In the search for new and innovative materials with exciting multifunctional properties, multiferroics and magnetoelectrics has been a keystone in condensed matter physics in the last decade [172, 173]. Several systems and compounds based on oxide perovskites have been reported as ideal candidates. In these systems, the presence of the ferroic orders can be induced and/or tuned by different physical constrains such as the case of the biaxial epitaxial strain [174] in thin films and superlattices form [175]. In this search, one of the main challenges is to induce a ferroelectric order in magnetic and non-magnetic perovskites. Then, taking the biaxial epitaxial strain as a control parameter, the condensation of a stable ferroelectric state has been successfully reported in $CaTiO_3$ [176], $SrTiO_3$ [20] and $CaMnO_3$ [177, 175] the first two of them paramagnetic materials at their ground state and the later antiferromagnetic (AFM) with a weak ferromagnetism (weak-FM) due to a magnetic canted structure [175]. Here, the strain couples with the softest mode and thus, induce a polar displacement achieving with this a phase transition to a polar state in a already AFM structure [178] and thus exceeding the so-called d^0-ness rule that is expected to prevent the formation of a FE phase in magnetic perovskites [179]. However, the possibility for new materials with these multifunctional properties in new stoichiometries is still evasive. Recently, fluorides have been reported as possible candidates for a multiferroic behavior with promising properties [18]. Nonetheless, none of the reported fluoride candidates belong to the most claimed perovskite family.

Lately we have shown that even if none of the fluoroperovskites is reported with a FE ground state (except $CsPbF_3$ [180, 181], and the theoretically predicted $NaCaF_3$ [86], and $NaCdF_3$ [182]) they have nevertheless the propensity to have a FE instability in their high symmetry cubic reference structure [2]. We have identified that the FE instability of the fluoroperovskites is related to a steric geometric effect when small cations lie at the A-site. The later contrary to the charge transfer or A-site stereochemically active lone pair origin observed in the oxides and to the phonon mode coupling origin present in improper and hybrid-improper FE [183]. Then and unfortunately, these fluoroperovskites keep the "undesired" competition between the FE and antiferrodistortive instabilities such as the AFD dominate in the bulk ground states. Thus, the possible tuning of the ferroelectricity taken advantage of this hidden polar mode in the paraelectric

room temperature ground state becomes interesting and promising. Additionally, in oxides, the FE strain-induced state can be only obtained through tensile strain, instead compressive one, in which the frequency of soft polar mode goes to higher values. Besides, a linear behavior of the FE–frequency as a function of strain has been observed [178]. Then, based in the different origin of the polar instability in fluorides, a different strain-polarization coupling should be expected. Moreover, it is worth to mention that one of the key factors in the search for new magnetoelectrics with a strong ME coupling is the requirement for a large ferromagnetic canting [184, 185] (induced by the Dzyaloshinsky-Moriya interaction [156, 157]) which in the fluoroperovskites tend to be higher (see Chapters 3 and 4). This need for a large FM canting is based in the weaker effect of electric field in magnetism than the effect of an applied magnetic field on the ferroelectric polarization [186, 184].

Though the sections of this chapter the reader can find the study on the multiferroic state of $NaMnF_3$ under epitaxial strain and its non-linear ferroelectric behavior as a function of epitaxial strain. It is shown that in this material a multiferroic state can be realized for tensile or compressive strain, this completely different in comparison with oxides [176, 20, 175]. Additionally, out-of-plane polarization is observed instead of the ac *Pnma* in-plane spontaneous polarization reported in oxides. An B-site contribution is observed for negative strain values, therefore an A- and B-sites leaded FE was found in the $Pna2_1$ strained structure. Magnetoelectric coupling allowed by symmetry is studied in the AFM+FM+FE $Pna2_1$ $NaMnF_3$. Then, it can be concluded that according to our knowledge, the $NaMnF_3$ is the only reported multiferroic/magnetoelectric fluoroperovskite material obtained so far.

5.1 Computational Details

Here again, we used DFT as implemented in VASP code [66, 67] as the framework of this work. PAW [64] pseudo-potentials were used to represent the valence and core electrons. The electronic configurations taken into account in pseudopotential as valence electrons are presented in Table 2.1. The exchange correlation was represented within the GGA - PBEsol parametrization [39]. Due to the magnetic character of these systems, we included the electron-spin in the calculations. The d-electron localization is corrected by means of the GGA+U, with $U = 4.0$ eV and J = 0.0 eV within the Liechtenstein formalism [43]. The periodic solution of these crystalline structures was represented by using Bloch states with a Monkhorst-Pack k-point mesh of 6×4×6 and 700 eV energy cut-off, which has been tested already to give forces convergence to less than 0.0001 eV/Å. Spin-Orbit coupling (SOC) was include into non-collinear calculations [68]. Born effective charges and phonon calculations were performed within the DFPT formalism [69]. The dynamical matrix was then unfolded using the Phonopy code [70]. The ferroelectric spontaneous polarization was computed through the Berry

phase approach [71] as implemented in the VASP code. The ME coupling was obtained by computing the spontaneous polarization as a function of the applied Zeeman magnetic field as implemented by Bousquet *et al.* [65] within the LDA approach —for more details see Chapter 1—. Besides, we have evaluated the ME response against the U and J parameters of the DFT+U as shown later.

5.2 Epitaxial strain in *Pnma* $NaBF_3$ Fluorides

Up to this point, with all the acquired knowledge about the vibrational properties of the fluoroperovskites (Chapter 2) and the effect of the isotropic pressure in these compounds (Chapters 3 and 4) we now continue by analyzing the biaxial or epitaxial strain (ε) effect into their properties. For that purpose we selected the $NaBF_3$ family based in the results discussed in Chapter 2. In Fig. 5.1 we present the frequency value of the FE instability (T_{1u}) at the cubic high temperature symmetry as well as the softest B_{2u} mode in the *Pnma* ground state for B = Mn, V, Zn, and Ni (in their ionic radii order). It can be easily observed that both modes, T_{1u} and B_{2u} follow the ionic radii size trend. Then, it is obviously expected that as bigger is the instability, softest is the polar B_{2u} mode and then, easier is the destabilization of the mode to induce ferroelectricity as the ionic B-site radii increases.

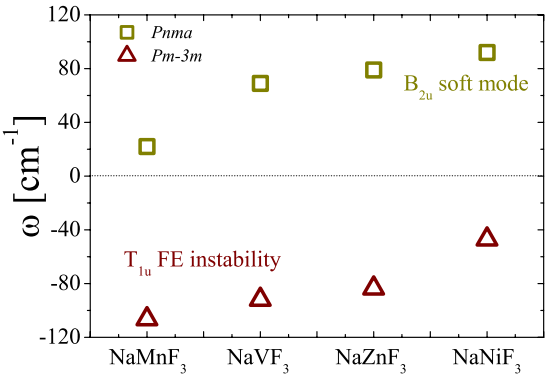

Figure 5.1: Ferroelectric instability T_{1u} at the cubic $Pm\bar{3}m$ as well as the frequency values for the softest B_{2u} mode in the *Pnma* $NaBF_3$ (B = Mn, V, Zn, and Ni) compounds.

Based on an experimental point of view, we suppose a cubic perovskite substrate where $a = c = \sqrt{2}a_o$. Thus, the 0% strain value corresponds to $a_o = \frac{a_i+c_i}{2}$ where a_i and c_i are the unstrained relaxed cell parameters of the *Pnma* phase defining $\varepsilon = \frac{a-a_o}{a_o}100\%$. After the analysis and calculations, the only fluoroperovskite that exhibit a ferroelectric instability under epitaxial strain is the $NaMnF_3$ compound which is indeed, the compound with the largest ferroelectric instability (around 107 icm^{-1}) and the lowest soft mode at the ground state (see

Fig. 5.1). Thus, a detailed research in the later was carried out and all the results are presented in the following sections.

5.3 Strain-Induced Ferroelectricity in $NaMnF_3$

As commented previously, sodium-manganese fluoride, $NaMnF_3$ crystallizes in the *Pnma* structure at room conditions. For this phase, lattice parameters obtained by us within DFT methodology are $a_i = 5.750$ Å, $b_i = 8.007$ Å and $c_i = 5.547$ Å in well agreement with experimental reports by Daniel *et al.* [137]. At high temperature cubic $Pm\bar{3}m$ structure, $NaMnF_3$ presents antiferrodistortive (AFD) modes related to octahedral Mn–F_6 tilting and rotations at the M–R branch as well as antipolar displacements at the X-point according to the phonon-dispersion curves (see Chapter 2). The FE-mode amplitude is comparable with the rotations, AFD distortions and antipolar displacements modes with values of 94 icm^{-1}, 132 icm^{-1}, 131 icm^{-1} and 96 icm^{-1}, for R_5^+, M_3^+, R_4^+ and X_5^+ respectively (see Chapter 2 and Ref. [2]). Thus, the competition between ferroelectric, antipolar displacements and AFD distortions at the ground state are present in this fluoride and the balance between those is really delicate. Despite the presence of the FE mode, as discussed above, the ground state belongs to a non-polar orthorhombic *Pnma* structure. However, as we found, the ferroelectric instability in fluorides present a totally different origin, which is related to A-site geometrically driven polar displacements [2].

In FE oxides it is well known that in some particular cases, the epitaxial strain can induce ferroelectricity in the *Pnma* phase [177] or enhance it in compounds with different ground states and symmetries such as $PbTiO_3$ or $BiFeO_3$ [178]. In $NaMnF_3$ the lowest FE mode has the B_{2u} symmetry and it is polarized perpendicular to the biaxial constraint (the orthorhombic b-axis). Unexpectedly, this mode becomes unstable whatever the value of the epitaxial strain in compression or expansion regime as presented in Fig. 5.2a. By freezing the unstable mode at Γ and performing the structural relaxation, the new ferroelectric ground state is the polar $Pna2_1$ space group as it can be observed from the double well energy curve presented in Fig. 5.2c. Then, the ground state of the epitaxially constrained structure is always ferroelectric and thus multiferroic due to the G-type AFM $NaMnF_3$. This finding is completely different from oxides in which some of them, originally paraelectric, can only reach the ferroelectric state for strain values above 1.5% such as in $CaTiO_3$ [176], 0.8% in $SrTiO_3$ [20] and 2.3% in $CaMnO_3$ [175]. Additionally, for negative or positive strain, the polarization is enhanced up to a value of 12 $\mu C \cdot cm^{-2}$ at +5% and 9 $\mu C \cdot cm^{-2}$ at -5% respectively, and here again, a strong difference with previous observations and reports in ferroelectric oxides [174]. We note also that the polarization develops in the direction where the antipolar motions of the X_5^+ mode are absent and thus, where there is still possibility for the A-site to move in the remaining flat energy landscape direction obtaining a FE stable state along b-axis with an anti-polar character in the ac-plane.

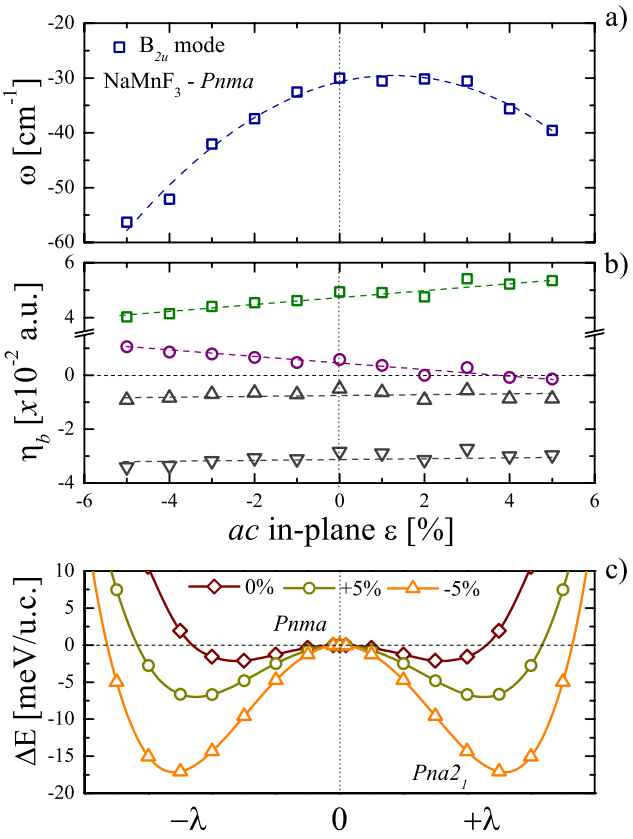

Figure 5.2: a) Epitaxially strain induced B_{2u} instability in *Pnma* $NaMnF_3$ in which a nonlinear coupling is observed, imaginary frequencies are represented as negative values by notation. b) Eigendisplacements of the polar B_{2u} along b-axis (η_b) for each site (Na in green squares, Mn in violet circles and $F_\perp$, $F_\parallel$ in upper and down triangles respectively) in $NaMnF_3$ in *Pna2$_1$*. c) Ferroelectric mode freezing in which the transition from the paraelectric *Pnma* to a polar *Pna2$_1$* phase is observed at equivalent 0% in the ac-plane.

In order to understand the origin and physical phenomena within the transition and the stable FE ground state, we analyzed the eigendisplacements of the unstable mode B_{2u} under epitaxial strain (see Fig. 5.2b). From this figure it can be concluded first that as in oxides, the Na alkali-metal ion (in this case the A-site) tries to annihilate the ferroelectricity when the strain goes from 5%, to -5% with eigendisplacements of 0.257 and 0.193 for Na respectively. However, the antipolar motion of B-site (Mn in this case) decrease and the eigendisplacements of this site begins to present a polar contribution to the b-axis that compensates the decrease in contribution of the Na site (see Table 5.1). This can explain the anomalous behavior of FE-instability at compression epitaxial strain. The fluorine displacements remain almost invariant for expansion or compression strain with no significant effect on the instability behavior. The analysis of the Born effective charges (Z^* in the Table 5.1) reveal that values of this parameter are

Table 5.1: Born effective charges (Z^*, in e^-) of selected strain values (ε). $F_\perp$ and $F_\parallel$ represent the Born effective charge of the F atom when it is displaced respectively against the Mn cation and along the perpendicular direction. Eigendisplacements (η_b) of the FE unstable mode along the b-axis in $NaMnF_3$. $F_\perp$ and $F_\parallel$ have the same sense as given in Born effective charges.

	Z^* [e^-]				η_b [a.u.]			
ε [%]	Na	Mn	$F_\perp$	$F_\parallel$	Na	Mn	$F_\perp$	$F_\parallel$
Nominal	1	2	-1	-1	—	—	—	—
+3%	1.15	2.22	-0.84	-1.69	0.260	0.021	-0.024	-0.119
0%	1.18	1.99	-0.71	-1.75	0.237	0.043	-0.022	-0.123
−3%	1.17	2.21	-0.83	-1.72	0.211	0.059	-0.031	-0.139

close to nominal ones (+1, +2 and −1 for Na, Mn, and F respectively) which is related to a geometric origin of the ferroelectricity in $NaMnF_3$ as expected [2] instead of a charge-transfer phenomena found in most of the ferroelectric oxide perovskites [83].

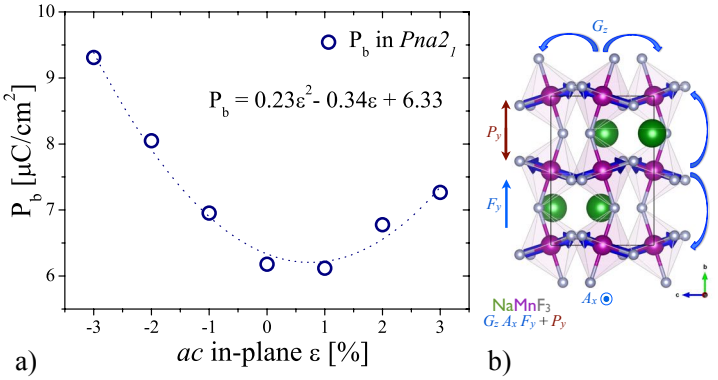

Figure 5.3: a) Polarization along b-axis in $NaMnF_3$ in $Pna2_1$ symmetry. The second-order dependence of the polarization as a function of ac-plane epitaxial strain is observed as a result of the non-linear piezoelectricity in this perovskite fluoride. b) $NaMnF_3$, $Pna2_1$ structure is also presented where Na, Mn and F ions are depicted in green, violet and grey respectively. Additionally, the non-collinear magnetic ground state as well as the polarization vector along the b-axis are schematically depicted in the figure showing the multiferroic character of this fluoroperovskite.

5.3.1 *Second-order piezoelectricity in* $Pna2_1$ *NaMnF*$_3$

We found a non-linear ferroelectricity-strain coupling in this compound becoming another different property in the engineered multiferroicity in $Pna2_1$ when

comparing to oxides. This fact is demonstrated by the quadratic dependence of the spontaneous polarization as a function of epitaxial strain as observed in Fig. 5.3 and expressed in terms of the strain, piezoelectric constants and polarization in Eq. 5.1. To our knowledge, this piezoelectric property has been found only in very few compounds, where some happen to be zinc-blende semiconductors [187] and now this fluoride perovskite. The behavior of the polarization as a function of the strain is expressed as follows:

$$P_\mu = \sum_j e_{\mu j}\varepsilon_j + \sum_{j,k} B_{\mu jk}\varepsilon_j\varepsilon_k, \tag{5.1}$$

where P_μ is the spontaneous polarization with $\mu = 1$, 2, and 3 for the Cartesian components x, y, and z respectively. The strain tensor is represented by ε_j with $j = 1$, 2,...., 6 as the components of the tensor in the Voigt notation. Finally, $e_{\mu j}$ and $B_{\mu jk}$ are the linear and quadratic piezoelectric coefficients respectively. If we oriented the plane of epitaxial strain into the xz-plane, we have that $\varepsilon_4 = \varepsilon_5 = \varepsilon_6 = 0$ and $\varepsilon_1 \approx \varepsilon_3$[1]. Additionally, the in- and out-of plane strain relationship can be related to the Poisson ratio such as $n = -(\varepsilon_1/\varepsilon_2)$. If we expand up to second order the polarization as a function of strain in order to obtain the piezoelectric constants allowed in the $NaMnF_3$ we find the expression shown in Eq. 5.1 which can now be expressed as follows:

$$\begin{aligned} P_y = &\left(e_{21} + e_{23} - \frac{e_{22}}{n}\right)\varepsilon_1 + ... \\ &+ \frac{1}{2}\left(B_{211} + B_{233} + 2B_{213} - 2\frac{B_{221} + B_{223}}{n} + \frac{B_{222}}{n^2}\right)\varepsilon_1^2 \end{aligned} \tag{5.2}$$

The computed linear piezoelectric coefficients e_{21}, e_{23}, e_{22}, e_{16}, and e_{34} at 0% strain are equal to 1.010, -0.672, 0.064, -0.108, and 0.058 $C{\cdot}m^{-2}$ respectively and are not far from the ones observed in $BaTiO_3$ [188, 189]. Nonetheless, the computation of quadratic order components is beyond of the reach of this chapter and the description and analysis of those parameters needs further studies. Nevertheless, from the quadratic fitting observed in Fig. 5.3 we can extract that the non-linear contribution related to the sum of the $B_{\mu jk}$ component is at least the 60% of the linear piezoelectric constants which points out the necessity for a further study of this property in this material.

1 In the *Pnma* structure that a and c parameters are not exactly the same and an average between them is taken in order to apply the bi-axial strain. Then, an small plus and minus strain is intrinsically applied to the a and c parameters respectively.

5.4 Non-Collinear magnetism and ME coupling in *Pna2₁* $NaMnF_3$

With the idea to understand better the magnetic ordering in $NaMnF_3$, we performed a theoretical characterization of *Pna2₁* phase. Based on group theory analysis, the possible magnetic orderings and couplings were obtained. Character table and possible magnetic couplings and orderings are presented in Table 5.2. In the *Pna2₁* independent of the possible magnetic states, the magnetoelectric coupling is allowed by symmetry (Table 5.2). For the *Pnma* phase it is expected a predominant G-type AFM behavior, with a canted structure and a weak magnetization along c-axis as reported by Shane [190], however, no more experimental or theoretical reports has been carried out to generate a deeper understanding of the magnetic structure. Despite of the experimentally reported ground state, an $G_xC_yA_z$ magnetic ordering structure was found over a wide range of U and J values (from 0 to 9 eV and 0 to 1.0 eV for U and J respectively) within the PBEsol exchange-correlation functional. The later in complete disagreement with the experimental findings [190]. Within the LDA approximation, the magnetic ground state is fully converged and it is in complete agreement with the experimental reports showing a $G_zA_xF_y$ magnetic ordering. In the *Pna2₁* phase, the same ground state remains after the structural transition from the *Pnma* structure and none magnetic state transformation was observed. It is important to remark that as explained in the computational details section, the Zeeman effective magnetic field is only implemented within the LDA approach, thus, for the non-collinear magnetic ordering and ME-coupling analysis, the LDA formalism is taken from now on.

The magnetic ground state in the *Pna2₁* was analyzed according to the orderings proposed in Table 5.2. $G_zA_xF_y$ was found as the ground state and it is depicted in Fig. 5.3b. Analyzing the noncollinear magnetic structure we noted the ferromagnetic component F_y is $m_y = 0.02\ \mu_B$/atom. This FM component lies at the same order of magnitude as expected from some weak ferromagnets such as $CaMnO_3$ perovskite where the FM component is $m_y = 0.04\ \mu_B$/atom [175]. Nonetheless, a larger magnetic canting should be expected according to its trend as a function of the B-site ionic radii and octahedral rotation shown in Table A.1. Based on the magnetic point symmetry group (*m'm'2*) found for the magnetic $G_zA_xF_y$ ground state, all the magnetic, electric and magnetoelectric couplings are permitted by symmetry within the thermodynamic potential expansion, as shown in Ref. [191]. Thus, a second order ME can be expected for the $NaMnF_3$. In agreement with the later statement, all the couplings and interactions that affects the electric polarization for this fluoroperovskite are included and defined in the Eq. 5.3 as follows:

$$P_i = \alpha_{ik}H_k + \frac{1}{2}\beta_{ijk}H_jH_k + \gamma_{jik}H_jE_k, \tag{5.3}$$

where P_i is the spontaneous ferroelectric polarization along each particular Cartesian axis ($i = x$, y and z). H_j is the applied magnetic field along the j axis. α_{ik} is the linear magnetoelectric matrix, and β_{ijk}, γ_{jik} are the second order ME coupling tensors.

Table 5.2: Allowed magnetic orderings in the D_{2h} point symmetry group [147, 148] for *Pnma* [175] and epitaxially-induced phase $Pna2_1$. Besides, the magnetoelectric couplings [191] for $Pna2_1$ are shown depending to the non-collinear ordering and the magnetic group.

Magnetic	$Pna2_1$		
Ordering	Character	ME-linear	ME-second order
C_x, G_y, F_z	A_2	α_{yz}, α_{zy}	β_{ijk}, γ_{jik}
A_x, F_y, G_z	B_1	α_{xx}, α_{yy}, α_{zz}	β_{ijk}, γ_{jik}
F_x, A_y, C_z	B_2	α_{xz}, α_{zx}	β_{ijk}, γ_{jik}
G_x, C_y, A_z	A_1	α_{xy}, α_{yx}	β_{ijk}, γ_{jik}

The magnetoelectric coupling was computed for several strain values according to the implementation of finite magnetic field given in Ref. [65] and explained in Chapter 1. The results are condensed in Fig. 5.4 and in Table 5.3. In Fig. 5.4 we report the evolution of the electric polarization with respect to the amplitude of the applied magnetic field along different directions. In Table 5.3 we report the extracted ME coefficients at three different epitaxial strains. Our results reveal that a sizeable non-linear ME coupling is present when the magnetic field is applied along the y-axis (parallel to the weak-FM moment and the spontaneous polarization). When the field is applied along the x-axis, we observe a linear ME response along the same direction (α_{xx}) and a non-linear one along the y-axis (β_{yxx}).

In comparison to Cr_2O_3 that has been widely studied and in which the experimental reports show a ME coupling in the range between 0.67 – 1.59 ps·m^{-1} [192, 193, 194, 195], the linear magnetoelectric response in $NaMnF_3$ is in the range, when the strain is close to +3%. Additionally, the ME response in this fluoroperovskite is of the same order as in $CaMnO_3$ [175].

Additionally, it can be noted that all the ME coefficients increase when the strain goes from positive to negative values (for example the α_{yy} coefficient varies from -0.314 to -0.796 ps·m^{-1} for +3% to −4% respectively), which is consistent with the fact that the polarization contribution of the magnetic Mn atoms is larger for compressive strains and thus we can expect a stronger coupling between electric polarization and magnetism. The global form of the ME responses in this fluoroperovskite is very similar to the one predicted for $CaMnO_3$ [175], which shows that this might be a general rule for strain-induced FE in the *Pnma* structure. Finally, we also note that the ME response is observed in spite

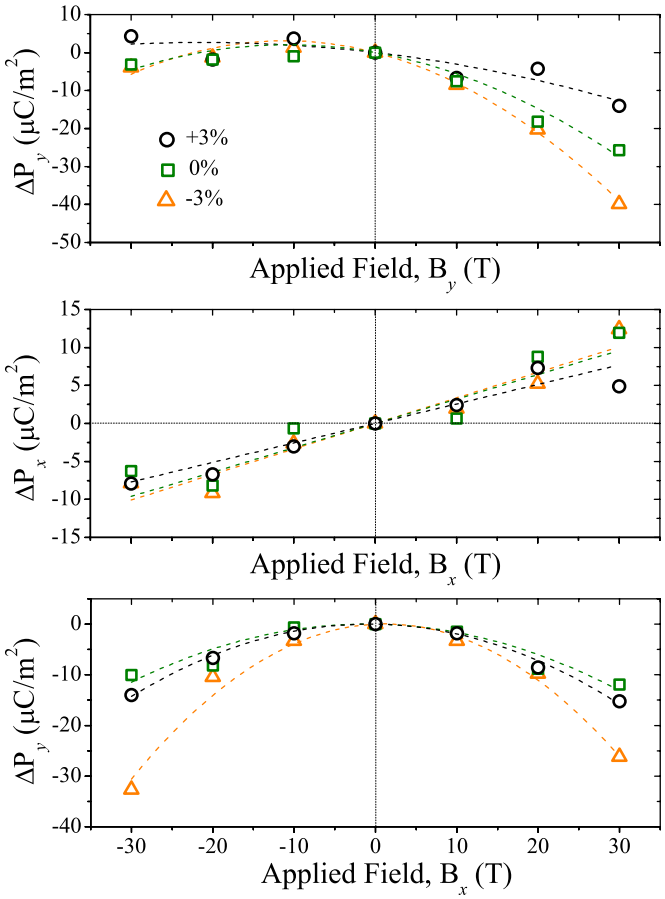

Figure 5.4: Magnetoelectric coupling in $NaMnF_3$ in $Pna2_1$ structure where ΔP_y vs B_y (upper panel), ΔP_x vs B_x (center panel) and ΔP_y vs B_x (lower panel) are presented. In dashed lines are presented the linear and quadratic fitting according to the Eq. 5.3. The second-order ME coupling can be appreciated from this figure. Additionally, an increase of the non-linear behavior as a function of the epitaxial strain is observed. The computed first and second order ME tensor are presented in Table 5.3.

Table 5.3: ME coefficients of strained $NaMnF_3$ $Pna2_1$ expressed as in the Eq. 5.3, α_{ik} in [ps·m^{-1}] and β_{jik} in [$\times 10^{-8}$ ps·A^{-1}].

Strain, ε [%]	α_{yy}	α_{xx}	β_{yyy}	β_{xxx}	β_{yxx}
+3%	-0.314	0.322	-0.927	0.000	-2.625
0%	-0.480	0.403	-2.232	0.000	-2.156
−3%	-0.698	0.423	-3.931	0.000	-4.973
−4%	-0.796	0.430	-6.818	0.000	-7.061

of a non Mn-driven polar distortion which claims for a study of the ME-coupling source as discussed next.

5.4.1 *Field-induced distortions as the source of the ME coupling*

A phonon projection was carried out, then, the effect of the magnetic field and the related modes activated as a function of it were analyzed. In Fig. 5.5 we plot the overlap between the magnetic B-field induced distortions in the $Pna2_1$ phase (at 30 T amplitude of the field along the y-axis, here denoted as $|\delta\rangle$ in Fig. 5.5) and the *Pnma* phonon eigendisplacements basis set ($|\eta\rangle$ in Fig. 5.5) for epitaxial strain values of -3%, 0%, and $+3\%$. The eigendisplacements are normalized as follows $\langle\eta_i|M|\eta_i\rangle = 1$ where M is the mass matrix of the atoms.

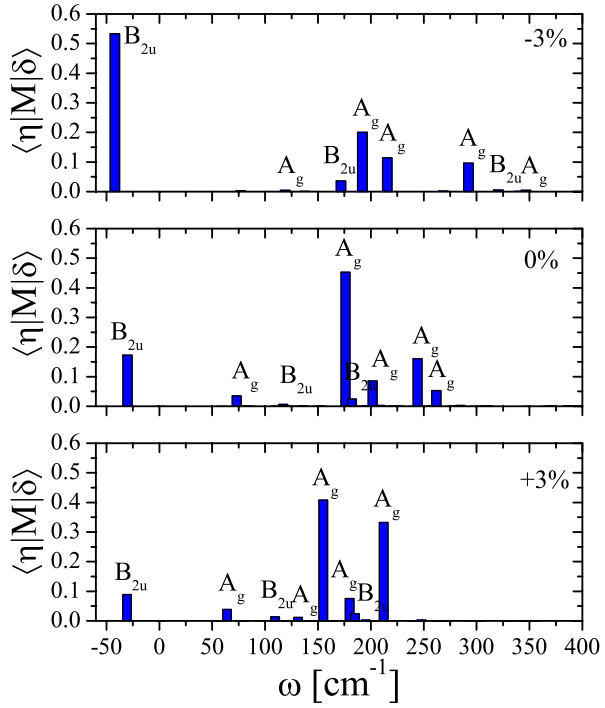

Figure 5.5: Projection of the magnetic B-field induced distortions (at 30 T in the $Pna2_1$ FE phase) against the phonon basis set of the *Pnma* phase for -3%, 0%, and +3% values of the epitaxial strain. We note that the B_{2u} FE unstable mode (the one with negative frequencies) is strongly dominant at compressive strain while the A_g modes are more dominant at tensile strains. This fulfills the fact that at compressive strain the FE distortions are much more Mn-driven (and thus much more sensitive to magnetic field) than at tensile strains and this also explains why under compressive strain the ME response is larger than under tensile strains.

Our results suggest that the mechanism driving the magnetoelectric coupling in the $NaMnF_3$ is related to the activation of the A_g modes (Na+F sites) induced by applied magnetic field (see Fig. 5.5). Thus, the activation of those modes modify the eigendisplacements of the polar B_{2u} phonon and then, tunes the FE polarization. This type of ME effect in which, a field-induced distortions are dominated by different phonon modes others than the responsible for the

ferroelectric polarization has been previously demonstrated in the $LiNiPO_4$ [196]. Additionally, the increase of the B_{2u} activation under the magnetic applied field as a function of the strain, going from $+3\%$ to -3% explains the increase in the α_{xx} and α_{yy} ME components.

5.4.2 *Effect of the U and J into the ME coupling in* $Pna2_1$ *$NaMnF_3$*

In order to analyze the effect of the Coulomb repulsion and exchange interaction on the magnetoelectric coupling, calculations for different U and J constants were performed. In Table 5.4 presentes the computed constants for the α_{ik} and β_{jik} terms. It can be observed that the linear ME terms decreases by approximately 0.2 $ps{\cdot}m^{-1}$ for α_{xx} and α_{yy}. However, the second-order coupling term β_{jik} increases by one order of magnitude. Additionally, it can be appreciated that all the tensor components decreases when the J term increase from 0.0 to 0.4 eV. In conclusion, even when the values for the magnetoelectric coupling changes, the deviation is rather small and the effect in the ME coupling is not very large when LDA+U approach is used. Besides, the presence of the ME-coupling is strongly supported by the symmetry analysis.

Table 5.4: ME coefficients (α_{ik} and β_{jik} in $ps{\cdot}m^{-1}$ and $\times 10^{-8}$ $ps{\cdot}A^{-1}$ respectively) of strained $NaMnF_3$ as a function of U and J parameters [in eV] for the 0% value.

U, J [eV]	α_{yy}	α_{xx}	β_{yyy}	β_{yxx}
0, 0.0	-0.480	0.403	-2.232	-2.156
4, 0.0	-0.036	0.231	-22.262	-22.676
4, 0.2	-0.617	0.282	-11.183	-17.711
4, 0.4	-0.470	0.189	-17.519	-15.522

5.4.3 *Special remark: some ferroelectrics under strain*

The B term in the Eq. 5.1 reflects the non-linear character of the strain-polarization coupling of a FE crystal. In order to check whether this nonlinearity is really specific to materials presenting a steric geometric origin of the FE, we have analyzed the polarization-strain coupling in different cases. We first looked at this response in $BaCoF_4$ (see Fig. 5.6), which is known to be a geometric FE without anomalous Z^*. Interestingly, we found the same parabolic polarization vs. strain behavior as for $NaMnF_3$ where the B-term is approximately 38% of the linear one.

We also report in the figure the polarization vs. strain (P vs. ε) of cubic $BaTiO_3$, cubic $CaTiO_3$ and cubic $NaMnF_3$ (*i.e.* in the absence of the AFD motions in the last two of them). We can see that in $BaTiO_3$ the P vs. ε coupling is linear while

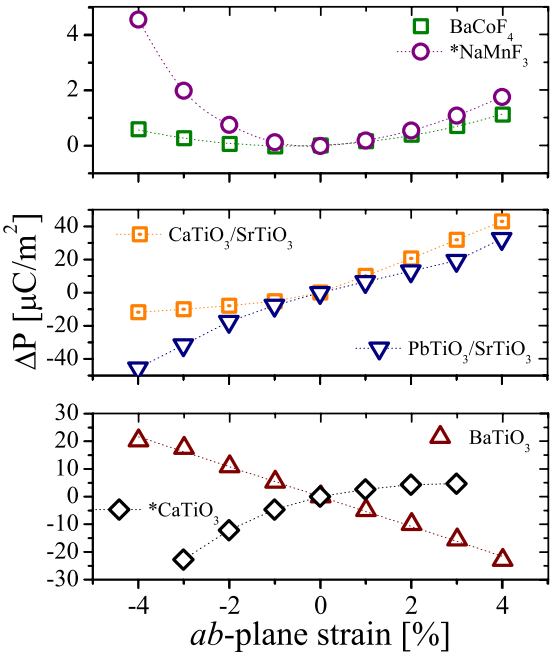

Figure 5.6: Polarization (out-of-plane) vs. epitaxial strain in the ab-plane for the geometric FE $BaCoF_4$, for cubic $BaTiO_3$, cubic $NaMnF_3$ and cubic $CaTiO_3$ case in which we simply relax the polar distortion without the AFD motions, and for improper-FE $PbTiO_3/SrTiO_3$ and $CaTiO_3/SrTiO_3$ superlattices. We note that the strong non-linear polarization/strain coupling is present mostly in steric geometric FE crystals such as $NaMnF_3$ and $BaCoF_4$.

it is strongly non-linear for $NaMnF_3$ (which means that the octahedral motion do not play a determinant role for this mechanism). We note that for $CaTiO_3$, the P vs. ε is linear but it also exhibits some non-linearity. We would thus conclude that $BaTiO_3$ is driven by a charge transfer mechanism while in $CaTiO_3$ a mixed charge transfer and steric geometric effect are present. To go beyond, we also performed the same analysis in improper-FE superlattices $PbTiO_3/SrTiO_3$ (PT/ST) and $CaTiO_3/SrTiO_3$ (CT/ST) and we found that in PT/ST the P vs. ε is linear and slightly non-linear in CT/ST. Improper-FE is thus not necessarily related to a geometric effect in the sense of our steric definition and thus $NaMnF_3$ has a unique response in the perovskite family. This reinforces the idea that the linear vs. non-linear polarization-strain coupling can be a key ingredient to distinguish between a charge transfer FE and a steric geometric FE but further studies would be welcome to confirm this hypothesis. Nonetheless, it seams that this large non-linear piezoelectric response is very unique to the steric geometric origin of the ferroelectricity.

5.5 Conclusions

Using density functional theory we studied the effect of the epitaxial strain on the structural, electronic, and magnetic properties in the fluoride perovskite $NaMnF_3$. A multiferroic-induced state was predicted for $NaMnF_3$ under epitaxial strain at compressive or tensile strain. A non-linear behavior of ferroelectric instability, and then, a non-linear piezoelectric response as a function of epitaxial strain was found. The later completely different as it has been reported in perovskite oxides. Additionally, an out-of-plane polarization, with respect to the epitaxial strain, was observed again in opposite trend when comparing to oxides. A cooperative FE ordering between Na and Mn sites was found for compressive strain. The later against a pure A-site geometrically driven ferroelectricity at tensile values of orthorhombic ac-strain. Magnetic ordering reveals a non-collinear ground state under the $G_zA_xF_y$ representation. And even more interesting, and non-linear magnetoelectric coupling was found in this material under the strained $Pna2_1$ ground state. We hope that our results can motivate to experimentalist in the search of this material which is, to our knowledge, the first perovskite-fluoride in which non-linear piezoelectric and magnetoelectric response co-exist.

Part IV

OXYFLUORIDES ABO_3/ABF_3 INTERFACES

Perovskite interfaces have demonstrated to be a huge source of novel and exciting properties that are completely absent in their bulk counterparts. This has been recognized by the large number of research performed in many different oxide interfaces. In the following we will present a study of the unexplored fluoride/oxide interfaces.

6

2DEG, 2DHG, FE, AND MAGNETISM IN OXYFLUORIDES ABO_3/ABF_3 INTERFACES

Novel electronic properties in oxide/oxide interfaces can be accomplished by tuning the ferroic and spin properties of the chosen component materials and guided by the complex electron-electron interactions known in strongly correlated material interfaces, which gives rise to a large set of intriguing phenomena (see Fig. 6.1). In oxide/oxide interfaces these phenomena include two-dimensional electron gases (2DEG) at oxide insulator/insulator interfaces [197, 198] exotic electronic states due to strong spin-orbit coupling with an intriguing spin-texture structure [199], metal-insulator transitions tunable by electric fields [111], interface magnetic phases [200], improper ferroelectricity [19, 201, 202], and multiferroic interactions [203]. While studies of these phenomena have focused only on complex oxide materials, there are strong indications that complex fluorides may have analogous, or even enhanced properties with respect to the oxide materials. In particular, our recent computational work on fluoride perovskites, (ABF_3) indicates that interfaces between ABF_3 and other fluorides, or hybrid systems with isostructural oxide perovskites ABO_3, have unique advantages in terms of their magnetic, magneto-transport, and multiferroic properties [18]. To date little experimental work has been devoted to fluorides, either in bulk [204, 166] or in thin film forms [205] and therefore there is very limited knowledge about their surfaces, and interface properties. Then, the aim of our work is to overcome this lack of knowledge by performing a first-principles investigation in fluoride-based interfaces and superlattices. This, will lead to a novel strategies for searching new and complex perovskite fluoride-based magneto-electronic materials.

In addition to the studies in bulk fluorides, much less is known about the magnetoelectric properties of interfaces and surfaces of complex fluorides. There are a few reported examples of complex fluorides thin films and the corresponding interface characterization. These include $Fe/KFeF_3$ bilayers [205] and the trilayered system $Fe/KNiF_3/FeF_2$ [206] that has a dynamic and rotatable exchange anisotropy. These systems exhibit exchange bias phenomena, which results in a center shift of the hysteresis loop of the ferromagnetic Fe layer away from $H = 0$, as a result of the magnetic interface interaction with the antiferromagnetic material.

Recently, several efforts have been dedicated to study and to understand mixed systems by considering the effect of fluorine replacement by oxygen ions in ox-

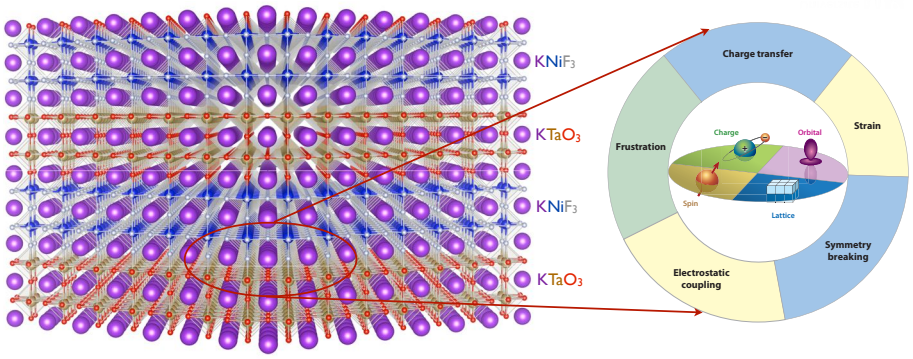

Figure 6.1: Some of the physical phenomena that have lead to several multifunctional properties found in oxides/oxides interfaces and expected in the mixed oxide/fluoride ($KTaO_3$ and $KNiF_3$ in the figure) interfaces. The diagram properties has been taken from Zubko *et al.* [111].

ide perovskites with different stoichiometries. Thus, a process called "fluorination" has been successfully applied to epitaxial growth of $SrFeO_{3-x}F_x$ (x from 0 to 1) thin films [207] where substantial changes in the electric conductivity and transport properties has been demonstrated, mainly due to an induced change in the nominal oxidation state of the Fe cation. Then, an even more surprisingly, multifunctional properties such as superconductivity in $Sr_2CuO_2F_{2+\delta}$ [208], ionic conductivity at $BaFeF_xO_{3-\delta}$ [209], and robust antiferromagnetism in $Ba_{0.8}Sr_{0.2}FeF_xO_{3-\delta}$[210] can be tuned or modified in fluorinated oxides —also called oxyfluorides—.

Even though, there are only a few publications in relation to fluoride-based interfaces meanwhile, the reported results on bulk systems shows that a research in this topic could open an opportunity to find interesting and appealing properties. Therefore, we propose a series of important questions that we will try to address: Is there a presence of another interesting electronic phenomena such as 2DEG, or polar catastrophe in fluoride/oxide interfaces in analogy with some oxide/oxide structures? if that is the case, is the mechanism the same? What is the influence and effect of the O–B–F bonding on the electronic properties, the crystal-field splitting and the magnetic ordering? Is there a possibility to change the confinement of the 2DEG at the interface due to the fluoride layer and its lower covalence? Is there an occurrence or enhancement of ferroelectricity in fluoride-based systems at the interface? Is there a presence of improper ferroelectricity due to interfaces in superlattice structures as it has been reported in some oxide systems? What is the influence of magnetic ordering in the possible ferroelectric behavior at interfaces? What is the multiferroic (or magnetoelectric if exist) behavior at the interface and then at the superlattices? Then having all these unanswered questions and more to come on the road, we present in the next sections our results that aim to shed light onto these novel heterostructures.

6.1 Computational Details

In this chapter, two different codes were used based in their particular abilities to compute several properties.

VASP [66, 67]— We used PAW [64] pseudo-potentials to represent the valence and core electrons. The electronic configurations taken into account in the pseudopotentials as valence electrons are presented in Table 6.1. The exchange correlation was represented within the GGA - PBEsol parametrization [39]. The magnetic character of these system was include and d-electron localization corrected by means of the GGA+U within the Liechtenstein formalism [43], for which, the U value was found by fitting the electronic gap and magnetic moment. The periodic solution of these crystalline structures was represented by using Bloch states with a centered gamma k-point mesh of $6\times6\times x$ (x dependent of the c parameter longitude of the computational cell) and 700 eV energy cut-off, which has been tested already to give forces convergence to less than 0.001 eV/Å. Spin-Orbit coupling was include such that non collinear magnetic configurations can be attained [68]. Born effective charges and phonon calculations were performed within the density functional perturbation theory (DFPT) [69].

Table 6.1: Electronic configuration of pseudopotentials used in the analysis of this chapter. Valences and semicore electrons taken into account for calculations.

A-site	B-site	X-site
K ($3p^6 4s^1$)	Ta ($5p^6 5d^5 6s^2$)	O ($2s^2 2p^4$)
Na ($2p^6 3s^1$)	Zn ($3d^{10} 4s^2$)	F ($2s^2 2p^5$)
La ($5s^2 5p^6 5d^1 6s^2$)	Ni ($3p^6 3d^8 4s^2$)	
	Mn ($3p^6 3d^5 4s^2$)	
	Sc ($3p^6 3d^1 4s^2$)	

CRYSTAL14— Due to the fact that some of the interesting interfaces count with a large number of atoms and in order to describe correctly the strongly correlated nature of the electrons, hybrid calculations have been performed using the linear combination of atomic orbitals (LCAO) as implemented in the CRYSTAL code [72]. This code uses a Gaussian-type basis set to expand the Kohn-Sham orbitals, including polarization effects, with the advantage that less number of the basis is required, which impact into the requirements of the computational time used to calculate strongly correlated materials when compared to plane wave basis set as it is the case of VASP. Additionally, all the electrons have been included in K, Ni, Zn, O, and F while a pseudopotential method has been used for the case of Ta. For the exchange-correlations term, the hybrid functionals taken into account are the B1WC [52], B3LYP [211, 212], and PBEsol0 (derived from the PBE0 functional but based in the PBEsol approximation) [51] all of them with a

16%, 20%, and 25% of exact exchange-correlation term respectively (see Chapter 1).

6.2 Oxyfluorides $KNiF_{2.5}O_{0.5}$ and $KTaO_{2.5}F_{0.5}$

As commented previously, oxyfluorides have been used in several technological applications based on the tuning of their properties by means of the control of the fluorine/oxygen ratio. Here, as a first approach to the mixed X-site systems with oxide/fluoride interfaces, we analyzed the electronic properties of the $KTa(O/F)_3$ and $KNi(F/O)_3$ oxyfluorides. The precursor compounds (*i.e.* $KTaO_3$ and $KNiO_3$ respectively) exhibit a cubic ground state at room conditions. Thus, just one atom of the X-site is replaced, which is equivalent to a composition of $KNiF_{2.5}O_{0.5}$ and $KTaO_{2.5}F_{0.5}$ respectively. This composition is graphically understood as the replacement of one X-site in the MX_6 octahedra as shown in Fig. 6.3 and 6.4. Both oxyfluorides were fully relaxed by means of the PBEsol approach. It can be observed that the $KTaO_{2.5}F_{0.5}$ oxyfluoride present a tetragonal expansion with lattice parameter $a = b = 3.984$ Å and $c = 4.127$ Å. In contrast to this compound, the $KNiF_{2.5}O_{0.5}$ present a tetragonal compression with $a = b = 4.004$ Å and $c = 3.837$ Å. These tetragonal distortions can be understood based in terms of the bonding strength and length, which, in the oxide case is stronger and shorter in comparison to the metal–fluoride bonding. This is also responsible for the polarization induced in the cell due to the off-centering of the B-site.

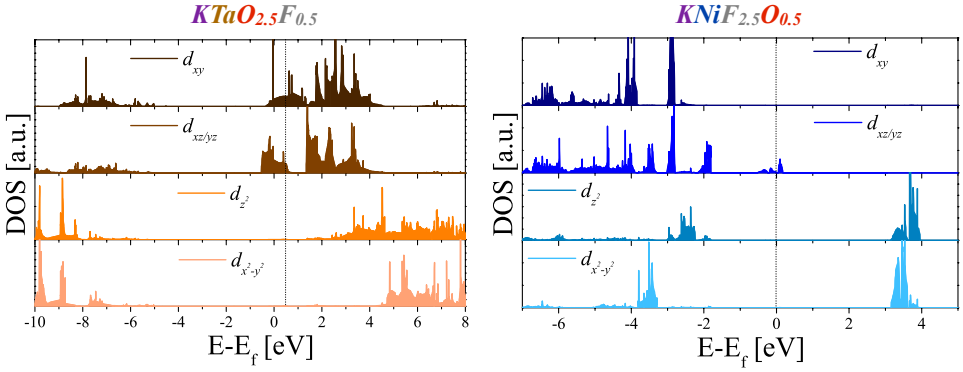

Figure 6.2: Localized-DOS for the 3d-Ni and 5d-Ta at the $KNiF_{2.5}O_{0.5}$ and $KTaO_{2.5}F_{0.5}$ oxyfluorides respectively. This DOS was computed by means of the hybrid functional HSE06.

As expected, the different octahedral coordination has an effect in the electronic structure due to the change in the oxidation states of the central B-site metal cations. For example, the Ta-site is going from a +5 oxidation to a $+(5-\delta)$ state —equivalent to a d-orbital occupation $d^{(0+\delta)}$—. Accordingly, the Ni-site is going from +2 to a $+(2+\delta)$ oxidation state —equivalent to an occupation $d^{(8-\delta)}$— as observed in Fig. 6.3 and 6.4. This in agreement with the experimental results

in $SrFeO_{3-x}F_x$ thin films [207]. Then, the tetragonal distortion and the change in the electronic occupation of the metal cations can induce a tetragonal (T) splitting of the d-orbitals.

In order to understand in more detail, we computed the localized DOS by means of the hybrid functional HSE06 (Heyd-Scuseria-Ernzerhof) [55]. This functional is known to be more precise in the electronic structure calculations correcting the problems due to the a lack in the description of the exchange-correlation energy (see Fig. 6.2). In $KTaO_{2.5}F_{0.5}$ the lowest orbitals are the $d_{xz/yz}$ followed by d_{xy}. These orbitals exhibit a partial occupation that is in agreement with the expected Ta oxidation state as discussed previously. The electronic configuration of the d-orbitals for the Ta are depicted in Fig 6.3. In the $KNiF_{2.5}O_{0.5}$ oxyfluoride we can see that the lowest occupation belongs to the d_{xy} orbital, followed by the $d_{xz/yz}$ orbitals. It is important to note that the $d_{xz/yz}$ is slightly occupied, which is induced by the $d^{(8-\delta)}$ Ni state. Next, we can observe a half occupied $d_{x^2-y^2}$ orbital and right after, around -2 eV, the d_{z^2} orbital. This electronic configuration corresponds to the T-compression configuration as depicted in Fig. 6.4. A magnetic moment is observed in the Ni case and the ordering remains G-type AFM as expected from the former $KNiF_3$. Nonetheless, in the Ta-based case, we do not observe a magnetic moment for the partial 5d occupation.

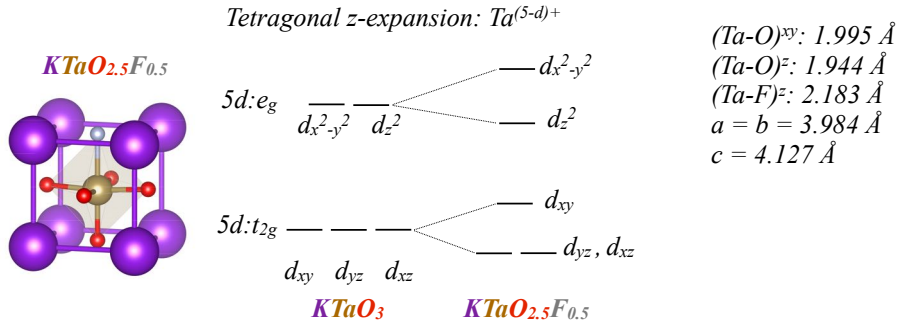

Figure 6.3: Electronic configuration corresponding and crystal-field splitting of the $KTaO_3$ oxide and the $KTaO_{2.5}F_{0.5}$ oxyfluoride.

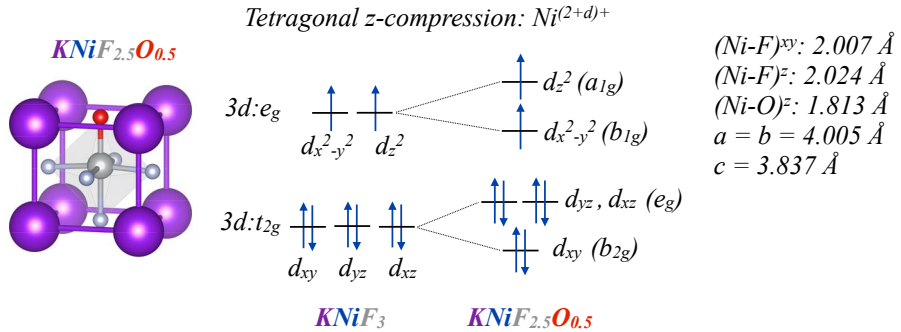

Figure 6.4: Electronic and magnetic configuration corresponding to the crystal-field splitting for the $KNiF_3$ fluoride and the $KNiF_{2.5}O_{0.5}$ oxyfluoride.

Therefore, we should expect these type of distortions and alterations of the electronic structure close to the interface when oxides and fluorides are displaced for mixed systems which could induce an unobserved electronic behavior.

6.3 $KTaO_3/KBF_3$ (B = Zn and Ni) superlattices

As a first fluoride/oxide superlattices, we considered two different pristine materials: $KTaO_3/KBF_3$ with B = Zn and Ni. These structures are formed by a polar layered oxide with $(TaO_2)^{+1}$ and $(KO)^{-1}$ layers and a neutral fluoride with $(MF_2)^0$ and $(KF)^0$ layers. Superlattices with ratios m/l were used where m=l= 1, 2, ..., 8 with alternating *p*- ($Zn^{+2}F_2^{-1}/K^{+1}O^{-2}$) and *n*-type ($Ta^{+5}O_2^{-2}/K^{+1}F^{-1}$) interfaces (see Fig. 6.5). It is observed a considerable increase of the polar distortion of the B-site with respect to the X-site apical planes for all the superlattices. The later can be concluded from Fig. 6.6 for the 7/7 case taken as example. This distortion is larger at the TaO_2/KF and ZnF_2/KO interfaces and then, it is almost constant up to the next interface. The off-centering shows opposite directions for the Ta and Zn respectively, suggesting opposite polarization directions within the $KTaO_3$ and $KZnO_3$ layers.

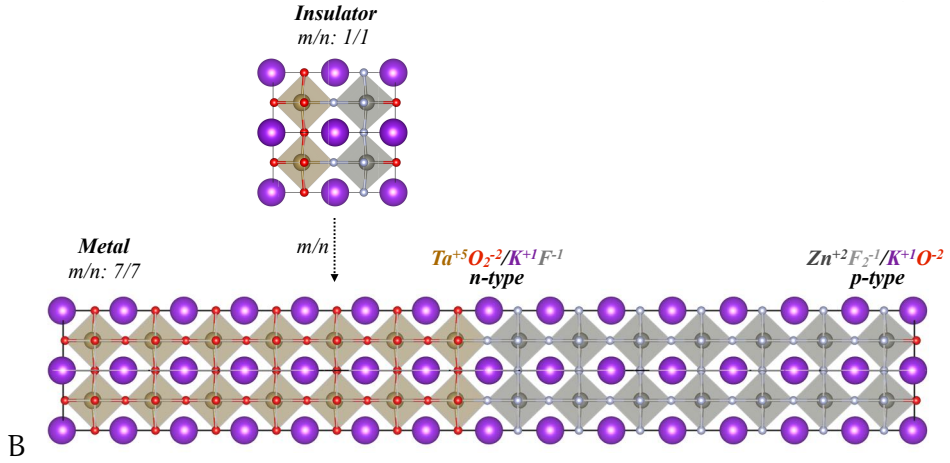

Figure 6.5: 1/1 and 7/7 superlattices at which the insulator-to-metal transitions takes place. The TaO_2/KF and ZnF_2/KO interfaces can be observed.

Additionally, the structural characterization of the superlattices shows a large c-lattice parameter deviation in addition to the large displacements of the B-sites for each oxide and fluoride cases as commented before. For example, the K–K lattice that contains the TaO_2/KF interface (see Figs. 6.5 and 6.6) exhibits a large expansion from 4.05 Å to 4.25 Å as shown in Fig. 6.6. At the same time, the ZnF_2/KO interface induces a strong compression of the lattice parameter from 4.1 Å to 3.9 Å, this can caused by changes in the electronic environment and coordination as discussed in previous oxyfluoride section.

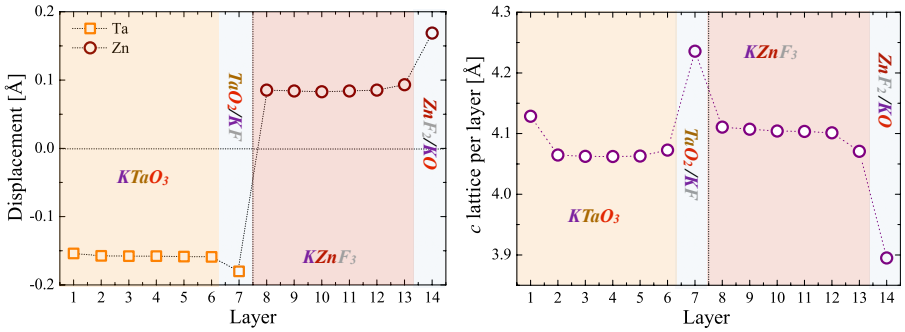

Figure 6.6: Atomic displacements of the B-sites along the z-axis (left) with respect to the oxygen apical plane for the 7/7 superlattice. K–K c-lattice parameter in which, a large expansion and compression can be observed at the TaO_2/KF and ZnF_2/KO interfaces respectively (right).

In order to understand better the effect of the correlation in this superlattice system, we analyzed the electronic structure of the 1/1 superlattice ratio by means of the HSE06 hybrid functional implemented in VASP [55]. We obtained the localized density of states for $KTaO_3/KZnF_3$ and $KTaO_3/KNiF_3$ as shown in Fig. 6.7. For the non-magnetic structure (B= Zn), we noticed that the electronic gap of 3.8 eV is close to the experimental value for the $KTaO_3$ bulk compound (3.58 - 3.79 eV [213]). It can be observed that the valence bands close to the Fermi energy (here at 0 eV by notation) are dominated by oxygen p-orbitals and the fully occupied Zn states lies below -2 eV. The conduction bands are mainly composed by the 5d:Ta orbitals and a small contribution of the oxygen sites due to the p–d hybridization. In the magnetic case (*i.e.* B = Ni) the electronic band gap is still close to the $KTaO_3$ value, besides, the valences states are composed by the O and half occupied Ni states. The empty states are formed by 5d–Ta in addition to the 3d–Ni (e_g) levels.

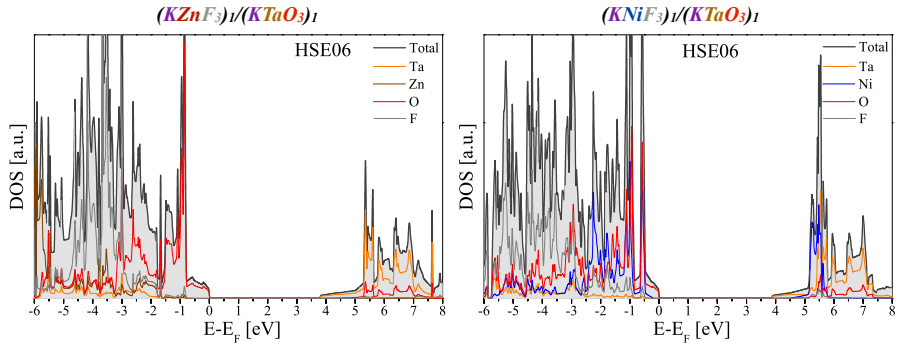

Figure 6.7: Localized density of states for M = Zn and Ni in the 1/1 superlattice ratio obtained considering the HSE06 hybrid functional.

As a next step, we analyzed the magnetic moment per Ni-atom as a function of U (within the GGA+U approach) and we correlated the results with the findings

obtained based in the hybrid functional calculation. We found that the correct electronic structure and magnetic moment is expected for U values above 4.7 eV. Besides, without the use of an U value within the GGA calculations, the unoccupied Ni states are located between the valence oxygen states and the conduction Ta bands, which represents a wrong description of the electronic structure when is compared to the one obtained from the use of the hybrid functional.

Within the hybrid functional calculations, we also found a weak magnetic moment of $m = 0.012\ \mu_B$/atom localized on the Ta cations. These moments are following a FM interaction along z with respect to the Ni sites ordered antiferromagnetically with $m = 1.764\ \mu_B$/atom in agreement with a Ni^{+2}. This is explained by the strongest FM interaction between half-occupied 3d–Ni e_g and the empty 5d–Ta [214] rather that an AFM interaction driven by the super-exchange interaction between the Ni–O–Ta or Ta–F–Ni.

The dynamical and vibrational stability of the 1/1 superlattice was investigated by computing the phonon-dispersion curves. We found no unstable mode in the full Brillouin zone, which suggests a stable structure of the superlattice configuration as shown in Fig 6.5.

6.3.1 *2DEG and 2DHG in $KTaO_3/KBF_3$ superlattices:*

The basic superlattice structure is shown in Fig. 6.5 for B = Zn where alternating n- and p-type interfaces can be appreciated. The insulator-to-metal transition (IMT) is a function of the number of layers taken into account in the calculations. This is in full agreement with the "polar catastrophe" scenario expected from unbalanced charge at the $Zn^{+2}F_2^{-1}/K^{+1}O^{-2}$ and $Ta^{+5}O_2^{-2}/K^{+1}F^{-1}$ interfaces [215]. Then, after several number of layers we found the presence of two-dimensional electron gases (2DEG) and a two-dimensional holes gases (2DHG) in $KTaO_3/KBF_3$ superlattices induced by the polar catastrophe and the local electronic density reconstruction which, is discussed in detail below.

First, we found a decreasing band gap with an increasing of the number of layers in each compound with a stoichiometry $(KTaO_3)_n/(KBF_3)_l$, where n and l are the number of atomic layers in each compound. This occurred mainly due to the electrons and holes donated by each layer at the interface and the compensation of the electrostatic potential generated by the additional electrons in the system due to the O–B–F bondings. The insulator-to-metal transition was observed for the $n = l = 7$ in both cases. It is important to note that the transition is achieved with less polar/non-polar layers than in oxides systems such as $LaAlO_3/SrTiO_3$ in which, the IMT is observed for values above 12/12 ratio [215]. Another point that is important to remark is the localization of the 2DEG and 2DHG (Fig. 6.8) that, according to our results comes from the d_{xy}–Ta and O p-orbital respectively. Thus, the fluoride film is not actively having an effect close to the Fermi energy in the electronic structure and the electrons and holes are only present at the oxide film. Then, the fluoroperovkite film is acting as a "condensating" layer retaining the 2DEG and 2DHG at the oxide layers. Additionally, from the electrostatic point

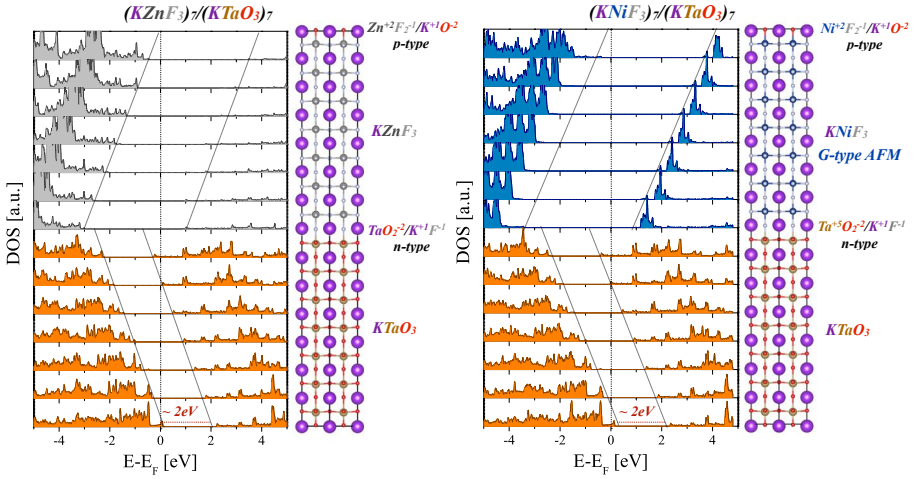

Figure 6.8: Layered revolved DOS for the $KTaO_3/KZnF_3$ and $KTaO_3/KNiF_3$ (7/7) superlattices where a 2DEG and 2DHG are observed at the TaO_2/KF and MF_2/KO.

of view a larger electric field across the entire system was found in both cases in comparison to the LAO/STO oxide/oxide counterpart. For example, when B = Zn: $\mathcal{E}$ = 105 mV/Å against $\mathcal{E}$ = 38 mV/Å [215]. At the metallic interface we observed that the effective masses in both cases (B = Zn and Ni) are close to $0.3m_e$ for the electrons at the 2DEG that lies in the lowest $5d_{xy}$:Ta band. In contrast, heavier hole carriers with m^* of $1.1m_e$ at the 2DHG localized at the p-orbital of the oxygens at the KO layer. Then, in the 2DEG we have a high mobile carriers at the interfaces, lighter that in the $SrTiO_3/LaAlO_3$ [215]. In order to explain the electrostatic behavior and the formation of the 2DEG and 2DHG we presented the Band-edge diagram built for this system in Fig. 6.9. We can see that the conduction fluoride band-edge lies well above the Fermi level, besides, the valence band is almost 500 meV below the Fermi energy. Then, it is again observed that the 2DEG and the 2DHG are localized at the oxide layer.

6.3.2 *Magnetic ordering in $KTaO_3/KNiF_3$ superlattice:*

Now, we study the magnetic ordering as another degree of freedom in the oxyfluorides system for the case of B = Ni. Our results suggest a non-collinear magnetic ordering at NiF_2/KO interface, which resulted in a large net magnetization around 3.5 μ_B/atom near the interface for the 3/3 superlattices at low U values. Nonetheless, for U values above the fitted one ($U > 5$ eV) the magnetic ordering converged to a pure G-type AFM.

The O–B–F bonding is one of the main points and differences with respect to other oxides-based superlattices that completely introduces a new degree of freedom to the oxyfluoride interfaces never explored before. This bonding induces strong differences in the electronic structure and orbital distribution at the in-

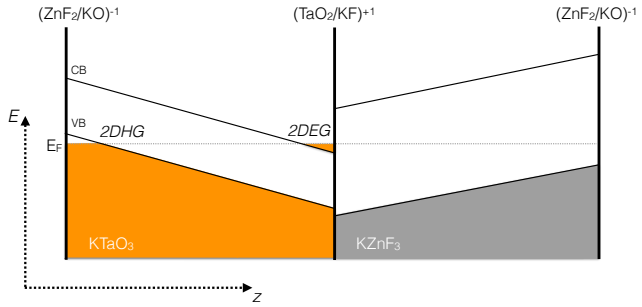

Figure 6.9: Band-edge diagram for the electrostatic behavior of the system where the electric field profile and the 2DEG (2DHG) formation are presented at the oxyfluoride TaO_2/KF (ZnF_2/KO) interface. This was obtained based on the layered resolved DOS (see Fig 6.8). CB, VB an E_F denotes the conduction-band, valence-band and the Fermi energy respectively.

terfaces as it can be observed in Fig. 6.4. In this figure we can see the breaking of the degeneracy of the d-orbitals due to the tetragonal (T) like distortions. Besides, the d-orbital configurations for both types of interfaces can be the source of the particular magnetic behavior. Due to the strong electronic correlation in the partially occupied 5d Ta orbitals and the T Ni states at the interfaces as shown previously, we can see that the magnetic ordering at the interface is changing with respect to the U value. We can observe, for the 3/3 superlattice, that the magnetic state goes from a pure G-type AFM at U=0 eV to a C-type AFM plus a FM layer at the interface for U = 5.0 eV. To get a closer look in the disagreement, calculations based on hybrid functionals were carried out.

In order to corroborate the results related to the magnetic ordering and because of the limitations in the computational efficiency of the calculation with hybrid functionals within the plane-wave expansion, we used the CRYSTAL code. Using this code, we selected three different approaches within the hybrid approximation: B1WC, B3LYP, and PBEsol0. Several magnetic orderings were tested, G-, C-, A-AFM respectively and mixed G-AFM+FM layer (at the NiF_2 immediately after the TaO_2/KF interface and at the NiF_2/KO layer). Nevertheless, according to the calculations the magnetic ordering always converges to the G-type AFM as ground state in the $KNiF_3$ film. These results are in full agreement with those obtained with the GGA+U approximation for U values above 6 eV. However, it is important to mention that the mixed G-AFM+FM-layer (at the NiF_2/KO) state is very close in energy, ΔE = 0.73 meV/atom, closer than other magnetic ground state (*i.e.* A- and C-AFM).

Interestingly, there is a magnetic-moment modulation across de entire thickness of the magnetic counterpart in all the superlattices taken into account. This modulation can be observed in Fig 6.10 where variations between a range of 0.04 μ_B/atom are expected.

Even if a charge-transfer, charge-ordering, and orbital ordering is not achieved in these interfaces due to the small valence deviations at the interfaces (as dis-

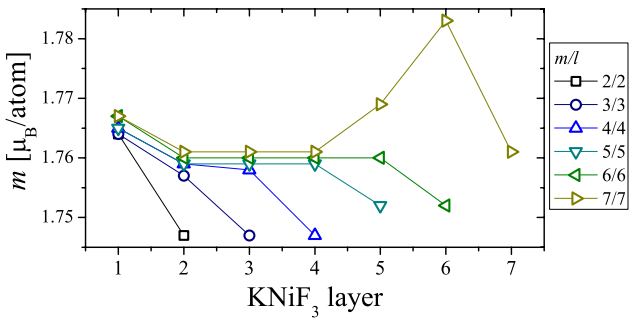

Figure 6.10: Magnetic moment per layer at the $KTaO_3/KNiF_3$ superlattices. A moment modulation can be appreciated when n/l ratio is varied from 2/2 to 7/7.

cussed in the oxyfluoride section) we have to keep in mind that fluorides can be better candidates for a charge-ordering state where a larger charge-disproportion cation is observed [216] in comparison to their oxide counterparts.

6.3.3 *Isolated p- and n- interfaces:*

With the main idea to understand the isolated *p*- and *n*-type interfaces, we have studied both terminations. A KO/ZnF_2 and TaO_2/KF terminated computational cells were used respectively where a KO plane is set at the center as a mirror symmetry plane of the full heterostructure. Then a 12 u.c. was used, 6–$KTaO_3$ and 6–$KZnF_3$ respectively. After full relaxation we have found magnetism and interestingly, this magnetism is coming from two different sources. In the *p*-type interface, p-orbital magnetism has been found in agreement with the electron vacancies and the 2DHG formed at the interface (see Fig 6.11). The magnetic structure shows a AFM-type ordering with $m_{Ta} = 0.018\mu_B$/atom and $m_O = 0.072\mu_B$/atom. On the other hand, in the *n*-type interface a 2DEG is clearly formed as shown in Fig 6.11. This in addition to the d-orbital magnetism coming from the Ta:d_{xy} (see inset in Fig 6.11) orbital in a A-type AFM with a magnetic moment m_{Ta} of $0.066\mu_B$/atom at the surface and a $0.044\mu_B$/atom at the layer right below. From these interfaces it can be noted as well that the effective electron masses for hole and electron carriers are $1.3m_e$ and $0.3m_e$ respectively. Thus, the *n*-carriers are lighter and with a high mobility perfect for electronic applications [217]. It is important to note that the fluoride layer (*i.e.* in this case $KZnF_3$) is not actively participating in the phenomena, however, is acting as insulating-confining layer.

We presented in Fig. 6.12 the bands for the case of the magnetic fluoride layer. We can observe that the carriers in the *n*-type interface are slightly heavier in comparison to the non-magnetic case (*i.e.* $m^* = 0.4m_e$ against $m^* = 0.3m_e$). For the *p*-type case, the hole carrier present almost the same behavior with $m^* = 1.3m_e$. Additionally and surprisingly, in the *n*-type interface we observed a charge-ordering at the third lower layer with respect to the surface. This is concluded

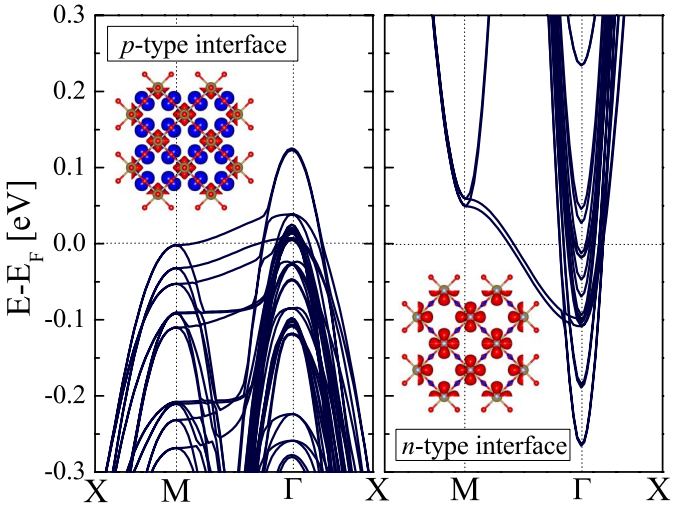

Figure 6.11: Bands structure for the *p*- (left) and *n*-type (right) interfaces along the X–M–Γ–X path in the Brillouin zone for the $KTaO_3/KZnF_3$ system. The formation of the 2DHG and 2DEG at the *p*- and *n*- interfaces can be appreciated.

from a change in the magnetic moment from -1.811 μ_B/atom to 0.034 μ_B/atom suggesting an d^8 – d^6 occupation. This could explain the deeper penetration of the 2DEG below the Fermi level, indicating a larger carrier density in the B = Ni *n*-type interface than in the B = Zn one.

In the *p*-type interface Fig. 6.12, we do not observe a charge-ordering. We found that the magnetism at the $KNiF_3$ remains in its G-type AFM ordering in addition to the p-orbital magnetism. The later is also observed in the oxyfluoride interface explained previously with a non-magnetically active B-site.

In comparison, even when the carriers in the *n*-interface are heavier for B = Ni, it is important to mention that the 2DEG is more pronounced, which in this case lies at −0.5 eV against −0.26 eV for B = Zn. Knowing that the in-plane lattices parameters and polarization across the interface are quite the same, it can be suggested that the charge missing at the $KNiF_3$ layer is transferred directly to the 2DEG increasing the amount of density carriers at the 2DEG in the interface. However, further studies and analysis are needed to explain and exploit this particular behavior in the $KTaO_3/KNiF_3$ *n*-interface oxyfluoride.

6.4 Cubic-Rashba spin-splitting at oxyfluoride interface

Recently it was claimed that in oxide interfaces such as $SrTiO_3/LaAlO_3$ [218, 199, 219, 220] the appearance of spin-splitting and then, a complex spin-texture related to a Rashba-effect [221] is achievable. Besides, some reports have appeared

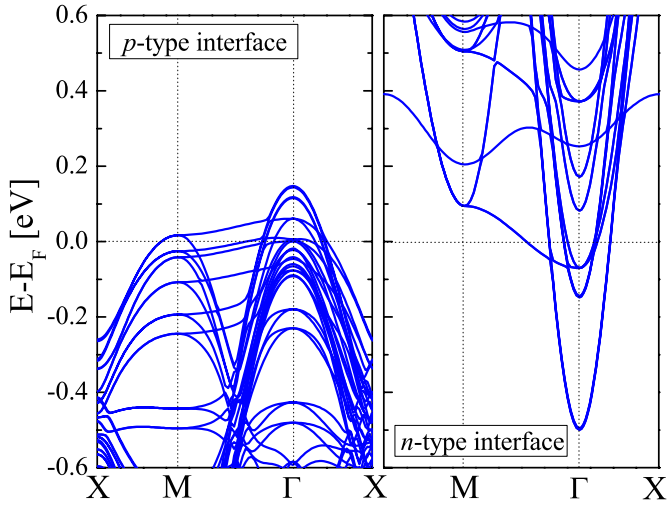

Figure 6.12: Bands structure for the p- (left) and n-type (right) interfaces along the X–M–Γ–X path in the Brillouin zone for the $KTaO_3/KNiF_3$ system. The 2DHG and 2DEG at the p- and n- interfaces can be appreciated. Besides, and empty Ni:e_g band is observed between 0.2 to 0.4 eV respectively.

showing a similar behavior in $SrTiO_3$- and $KTaO_3$-based transistors [222, 223]. Then, for these single perovskite-based devices, a k-cubic dependence of the splitting was found (see Eq 6.1) in contrast to the linear plus cubic dependence of the Rashba splitting at the $LaAlO_3/SrTiO_3$ interface due to the $d_{xy} - d_{xz/yz}$ multiorbital nature of the lowest bands [219]. Additionally, in the case of Au(111) metal surface, it has been shown that even when the surface states exhibit a mainly p–orbital character, the d-orbitals drives the Rashba splitting and dictates the direction of the spin by means of the orbital-angular momentum (OAM) [224, 225]. Therefore, the transition metal d-orbitals at perovskite structures can be the key parameter for a large and controllable electron band splitting in future spintronic and spin-orbitronic devices [224, 226]. This later property gives an additional degree of freedom to the already rich field of multifunctional perovskites. Then, in order to look for the spin-texture and spin-orbit coupling effects in the oxyfluoride interfaces, the analysis of the electronic structure is done by taking into account the SOC. Due to the large computational cost, the study of the bands was performed in the 4/4 superlattice. Notice that these results can be traced up to the 7/7 system where, the 2DEG and 2DHG is formed and the IMT takes place as shown previously. Thus, the results presented here can be extrapolated to larger n/l superlattices. in Fig 6.13 it can be observed the band structure along the k_x path in which, the s_x, s_y, and s_z spin components are presented separately and a colors notation of the up (red) and down (blue) spin was adopted. First, it can be noted that the electronic structure and the spin-texture at the conduction bands above to Fermi level (and thus, close to the TaO_2/KF interface at the 7/7) are entirely 2D spin-polarized at the k_x–k_y plane. Therefore, no band-dispersion is observed for the s_z spin component. Surprisingly, a large spin-splitting of the

bands is appreciated for an energy around $E = 2.0$ eV. Additionally, the SOC effect is observed at the heavy $d_{xz/yz}$ crossing with the d_{xy} lighter bands (see the upper inset in Fig 6.13).

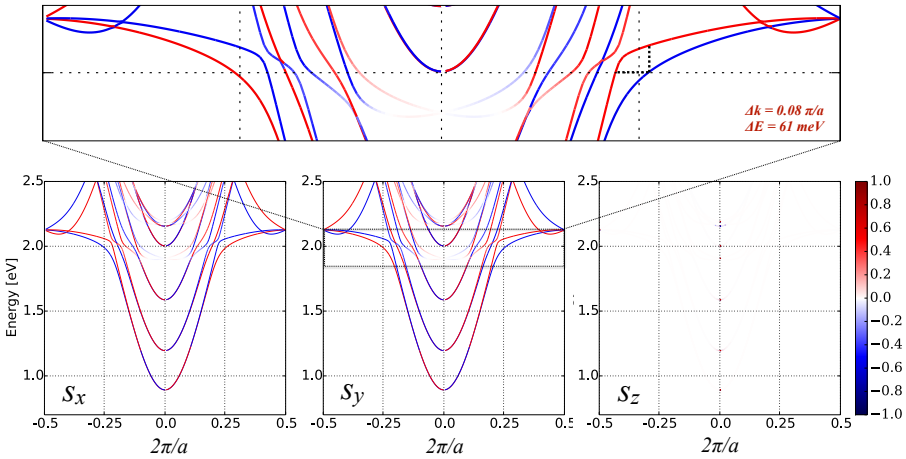

Figure 6.13: Band structure for the k_x path in which, s_x, s_y, and s_z spin components are taken into account. The up and down orientation of the spin are represented by red and blue colors respectively.

The observed Rashba splitting is of the cubic-type character as observed in oxide surfaces and interfaces and is expressed by the Hamiltonian presented in Eq. 6.1:

$$H_{R3} = \alpha_3 \mathcal{E}_z i(k_-^3 \sigma_+ - k_+^3 \sigma_-), \tag{6.1}$$

where α_3 is the cubic-Rashba coupling term which measures the strength of the splitting (in units of eV·Å^3), $\sigma_\pm = 1/2(\sigma_x \pm i\sigma_y)$ and $\sigma_{x,y}$ are the Pauli matrices. The $\mathcal{E}_z$ is the electric field perpendicular to the electron plane movement denoted by $k_\pm = (k_x \pm ik_y)$ [222]. Here, the E vs. k profile for the bands is represented by the relationship:

$$E^\pm(k) = \frac{\hbar^2 k^2}{2m^*} \pm \alpha_3 k^3. \tag{6.2}$$

This type of spin-splitting can be understood like an opposite rotation of the lowest spin–up band with respect of the spin-down around an axis fixed at the vertices of the parabolic d-bands. This is in contrast with the linear horizontal displacement (or offset) of the spin–up and spin–down bands respectively observed in the most common linear-Rashba effect[1] present in materials such as BiTeI [227].

1 The linear-Rashba effect has the E vs. k form: $E^\pm(k) = (\hbar^2 k^2/2m^*) \pm \alpha|k|$ coming from the Hamiltonian of the form $H_R = \alpha \mathcal{E}_z i(k_- \sigma_+ - k_+ \sigma_-)$

In order to get an idea of the order of magnitude of the spin-splitting, we compare it with similar systems as follows. At the energy value of 2.0 eV we found that $\Delta k = 0.044$ Å^{-1} which is more than twice of the one found at the $KTaO_3$-based transistor (*i.e.* Au/parylene-Al/$KTaO_3$) [217]. Besides, the vertical energy difference between the up and down spins is $\Delta E = 64$ meV at the same bands as shown in Fig 6.13. In comparison with an oxide/oxide interface we computed the spin-texture of the $SrTiO_3/LaAlO_3$ system under the same conditions in a $4/4$ superlattice. We found that $\Delta k = 0.011$ Å^{-1} and a $\Delta E = 11$ meV. Then, this spin-splitting is four-times smaller in comparison to 0.044 Å^{-1} and 64 meV at the oxyfluoride interface.

Going further and with the aim to understand these results we first computed the spontaneous polarization, which is directly related to the electric field $\mathcal{E}_z$ in Eq. 6.1. The layer-by-layer polarization is presented in the Table 6.2. It is observed that the polarization is in average close to -2.8 μC·cm^{-2} per KTO layer. For this case, $n = l = 4$, the total polarization is -11.14 μC·cm^{-2} at the oxide side. Moreover, the polarization is in the opposite direction of the fluoride layer with a value of $+5.35$ μC·cm^{-2}. Then, at the end, a total polarization of -5.79 μC·cm^{-2} is still present along the entire superlattice structure. This big difference suggests that the depolarizing field is not enough to compensate the polarization along the entire supercell. Besides, the opposite directions of the polarizations is explained in the breaking of symmetry due to the O–M–F bonding along z. Therefore, by increasing the number layer (*i.e.* the n/l ratio), the $KTaO_3$ polarization will increase and then, is expected that the spin-splitting will be incremented directly it is in agreement with the Eq 6.1. Ultimately, it is important to note that the SOC coupling in the Ta is at least 11 times larger that the one in the Ti cation. This can be taken as advantage in the mixed oxide/fluoride interfaces due to the large lattice parameters of the fluorides perovskites that allows the incorporation of bigger perovskite oxides with 5d orbitals in novel superlattices and interfaces with mixed properties.

Table 6.2: Layer-by-layer spontaneous polarization along the z-axis (P_z in μC·cm^{-2}) in the $4/4$ superlattice is shown. Besides, the oxide and fluoride polarizations are P_{KTaO_3} = -11.14 μC·cm^{-2} and P_{KZnF_3} = 5.35 μC·cm^{-2} respectively.

	KTaO$_3$				*KZnF$_3$*			
Layer	1	2	3	4	5	6	7	8
P_z	-2.85	-2.52	-2.72	-2.86	1.43	1.15	1.20	1.58

From the magnetic superlattice, $KTaO_3/KNiF_3$ we noticed that the same spin-texture remains at the TaO_2/KO. Nonetheless, the spin-texture is becoming more complex due to the overlapping of the 5d:Ta band with the unoccupied $3d(e_g)$:Ni states above the Fermi level.

It is important to take advantage of the fact that the magnetic properties can be conserved in the $KNiF_3$. Then, a mixed multifunctional properties of

2DEG+2DHG+k^3-Rashba-splitting+G-AFM are condensed in the same heterostructure where a possible A-site driven ferroelectricity can be engineered in systems such as $KTaO_3/NaMnF_3$.

It is also important to remark that the relevance of the k^3-Rashba dependence has been highlighted in the field of multifunctional properties based in the significant difference in the effective field symmetry between the k-linear and the k^3 Rashba. Thus, the k^3 symmetry influences all of the SOC related phenomena in materials, which, is not the case of the the k-linear Rashba term. For example, in case of the spin Hall effect, it has been predicted the k-cubic Rashba term can give rise to a larger spin Hall conductivity [228, 229].

The possible tuning of the energy position of the 5d:Ta bands with respect of the Fermi energy by controlling the n/l ratio stand as an additional feature of these systems. Therefore, the amount of splitting and consequently, the spin-transport properties can be tuned as well. The later making even more interesting and appealing this type of interfaces.

6.5 Charge-ordering, magnetism, and ferroelectricity in $LaScO_3/NaMnF_3$ superlattice

As demonstrated for the multiferroic properties in $NaMnF_3$ and the electronic properties in superlattices and interfaces of $KTaO_3/KBF_3$, in fluoride-based systems, the tuning of properties can be achieved independently. For example, the FE order in the $NaMnF_3$ is tuned by epitaxial strain and driven by the A-site, meanwhile the magnetism is raised from the B-site avoiding the d^0-ness rule. Another example of this behavior is the magnetic properties that remains in the $KNiF_3$ and the 2DEG and 2DHG localized at the $KTaO_3$ in the $KTaO_3/KNiF_3$ heterostructure. Then, an additional effort was carried out in order to tune several properties into a single superlattice. This is the case of the $LaScO_3/NaMnF_3$ system where MF/ME and 2DEG can be expected coming from the fluoride and oxide layer respectively.

In this heterostructure, we used at the beginning the ground state at room conditions of both perovskites. Both belongs to the orthorhombic *Pnma* (space group No. 62) for which, experimental lattice parameters of a = 5.791 Å (5.548 Å), b = 8.095 Å (5.751 Å), and c = 5.680 Å (8.008 Å) were used for the $LaScO_3$ ($NaMnF_3$) in the calculations. Then, an equivalent strain of 2.4% and 0.7% for the a- and c-axis is expected respectively at the interface. This due to the approach in superlattices for which the ac-plane is fixed to the average between the lattice parameters of the two compounds for each axis.

As a starting point, we begin the analysis with the 7/7 superlattice. For this superlattice ratio after full electronic relaxation (with $U = 6$ eV at the Mn cation), an insulator state remains with an electronic band gap close to 500 meV was observed. We expect an IMT above the 8/8 superlattice, in which, according

to the previous results an interesting spin-texture and spin-splitting should be observed at the Sc d-orbitals.

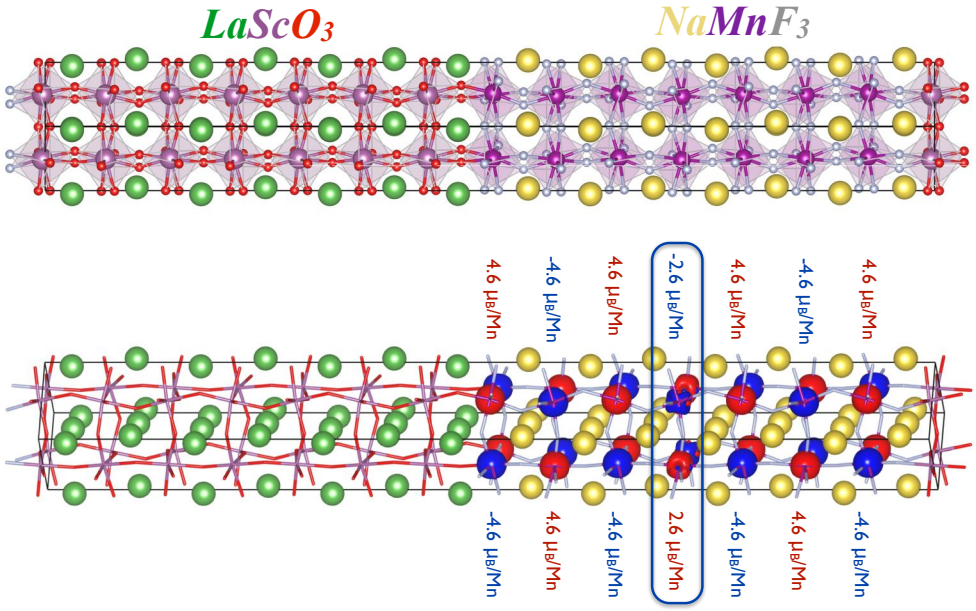

Figure 6.14: $LaScO_3/NaMnF_3$ (7/7) superlattice. The AFD distortions and rotations can be observed in the upper figure in which the KO/MnF_2 and ScO_2/KF interfaces can identified. In the lower figure it is shown the spin-polarized charge density, red and blue colors denote the up and down magnetic moment directions. The G-type AFM ordering is observed as well as the CO state.

The results shows a charge-ordering (CO) state found at the middle Mn layer in the fluoride $NaMnF_3$ part (see Fig. 6.14). The CO state is demonstrated by a change in the magnetic moment from 4.6 μ_B/atom to 2.6 μ_B/atom as shown in Fig. 6.14. This moment difference suggests an d^5 – d^3 Mn occupation. Nonetheless, for a $U = 4$ eV (value normally used in Mn at oxides and fluorides [1, 2, 3]), the CO-state remains but now, the magnetic moment at the middle of the layer goes from 2.6 μ_B/atom to 0.9 μ_B/atom. The later claims for a deeper study and understanding of the exchange-correlation in this particular oxyfluoride. We observed that this CO state remains after several U values (from 4 to 7 eV). Besides, the main magnetic ordering exhibit a G-type AFM after testing several possible states (*i.e.* G-, C-, and A-type AFM and FM).

The analysis of the spontaneous polarization reveal values of $P_z = 15.45\ \mu C{\cdot}cm^{-2}$ and $P_{xy} = 2.41\ \mu C{\cdot}cm^{-2}$. Here, the P_z is induced by the symmetry breaking at the KO/MnF_2 and ScO_2/KF interfaces and the F–Mn–O and O–Sc–F bondings respectively as can be seen in Fig. 6.14. This polarization cannot be reversed, nonetheless, can be used to enhance the polar catastrophe phenomena and tune the 2DEG as demonstrated in $SrTiO_3/PbTiO_3$ [230], in this interface the polar catastrophe is neglected due to the neutral character of the atomic layers. How-

ever, the ferroelectric polarization along the PTO layer induce a 2DEG. It is important to note that possibly this polarization can be coupled with the strain-induced P_z in the $NaMnF_3$ as shown in the Chapter 5. The P_{xy} component is explained in terms of the hybrid-improper FE phenomena where different A-sites at the orthorhombic interfaces brakes the anti-polar displacements and a net polarization can be obtained in the xy-plane [202]. This type of displacements can be observed in the Table 6.3 in which are presented the atomic displacements per layer at the xy-plane

Table 6.3: A-site displacements per layer in the xy-plane taking the high-symmetry position in the cubic symmetry as reference. Displacements in Å units.

$LaScO_3$						
−0.27	+0.23	−0.28	+0.24	−0.27	+0.25	−0.29

$NaMnF_3$						
+0.22	−0.27	+0.24	−0.25	+0.27	−0.21	+0.24

This preliminary results are very promising but further studies are needed in order to unveil the geometric+hybrid-improper ferroelectricity in these superlattices. Besides, the possible coupling of the FE with the CO-state and the magnetic degrees of freedom needs to be investigated.

The n/l ratio effect for several n and l values and the study of the 2DEG above the 8/8 superlattice ratio is on their way.

6.6 Conclusions

We have analyzed by means of first-principles calculations the electronic and structural properties of oxyfluorides $(KTaO_3)_n/(KBF_3)_l$ B = Zn and Ni interfaces. We found that the orbital levels symmetry at the interfaces is strongly modified as a function of the O–B–F coordination. The polar catastrophe phenomena also takes place in the oxyfluoride interfaces, however, we found that less number of layers are needed in order to achieve the insulator-to-metal transition. We observed that the magnetism in the $KTaO_3/KNiF_3$ exhibits a moment magnitude modulation. Nevertheless, the magnetic structure keeps the G-type AFM such as in the bulk former compound. Surprisingly, we observed a large k^3-Rashba type splitting in at the oxyfluoride interfaces, at least four times larger than the one reported in $SrTiO_3/LaAlO_3$ interface and twice of the $KTaO_3$-based transistor.

Looking for novel oxyfluoride multiferroics, the $LaScO_3/NaMnF_3$ was studied. This interface show promising preliminary results where charge-ordering, G-type AFM, hybrid-improper ferroelectricity and possible tuning of the electronic band

gap by means of the polar-catastrophe can be achieved.

7

CONCLUSIONS AND PERSPECTIVES

In this thesis we have explored several aspects of fluoride-perovskites, for which we have employed state of the art first-principles calculations. The main achievements of this work were: i) To understand the vibrational properties of fluoride perovskites. ii) To analyze the effect of external agents as the pressure and biaxial strain. iii) To study novel oxide/fluoride interfaces and understand their properties. Therefore, in this investigation we have particularly found that:

The fluoride-perovskites ABF_3-type materials (A = Li and Na, B = Ca, Zn, Mn, Ni, and V) exhibit a huge potential to be ferroelectric with a large polar instability. This ferroelectricity, at first glance potentially similar to that of oxide perovskites, revealed to have a different origin, being based on a A-site geometric instability. On the top of ferroelectricity, this is suggesting the possibility to find new multiferroics within the fluoride family. We then predicted that this could indeed be realized in $NaMnF_3$ thin films under appropriate epitaxial strain. In these films, we discovered an unprecedented non-linear polarization/strain coupling, related to the geometric origin of ferroelectricity. We have predicted that the strained $NaMnF_3$ can exhibit a unique multiferroic state driving large and uncommon second-order piezoelectric and non-linear magnetoelectric responses. In a close collaboration with experimentalists, this fluoroperovskite has been successfully grown and its multiferroic properties are under experimental confirmation. Interestingly, we observed that the strong nonlinear polarization-strain coupling is only observed for the steric geometric FE crystals, which confirms that this property is unique to geometric FE systems. The latter conclusion extracted when comparing the geometric FE $BaCoF_4$, the regular FE $BaTiO_3$, and improper FE $PbTiO_3/SrTiO_3$ superlattice.

Independently, based on DFT calculations and symmetry analysis, we have also shown that ABX_3 post-perovskite phases, with an active magnetic B-site cation, have the possibility to present a non-collinear magnetic behavior. With these findings, we clarified some of the magnetic properties experimentally observed in this particular high-pressure form of perovskites found in the Earth's mantle. Additionally, we identified a similar perovskite to post-perovskite's transition in $NaMnF_3$ under isotropic pressure, yielding a phase in which the non-collinear ferromagnetism shows a large canted magnetization.

We have also analyzed from first-principles the electronic and structural properties of oxyfluorides $(KTaO_3)_n/(KBF_3)_l$ superlattices (B = Zn and Ni). We found that the orbital splitting at the interfaces is strongly dependent of the O–B–F coordination. Moreover, a polar catastrophe phenomena, similar to that reported at the $LaAlO_3/SrTiO_3$ interface, also takes place in the oxyfluoride polar interfaces. We observed that the thickness required to achieve the insulator-to-metal transition is however smaller than in the oxides. We observed that the magnetism in the $KTaO_3/KNiF_3$ system exhibits a modulation of the magnetic moment amplitude across the entire superlattices. Surprisingly, we reported a large k^3-Rashba-type splitting at the oxyfluoride interfaces, at least four times larger than that reported in $SrTiO_3/LaAlO_3$ interface and twice that of the $KTaO_3$-based transistor.

As demonstrated for the multiferroics properties in the $NaMnF_3$ and the electronic properties in superlattices and interfaces of $KTaO_3/KBF_3$, in fluoride-based systems, the tuning of properties can be achieved independently. For example, the FE in the $NaMnF_3$ is tuned by the A-site and the magnetism from the B-site avoiding the d^0-ness rule. Another example of this behavior is the magnetic properties that remains in the $KNiF_3$ and the 2DEG and 2DHG localized at the $KTaO_3$ in the $KTaO_3/KNiF_3$ system. Then, an additional effort was carried out in order to tune the magnetic and electric properties. This is the case of the $LaScO_3/NaMnF_3$ systems in which, MF/ME and 2DEG can be expected from the fluoride and oxide layer respectively.

On the side of what we presented in the main manuscript we also performed side projects that are presented in the Appendices. In Appendix C, we present the study of the multiferroic behavior of $BaCoF_4$ thin films under epitaxial strain where we found a non-linear dependence of the spontaneous polarization as a function of the external constrain. Besides, several magnetic transitions were explained in terms of the non-collinear magnetic ordering. In Appendix D we present a study of the electronic and particularly, spin-texture properties of the $SrBO_3$ (001) with B = Ti and Hf surfaces. We found a tangible Rashba-type splitting for B = Hf, besides, despite the reported giant-splitting for B = Ti, we did not found such spin-splitting. Finally, in Appendix E we report the insulator-to-metal transition control and tuning at the $LaAlO_3/SrTiO_3$ interface by means of OH and H molecules implantation at the $LaAlO_3$ surface.

Additional perspectives of this work cover also the field of superconductivity based in the mixed valence of the oxyfluorides [231]. For example, this is the case of the superconductivity in oxyfluorides such as $Sr_2CuO_2F_{2+\delta}$ [208, 232] where the Cu present a valence close to +(2-δ) and has a mixed octahedral coordination in a Cu-O_4F_2 octahedra. Then, we believe that it is possible to achieve a high-T_c superconductor in systems such as $KTaO_3/KCuF_3$ and/or $LaCuO_3/KCuF_3$. In these systems, higher T_c than the one found in $KTaO_3$ (T_c = 57 mK [233]) could be obtained. Additionally to superlattices, thin films can be also analyzed

in order to study the surface effects and the isolated interfaces that are formed depending on the chosen substrate. For example future studies can be focused on $SrTiO_3(001)/NaMnF_3(010)$ and $LaMnO_3(010)/NaMnF_3(010)$ thin films.

Finally, we believe that the discovery of new multiferroic materials could lead to new possible solutions for the challenges in the field, even though the present result does not fully achieve the "ideal" target of room temperature magnetoelectrics. Moreover, we hope that the results we have presented in this thesis will motivate further theoretical and experimental studies in the search of new and exotic multifunctional properties in fluoride and oxyfluoride-based perovskites.

CONFERENCES AND MEETINGS

In the next section are listed the conferences and meeting in which, the thesis results were presented:

– XIII Meeting on Ferroelectricity, Talk: *Novel magnetoelectric and non-linear ferroelectricity-strain coupling in $NaMnF_3$ fluoroperovskite*, Porto, Portugal, from 26 June to 3 of July, 2015.

– VI Workshop Chile-México about Magnetism, Nanoscience and their Applications, Talk: *Unexpected Large Canting and Non-collinear Magnetism in Fluoride-Perovskites ABF_3 by First-principles*, Cancún, from 21 to 23^{th} of May, México, 2014.

– 2014 Workshop on Fundamental Physics of Ferroelectrics, Talk: *Geometric Ferroelectricity in Fluoro-Perovskites*, Washington DC, from 25 to 29th of January, USA, 2014.

– Invited talk: *Multiferroic Phenomena with Geometry Ferroelectricity in Fluoroperovskites*, Physics Department, West Virginia University, USA, February 7^{th}, 2014.

– Response Treatment for Dynamical Properties of Materials with the ABINIT Package, Zürich, from 22 to 26^{th} of October, Switzerland, 2012.

– IV Workshop Chile-México about Magnetism, Nanoscience and their Applications, México-City, from 18 to 21^{th} of March, México, 2012.

Part V

APPENDIX

The next appendix list condenses the work related to scientific collaborations that lead to an important learning in my PhD formation but, that are not directly related with the main topic of the thesis. Nonetheless, the study keep its focus on the electronic structure of fluorides and some perovskites.

A

OVERVIEW OF THE MAGNETIC INTERACTIONS IN FLUOROPEROVSKITES

Now that we have explored the vibrational landscape of the fluoroperovskites, we move forward by analyzing the magnetic behavior in these materials. As it is well known, most of the fluorides perovskites present a magnetic ordering due to their 3d B-site magnetically active cation. We focus in this section on the non-collinear magnetism, weak-FM interaction due to a magnetic canting. First, in the Table A.1 we present the weak magnetic moment for several oxides and fluoride perovskites most of them in the orthorhombic *Pnma* structure, except for the $RbFeF_3$. In this space group, the magnetic ordering exhibit a non collinear $G_zA_xF_y$ configuration, which corresponds to a G-type AFM along the z-axis, and A-type AFM along x and a weak-FM along y.

Table A.1: Magnetic canted moment F_y (μ_B/atom) at low temperature in *Pnma* ABF_3 systems. The large magnetic canting for fluorides compounds can be noted in the $G_zA_xF_y$ configuration. The ionic radius of the magnetic B-site (r_B) was taken into account the valence state and the bonding coordination [98].

Compound	F_y		Structural parameters		
ABX_3	U=0 eV	Exp. [234]	d-Occ.	r_B [pm]	ϕ^a [deg]
$KMnF_3$	0.002	0.004	d^5	97	9.70
$NaNiF_3$	0.039	0.058	d^8	83	17.37
$NaCoF_3$	—	—	d^7	88.5	17.93
$NaFeF_3$	0.043	0.125	d^6	92	18.53
$NaMnF_3$	0.410	—	d^5	97	19.06
$RbFeF_3$ [b]	—	0.270	d^6	92	—
$CaMnO_3$	0.036	0.040	d^3	67	10.68
$LaFeO_3$	0.035	0.044	d^5	78.5	11.20
$YCrO_3$	0.050	0.033	d^3	75.5	18.30

a Computed form experimental lattice parameters.
b $RbFeF_3$ in hexagonal structure [88].

In Table A.1 is presented a summary of the weak-FM component, experimental and computed in oxides and fluorides. Here are also included the d-orbital

Table A.2: Experimentally reported exchange interaction (J) constants in ABF_3 compounds [234]. The components of the DM vector are in meV.

ABX_3	J_1	J_2	Structure
$KMnF_3$	0.327	0.010	$Pnma$
$KFeF_3$	0.603	—	$Pm\bar{3}m$
$KNiF_3$	2.929	—	$Pm\bar{3}m$
$KCuF_3$	16.372	0.017	$I4/mcm$
$NaFeF_3$	0.434	0.417	$Pnma$
$NaMnF_3$	0.198	0.155	$Pnma$
$LaFeO_3$	6.74	6.83	$Pnma$
$BiFeO_3$	6.52	6.68	$R3c$

occupation, B-site radii, and the tilt angle, ϕ. For fluorides it can be noted that the rotation angle are almost twice of the ones found in the oxides (see Fig. A.1). Additionally, the weak-FM follows a trend with the octahedral angle: higher is the angle, larger is the F_y magnetic moment. At the same time, the octahedral rotation increases when the B radii does it is shown in Table A.1. The later magnetic behavior is in agreement with the Dzyaloshinskii-Moriya interaction [156, 157], then: $D_{ij} \propto \hat{x}_i \times \hat{x}_j$ where $\hat{x}_{i,j}$ are the unitary vector along the M–X–M bondings. We can observe the reported weak-FM component for the $NaFeF_3$ is rather large, around 0.125 μ_B/Fe, following the rotation and radii trend. Therefore, the expected F_y component in the $NaMnF_3$ should be around 0.2 μ_B/Fe, which is one order of magnitude large that the ones found in perovskite oxides. Unfortunately, the computed values are not in well agreement with the reported experimental moments. Then, a careful research within the DFT+U+J needs to be carried out in future studies. The $RbFeF_3$ compound shows the largest F_y component, nonetheless, its ground state belongs to an hexagonal structure and the structural differences needs to be taken into account in the analysis.

As expected from the weak covalent bonding in fluorides, comparing with oxides, the exchange-constants, J_i are smaller by at least one order of magnitude as it is presented in Table A.2. The $KCuF_3$ compound exhibit a quite large J_1 component due to the Jahn-Teller distortion presented in the partially occupied d^9-orbital. Surprisingly, the $KNiF_3$ shows large exchange interaction. These low exchange interactions can explain the low magnetic transition temperatures observed in fluoride perovskites. Therefore, even when the wake ferromagnetism tend to be larger than in oxides, the temperature regime for this particular magnetic behavior seems to be very low. The later statement needs to be taken into account in the application of these type on materials in further technological applications. Nonetheless, compound with several phenomena, such as the Jahn-Teller

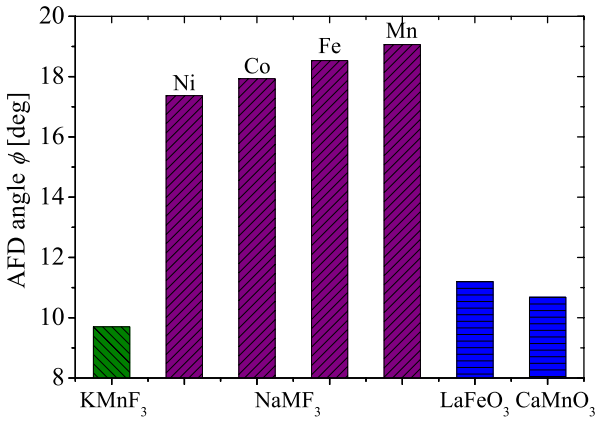

Figure A.1: Octahedral rotation ϕ for several oxides and fluorides compounds. The fluoroperovskites are ordered according to the B-site radii.

distortion can be used in order to increase the magnetic exchange interactions, and then, the magnetic transition temperatures.

B

GROUP THEORY ANALYSIS TO THE NON-COLLINEAR MAGNETISM IN PPV

The first step into the analysis is to identify the space group and its point group. In the case of the post-perovskites we have a *Cmcm* space group (No. 63) with a D_{2h} point group, this point group have the symmetry operations: I, $-I$, 2_z, 2_y,2_x, m_z, m_y, and m_x extracted from the Bilbao Crystallographic Server [147, 148]. Then, we have:

$$
\begin{aligned}
I &= \begin{bmatrix} 1 & 1 & 1 \end{bmatrix} \\
-I &= \begin{bmatrix} -1 & -1 & -1 \end{bmatrix} \\
2_z &= \begin{bmatrix} -1 & -1 & 1 \end{bmatrix} + \tau(0,0,1/2) \\
2_y &= \begin{bmatrix} -1 & 1 & -1 \end{bmatrix} + \tau(0,0,1/2) \\
2_x &= \begin{bmatrix} 1 & -1 & -1 \end{bmatrix} \\
m_z &= \begin{bmatrix} 1 & 1 & -1 \end{bmatrix} + \tau(0,0,1/2) \\
m_y &= \begin{bmatrix} 1 & -1 & 1 \end{bmatrix} + \tau(0,0,1/2) \\
m_x &= \begin{bmatrix} -1 & 1 & 1 \end{bmatrix}
\end{aligned}
$$

Additionally to all the previous operations, a translational operation of $[\tau(1/2, 1/2, 0)]$ needs to be applied in order to obtain the total of 16 allowed symmetry operations. Now, we note that in our unit cell we have four different magnetic sites at the crystallographic positions as follows:

Table B.1: Crystallographic positions of the magnetic cations, M at the post-perovskite *Cmcm*.

Atom	M_1	M_2	M_3	M_4
Coordinate	(0, 0, 0)	(0, 0, 1/2)	(1/2, 1/2, 0)	(1/2, 1/2, 1/2)

Now, we analyze how the magnetic sites transform under the allowed symmetry operations it can be observed that, for example, the M_1 cation transforms to the M_2 under the 2_z operation as follows:

$$2_z \cdot \mathbf{M_1} = \begin{bmatrix} -1 & 0 & 0 \\ 0 & -1 & 0 \\ 0 & 0 & 1 \end{bmatrix} \cdot \begin{bmatrix} 0 \\ 0 \\ 0 \end{bmatrix} + \begin{bmatrix} 0 \\ 0 \\ 1/2 \end{bmatrix} = \begin{bmatrix} 0 \\ 0 \\ 1/2 \end{bmatrix} \equiv \mathbf{M_2} \tag{B.1}$$

Therefore we have that all the magnetic sites transforms under the symmetry operations as follows obtaining the Table B.2:

Table B.2: Transformation of the magnetic sites under the symmetry operations. The numbers in the table are the i index of the M_i magnetic cation.

	I	2_z	2_y	2_x	$-I$	m_z	m_x	m_x
M_1	1	2	2	1	1	2	2	1
M_2	2	1	1	2	2	1	1	2
M_3	3	4	4	3	3	4	4	3
M_4	4	3	3	4	4	3	3	4
$+ \tau(1/2, 1/2, 0)$								
M_1	1	4	4	3	3	4	4	3
M_2	2	3	3	4	4	3	3	4
M_3	3	2	2	1	1	2	2	1
M_4	4	1	1	2	2	1	1	2

Here, at this point, we know how the magnetic sites transform under the symmetry operations. We now proceed with the analysis of the magnetic moments transformation. For this purpose, we have to define the possible magnetic configurations into the collinear level. The selected notation is F for ferromagnetic, and A, C, and G for A-, B- and G-type antiferromagnetic orderings. Then, we have:

In Table B.3 the + and − signs are for up and down spin orientation respectively. We proceed by calculating how the spin transforms under the same symmetry operations such as the magnetic sites does. Therefore, we have to include the non-collinear orderings by defining the spin pseudo-vector such as $\mathbf{s} = (s_x, s_y, s_z)$. Due to the pseudo-vector character of the spin and in order to understand how it transforms, we need to be defined such pseudo-vector as the product of $\mathbf{A}$ (where $\mathbf{A} = (x, y, z)$) and $\mathbf{B}$ (with $\mathbf{B} = (x',y',z')$) as follows: $\mathbf{s} = \mathbf{A}\times\mathbf{B}$. Then, $\mathbf{s} = (yz' - zy',\ zx' - xz',\ xy' - yx')$.

Table B.3: Definition of the different magnetic orderings. The G, A-, and C-type antiferromagnetic orderings and the ferromagnetic F state are defined for each magnetic cation where + and − denoted up and down spin orientations.

	M_1	M_2	M_3	M_4
F	+	+	+	+
A	+	+	−	−
C	+	−	+	−
G	+	−	−	+

To exemplify how proceed, we show how the spin will transform under the 2_z operation as follows:

$$2_z \cdot \mathbf{s} = \begin{bmatrix} -1 & 0 & 0 \\ 0 & -1 & 0 \\ 0 & 0 & 1 \end{bmatrix} \cdot \begin{bmatrix} yz' - zy' \\ zx' - xz' \\ xy' - yx' \end{bmatrix} = \begin{bmatrix} -yz' + zy' \\ -zx' + xz' \\ xy' - yx' \end{bmatrix} \equiv \begin{bmatrix} -1 \\ -1 \\ +1 \end{bmatrix} \cdot \mathbf{s} \tag{B.2}$$

Then, after applying to all the operations we have that the spin transforms as condensed in Table B.4. It is important to note that the **s** transforms under the −I as $-\mathbf{s} = \mathbf{B}\times\mathbf{A}$. Nonetheless, the spin must be exchanged and undistinguible, therefore, it transforms in the same way for the −I as for the I symmetry operation. The later statement is also valid for the m_z, m_y, and m_x.

Table B.4: Transformation s_x, s_y, and s_z spin orientations under the symmetry operations. The transformation of each magnetic ordering under each symmetry operation is labeled as +1 and -1, which indicates when the ordering is invariant under the related transformation (*i.e.* +1) or when it is reversed under the application of the symmetry operation (*i.e.* −1).

	I	2_z	2_y	2_x	I	m_z	m_y	m_x
s_x	+1	−1	−1	+1	+1	−1	−1	+1
s_y	+1	−1	+1	−1	+1	−1	+1	−1
s_z	+1	+1	−1	−1	+1	+1	−1	−1

Finally, to obtain how the non-collinear magnetic orderings transforms we take the Tables B.2, B.3 and B.4. The symmetry characters are obtained as follows: For example, for the C_x component under the 2_z operation, originally −1 from Table B.4, we see, from Table B.2, that the M_1 transforms into M_2, and then looking at Table B.3 we observed that changes from + to −. Therefore, the C_x under the 2_z symmetry operation is reversed and +1 is obtained. The characters for each ordering along each Cartesian axis are presented in the Table B.5.

Table B.5: Transformation of the magnetic ordering under the allowed symmetry operations.

	I	2_z	2_x	2_x	$-I$	m_z	m_y	m_x	
F_x	+1	−1	−1	+1	+1	−1	−1	+1	B_{3g}
F_y	+1	−1	+1	−1	+1	−1	+1	−1	B_{2g}
F_z	+1	+1	−1	−1	+1	+1	−1	−1	B_{1g}
A_x	+1	−1	−1	+1	+1	−1	−1	+1	B_{3g}
A_y	+1	−1	+1	−1	+1	−1	+1	−1	B_{2g}
A_z	+1	+1	−1	−1	+1	+1	−1	−1	B_{1g}
C_x	+1	+1	+1	+1	+1	+1	+1	+1	A_g
C_y	+1	+1	−1	−1	+1	+1	−1	−1	B_{1g}
C_z	+1	−1	+1	−1	+1	−1	+1	−1	B_{2g}
G_x	+1	+1	+1	+1	+1	+1	+1	+1	A_g
G_y	+1	+1	−1	−1	+1	+1	−1	−1	B_{1g}
G_z	+1	−1	+1	−1	+1	−1	+1	−1	B_{2g}

By re-grouping the orderings into the same symmetry character we obtain the Table B.6.

Table B.6: Magnetic ordering allowed in the *Cmcm* structure according to the D_{2h} point group [147, 148].

Magnetic Ordering	I	2_y	2_y	2_x	$-I$	m_z	m_y	m_x	
F_x, A_x	+1	−1	−1	+1	+1	−1	−1	+1	B_{3g}
F_y, A_y, C_z, G_z	+1	−1	+1	−1	+1	−1	+1	−1	B_{2g}
F_z, A_z, C_y, G_y	+1	+1	−1	−1	+1	+1	−1	−1	B_{1g}
C_x, G_x,	+1	+1	+1	+1	+1	+1	+1	+1	A_g

To obtain the possible non-collinear states we take into account the superexchange interaction in order to avoid unprovable orderings. Besides, we neglect the ferrimagnetic orderings. Then, finally we have that the allowed states are C_zF_y, C_zA_y, C_yF_z and G_yA_z.

For more details in the group theory analysis applied to the non-collinear magnetism the reader can check the Ref. from Bertaut [235].

C

$BaCoF_4$ THIN FILMS

The orthorhombic fluoride family $BaMF_4$, with M = Mn, Fe, Co, Ni, and Zn [236, 237, 238] was intensively studied four decades ago [18] due to their interesting multifunctional properties and physics discovered. These fluorides exhibit simultaneously antiferromagnetic and ferroelectric long-range orders. While the antiferromagnetic order has a pronounced two-dimensional character, the ferroelectricity mechanisms are fundamentally different from the "classical" charge-transfer phenomena widely known in ferroelectric perovskites oxides such as $BaTiO_3$ and $PbTiO_3$ [82, 81]. Recently, new theoretical analysis [17, 239] that includes a predicted magnetoelectric effects present in some of those materials (for example in $BaNiF_4$) motivated further experimental studies on those multiferroic systems. As commented before, the $BaMF_4$ compounds crystallize in orthorhombic lattice with the space group $Cmc2_1$ No. 36 [88]. In this structure, a shared-corners distorted fluorine octahedra $M–F_6$ in the ac-plane form puckered sheets, which are separated by Ba layers along the crystallographic b-axis [88, 239]. A few years ago was theoretically described the ferroelectric long range order for the family members M = Mn, Co, Fe and Ni which has its origin in a combination of octahedral rotations in $M–F_6$ and polar displacements of Ba cations, in a so-called geometric proper ferroelectricity [239] making it very appealing to tune multifunctional properties. Previous experimental reports have revealed ferroelectric switching in two members of the family, $BaCoF_4$ and $BaNiF_4$ with ferroelectric saturation polarization along the a-axis and P_s = 8.0 $\mu C \cdot cm^{-2}$ and 6.7 $\mu C \cdot cm^{-2}$, respectively [240]. However, no switching has been observed for $BaFeF_4$ and $BaMnF_4$, nonetheless, the analysis by Ederer and Spaldin [17] proposed that the ferroelectric switching in those materials is likely possible by means of higher electric fields. From the magnetic point of view, magnetic moments of M^{2+} have their strongest antiferromagnetic interactions in the ac-plane, with nearly linear M–F–M–F chains along the c-axis, and a zig-zag M–F–M–F configuration along the a-axis [237, 241]. Since the interplanar spacing along the b-axis is much larger (*i.e.* about 14 Å) than the intraplanar ones (about 4-6 Å), the antiferromagnetism in $BaMF_4$ has a pronounced two-dimensional character. Spins are oriented along the b-axis [238] except in $BaCoF_4$, where they lie along the a-axis. It is important to remark that two antiferromagnetic phases have been found in case of $BaCoF_4$ [241]: phase A and phase B being distinguished by the sign of the interplanar coupling along the b-axis, negative and positive, respectively (see Fig. C.3). Then, in this appendix we present the calculations and analysis that support the experimental synthesis of multiferroic $BaCoF_4$ fluoride thin films which are for first

time achieved. For more details in this work please check the Ref. of Borisov *et al.* [6].

C.1 Computational Details

First-principles calculations were performed within DFT as implemented in VASP [66, 67]. PAW [64] pseudo-potentials were used to represent the valence and core electrons. The electronic configurations taken into account in pseudo-potential as valence electrons were Ba ($5s^2 5p^6 6s^2$), Co ($3p^6 3d^7 4s^2$) and F ($2s^2 2p^5$). The exchange correlation was represented within the GGA approach with PBEsol parametrization [39]. The periodic solution of these crystalline structures was represented by Bloch states with a Monkhorst-Pack with a k-point mesh of (4×4×6) and 600 eV energy cut-off, which has been previously tested to give converged forces to less than 0.0001 eV/Å. Additionally, the correct description of the d-electron localization was achieved through the DFT+U approximation with U = 4.0 eV [43]. Spin-orbit coupling (SOC) in the non-collinear analysis was included according to the implementation by Hobbs *et al.* [68]. In order to take into account the AFM magnetic interactions along the a-axis, a (2×1×1) (48 atoms) cell was used for all the calculations. Finally, the spontaneous polarization was computed within the Berry phase approach as implemented in VASP [66, 67]. Isotropic strain calculations were carried out for strain values ranging between -4% and +4%, calculated as $(d - d_0)/d_0$, where d and d_0 are the strained and optimized theoretical $Cmc2_1$ bulk lattice parameters, respectively. The strain was applied with the same magnitude and sign to a and c unit cell directions, allowing relaxation along the b-axis as well as for the inner coordinates, until forces and the stress along the b-axis vanished.

In the next sections we will discuss the results regarding the effect on the xz-plane due to an applied epitaxial strain in $BaCoF_4$ thin films. Thus the multiferroic state is detailed analyzed by means of the employed theory. In particular, the spontaneous polarization as the non-collinear magnetism as a function of the strain is studied.

C.2 Strain Effect in $BaCoF_4$ Fluoride:

In order to understand the ferroelectric and magnetic behavior of $BaCoF_4$ thin films, the density functional theory calculations were performed. According to the experimental findings, when $BaCoF_4$ grows on Al_2O_3 substrates [010] orientation is the prefer one, which defines the specific crystallographic directions where the theoretical part should focused. Such as it is well known, the strain can induce phase transitions in materials when deposited into a substrate enhancing their properties with a considerable mismatch, even less than 3%. This is the case of $SrTiO_3$ [20], $CaTiO_3$ [177, 175] and $NaMnF_3$ [2, 1], the first two ox-

ide perovskites and originally paraelectrics, which under epitaxial strain becomes ferroelectric. The fluoride case is rather different due to its larger sensitivity to strain in which a paraelectric to ferroelectric transition is achieves for values of strain less than 0.5%. Then, keeping fixed the ac-lattice plane to the experimental values, internal coordinates and z-axis are allowed to fully relax. After this structural relaxation a new phase for the strained $BaCoF_4$ was found, going from the $Cmc2_1$ (symmetry group No. 36) to $Pca2_1$ (symmetry group No. 29). In this new phase, the ferroelectric behavior remains unchanged due to the polar nature of the structure as in the $Cmc2_1$ phase. This transition in driven by atomic distortions (represented as red arrows) according to the Γ_1 mode as shown in Fig. C.1.

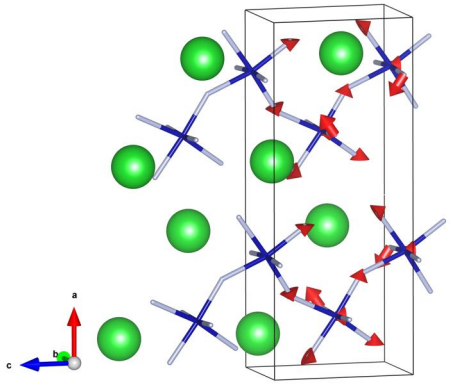

Figure C.1: $BaCoF_4$ [112] supercell in which the red arrows represent the distortion to go from the $Cmc2_1$ to $Pca2_1$ space groups. Atoms in green, blue, and grey colors for Ba, Co, and F species respectively. This figure was elaborated with the support of the VESTA code [168].

As a next step and with the goal to test the thermal stability of the new $BaCoF_4$ phase, phonon dispersion calculations were performed in the relaxed strained structure with lattice parameters such as found in thin films (approx. +1.2%). No imaginary modes traduced in unstable modes were found, which suggest a stable $Pca2_1$ phase structure for this value of strain. After the later analysis, we proceeded to compute the ferroelectric and magnetic properties in the relaxed $BaCoF_4$ structures for strains between -4% to +4% to complete the landscape of the multiferroic properties as a function of the epitaxial strain such as in experimentally growth thin films.

Fig. C.2, we present the behavior of spontaneous polarization as a function of the ac-plane strain. It can be observed the non-linear coupling of the polarization as a function of the strain, which suggest a non-linear piezoelectric effect in this fluoride compound, which is quite rare in these materials [2]. As expected, the polarization develops along the crystallographic b-axis such as has been found in bulk compounds [187]. Nonetheless, small components of polarization along x and z are observed but are not shown here (with an order of 0.1 $\mu C/cm^2$).

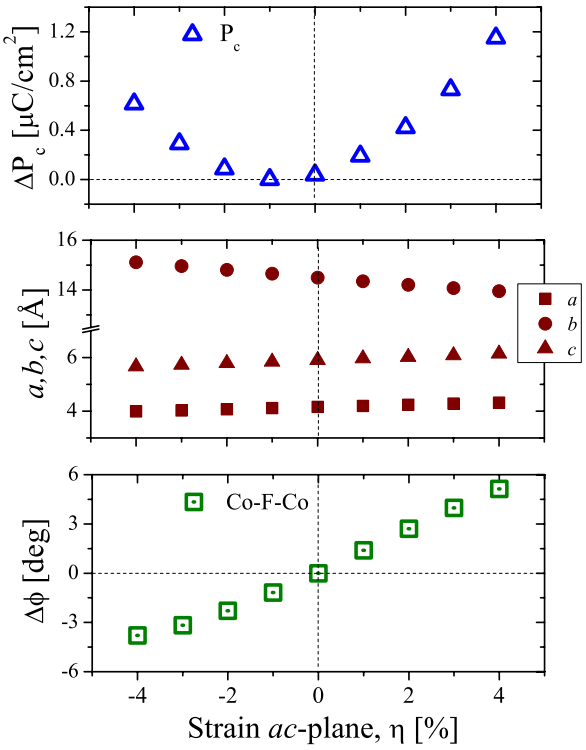

Figure C.2: (Top) Spontaneous polarization along the b-axis. a, b, and c lattice parameters (Middle) and behavior of the octahedral angle bonding (Co–F–Co) along the x-axis (bottom) as a function of the ac epitaxial strain respectively.

This can be due to the additional distortion of the CoF_6 octahedra induced by the epitaxial strain. For values of an epitaxial strain close to those observed in the $BaCoF_4/Al_2O_3$ (0001) thin films, which is close to 1.2%, we compute a polarization value of $P_s = 6.85$ μC·cm^{-2}. Additionally, Fig. C.2 also shows that the b lattice parameter decrease as a and c increase as can be expected from the Poisson ratio.

Regarding the magnetic ordering in the collinear approach, three different configurations have been proposed. These configurations are labeled as A, B and C respectively as depicted in the Fig. C.3,. We found that the B-phase is the most stable, however, the A and C are at 0.11 and 0.06 μeV/f.u. larger in energy. This fact suggests an easy switching of the ordering achieving by small fields and even temperature with that takes an AFM to AFM magnetic transition.

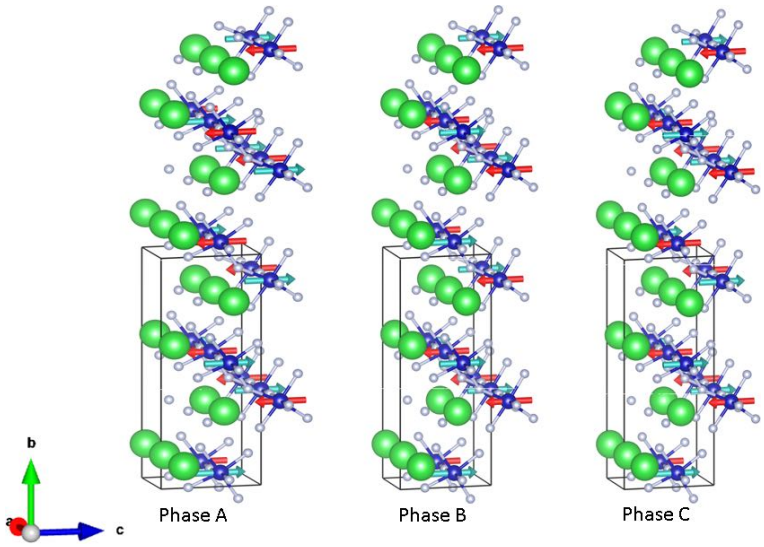

Figure C.3: From left to right, the A, B and C collinear magnetic orderings. In green, blue navy and grey are Ba, Co and F ions respectively. Magnetic moments in each atom are located along the y-axis. In the figures can be observed the unit cell in black lines as well as the computation magnetic cell that takes into account 48 atoms.

C.3 Noncollinear Magnetism and Multiferroic Behavior

The calculations presented in this section were obtained taking the B-phase type magnetic ordering as the main magnetic structure. Based on this structure and the octahedral tilting in the $BaCoF_4$, a weak-AFM is allowed as a slave ordering of the main AFM with a z-easy axis. Nonetheless, the strain induces an increase of the Co–F–Co bonding angle ϕ along the x-axis. Additionally, within the $Pca2_1$ space group, several magnetic point groups such as *m2m*, *m2m1*, *m'2m'*, *m2'm'*, *m'2'm* are allowed and possible some of them can exhibit weak-FM (see note 3). Taking this into account, a weak-FM ordering can be also observed in agreement with the experimental results that show a weak-FM behavior at low temperatures below 25 K. Then, three different orderings can be found of each of the Cartesian axis, a G-type AFM as the main AFM ordering with easy axis along z, a weak-AFM along y-axis as a first slave ordering (called C-type) and a second weak-FM slave along x-axis (F_x). Thus, three magnetic states were tested: G_z , G_zC_y and $G_zC_yF_x$.

From Table C.1 we can note that independently of compression or expansion strain, the ground state in the $BaCoF_4$ is pure AFM with a weak-AFM as slave (G_zC_y). However, for small strain values (close to 1% as observed in the experimentally synthesized thin films), the ground state corresponds to an AFM (G_z) configuration coupled to the weak-AFM (C_y) and weak-FM (F_x) that is in agree-

ment with the experimental findings ($G_zC_yF_x$). It is important to remark that the weak-AFM ordering exhibit two different magnetic moment components which are in agreement with the different octahedral tilting of the CoF_6 in the xz-layer such as can be observed in the Fig. C.3 and in the values presented in the Table C.1.

Table C.1: Magnetic moment per atom (or Co atom) along each axis (x, y and z) for each magnetic ordering where the G_z is the main collinear AFM order and C_y and F_x are the weak-AFM and weak-FM spin orders, respectively. All strains are isotropic in the ac-plane, except for the 1.2% strain result which was calculated with strain applied only along the z-axis, per experimental results.

Strain	m_i [μ_B/atom]		
ac-plain	G_z	C_y	F_x
-4%	2.775	0.107,0.069	0.000
0%	2.762	0.130,0.044	0.038
+1.2% (exp.)	2.766	0.124,0.051	0.039
+4%	2.789	0.103,0.080	0.000

Surprisingly, the m_x magnetic moment induced by the non-collinear magnetism remains almost constant with small deviations within the error regime, thus no observable trend as a function of the epitaxial strain was found even to a largest stress values (around 4%). This can be explained in terms of the competition between the Dyzaloshinskii-Moriya interaction and the single-ion anisotropy (SIA), such as it has been found in the oxide compound $CaRhO_3$ [4]. Besides, the highly distorted CoF_6 octahedral can induce structural contributions to the non-collinear ordering.

If we analyze the complete collinear arrangement at the 1.2% strain (which is the equivalent to the one found in the thin films), we observed a total energy of -5.5609377938 eV/atom for the B-phase (G_z) ground state. Thus, based in the energy difference landscape between the magnetic phases, taken the total energy of the G_zC_y and $G_zC_yF_x$ orderings from the table 1, we can expect a possible magnetic transitions sequence such as $G_zC_yF_x \Rightarrow (\Delta E = 1.22$ meV/atom) $G_zC_y \Rightarrow (\Delta E = 17.67$ meV/atom) G_z respectively as the temperature goes from 0 K to T_N. These results can explain the magnetic transitions experimentally found in the M vs. T measurements.

It is important to note that according to the experimental reports, a possible magnetic transition can be achieved by pressure applied along the y-axis making the octahedral layers closer and changing the weak interlayer interaction [242].

C.4 Conclusions

We have studied by means of first-principles calculations, the behavior of the magnetic and ferroelectric properties of the $BaCoF_4$ as a function of the ac-plane epitaxial strain. We found a phase transition from the $Cmc2_1$ to $Pca2_1$ phase as a function of the epitaxial strain was found. A non-linear polarization-strain coupling was observed suggesting a second order dielectric behavior allowed in the $BaCoF_4$ fluoride. An enhancement of the polarization is observed for values of strain $>$ 0%. For the value of epitaxial strain correlated to the experimental thin films, a non-collinear ground state was found. Besides, a possible path of magnetic transitions such as $G_zC_yF_x \Rightarrow G_zC_y \Rightarrow G_z$ is observed according to the total energy differences. Non trend in the weak-FM as a function of the strain was observed even when the Co–F–Co bonding exhibit a change from 6° to 16° going from -4% to +4% strain respectively. The full understanding of the non-collinear magnetism and its origin is still unclear and needs further studies.

D

SPIN-TEXTURE IN $SrBO_3$ (B) = Ti AND Hf (001) SURFACES

Oxide perovskites exhibit a very large variety of physical properties, which allow their use in a wide range of applications such as spintronics or thermoelectricity [158, 243, 244]. In particular, during the last decade it has been observed new and exotic functional properties at the surface of oxide crystals with no parallel to their bulk counterpart [111, 245]. In this field of multifunctional oxide materials, $SrTiO_3$ (STO) has attracted a lot of attention due to its wide range of physical and chemical properties that goes from superconductivity [246] to engineered ferroelectricity [20]. In various studies a two-dimensional electron gas (2DEG) has been reported at the (001) surface of STO crystal, both theoretically[247] and experimentally by using angle-resolved photoemission spectroscopy (ARPES)[248, 249], which appeared to be induced by the presence of oxygen vacancies and explained by an electronic charge redistribution at the surface. The dynamics of the Ti–d electron quasiparticle on this surface have been experimentally characterized and the appearance of cooperative effects of the electrons has been reported, giving rise to an orbital ordering itself leading to a Rashba-like splitting at the d_{xy} - $d_{xz/yz}$ bands crossing close to the Fermi level[249]. Recently, a mixed character of the confined electrons of the (001) surface of STO displaying a complex spin texture at the Fermi surface has been reported. This unexpected result was ascribed to a Zeeman interaction plus Rashba-like splitting of the lowest d_{xy} owed as well to oxygen vacancies[250].

As commented previously, similar Rashba-effect[221] in oxides has been observed in the $LaAlO_3/SrTiO_3$ interface [218, 199, 219, 220] or in $SrTiO_3$- and $KTaO_3$-based transistors [222, 223]. For these single perovskite-based devices, a k-cubic dependence of the splitting was found in contrast to the linear+cubic dependence of the Rashba splitting at the $LaAlO_3/SrTiO_3$ interface due to the d_{xy} – $d_{xz/yz}$ multiorbital nature of the lowest bands [219]. As in the case of Au(111) surface, where it has been shown that even when the surface states exhibit a mainly p–orbital character, the d–orbitals drives the Rashba splitting and dictates the direction of the spin by means of the orbital-angular momentum (OAM) [224, 225]. Therefore, the d-orbitals of the transition metal atom of perovskite oxides can be the key parameter for a large and controllable electron band splitting in future spintronic devices [224, 226]. This later property gives an additional degree of freedom to the rich field of multifunctional perovskites. However, the recent findings of a giant spin-splitting at the STO surface, opens some questions about the nature of the spin-splitting in this type of materials, such as: What is the origin of this giant-splitting? Could it be manipulated or observed

in similar compounds? What is the role of the spin-orbit coupling strength in the Rashba splitting of d-orbitals in oxide perovskites? Since magnetism at the surface was reported, how does it couple with the splitting?. From the theoretical point of view, it is well known that density-functional theory formalism provides invaluable information related to the structural, magnetic and electronic structure of oxide interfaces, superlattices and surfaces [251, 252, 111, 219]. This has been particularly true for the $SrTiO_3/LaAlO_3$ interface [252, 253] or the STO surface [253] where DFT helped in understanding the origin of the 2DEG through the polar catastrophe scenario. In the present appendix we address the previous questions by performing such DFT calculations on the (001) STO surface with oxygen vacancies in order to (i) shed light onto this novel experimental finding and (ii) to scrutinize the microscopic origin of the giant Rashba spin-splitting and the Ti d-orbitals spin-texture.

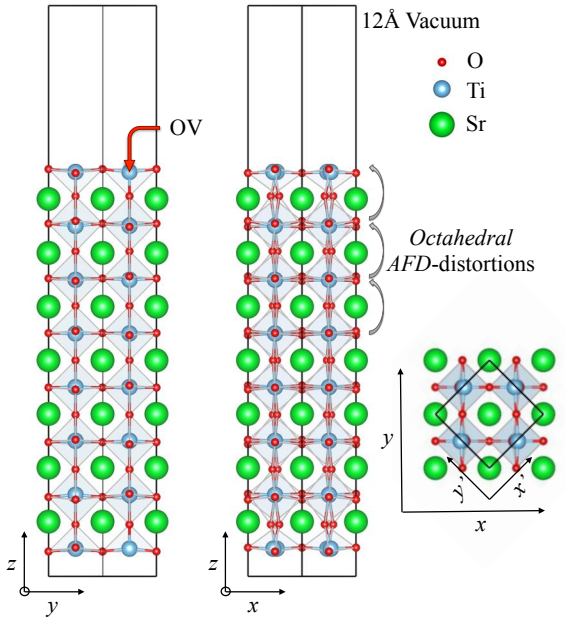

Figure D.1: Schematic view of the $SrTiO_3$: $TiO_{2-\delta}$ (001) surface used in the calculations with an oxygen vacancy (OV) at the yz- (left) and xz-plane (right) respectively. The OV is located at the $(\frac{1}{4}, \frac{1}{4}, z)$ position with respect to the computational x′- and, y′- coordinates). The amplification of the AFD distortions due to the oxygen vacancy can be clearly appreciated. Additionally, a surface induced off-centering of the Ti along the z direction is observed with respect to the oxygens (rumpling), inducing an electric dipole. In the right bottom part we present a top view of the unit cell in the xy-plane. This figure was elaborated with the support of the VESTA code [168].

D.1 Computational Details

The first-principles calculations have been performed within the DFT as implemented in VASP [66, 67]. The interaction between ion cores and valence electrons was treated by the projector augmented wave method [64]. The orbitals considered as valence electrons in the atomic pseudo-potentials were: Sr ($4s^2 4p^6 5s^2$), Ti ($3s^2 3p^6 4s^2 3d^2$), Hf ($5s^2 5p^6 5d^2 6s^2$), and O ($2s^2 2p^4$). To describe the exchange-correlation energy, we used the General Gradient Approximation (GGA) with the PBEsol parameterization [39]. In order to account for the magnetic character of the system we performed spin polarized calculations. The Hamiltonian contained the scalar relativistic corrections and the spin-orbit coupling was taken into account by the second variation method [68]. A Monkhorst-Pack k-point grid of (8×8×1) for reciprocal space integration and 600 eV energy cut-off of the plane wave expansion have been used to get a residual error on the forces below 1 meV/Å and a fully converged electronic structure including SOC. To correctly describe the (001) surface and avoid interactions between periodic slabs, we used a supercell with a vacuum space of 12 Å. Additionally, in order to take into account the octahedra rotations and tilting, we considered a ($\sqrt{2} \times \sqrt{2} \times 7$) cell as shown in Fig. D.1, enforcing the cubic symmetry at the cell center. Aiming to prevent a fake polarization along the z-axis, the central plane is used as m_z mirror symmetry such as the slab is repeated along the z direction.

In what follows, the electronic characterization of the Rashba-like splitting for $SrBO_3$ with B = Ti and Hf, including surface oxygen vacancies at the BO_2 termination according to experiments [250] is discussed. Great emphasis is done on the size of the splitting and the spin structure.

D.2 STO : TiO_2 terminated surface

Fully relaxed STO surface reveals a change in the interatomic distances close to the surface due to the missing Ti–O surface bonds (rumpling). The Ti–Ti distance calculated between the Ti surface layer and the next just below is 3.821 Å, which is much smaller than the STO bulk distance of 3.905 Å. Additionally, the out-of-plane Ti–O bond length at the surface changes its distance from 1.948 to 1.950 Å, leading to a local polar like displacement. We also found a substantial lowering of the calculated electronic gap, which goes from 2.0 eV at the bulk level to 0.8 eV in the slab geometry. We computed the electronic band structure with and without SOC and we did not observe substantial differences, which implies that SOC has a small contribution to the changes in the electron band structure compared with the geometrical changes. Furthermore, no octahedral rotations or tilting were observed in the fully relaxed surface when the cubic symmetry is imposed at the central slab plane.

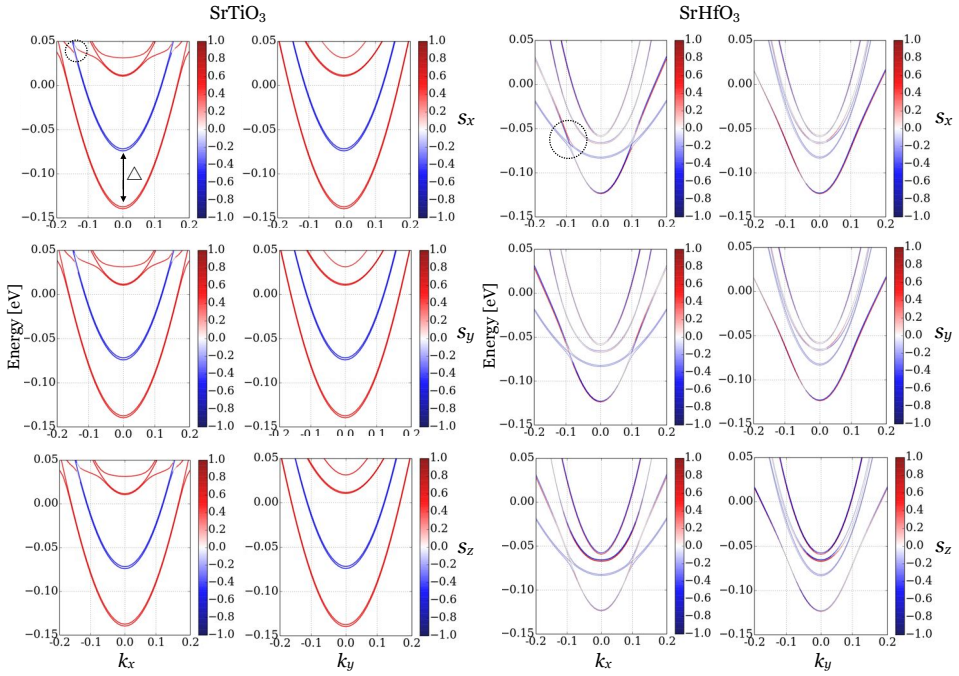

Figure D.2: Band structures around Γ-point for $SrTiO_3$ and $SrHfO_3$ with an oxygen vacancy on the BO_2 terminated surface. Red and blue denote positive and negative projection of spin vector $\vec{s}$ on Cartesian axes, units of the k-vector in units of π/a. The non spin-polarized bands are depicted in dark grey. The effect of the SOC and a Rashba-type splitting is observed in the d_{xy} and $d_{xz/yz}$ bands crossing (noted with the dashed circles) as well as the vertical energy shift $\Delta \equiv \Delta E_{Zeeman} + \Delta E_l$. For SHO a spin-splitting of the lower bands is observed for the x and y components around E = –0.1 eV. Figures were created by using the PyProcar script [254].

D.3 $STO : TiO_{2-\delta}$ surface with oxygen vacancies

Experimentally, STO surface samples become conducting in the presence of oxygen vacancies [255, 256]. In order to analyze their effect, we performed full structural relaxation of the STO:TiO_2 surface by removing one oxygen in the last TiO_2 termination layer ($\delta = 0.5$), imposing a bulk cubic symmetry to allow us a direct comparison with the pristine case. As we illustrate it in Fig. D.1, octahedral tilting and rotations are now observed in the presence of oxygen vacancies (the rotation angle is 10.9° with respect to the z-axis for the tetrahedral closest to the vacancy), in contrast to the surface without oxygen vacancies, where no rotation was observed.

In what follows we study the electronic and spin structure of the (001) STO:$TiO_{2-\delta}$ surface. In Fig. D.2, we report the calculated electronic band structure around the Γ–point including non-collinear magnetism and SOC. We found a conducting behavior very similar to what has been observed at the $LaAlO_3/SrTiO_3$ interface [253], where the lowest energy bands are the Ti–3d orbitals. At the bulk level, the

Ti–3d orbitals present in the TiO_6 octahedra are expected to split into t_{2g} (d_{xy}, d_{xz}, d_{yz}) and e_g (d_{z^2}, $d_{x^2-y^2}$) due to the crystal-field splitting. Here, we remark that small distortions in the octahedral geometry, as the one observed at the surface, generate a small shifting in the energy-values of the electron levels (ΔE_l) and a possible mixing of the t_{2g} and e_g states, mainly due to the symmetry breaking and the uncompensated TiO_6 octahedra at the surface [257]. In the oxygen vacancy STO surface we found that the lower d–levels bands corresponds to the d_{xy} orbitals in the paths that runs from -0.5k_x – Γ – +0.5k_x and -0.5k_y – Γ – +0.5k_y. In addition, we also found a magnetic moment on the Ti atoms close to the surface. The amplitude of these magnetic moments is around 0.212 μ_B/Ti-atom in the surface and 0.026 μ_B/Ti-atom in the sub-surface layer. These results are in agreement with the experimental observation of magnetism in STO with oxygen vacancies [258] and other theoretical works of the same system [259, 260, 261]. The spin polarization is analyzed by plotting the s_x, s_y and s_z components of the magnetization for each path, where up and down spin orientations are depicted by red and blue colors respectively. We can appreciate that lower light bands close to the Fermi level are separated vertically due to an induced Zeeman splitting (ΔE_{Zeeman}) as expected from the magnetism found at the surface and the energy splitting ΔE_l. This magnetic moment is induced by the effect of the electron surface density rearrangement as a response of the uncompensated orbitals, thus oxygen vacancy acts as a magnetic impurity [261, 259].

From Fig. D.2 we can also see the parabolic-like shape of the d-bands, which is a characteristic of a 2DEG, as reported in previous studies [262, 248, 256]. Here, it is important to note that this 2DEG is induced by the electronic reconstruction related to the confinement of the electrons at the surface [255, 261], rather than a polar catastrophe origin as mentioned for the $SrTiO_3/LaAlO_3$ interface [252]. Thus, we can expect that the behavior of the conducting electrons in STO differs from the one found in the oxide/oxide interfaces.

The effect of the SOC can be clearly appreciated in the Rashba-like spin-splitting at the d_{xy} and $d_{xz/yz}$ crossing (pointed out by the dashed circles in Fig. D.2), similarly to what has been previously reported in this surface [249]. For the d_{xy} state, we obtain an effective mass of 1.6 m_e for the orbital located at the second layer of TiO_2. This calculated effective mass is two times larger than the one reported in Ref.[249] (0.65 m_e), which is too small for d like states [263]. However, a spin-splitting such as in a classical Rashba picture is not observed (*i.e.* crossing of the spin up and down bands) between the light branches or a spin inversion within the d_{xy} bands for any of the spin-orientations along the k_x and k_y paths. This result is in contrast with the interpretation of the experimental measurements of Santander-Syro *et al.* [250] who reported a giant spin-splitting in the lowest d-bands of the (001) STO surface. One possible explanation of this splitting is that it can be a consequence of the surface ionic vibrations. In that respect, we have performed ab–initio molecular dynamics calculations at constant temperature of 400 K for the slab geometry. Selected uncorrelated frames were taken from the simulation and electronic band structures were calculated for each

case. As for the 0 K ground state, we did not observe any Rashba splitting like the one reported in Ref [250], which indicates that at least for low temperatures there is no coupling between the ionic vibrations and the electronic response.

Another possibility could be that it comes from anharmonic vibrations at much higher temperatures, a possibility we do not explore in this work. The absence of a large spin-splitting can be understood from the small SOC present in the 3d–Ti orbitals. To test this hypothesis, we performed a computer experiment by replacing all the Ti atoms by a heavier cation with much larger SOC such as Hafnium. Taking the advantage that the Hf atom has the same electronic configuration as the Ti but with 5d orbitals [1]. In these calculations cell lattice parameters and internal coordinates of the optimized geometry of the STO surface were fixed in order to keep the same structure. The 2DEG generated at the HfO_2 surface with oxygen vacancies presents the same main features as in the STO case. However, a large change in the spin-splitting state is observed in the electron dispersion as shown in Fig. D.2, and somehow closer to the experimental suggestion of A. F. Santander-Syro *et al.* [250], who claimed for a spin-inversion direction within the lowest d-band. In both, k_x and k_y paths in Fig. D.2 and at the Fermi level the bands are mainly composed by s_z spin direction. The spin switching is observed for the light d_{xy} Hf band at E = –0.1 eV and reciprocal points close to –0.1 and 0.1 for s_x and s_y spin components respectively. This suggests that a strong surface polarization is not enough to induce a Rashba-like spin-splitting and the presence of high-Z cations in the structure is also necessary to achieve this spin state as previously reported for Ag, Cu, and Au surfaces [264]. The Rashba-like splitting in the $SrHfO_3$ (SHO) is only observed for the s_x and s_y spin components of the xy-plane perpendicular to z-axis as expected from the Rashba Hamiltonian $\mathcal{H}_{\mathcal{R}} = \alpha_R(\vec{e}_z \times \vec{k}) \cdot \vec{s}$ [221].

In addition to the band analysis, we have also extracted the in-plane spin-texture as shown in the Fig. D.3. In Fig. D.3 we can see two concentric rings for up and down spin polarization respectively for the STO (at E = 0 eV) and one single ring for SHO (E = –0.1 eV) surface. The rings in the STO appears as a result of the vertical splitting due to $\Delta E_{Zeeman}+\Delta E_l$, where ΔE_l is induced by the lowering of the d_{xy} energy bands in comparison to d_{yz} and d_{zx} orbitals as discussed before. In the case of SHO (Fig. D.3), spin precession in the lower ring is observed in addition to a spin switching of the d_{xy} band in agreement with the bands in Fig. D.2) as expected for the Rashba-type splitting.

The absence of the spin-splitting in the STO surface could be also linked to magnetism, as observed at the the Gd(0001) surface [265] where the presence of magnetism and a Rashba-type splitting has been reported. For this system the splitting is lower than 0.1 $Å^{-1}$ even with the large SOC present in Gd (around 9 times larger than in Ti)[265]. Moreover, due to the presence of ΔE_{Zeeman}, there is no crossing of the bands and the direction of the magnetization vector ($\vec{M}$) determine the presence of the spin-splitting. This is due to the fact that the

1 The spin-orbit coupling in Hf is around 11 times larger than in Ti based in the $(Ze^2/\hbar c)^2$ expression

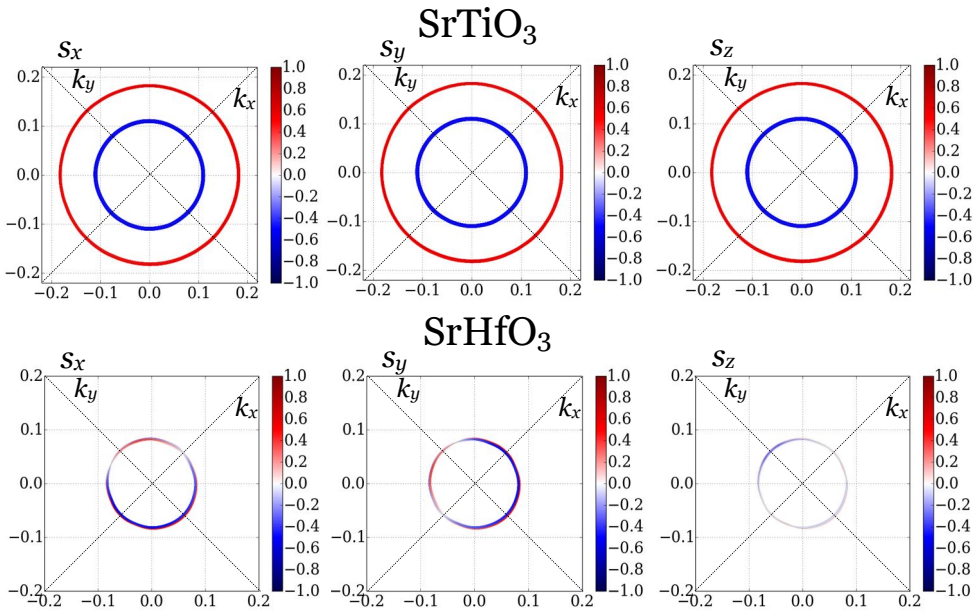

Figure D.3: Band structure at the k_x-k_y plane (in π/a) where the spin-texture is calculated for each spin component along the cartesian axis (*i.e.* s_x, s_y and s_z). For $SrTiO_3$ compound (above, E = 0 eV) simple concentric rings for up (red) and down (blue) spin polarizations are observed. In contrast a Rashba-like splitting is observed by replacing the Ti cation by the heavier Hf in the $SrHfO_3$ (bottom, E = − 0.1 eV). Figures were created by using the script PyProcar [254].

Rashba-splitting vanishes for $\vec{k} \parallel \vec{M}$ and only ΔE_{Zeeman} remains [265]. The later statement needs to be carefully taken into account in the STO case for which we find a magnetic moment components at the surface m_x =0.213, m_y =0.212 and m_z =0.212 μ_B/Ti-atom respectively and thus after considering several possible magnetic orientations. Different starting magnetic configurations, along x- y- and z-axis respectively were taken into account and full structural and energy minimizations were applied. Nonetheless, the system always relaxed toward the same magnetic ground state in which a diagonal direction of the magnetic moment is observed with respect to the surface. No traces of magnetization were observed at the oxygen sites confirming the Ti–localized magnetic moments. Thus, this rather large in- and out-of-plane magnetic moments have the tendency to prevent the possibility to have a giant Rashba splitting, in addition to the small SOC discussed previously.

In the case of SHO, we obtain that the Hf magnetic moments are strongly reduced to m_x =0.034, m_y =0.034 and m_z =0.032 μ_B/Hf–atom respectively close to the surface, which strongly reduced the ΔE_{Zeeman}. Fig. D.3 shows that the lowest d-band in SHO only exhibit spin components along the xy-plane. Nonetheless for higher energy values, the bands are mainly spin-polarized along the z-axis, demonstrating a very complex spin structure with a unique spin-texture. There-

fore, only a deep understanding of this subtle competition between the polar distortions, the symmetry conditions, SOC, and magnetism would allow us to tune the Rashba-splitting at the (001) BO_2 surface.

In order to test the validity of our results against the exchange-correlation functional, we also carried out the same calculations with both the Local Density Approximation [266] (LDA) and the GGA PBEsol+U functionals. Using the LDA approximation, we did not find substantial differences with the GGA PBEsol calculations. Due to the strong correlation of the d-orbitals that drives the magnetism, we might expect the DFT+U formalism [267] to enhance the electron correlation and change the physical picture discussed previously. Indeed, above $U = 2$ eV, we observe an insulating state of the STO surface with the oxygen vacancy, which do not agree with the experimental measurements [248, 250, 249]. Then, for whatever U value below 2 eV, we do not observe a large Rashba+Zeeman (RZ) type spin-splitting. In order to test the oxygen vacancy position effects, we performed a second set of calculations considering the oxygen vacancy in the second inner layer from the surface instead of the first layer and, as before, we did not observe a Rashba spin-splitting in the STO surface within this configuration.

D.4 *Pbnm* $SrHfO_3 : HfO_2$ surface with oxygen vacancies

We completed the analysis of the Rashba splitting mentioned above by analysing the spin textures in the $SrHfO_3$ ground state, *i.e.* in the *Pbnm* phase with $a = 5.7516$ Å, $b = 5.7646$ Å, and $c = 8.1344$ Å [268]. To analyze the new SHO surface in its *Pnma* phase, we fully relaxed the surface including an oxygen vacancy in the $HfO_{2-\delta}$ termination slab. Our results reveal an increase of octahedral tilting and rotations as a result of the free surface plus the oxygen vacancy, which induce a structural reconstruction with respect to the bulk (see Fig D.4).

From the electronic structure analysis we observe a strong reduction of the band gap, from 3.22 eV in the bulk to 0.06 eV in the surface with oxygen vacancy and thus an absence of the 2DEG. Additionally, from the band structure plotted for each spin orientation (see Fig. D.4, bands around the Γ–point along k_x and k_y paths) we can appreciate that the lowest Hf bands corresponds to 5d-levels, and more precisely to the $5d_{xy}$ states. According to Fig. D.4, we note that the major spin components for the 5d bands are along the z-axis and a Rashba-type splitting is also observed for this orientation in most of the branches, which happen to be out-of-plane and perpendicular to the surface according to our results. This behavior can be explained in terms of the polarization close to the surface and the Rashba Hamiltonian expressed before. Here, the bands present a spin-splitting for a dispersion along a $\vec{k}$-vector perpendicular to the electric field $\vec{e}_{xy}$. To confirm this hypothesis, we computed the spontaneous polarization by means of the Berry phase approach [269]. We obtained that the P_z component is zero by construction and the in-plane components are equal to 0.44 $\mu C \cdot cm^{-2}$ and

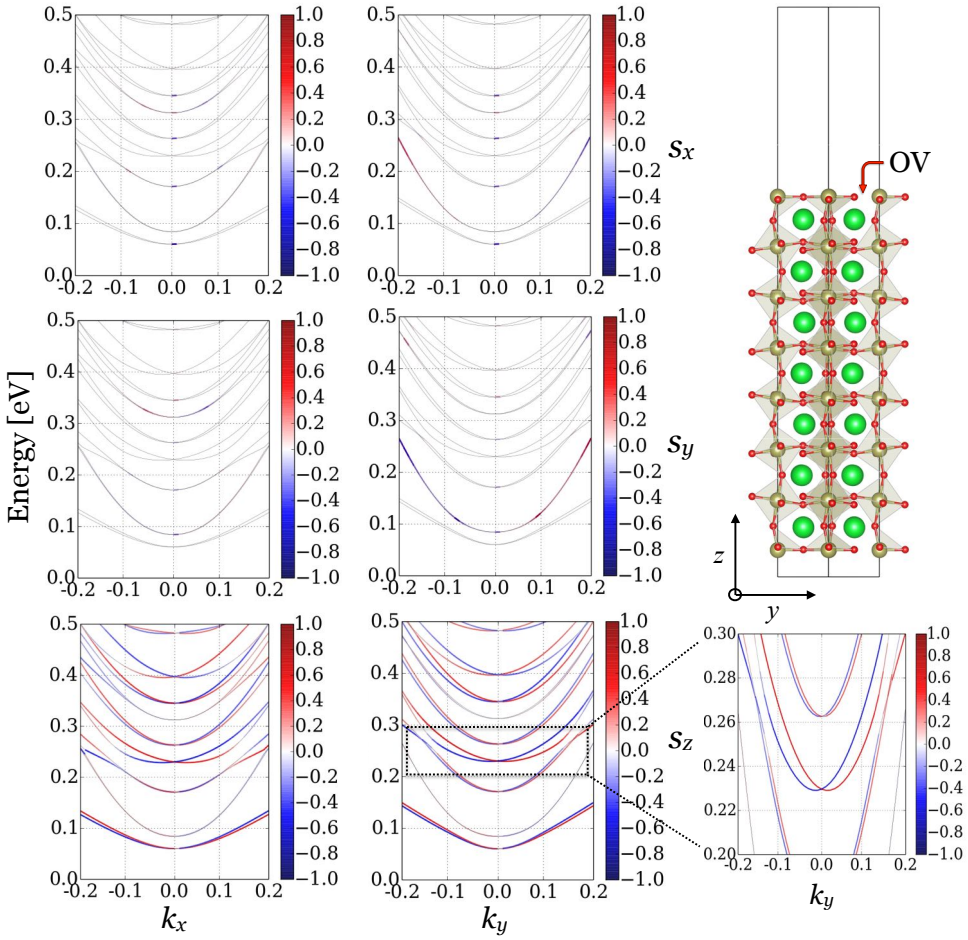

Figure D.4: Band structures around the Γ-point along k_x and k_y for $SrHfO_3$ surface with an oxygen vacancy on the top of the HfO_2 layer for each direction of the spin. Red and blue colors represent the up and down spin directions respectively. A larger Rashba-type splitting of the bands is observed for the z component as appreciated for the $k_y - s_z$ extracted image. The SHO slab structure is also shown in which the large octahedral tilting can be observed. Figures were created by using the script PyProcar [254].

1.15 $\mu C \cdot cm^{-2}$ found along the x-axis (P_x) and y-axis (P_y) respectively. This in-plane polarization in orthorhombic perovskites is quite well known and is related to the presence of anti-polar motion of the A-site in the xy-plane, which, in the case of the surface symmetry breaking, do not cancel out from layer to layer and thus resulting in an effective spontaneous polarization along the xy-plane [202, 270]. Interestingly, and in contrast to the STO case, we do not find any presence of magnetism in the *Pbnm* SHO surface with oxygen vacancies and at the same time the Rashba-splitting is considerably enhanced, confiming the rule discussed above. Interestingly, when replacing the Hf by Ti in the relaxed Pbnm $SrHfO_3$ surface, the magnetism appears again and the Rashba splitting dissapear.

All of that confirms the influence of the magnetic ordering and the SOC strength of the B-site at the spin-texture of $SrBO_3$ surfaces with oxygen vacancies.

D.5 Summary and Discussions

We have analyzed from first principles calculations the (001) $SrBO_3$, (B = Ti and Hf) surface with oxygen vacancies. We found an insulator to metal transition behavior when an oxygen vacancy is included in STO at the TiO_2 surface, which produces an electronic charge rearrangement that results into a 2DEG located at the surface and magnetization of the Ti–d orbitals close to the vacancy. In the limits of our DFT calculations, it is unlikely that a large Rashba-type splitting in the light lowest d_{xy} bands exists in the presence of an oxygen vacancy at the STO:TiO_2 surfaces. This is in contrast with the giant spin-splitting of about 0.1 $Å^{-1}$ reported by Santander-Syro *et al.* [250] in their experiments. This discrepancy can come from different origins. On the experimental side, due to the methodology of the spin-ARPES technique used by Santander-Syro *et al.*, excited states could have been induced at the surface, with a different spin-polarization of the photoelectrons. Then, these states can become accessible and be measured by this technique as already reported before [271, 272, 273]. There is also a possibility of high temperature gradients at the surface due to the high energy from the laser field. This could create large ionic vibrations, which can create large ionic vibrations, even if the adiabatic approximation still holds [274]. On the calculation side, it is possible that the configuration chosen for the oxygen vacancy does not correspond to what is present experimentally. In that respect imaging techniques such as STM would be of use in order to check the surface structure.

It has been shown from photoemission spectroscopy that the Rashba spin-splitting in these 2DEG systems is extremely sensitive to the charge and orbital ordering, the SOC or the lattice degrees of freedom [249]. We observed such a sensitivity when replacing Ti by Hf atom with a much larger SOC, which induces a larger change in the spin-splitting landscape at fixed lattice degrees of freedom. Indeed, when relaxing toward the SHO ground state, we observe a totally different magnetic and Rashba spin-splitting states, all of that confirming the strong spin structure sensitivity of these surfaces. However, in all the configurations we considered, we never obtained a Rashba spin-splitting as large as the one reported by Santander-Syro *et al.* and the fact that it is much larger than the one observed in the $LaAlO_3/SrTiO_3$ interfaces (<0.01 $Å^{-1}$ [218, 220] and supported by theoretical analysis [199, 219]) call for additional studies (theoretical and experimental) in order to understand this unexpected large splitting. Going beyond this discrepancy, we proved that sizeable Rashba-type splitting can be achieved in multifunctional perovskite oxides with large SOC, such as $SrHfO_3$ not observed before. These systems thus opens the possibility to tune exotic properties for new technological applications such as spin-orbitronics [275, 276].

E

ROLE OF SURFACE WATER ADSORPTIONS IN $SrTiO_3/LaAlO_3$ INTERFACE

The surface functionalization properties can significantly affect the performance of semiconducting electronics [277, 278]. On one hand, surface states can induce undesired carrier trapping [279]. On the other hand, surface assisted doping is also actively investigated for many material systems where bulk doping is restrained. Such systems include wide band gap semiconductors [280], two dimensional materials [281], nanostructures [278], and chemically fragile organic semiconductors [282]. $LaAlO_3/SrTiO_3$ heterostructure is another system where the surface related effects are vital [283]. The formation of interfacial two dimensional electron gas (2DEG) as well as the 2DEG's unique characters in metal-insulator transition [284], superconductivity [246], magnetism [285] and optical responses [286] have evoked widespread interest. A mechanism involving the charge transfer between the surface and the interface (polar catastrophe) were proposed to explain the formation of 2DEG [287, 252]. Possible carrier depletion by oxygen dangling bonds at the surface was suggested [288]. Different capping layers were explored to allow further tuning of the interface properties [288]. Effects of surface adsorbates formed in air can also be significant. Among the various airborne molecules, the dissociation and migration of water molecules on oxide surfaces bear particular technological importance [279]. In $LaAlO_3/SrTiO_3$ heterostructures, effects of liquid water on the interface electrical properties have been experimentally observed [289, 290]. In addition, reversible interface metal-insulator transitions controlled by conducting atomic force microscope (c-AFM) were previously reported [286, 289, 291]. Experiments performed in controlled environments later links the effects directly to the surface water [290]. Despite of these interesting experimental findings, clear understanding of the underlying mechanism is still lacking. Several critical questions remains open: How are water molecules adsorbed on $LaAlO_3$ surfaces and is the adsorption energetically stable? How do the surface dangling bonds and water adsorptions in air affect the metal-insulator transitions observed in heterostructures with different $LaAlO_3$ layer thicknesses? What are the dynamic processes of water adsorption and desorption? How do the adsorbed water respond to the external field or environment changes? In this work, we seek to shed light onto these open questions by systematic theoretical and experimental investigations. A partially dissociated water layer is found to strongly bond to the polar $LaAlO_3$ surface. The densities and distributions of adsorbed protons and hydroxides strongly affect the structural and

electrical properties of the $LaAlO_3/SrTiO_3$ heterostructures. Intrinsic interface carrier doping depending on the $LaAlO_3$ thickness and extrinsic contributions to the interface metallicity from dissociated water are both observed. Considering the weakly adsorbed molecular water layers also turned out fruitful in that the associated hydrogen bond network enables active surface proton transfer at room temperature. The tunable thermally activated proton hopping processes provide an effective pathway for engineering the interface properties from the surface. The multifaceted role of water revealed by this work is undoubtedly critical in understanding the unique characters at $LaAlO_3/SrTiO_3$ interfaces observed so far. Our results are also expected to provide valuable guidelines for the future development of oxides based surface engineering methodologies and device applications. For more information please check the Refs. [8, 7].

E.1 Computational Details

DFT calculations were performed using the VASP. PAW [66, 67] pseudo-potentials were used to represent the valence and core electrons. The electronic configurations taken into account in pseudo-potential as valence electrons were Sr ($4s^2 4p^6 5s^2$), Ti ($3s^2 3p^6 4s^2 3d^2$), La ($5s^2 5p^6 5d^1 6s^2$), Al ($3s^2 3p^1$) and O ($2s^2 2p^4$).The exchange correlation was represented within the GGA and PBEsol parametrization [39]. The periodic solution of these crystalline structures was represented by Bloch states with a Monkhorst-Pack with a (6×6×1) k-point mesh and an energy cut-off of 550 eV tested to give converged forces to less than 0.001 eV/Å. To correctly describe the system, 5u.c of $SrTiO_3$ (STO) as a substrate was taken into account. Then, 3u.c. and 5u.c of $LaAlO_3$ (LAO) were used as thin films for the analysis. Additionally, in order to avoid periodic interactions between periodic slabs, we used a supercell with a vacuum space of 12 Å along the z-axis. The dipole correction was applied along the out-of-plane z-axis to cancel dipole-dipole interactions and correct the errors caused by periodic boundary conditions [292]. In addition and in order to take into account the octahedral rotations and tilting, we considered a $\sqrt{2}\times\sqrt{2}$ cell in the xy-plane with lattice parameter fixed to the PBEsol relaxed STO $a = 3.8967$ Å.

E.2 Water dissociation in the surface

Different theoretical calculations have demonstrated that the electronic reconstruction induced by the polar catastrophe phenomena is the main responsible for the insulator-to-metal transition (IMT) in LAO/STO and the appearance of a 2DEG at the polar-nonpolar perovskite oxide interfaces (see for example Ref [252]). Therefore, modifications of the surface formal charges at the AlO_2 top layer is expected to change the interfacial properties. Then, a clear understanding of this phenomenon is crucial in order to explain the macroscopic electronic transport properties discussed in this work.

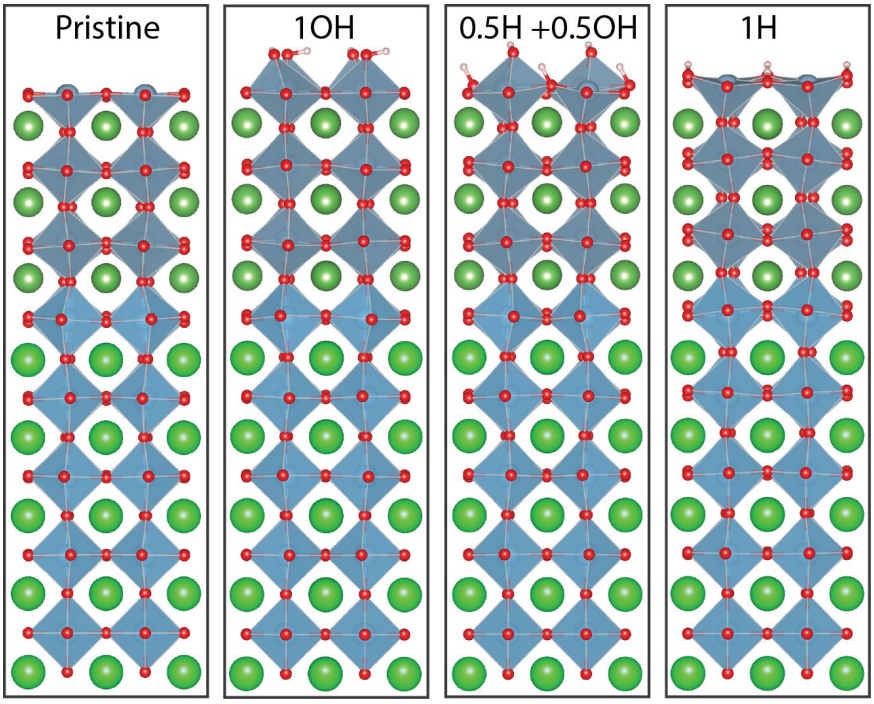

Figure E.1: Relaxed geometries for the pristine, and the OH, 0.5H+0.5OH, and H groups. It can be observed the octahedral tilting and rotation increase when the molecules are placed at the surface.

We have noticed that the octahedral rotations and tilts across the LAO layer —dissipating up to the STO substrate— increases when H and OH are placed at the LAO surface (see Fig E.1). These AFD distortions have a direct effect on the interfacial properties and specifically, at the carriers density at the interface as we have observed in a computational experiment where, the carried density was computed with and without full atomic relaxations. Here, it is important to remark that those distortions are present even in the pristine bulk structure due to the rhombohedral $R\bar{3}c$ ground state of the $LaAlO_3$ [293].

In the 3uc pristine case, the electric field of 75 mV/Å (computed from the layer resolved DOS) is clearly not enough to overcome the existing electron gap in the STO/LAO system, leading to the obtained insulated behavior (E_g = 0.2 eV). The water dissociation and the later removal of the $(OH)^-$ groups with the AFM tip leaves only absorbed hydrogen atoms on the surface which, according to our results, act as electron-donors. These additional electrons, under the effect of the electric field existing in the LAO film, are transferred to the interface, which then generate a 2DEG with d_{xy} character from the Ti orbitals. This electron transfer explains the induced IMT in the 3uc LAO, as depicted in Fig. E.4. Consequently, the absorbed hydrogen act as electron-donor and provide additional charge, which is enough to compensate the surface charge responsible for the polar discontinuity. The later clearly alters the out-of-plane electrostatic potential. For example, when

the surface is fully hydrogen saturated, the field takes a value of -86 mV/Å that is in opposite direction to the potential in the (AlO_2)- pristine surface. This field crosses through 0 mV/Å for 0.5H (see Fig. E.2), which demonstrates the direct effect of the electron-donors in the electrostatic response, as was expected. On the other hand, if we consider 5uc of $LaAlO_3$ on $SrTiO_3$ (001), the electric field is now close to 110 mV/Å across the entire LAO film as shown in Fig. E.3. This value is sufficient to overcome the present electronic band gap of the STO material and the system becomes metallic, as it is widely known. Additionally, a 2DEG and a 2DHG are created at the interface and surface respectively. Now, with the same process of water absorption and later $(OH)^-$ removal, as in the previous 3uc case, the hydrogen electron-donor alters the amount of electrons in the system. These additional electrons are transferred from the surface to the interface, similarly to the case of 3uc of $LaAlO_3$, and the amount of carriers density increase drastically as observed in Fig. E.4, as it is also supported from experimental results.

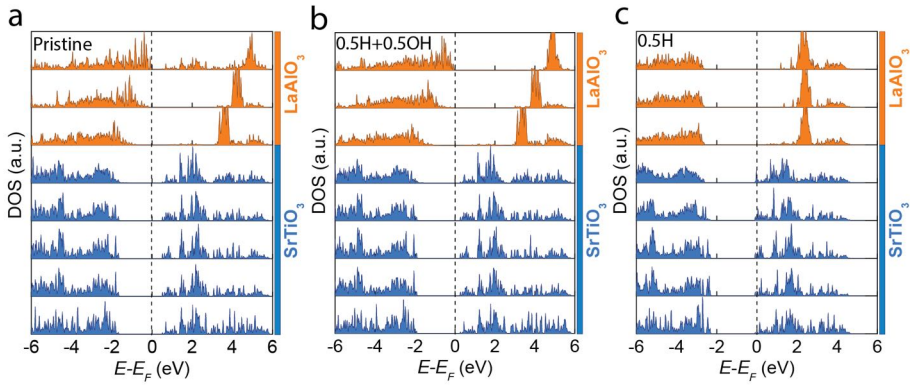

Figure E.2: Layer-by-layer density of states for the 3uc in which the electric field profile can be observed. A insulator-to-metal transition can be observed when going from the pristine to the H-doped structures.

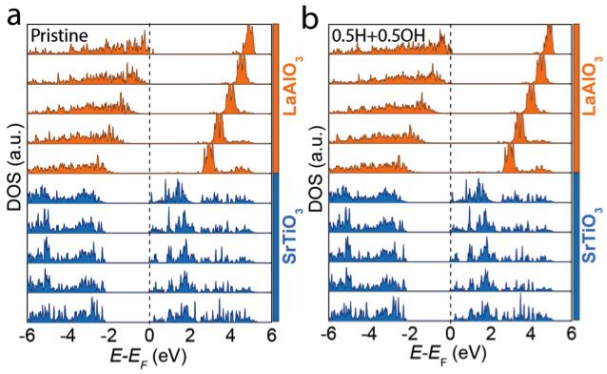

Figure E.3: Layer-by-layer density of states for 5uc for the pristine structure and the water dissociated at the surface.

Our theoretical analyses also reveal the appearance of magnetic moments at the interface for the 5uc case, as expected from the unpaired 3d-Ti orbitals occupation as it has been already reported [294]. In the 3uc case, magnetic moments are only observed at the 3d-Ti when the interface becomes metallic due to the bonded hydrogen. When only (OH)-groups are in the LAO surface, the magnetism is only present at the top layer. This is due to the electron holes at the localized oxygen p-orbitals as it has been shown in some d^0 semiconductor [295].

The fact we are considering oxides in which, strong electron correlations takes place, makes important to investigate the effect in the results of the exchange correlation functional by enhancing the electron-electron repulsion in the so called DFT+U [46]. This method allows to increase the electron correlation lacking in the d-orbitals and then improving the electron band gap, in closer agreement with experimental predictions. This correction can also affect negatively the searched properties because it changes at the same time some other orbitals. Thus, we have considered initially the 3uc case as a prototypical example. All results here were re-computed with a $U = 7.5$ and 5.8 eV for Ti and La respectively and $J = 0$ eV [296]. We found that the general description holds but the valence carrier density increases by more than one order of magnitude, which is not in agreement with the reported experiments. Therefore, our results reported here only correspond to the case of $U = J = 0$ eV.

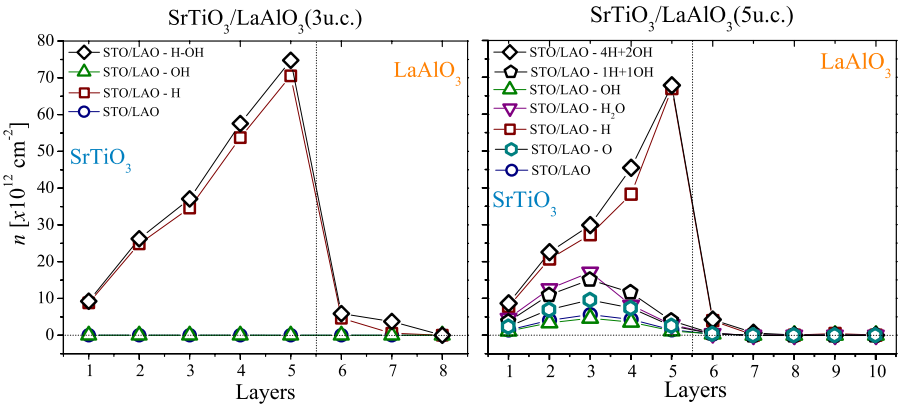

Figure E.4: Computed carrier density for 3uc and 5uc respectively. Here we considered several molecules as a dopant agent at the surface.

Now, if we think in the idea to reverse the voltage in the tip, and then, the H^+ is removed from the surface, the effect can be seen in the reduction of the electric field in the LAO film. This field goes from 110 mV/Å to 87 mV/Å for the pristine structure to the OH saturated surface. Nonetheless, according to our results, this field reduction is not having a major effect in the carrier density as can be appreciated in Fig. E.4. This can be explained by the fact that in the 5uc, the charge is already confined at the interface and there is no charge transfer going back to the surface, which is traduced in an increase of the holes at the

surface. In the 3uc case, the electric field is also reduced to 54 mV/Å and the system remains insulator.

We considered the possibility of reversing the voltage on the AFM tip, H^+ is removed and OH- are kept on the surface, such that there is a reduction of the electric field in the LAO film. This field goes from 110 mV/Å to 87 mV/Å for the pristine structure to the OH saturated surface respectively. However, according to our results, this field reduction is not having a major effect in the carrier density as can be appreciated in Fig. E.4. This can be explained by the fact that in the 5uc, the charge is already confined at the interface and there is no charge transfer going back to the surface, which is already saturated with OH. The later is traduced in an increase of the holes at the surface. In the 3uc case, where the heterostructure is already an insulator, the electric field is also reduced to 54 mV/Å and the system kept a finite electronic band gap.

LIST OF FIGURES

LIST OF TABLES

REFERENCES

[1] A. C. Garcia-Castro, A. H. Romero, and E. Bousquet, Phys. Rev. Lett. **116**, 117202 (2016).

[2] A. C. Garcia-Castro, N. A. Spaldin, A. H. Romero, and E. Bousquet, Phys. Rev. B **89**, 104107 (2014).

[3] A. C. Garcia-Castro, A. H. Romero, and E. Bousquet, Phys. Rev. B **90**, 064113 (2014).

[4] A. C. Garcia-Castro, A. H. Romero, and E. Bousquet, Physica Status Solidi (B) **252**, 689 (2015).

[5] A. C. Garcia-Castro, M. G. Vergniory, E. Bousquet, and A. H. Romero, Phys. Rev. B **93**, 045405 (2016).

[6] P. Borisov, T. A. Johnson, A. C. Garcia-Castro, A. KC, D. Schrecongost, C. Cen, H. Romero, Aldo, and D. Lederman, ACS Applied Materials and Interfaces **8**, 2694 (2016).

[7] W. Dai, S. Adhikari, A. C. Garcia-Castro, A. H. Romero, H. Lee, J.-W. Lee, S. Ryu, C.-B. Eom, and C. Cen, Nano Letters **16**, 2739 (2016).

[8] S. Adhikari, A. C. Garcia-Castro, A. H. Romero, S.-w. Park, C.-B. Eom, and C. Cen, Adv. Func. Mater. **Submitted**, (2016).

[9] S. Singh, A. C. Garcia-Castro, I. Valencia-Jaime, F. Munoz, and A. H. Romero, Adv. Mater. **To be submitted**, (2016).

[10] P. Borisov, T. A. Johnson, A. C. Garcia-Castro, E. Bousquet, K. Amit, D. Schrecongost, C. Cen, A. H. Romero, and D. Lederman, Journal of Applied Physics **To be submitted**, (2016).

[11] M. E. Lines and A. M. Glass, *Principles and applications of ferroelectrics and related materials*, clarendon press ed. (Oxford, 1977).

[12] G. Sághi-Szabó, R. E. Cohen, and H. Krakauer, Phys. Rev. Lett. **80**, 4321 (1998).

[13] N. A. Hill, J. Phys. Chem. B **104**, 6694 (2000).

[14] A. J. Lovinger, Science **220**, 1115 (1983).

[15] J. F. Scott and R. Blinc, Journal of Physics: Condensed Matter **23**, 113202 (2011).

[16] D. Guo and N. Setter, Macromolecules **46**, 1883 (2013).

[17] C. Ederer and N. A. Spaldin, Phys. Rev. B **74**, 020401 (2006).

[18] J. F. Scott and R. Blinc, Journal of physics. Condensed matter : an Institute of Physics journal **23**, 113202 (2011).

[19] E. Bousquet, M. Dawber, N. Stucki, C. Lichtensteiger, P. Hermet, S. Gariglio, J.-M. Triscone, and P. Ghosez, Nature **452**, 732 (2008).

[20] J. Haeni, P. Irvin, W. Chang, R. Uecker, and P. Reiche, Nature **430**, 583 (2004).

[21] H. Lee, H. Christen, and M. Chisholm, Nature **433**, 395 (2005).

[22] G. Hammerl and N. Spaldin, Science (New York, N.Y.) **332**, 922 (2011).

[23] M. J. Pitcher, P. Mandal, M. S. Dyer, J. Alaria, P. Borisov, H. Niu, J. B. Claridge, and M. J. Rosseinsky, Science **347**, 420 (2015).

[24] J. J. Videau and J. Portier, in *Inorganic Solid Fluorides*, edited by P. Hagenmuller (Academic Press, 1985) pp. 309 – 329.

[25] J. Ravez, in *Inorganic Solid Fluorides*, edited by P. Hagenmuller (Academic Press, 1985) pp. 469 – 475.

[26] R. Wolfe, A. J. Kurtzig, and R. C. LeCraw, Journal of Applied Physics **41**, 1218 (1970).

[27] J.-M. Dance and A. Tressaud, in *Inorganic Solid Fluorides*, edited by P. Hagenmuller (Academic Press, 1985) pp. 371 – 394.

[28] J.-M. Reau and J. Grannec, in *Inorganic Solid Fluorides*, edited by P. Hagenmuller (Academic Press, 1985) pp. 423 – 467.

[29] E. Kemnitz and S. Rudiger, "High surface area metal fluorides as catalysts," in *Functionalized Inorganic Fluorides* (John Wiley and Sons, Ltd, 2010) pp. 69–99.

[30] R. Martin, *Electronic Structure: Basic Theory and Practical Methods*, martin, richard ed. (Cambridge University Press, Cambridge, 2004).

[31] E. Kaxiras, *Atomic and Electronic Structure of Solids*, kaxiras, e ed. (Cambridge University Press, Cambridge, 2003).

[32] P. Hohenberg and W. Kohn, Phys. Rev. **136**, B864 (1964).

[33] W. Kohn and L. J. Sham, Phys. Rev. **140**, A1133 (1965).

[34] D. M. Ceperley and B. J. Alder, Phys. Rev. Lett. **45**, 566 (1980).

[35] P. Ghosez and J. Junquera, "First-principles modeling of ferroelectric oxide nanostructure," in *Handbook of Theoretical and Computational Nanotechnology*, edited by M. Rieth and W. Schommers (American Scientific Publishers, 2006) pp. 623–728.

[36] J. P. Perdew, K. Burke, and M. Ernzerhof, Phys. Rev. Lett. **77**, 3865 (1996).

[37] R. Armiento and A. E. Mattsson, Phys. Rev. B **72**, 085108 (2005).

[38] A. E. Mattsson and R. Armiento, Phys. Rev. B **79**, 155101 (2009).

[39] J. P. Perdew, A. Ruzsinszky, G. I. Csonka, O. A. Vydrov, G. E. Scuseria, L. A. Constantin, X. Zhou, and K. Burke, Phys. Rev. Lett. **100**, 136406 (2008).

[40] J. P. Perdew and Y. Wang, Phys. Rev. B **45**, 13244 (1992).

[41] R. Pentcheva and W. E. Pickett, Journal of Physics: Condensed Matter **22**, 043001 (2010).

[42] N. C. Bristowe, J. Varignon, D. Fontaine, E. Bousquet, and P. Ghosez, Nat Commun **6** (2015), article.

[43] A. I. Liechtenstein, V. I. Anisimov, and J. Zaanen, Phys. Rev. B **52**, R5467 (1995).

[44] S. L. Dudarev, G. A. Botton, S. Y. Savrasov, C. J. Humphreys, and A. P. Sutton, Phys. Rev. B **57**, 1505 (1998).

[45] B. Himmetoglu, A. Floris, S. de Gironcoli, and M. Cococcioni, International Journal of Quantum Chemistry **114**, 14 (2014).

[46] M. Cococcioni and S. de Gironcoli, Phys. Rev. B **71**, 035105 (2005).

[47] A. Georges, G. Kotliar, W. Krauth, and M. J. Rozenberg, Rev. Mod. Phys. **68**, 13 (1996).

[48] L. Hedin, Phys. Rev. **139**, A796 (1965).

[49] A. D. Becke, The Journal of Chemical Physics **98**, 5648 (1993).

[50] A. D. Becke, Phys. Rev. A **38**, 3098 (1988).

[51] J. P. Perdew, M. Ernzerhof, and K. Burke, The Journal of Chemical Physics **105**, 9982 (1996).

[52] D. I. Bilc, R. Orlando, R. Shaltaf, G.-M. Rignanese, J. Íñiguez, and P. Ghosez, Phys. Rev. B **77**, 165107 (2008).

[53] Z. Wu and R. E. Cohen, Phys. Rev. B **73**, 235116 (2006).

[54] J. Heyd, G. E. Scuseria, and M. Ernzerhof, The Journal of Chemical Physics **118**, 8207 (2003).

[55] A. V. Krukau, O. A. Vydrov, A. F. Izmaylov, and G. E. Scuseria, The Journal of Chemical Physics **125**, 224106 (2006).

[56] S. Baroni, S. de Gironcoli, A. Dal Corso, and P. Giannozzi, Rev. Mod. Phys. **73**, 515 (2001).

[57] X. Gonze, Phys. Rev. A **52**, 1086 (1995).

[58] K. Kunc and R. M. Martin, Phys. Rev. B **24**, 2311 (1981).

[59] H. J. Monkhorst and J. D. Pack, Phys. Rev. B **13**, 5188 (1976).

[60] D. S. Sholl and J. A. Steckel, "Dft calculations for surfaces of solids," in *Density Functional Theory* (John Wiley and Sons, Inc., 2009) pp. 83–112.

[61] D. R. Hamann, M. Schlüter, and C. Chiang, Phys. Rev. Lett. **43**, 1494 (1979).

[62] I. A. Kornev, L. Bellaiche, P. Bouvier, P.-E. Janolin, B. Dkhil, and J. Kreisel, Phys. Rev. Lett. **95**, 196804 (2005).

[63] I. a. Kornev and L. Bellaiche, Phase Transitions **80**, 385 (2007).

[64] P. E. Blöchl, Phys. Rev. B **50**, 17953 (1994).

[65] E. Bousquet, N. A. Spaldin, and K. T. Delaney, Phys. Rev. Lett. **106**, 107202 (2011).

[66] G. Kresse and J. Furthmüller, Phys. Rev. B **54**, 11169 (1996).

[67] G. Kresse and D. Joubert, Phys. Rev. B **59**, 1758 (1999).

[68] D. Hobbs, G. Kresse, and J. Hafner, Phys. Rev. B **62**, 11556 (2000).

[69] X. Gonze and C. Lee, Phys. Rev. B **55**, 10355 (1997).

[70] A. Togo, F. Oba, and I. Tanaka, Phys. Rev. B **78**, 134106 (2008).

[71] D. Vanderbilt, Journal of Physics and Chemistry of Solids **61**, 147 (2000).

[72] D. Roberto, O. Roberto, C. Bartolomeo, R. Carla, S. V. R., and Z.-W. C. M., Zeitschrift f¸r Kristallographie - Crystalline Materials **220**, 571 (2005).

[73] J. E. Dobson, G. Vignale, and M. P. Das, *International Journal*, Vol. 107 (Springer, Science+Business, New York, NY, 1998) pp. 1943–1953.

[74] D. S. Sholl and J. A. Steckel, "What is density functional theory?" in *Density Functional Theory* (John Wiley and Sons, Inc., 2009) pp. 1–33.

[75] D. S. Sholl and J. A. Steckel, "Dft calculations for simple solids," in *Density Functional Theory* (John Wiley and Sons, Inc., 2009) pp. 35–48.

[76] M. Fiebig, Journal of Physics D: Applied Physics **38**, R123 (2005).

[77] A. Poole, B. Roessli, O. Zaharko, and K. W. Kramer, Journal of Physics: Condensed Matter **23**, 266004 (2011).

[78] G. Nenert, Journal of Physics: Condensed Matter **20**, 335229 (2008).

[79] G. Nenert and T. T. M. Palstra, Journal of Physics: Condensed Matter **19**, 406213 (2007).

[80] W. Cochran, Phys. Rev. Lett. **3**, 412 (1959).

[81] P. Ghosez, X. Gonze, and J.-P. Michenaud, EPL (Europhysics Letters) **33**, 713 (1996).

[82] R. Cohen, Nature **358**, 136 (1992).

[83] P. Ghosez, J.-P. Michenaud, and X. Gonze, Phys. Rev. B **58**, 6224 (1998).

[84] P. Ghosez, E. Cockayne, U. V. Waghmare, and K. M. Rabe, Phys. Rev. B **60**, 836 (1999).

[85] M. Guennou, P. Bouvier, G. Garbarino, J. Kreisel, and E. K. H. Salje, Journal of Physics: Condensed Matter **23**, 485901 (2011).

[86] P. Edwardson, L. Boyer, R. Newman, D. Fox, J. Hardy, J. Flocken, R. Guenther, and W. Mei, Physical Review B **39**, 9738 (1989).

[87] Z. Friedman, M. Melamud, J. Makovsky, and H. Shaked, Phys. Rev. B **2**, 179 (1970).

[88] D. Babel, in *Structure and Bonding* (1967).

[89] J. W. Flocken, R. A. Guenther, J. R. Hardy, and L. L. Boyer, Phys. Rev. B **31**, 7252 (1985).

[90] W. Zhong, D. Vanderbilt, and K. M. Rabe, Phys. Rev. B **52**, 6301 (1995).

[91] D. Vanderbilt and W. Zhong, Ferroelectrics **206**, 181 (1998).

[92] N. A. Benedek and C. J. Fennie, The Journal of Physical Chemistry C **117**, 13339 (2013).

[93] S. Amisi, E. Bousquet, K. Katcho, and P. Ghosez, Phys. Rev. B **85**, 064112 (2012).

[94] A. Togo, F. Oba, and I. Tanaka, Phys. Rev. B **78**, 134106 (2008).

[95] X. Gonze, J.-M. Beuken, R. Caracas, F. Detraux, M. Fuchs, G.-M. Rignanese, L. Sindic, M. Verstraete, G. Zerah, F. Jollet, M. Torrent, A. Roy, M. Mikami, P. Ghosez, J.-Y. Raty, and D. Allan, Comp. Mater. Sci. **25**, 478 (2002).

[96] M. T. Dove, American Mineralogist **82**, 213 (1997).

[97] A. Katrusiak and A. Ratuszna, Solid State Communications **84**, 435 (1992).

[98] R. Shannon, Acta Crystallographica Section A: Crystal Physics **A32**, 751 (1976).

[99] H. Bethe, Annalen der Physik **395**, 133 (1929).

[100] E. Bousquet and P. Ghosez, Phys. Rev. B **74**, 180101 (2006).

[101] K. M. Rabe, C. Ahn, and J.-M. Triscone, *Springer* (2007) p. 398.

[102] P. Ghosez, X. Gonze, and J.-P. Michenaud, Ferroelectrics **194**, 39 (1997).

[103] I. a. Kornev and L. Bellaiche, Phase Transitions **80**, 385 (2007).

[104] F. Claeyssens, J. M. Oliva, D. Sanchez-Portal, and N. L. Allan, Chem. Commun. , 2440 (2003).

[105] D. Khomskii, in *Spin Electronics*, Lecture Notes in Physics, Vol. 569, edited by M. Ziese and M. Thornton (Springer Berlin Heidelberg, 2001) pp. 89–116.

[106] G. Sághi-Szabó, R. E. Cohen, and H. Krakauer, Phys. Rev. Lett. **80**, 4321 (1998).

[107] A. N. Morozovska, E. A. Eliseev, M. D. Glinchuk, L.-Q. Chen, and V. Gopalan, Phys. Rev. B **85**, 094107 (2012).

[108] C. N. R. Rao, Ferroelectrics **102**, 297 (1990).

[109] I. Žutić, J. Fabian, and S. Sarma, Rev. Mod. Phys. **76**, 234 (2004).

[110] H. Bea, M. Gajek, M. Bibes, and A. Barthemy, J. Phys. Cond. Matter **20**, 434221 (2008).

[111] P. Zubko, S. Gariglio, M. Gabay, P. Ghosez, and J.-M. Triscone, Annual Review of Condensed Matter Physics **2**, 141 (2011).

[112] Y.-H. Chu, L. W. Martin, M. B. Holcomb, and R. Ramesh, Materials Today **10**, 16 (2007).

[113] R. J. Angel, J. Zhao, and N. L. Ross, Phys. Rev. Lett. **95**, 025503 (2005).

[114] M. Murakami, K. Hirose, K. Kawamura, N. Sata, and Y. Ohishi, Science (New York, N.Y.) **304**, 855 (2004).

[115] T. Tsuchiya, J. Tsuchiya, K. Umemoto, and R. M. Wentzcovitch, Earth and Planetary Science Letters **224**, 241 (2004).

[116] K. Hirose, American Mineralogist **90**, 262 (2005).

[117] S. Tateno, K. Hirose, N. Sata, and Y. Ohishi, Phys. Chem. Minerals **32**, 721 (2005).

[118] C. D. Martin, W. a. Crichton, H. Liu, V. Prakapenka, J. Chen, and J. B. Parise, American Mineralogist **91**, 1703 (2006).

[119] H. Yusa, Y. Shirako, M. Akaogi, H. Kojitani, N. Hirao, Y. Ohishi, and T. Kikegawa, Inorganic Chemistry **51**, 6559 (2012).

[120] D. P. Dobson, S. a. Hunt, A. Lindsay-Scott, and I. G. Wood, Physics of the Earth and Planetary Interiors **189**, 171 (2011).

[121] Y. Shirako and H. Kojitani, American Mineralogist **97**, 159 (2012).

[122] N. A. Bogdanov, V. M. Katukuri, H. Stoll, J. van den Brink, and L. Hozoi, Phys. Rev. B **85**, 235147 (2012).

[123] T. B. Ballaran, R. G. Tronnes, and D. J. Frost, American Mineralogist **92**, 1760 (2007).

[124] Y. Shirako, H. Satsukawa, H. Kojitani, T. Katsumata, M. Yoshida, Y. Inaguma, K. Hiraki, T. Takahashi, K. Yamaura, E. Takayama-Muromachi, and M. Akaogi, J. Phys.: Conference Series **215**, 012038 (2010).

[125] H. Kojitani, Y. Shirako, and M. Akaogi, Physics of the Earth and Planetary Interiors **165**, 127 (2007).

[126] Y. Shirako, H. Satsukawa, X. X. Wang, J. J. Li, Y. F. Guo, M. Arai, K. Yamaura, M. Yoshida, H. Kojitani, T. Katsumata, Y. Inaguma, K. Hiraki, T. Takahashi, and M. Akaogi, Phys. Rev. B **83**, 174411 (2011).

[127] K. Ohgushi, Y. Matsushita, N. Miyajima, Y. Katsuya, M. Tanaka, F. Izumi, H. Gotou, Y. Ueda, and T. Yagi, Phys. Chem. Minerals **35**, 189 (2008).

[128] Y. Inaguma, K.-i. Hasumi, M. Yoshida, T. Ohba, and T. Katsumata, Inorg. Chem. **47**, 1868 (2008).

[129] Y. Shirako, H. Kojitani, M. Akaogi, K. Yamaura, and E. Takayama-Muromachi, Physics and Chemistry of Minerals **36**, 455 (2009).

[130] K. Yamaura, Y. Shirako, H. Kojitani, M. Arai, D. P. Young, M. Akaogi, M. Nakashima, T. Katsumata, Y. Inaguma, and E. Takayama-Muromachi, J. Am. Chem. Soc. **131**, 2722 (2009).

[131] M. Bremholm, S. E. Dutton, P. W. Stephens, and R. J. Cava, J. Solid State Chem. **184**, 601 (2011).

[132] S. Yakovlev, M. Avdeev, and M. Mezouar, J. Solid State Chem. **182**, 1545 (2009).

[133] F. L. Bernal, K. V. Yusenko, J. Sottmann, C. Drathen, J. Guignard, O. M. Lovvik, W. A. Crichton, and S. Margadonna, Inorganic Chemistry **53**, 12205 (2014), pMID: 25351883, http://dx.doi.org/10.1021/ic502224y .

[134] F. Birch, Phys. Rev. **71**, 809 (1947).

[135] X. Gonze, Phys. Rev. A **52**, 1086 (1995).

[136] X. Gonze, Phys. Rev. A **52**, 1096 (1995).

[137] P. Daniel, M. Rousseau, A. Desert, A. Ratuszna, and F. Ganot, Phys. Rev. B **51**, 12337 (1995).

[138] A. Lane, D. Sharp, and J. Barraclough, J. Chem. Soc. **94**, 94 (1971).

[139] V. Gava, A. L. Martinotto, and C. A. Perottoni, Phys. Rev. Lett. **109**, 195503 (2012).

[140] J. R. Shane, J. Appl. Phys. **38**, 1280 (1967).

[141] M. Akaogi, Y. Shirako, H. Kojitani, T. Nagakari, H. Yusa, and K. Yamaura, Physics of the Earth and Planetary Interiors **228**, 160 (2014).

[142] S. Tateno, K. Hirose, N. Sata, and Y. Ohishi, Phys. Earth and Planetary Interiors **181**, 54 (2010).

[143] M. O'keeffe, B. Hyde, and J. Bovin, Phys. Chem. Minerals **305**, 299 (1979).

[144] C. D. Martin and J. B. Parise, Earth and Planetary Science Letters **265**, 630 (2008).

[145] B. Beznosikov and K. Aleksandrov, Crystallography Reports **45**, 792 (2000).

[146] D. Babel and A. Tressaud, in *Inorganic Solid Fluorides*, edited by P. Hagenmuller (Academic Press, 1985) pp. 77 – 203.

[147] M. Aroyo, L, J. M. Perez-Mato, C. Capillas, E. Kroumova, S. Ivantchev, G. Madariaga, A. Kirov, and H. Wondratschek, Zeitschrift fur Kristallographie - Crystalline Materials **221**, 15 (2009).

[148] M. I. Aroyo, A. Kirov, C. Capillas, J. M. Perez-Mato, and H. Wondratschek, Acta Cryst **62**, 115 (2006).

[149] P. Anderson, Physical Review **79** (1950).

[150] J. Kanamori, Journal of Physics and Chemistry of Solids **10**, 87 (1959).

[151] J. C. Toledano and P. Toledano, *The Landau Theory of Phase Transitions* (World Scientific, Singapore, 1985).

[152] J. Kanamori, Prog. Theor. Phys. **17**, 177 (1957).

[153] J. Kanamori, Prog. Theor. Phys. **17**, 197 (1957).

[154] J. B. Goodenough, J. Phys. and Chem. Solid. **6**, 287 (1958).

[155] E. Bousquet and N. Spaldin, Phys. Rev. B **82**, 220402 (2010).

[156] I. Dzyaloshinsky, J. Phys. and Chem. Solid. **4**, 241 (1958).

[157] T. Moriya, Phys. Rev. **120**, 91 (1960).

[158] G. Maekawa, S., Tohyama, T., Barnes, S.E., Ishihara, S., Koshibae, W., Khaliullin, *Physics of Transition Metal Oxides* (Springer, Berlin, 2004).

[159] C. Xu, B. Xu, Y. Yang, H. Dong, A. R. Oganov, S. Wang, W. Duan, B. Gu, and L. Bellaiche, Phys. Rev. B **91**, 020101 (2015).

[160] L. Martin, Y.-H. Chu, and R. Ramesh, Materials Science and Engineering: R: Reports **68**, 89 (2010).

[161] M. Murakami, K. Hirose, K. Kawamura, N. Sata, and Y. Ohishi, Science **304**, 855 (2004).

[162] Y. Shirako, Y. Shi, A. Aimi, D. Mori, H. Kojitani, K. Yamaura, Y. Inaguma, and M. Akaogi, Journal of Solid State Chemistry **191**, 167 (2012).

[163] Y. Shirako, H. Satsukawa, X. X. Wang, J. J. Li, Y. F. Guo, M. Arai, K. Yamaura, M. Yoshida, H. Kojitani, T. Katsumata, Y. Inaguma, K. Hiraki, T. Takahashi, and M. Akaogi, Phys. Rev. B **83**, 174411 (2011).

[164] L. Du, X. Sheng, H. Weng, and X. Dai, EPL (Europhysics Letters) **101**, 27003 (2013).

[165] K. Yamaura, Y. Shirako, H. Kojitani, M. Arai, D. P. Young, M. Akaogi, M. Nakashima, T. Katsumata, Y. Inaguma, and E. Takayama-Muromachi, Journal of the American Chemical Society **131**, 2722 (2009).

[166] D. P. Dobson, S. A. Hunt, A. Lindsay-Scott, and I. G. Wood, Physics of the Earth and Planetary Interiors **189**, 171 (2011).

[167] C. Weingart, N. Spaldin, and E. Bousquet, Phys. Rev. B **86**, 094413 (2012).

[168] K. Momma and F. Izumi, Journal of Applied Crystallography **44**, 1272 (2011).

[169] H. J. Xiang, E. J. Kan, S.-H. Wei, M.-H. Whangbo, and X. G. Gong, Phys. Rev. B **84**, 224429 (2011).

[170] E. E. Rodriguez, F. Poineau, A. Llobet, B. J. Kennedy, M. Avdeev, G. J. Thorogood, M. L. Carter, R. Seshadri, D. J. Singh, and A. K. Cheetham, Phys. Rev. Lett. **106**, 067201 (2011).

[171] B. H. Kim and B. I. Min, New Journal of Physics **13**, 073034 (2011).

[172] W. Eerenstein, N. D. Mathur, and J. F. Scott, Nature **442**, 759 (2006).

[173] L. Martin, Y.-H. Chu, and R. Ramesh, Materials Science and Engineering: R: Reports **68**, 89 (2010).

[174] O. Diéguez, K. M. Rabe, and D. Vanderbilt, Phys. Rev. B **72**, 144101 (2005).

[175] E. Bousquet and N. Spaldin, Phys. Rev. Lett. **107**, 197603 (2011).

[176] C.-J. Eklund, C. Fennie, and K. Rabe, Phys. Rev. B **79**, 220101 (2009).

[177] T. Günter, E. Bousquet, a. David, P. Boullay, P. Ghosez, W. Prellier, and M. Fiebig, Phys. Rev. B **85**, 214120 (2012).

[178] C. Ederer and N. A. Spaldin, Phys. Rev. Lett. **95**, 257601 (2005).

[179] N. A. Hill, J. Phys. Chem. B , 6694 (2000).

[180] P. Berastegui, S. Hull, and S.-G. Eriksson, Journal of Physics: Condensed Matter **13**, 5077 (2001).

[181] E. H. Smith, N. A. Benedek, and C. J. Fennie, Inorganic Chemistry **54**, 8536 (2015).

[182] C.-g. Duan, W. Mei, J. Liu, W.-G. Yin, J. Hardy, R. Smith, M. Mehl, and L. Boyer, Phys. Rev. B **69**, 1 (2004).

[183] J. Young, A. Stroppa, S. Picozzi, and J. M. Rondinelli, Journal of Physics: Condensed Matter **27**, 283202 (2015).

[184] Y. J. Choi, C. L. Zhang, N. Lee, and S.-W. Cheong, Phys. Rev. Lett. **105**, 097201 (2010).

[185] S.-W. Cheong and M. Mostovoy, Nature Mater. **6**, 13 (2007).

[186] D. N. Argyriou, Physics **3**, 72 (2010).

[187] G. Bester, X. Wu, D. Vanderbilt, and A. Zunger, Phys. Rev. Lett. **96**, 187602 (2006).

[188] S. Sanna, C. Thierfelder, S. Wippermann, T. P. Sinha, and W. G. Schmidt, Phys. Rev. B **83**, 054112 (2011).

[189] T. Furuta and K. Miura, Solid State Communications **150**, 2350 (2010).

[190] J. R. Shane, Journal of Applied Physics **38**, 1280 (1967).

[191] A. S. Borovik-Romanov and H. Grimmer, International Tables for Crystallography **D** (2006).

[192] V. J. Folen, G. T. Rado, and E. W. Stalder, Phys. Rev. Lett. **6**, 607 (1961).

[193] E. Kita, K. Siratori, and A. Tasaki, Journal of Applied Physics **50**, 7748 (1979).

[194] H. Wiegelmann, A. G. M. Jansen, P. Wyder, J.-P. Rivera, and H. Schmid, Ferroelectrics **162**, 141 (1994).

[195] J. Íñiguez, Phys. Rev. Lett. **101**, 117201 (2008).

[196] E. Bousquet, N. A. Spaldin, and K. T. Delaney, Phys. Rev. Lett. **106**, 107202 (2011).

[197] J. Mannhart, D. Blank, H. Hwang, A. Millis, and J.-M. Triscone, MRS Bulletin **33**, 1027 (2008).

[198] A. Joshua, S. Pecker, J. Ruhman, E. Altman, and S. Ilani, Nature communications **3**, 1129 (2012).

[199] S. Caprara, F. Peronaci, and M. Grilli, Phys. Rev. Lett. **109**, 196401 (2012).

[200] B. R. K. Nanda and S. Satpathy, Phys. Rev. B **81**, 224408 (2010).

[201] N. Benedek and C. Fennie, Phys. Rev. Lett. **106**, 107204 (2011).

[202] A. T. Mulder, N. A. Benedek, J. M. Rondinelli, and C. J. Fennie, Advanced Functional Materials **23**, 4810 (2013).

[203] Z. Zanolli, J. C. Wojdeł, J. Íñiguez, and P. Ghosez, Phys. Rev. B **88**, 060102 (2013).

[204] M. A. Carpenter, E. K. H. Salje, and C. J. Howard, Phys. Rev. B **85**, 224430 (2012).

[205] W. Pang, R. L. Stamps, L. Malkinski, Z. Celinski, and D. Skrzypek, Journal of Applied Physics **95**, 7309 (2004).

[206] S. Widuch, R. L. Stamps, D. Skrzypek, and Z. Celinski, Journal of Physics D: Applied Physics **44**, 415003 (2011).

[207] E. J. Moon, Y. Xie, E. D. Laird, D. J. Keavney, C. Y. Li, and S. J. May, Journal of the American Chemical Society **136**, 2224 (2014).

[208] M. AI-Mamouri, P. P. Edwards, C. Greaves, and M. Slaski, Nature **369**, 382 (1994).

[209] M. Sturza, S. Daviero-Minaud, H. Kabbour, O. Gardoll, and O. Mentre, Chemistry of Materials **22**, 6726 (2010).

[210] M. Sturza, H. Kabbour, S. Daviero-Minaud, D. Filimonov, K. Pokholok, N. Tiercelin, F. Porcher, L. Aldon, and O. Mentre, Journal of the American Chemical Society **133**, 10901 (2011).

[211] A. D. Becke, The Journal of Chemical Physics **98**, 1372 (1993).

[212] A. D. Becke, The Journal of Chemical Physics **96**, 2155 (1992).

[213] in *Ternary compounds, organic semiconductors*, edited by O. Madelung, U. Rassler, and M. Schulz (Springer Berlin Heidelberg, 2000) pp. 1 – 8.

[214] P. Yu, Y. Chu, and R. Ramesh, Materials Today **15**, 320 (2012).

[215] N. Bristowe, E. Artacho, and P. Littlewood, Phys. Rev. B **80**, 045425 (2009).

[216] K. Yamauchi and S. Picozzi, Phys. Rev. Lett. **105**, 107202 (2010).

[217] P. D. C. King, R. H. He, T. Eknapakul, P. Buaphet, S.-K. Mo, Y. Kaneko, S. Harashima, Y. Hikita, M. S. Bahramy, C. Bell, Z. Hussain, Y. Tokura, Z.-X. Shen, H. Y. Hwang, F. Baumberger, and W. Meevasana, Phys. Rev. Lett. **108**, 117602 (2012).

[218] A. D. Caviglia, M. Gabay, S. Gariglio, N. Reyren, C. Cancellieri, and J.-M. Triscone, Phys. Rev. Lett. **104**, 126803 (2010).

[219] Z. Zhong, A. Tóth, and K. Held, Phys. Rev. B **87**, 161102 (2013).

[220] S. Hurand, A. Jouan, C. Feuillet-Palma, G. Singh, J. Biscaras, E. Lesne, N. Reyren, A. Barthélémy, M. Bibes, J. E. Villegas, C. Ulysse, X. Lafosse, M. Pannetier-Lecoeur, S. Caprara, M. Grilli, J. Lesueur, and N. Bergeal, Scientific Reports **5**, 12751 EP (2015).

[221] Y. A. Bychkov and E. I. Rashba, Journal of Physics C: Solid State Physics **17**, 6039 (1984).

[222] H. Nakamura, T. Koga, and T. Kimura, Phys. Rev. Lett. **108**, 206601 (2012).

[223] H. Nakamura and T. Kimura, Phys. Rev. B **80**, 121308 (2009).

[224] H. Lee and H. J. Choi, Phys. Rev. B **86**, 045437 (2012).

[225] S. R. Park and C. Kim, Journal of Electron Spectroscopy and Related Phenomena **201**, 6 (2015), special issue on electron spectroscopy for Rashba spin-orbit interaction.

[226] K. Shanavas, Journal of Electron Spectroscopy and Related Phenomena **201**, 121 (2015).

[227] K. Ishizaka, M. S. Bahramy, H. Murakawa, M. Sakano, T. Shimojima, T. Sonobe, K. Koizumi, S. Shin, H. Miyahara, A. Kimura, K. Miyamoto, T. Okuda, H. Namatame, M. Taniguchi, R. Arita, N. Nagaosa, K. Kobayashi, Y. Murakami, R. Kumai, Y. Kaneko, Y. Onose, and Y. Tokura, Nat Mater **10**, 521 (2011).

[228] O. Bleibaum and S. Wachsmuth, Phys. Rev. B **74**, 195330 (2006).

[229] R. Moriya, K. Sawano, Y. Hoshi, S. Masubuchi, Y. Shiraki, A. Wild, C. Neumann, G. Abstreiter, D. Bougeard, T. Koga, and T. Machida, Phys. Rev. Lett. **113**, 086601 (2014).

[230] B. Yin, P. Aguado-Puente, S. Qu, and E. Artacho, Phys. Rev. B **92**, 115406 (2015).

[231] J. T. Zhang, J. Kim, M. Huefner, C. Ye, S. Kim, P. C. Canfield, R. Prozorov, O. M. Auslaender, and J. E. Hoffman, Phys. Rev. B **92**, 134509 (2015).

[232] B. Morosin, E. Venturini, J. Schirber, R. Dunn, and P. Newcomer, Physica C: Superconductivity **241**, 181 (1995).

[233] K. Ueno, S. Nakamura, H. Shimotani, H. T., Yuan, N. Kimura, T. Nojima, H. Aoki, Y. Iwasa, and M. Kawasaki, Nat Nano **6**, 408 (2011).

[234] J. B. Goodenough and M. Longo, "3 crystallographic and magnetic properties of perovskite and perovskite-related compounds," in *Group III Condensed Matter, Part A*, Vol. 4A, edited by K.-H. Hellwege and A. M. Hellwege (Springer, Landolt-Bornstein, 1970) pp. 126–.

[235] E. F. Bertaut (Spin Configurations of Ionic Structures: Theory and Practice, New York, vol 3, (1963)).

[236] M. DiDomenico, M. Eibschütz, H. Guggenheim, and I. Camlibel, Solid State Communications **7**, 1119 (1969).

[237] E. T. Keve, S. C. Abrahams, and J. L. Bernstein, The Journal of Chemical Physics **53**, 3279 (1970).

[238] D. E. Cox, M. Eibschütz, H. J. Guggenheim, and L. Holmes, Journal of Applied Physics **41**, 943 (1970).

[239] C. Ederer and N. A. Spaldin, Phys. Rev. B **74**, 024102 (2006).

[240] M. Eibschütz, H. Guggenheim, S. Wemple, I. Camlibel, and M. DiDomenico, Physics Letters A **29**, 409 (1969).

[241] M. Eibschütz, L. Holmes, H. J. Guggenheim, and D. E. Cox, Phys. Rev. B **6**, 2677 (1972).

[242] R. Zorin, B. Al'shin, and D. Astrov, Soviet Physics JETP **35**, 634 (1972).

[243] M. Bibes and A. Barthélémy, Electron Devices, IEEE Transactions on **54**, 1003 (2007).

[244] S. Fusil, V. Garcia, A. Barthélémy, and M. Bibes, Annual Review of Materials Research **44**, 91 (2014).

[245] L. Martin, Y.-H. Chu, and R. Ramesh, Materials Science and Engineering: R: Reports **68**, 89 (2010).

[246] N. Reyren, S. Thiel, A. D. Caviglia, L. F. Kourkoutis, G. Hammerl, C. Richter, C. W. Schneider, T. Kopp, A.-S. Rüetschi, D. Jaccard, M. Gabay, D. A. Muller, J.-M. Triscone, and J. Mannhart, Science **317**, 1196 (2007).

[247] J. Shen, H. Lee, R. Valentí, and H. O. Jeschke, Phys. Rev. B **86**, 195119 (2012).

[248] A. F. Santander-Syro, O. Copie, T. Kondo, F. Fortuna, S. Pailhès, R. Weht, X. G. Qiu, F. Bertran, A. Nicolaou, a. Taleb-Ibrahimi, P. Le Fèvre, G. Herranz, M. Bibes, N. Reyren, Y. Apertet, P. Lecoeur, a. Barthélémy, and M. J. Rozenberg, Nature **469**, 189 (2011).

[249] P. D. C. King, S. McKeown Walker, A. Tamai, A. de la Torre, T. Eknapakul, P. Buaphet, S.-K. Mo, W. Meevasana, M. S. Bahramy, and F. Baumberger, Nature Communications **5**, 1 (2014).

[250] A. F. Santander-Syro, F. Fortuna, C. Bareille, T. C. Rödel, G. Landolt, N. C. Plumb, J. H. Dil, and M. Radović, Nat. Mater **13**, 1085 (2014).

[251] M. Dawber and E. Bousquet, MRS Bulletin **38**, 1048 (2013).

[252] N. C. Bristowe, P. Ghosez, P. B. Littlewood, and E. Artacho, Journal of Physics: Condensed Matter **26**, 143201 (2014).

[253] Z. Q. Liu, C. J. Li, W. M. Lü, X. H. Huang, Z. Huang, S. W. Zeng, X. P. Qiu, L. S. Huang, A. Annadi, J. S. Chen, J. M. D. Coey, T. Venkatesan, and Ariando, Phys. Rev. X **3**, 021010 (2013).

[254] A. H. Romero and F. Munoz, "Pyprocar," `http://sourceforge.net/p/pyprocar/PyPROCAR/HEAD/tree/` (2015).

[255] S. McKeown Walker, A. de la Torre, F. Y. Bruno, A. Tamai, T. K. Kim, M. Hoesch, M. Shi, M. S. Bahramy, P. D. C. King, and F. Baumberger, Phys. Rev. Lett. **113**, 177601 (2014).

[256] N. C. Plumb, M. Salluzzo, E. Razzoli, M. Månsson, M. Falub, J. Krempasky, C. E. Matt, J. Chang, M. Schulte, J. Braun, H. Ebert, J. Minár, B. Delley, K.-J. Zhou, T. Schmitt, M. Shi, J. Mesot, L. Patthey, and M. Radović, Phys. Rev. Lett. **113**, 086801 (2014).

[257] G. Khalsa, B. Lee, and A. H. MacDonald, Phys. Rev. B **88**, 041302 (2013).

[258] W. D. Rice, P. Ambwani, M. Bombeck, J. D. Thompson, G. Haugstad, C. Leighton, and S. a. Crooker, Nature materials **13**, 481 (2014).

[259] H. Choi, J. D. Song, K.-R. Lee, and S. Kim, Inorganic Chemistry **54**, 3759 (2015).

[260] L. P. Gor'kov, Journal of Physics: Condensed Matter **27**, 252001 (2015).

[261] C. Lin and A. A. Demkov, Phys. Rev. Lett. **111**, 217601 (2013).

[262] W. Meevasana, P. D. C. King, R. H. He, S.-K. Mo, M. Hashimoto, a. Tamai, P. Songsiriritthigul, F. Baumberger, and Z.-X. Shen, Nature materials **10**, 114 (2011).

[263] G. Hautier, A. Miglio, D. Waroquiers, G.-M. Rignanese, and X. Gonze, Chemistry of Materials **26**, 5447 (2014).

[264] F. Reinert, G. Nicolay, S. Schmidt, D. Ehm, and S. Hüfner, Phys. Rev. B **63**, 115415 (2001).

[265] O. Krupin, G. Bihlmayer, K. Starke, S. Gorovikov, J. E. Prieto, K. Döbrich, S. Blügel, and G. Kaindl, Phys. Rev. B **71**, 201403 (2005).

[266] J. P. Perdew and A. Zunger, Phys. Rev. B **23**, 5048 (1981).

[267] A. I. Liechtenstein, V. I. Anisimov, and J. Zaanen, Phys. Rev. B **52**, R5467 (1995).

[268] B. J. Kennedy, C. J. Howard, and B. C. Chakoumakos, Phys. Rev. B **60**, 2972 (1999).

[269] D. Vanderbilt, Journal of Physics and Chemistry of Solids **61**, 147 (2000).

[270] N. A. Benedek, J. M. Rondinelli, H. Djani, P. Ghosez, and P. Lightfoot, Dalton Trans. **44**, 10543 (2015).

[271] J. Sánchez-Barriga, A. Varykhalov, J. Braun, S.-Y. Xu, N. Alidoust, O. Kornilov, J. Minár, K. Hummer, G. Springholz, G. Bauer, R. Schumann, L. V. Yashina, H. Ebert, M. Z. Hasan, and O. Rader, Phys. Rev. X **4**, 011046 (2014).

[272] C.-H. Park and S. G. Louie, Phys. Rev. Lett. **109**, 097601 (2012).

[273] C. Jozwiak, C.-H. Park, K. Gotlieb, C. Hwang, D.-H. Lee, S. G. Louie, J. D. Denlinger, C. R. Rotundu, R. J. Birgeneau, Z. Hussain, and A. Lanzara, Nature Physics **9**, 293 (2013).

[274] J. M. Rondinelli and N. A. Spaldin, Phys. Rev. B **82**, 113402 (2010).

[275] T. Kuschel and G. Reiss, Nature Nanotechnology **10**, 22 (2014).

[276] W. Zhang, M. B. Jungfleisch, W. Jiang, J. Sklenar, F. Y. Fradin, J. E. Pearson, J. B. Ketterson, and A. Hoffmann, Journal of Applied Physics **117**, 172610 (2015).

[277] J. C. Ho, R. Yerushalmi, Z. A. Jacobson, Z. Fan, R. L. Alley, and A. Javey, Nat Mater **7**, 62 (2008).

[278] P. Zhang, E. Tevaarwerk, B.-N. Park, D. E. Savage, G. K. Celler, I. Knezevic, P. G. Evans, M. A. Eriksson, and M. G. Lagally, Nature **439**, 703 (2006).

[279] C. Di Valentin, G. Pacchioni, and A. Selloni, Phys. Rev. Lett. **97**, 166803 (2006).

[280] P. Strobel, M. Riedel, J. Ristein, and L. Ley, Nature **430**, 439 (2004).

[281] C. Coletti, C. Riedl, D. S. Lee, B. Krauss, L. Patthey, K. von Klitzing, J. H. Smet, and U. Starke, Phys. Rev. B **81**, 235401 (2010).

[282] S. Kobayashi, T. Nishikawa, T. Takenobu, S. Mori, T. Shimoda, T. Mitani, H. Shimotani, N. Yoshimoto, S. Ogawa, and Y. Iwasa, Nat. Mater. **3**, 317 (2004).

[283] J. Mannhart and D. G. Schlom, Science **327**, 1607 (2010).

[284] S. Thiel, G. Hammerl, A. Schmehl, C. W. Schneider, and J. Mannhart, Science **313**, 1942 (2006).

[285] B. Kalisky, J. A. Bert, B. B. Klopfer, C. Bell, H. K. Sato, M. Hosoda, Y. Hikita, H. Y. Hwang, and K. A. Moler, Nat Commun **3**, 922 (2012).

[286] P. Irvin, Y. Ma, D. F. Bogorin, C. Cen, C. W. Bark, C. M. Folkman, C.-B. Eom, and J. Levy, Nat Photon **4**, 849 (2010).

[287] N. Nakagawa, H. Y. Hwang, and D. A. Muller, Nat Mater **5**, 204 (2006).

[288] A. Janotti, L. Bjaalie, L. Gordon, and C. G. Van de Walle, Phys. Rev. B **86**, 241108 (2012).

[289] C. Cen, S. Thiel, J. Mannhart, and J. Levy, Science **323**, 1026 (2009).

[290] F. Bi, D. F. Bogorin, C. Cen, C. W. Bark, J.-W. Park, C.-B. Eom, and J. Levy, Applied Physics Letters **97**, 173110 (2010).

[291] C. Cen, S. Thiel, G. Hammerl, C. W. Schneider, K. E. Andersen, C. S. Hellberg, J. Mannhart, and J. Levy, Nat Mater **7**, 298 (2008).

[292] J. Neugebauer and M. Scheffler, Phys. Rev. B **46**, 16067 (1992).

[293] C. L. Jia, S. B. Mi, M. Faley, U. Poppe, J. Schubert, and K. Urban, Phys. Rev. B **79**, 081405 (2009).

[294] M. Gabay and J.-M. Triscone, Nat Phys **9**, 610 (2013), news and Views.

[295] H. Peng, H. J. Xiang, S.-H. Wei, S.-S. Li, J.-B. Xia, and J. Li, Phys. Rev. Lett. **102**, 017201 (2009).

[296] S. Nazir, C. Bernal, and K. Yang, ACS Applied Materials & Interfaces **7**, 5305 (2015).

DECLARATION

This thesis is a presentation of my original research work. Wherever contributions of others are involved, every effort is made to indicate this clearly, with due reference to the literature, and acknowledgement of collaborative research and discussions. The work was done under the guidance of Professor Aldo Humberto Romero Castro at Cinvestav-Querétaro and Dr. Eric Bousquet at Université de Liège.

Querétaro, Abril 2016

Andrés Camilo García
Castro, Abril 2016

EL JURADO DESIGNADO POR LA UNIDAD QUERÉTARO DEL CENTRO DE INVESTIGACIÓN Y DE ESTUDIOS AVANZADOS DEL INSTITUTO POLITÉCNICO NACIONAL Y LA UNIVERSITÉ DE LIÈGE, APROBÓ LA TESIS DOCTORAL DE ANDRÉS CAMILO GARCÍA CASTRO TITULADA: "ESTUDIO Y CARACTERIZACIÓN DE MATERIALES MULTIFERROICOS Y MAGNETOELECTRICOS MEDIANTE CALCULOS DE PRIMEROS PRINCIPIOS", FIRMAN AL CALCE DE COMÚN ACUERDO LOS INTEGRANTES DE DICHO JURADO, EN LA CIUDAD DE QUERÉTARO, QRO., A LOS DOCE DÍAS DEL MES DE ABRIL DEL DOS MIL DIECISÉIS.

Dr. Aldo Humberto Romero Castro, CINVESTAV-Querétaro

Dr. Eric Bousquet, Université de Liège

Dra. Nicola Spaldin, ETH-Zürich

Dr. Philippe Ghosez, Université de Liège

Dra. Rebeca Castanedo Pérez, CINVESTAV-Querétaro

Dr. Sergio Jiménez Sandoval, CINVESTAV-Querétaro

Dr. Arturo Mendoza Galván, CINVESTAV-Querétaro

THE THEIS JURY DESIGNATED BY THE CENTRO DE INVESTIGACIÓN Y DE ESTUDIOS AVANZADOS DEL INSTITUTO POLITÉCNICO NACIONAL QUERETARO UNIT AND THE UNIVERSITÉ DE LIÈGE, APPROVED THE PH.D THESIS OF ANDRÉS CAMILO GARCÍA CASTRO ENTITLED "STUDY AND CHARACTERIZATION OF MAGNETIC AND MULTIFERROIC MATERIALS BY FIRST-PRINCIPLES CALCULATIONS". BELOW THE MEMBERS OF THIS JURY SIGN IN COMMUN AGREEMENT IN THE CITY OF QUERETARO, QRO., AT THE TWELVE DAYS OF APRIL OF TWO THOUSAND AND SIXTEEN.

Dr. Aldo Humberto Romero Castro, CINVESTAV-Querétaro

Dr. Eric Bousquet, Université de Liège

Dra. Nicola Spaldin, ETH-Zürich

Dr. Philippe Ghosez, Université de Liège

Dra. Rebeca Castanedo Pérez, CINVESTAV-Querétaro

Dr. Sergio Jiménez Sandoval, CINVESTAV-Querétaro

Dr. Arturo Mendoza Galván, CINVESTAV-Querétaro